Department of Spatial Sciences

Validating methods to infer mass changes from satellite gravity measurements using Synthetic Earth Gravity Modelling

Ira Mutiara Anjasmara

This thesis is presented for the Degree of
Doctor of Philosophy
of
Curtin University

May 2013

Declarations

To the best of my knowledge and belief this thesis contains no material previously published by any other person except where due acknowledgement has been made.

This thesis contains no material which has been accepted for the award of any other degree or diploma in any university.

Signature: .....

Date: .....

Abstract

Knowledge of the Earth's gravity field has been significantly improved by the introduction of the dedicated satellite missions CHAMP (Challenging Mini-satellite Payload), GRACE (Gravity Recovery and Climate Experiment) and GOCE (Gravity field and Ocean Circulation Explorer). These missions indirectly derive mass changes from detected gravity changes with unprecedented high spatial and temporal resolution and accuracy. This has gained much interest amongst all geosciences as tool for improved understanding of Earth's processes.

To infer mass changes from gravity changes, various methods have been proposed. Due to the presence of high-frequency errors and noise, these techniques frequently apply filters that imply spatial smoothing, which can introduce considerable errors into the inferred masses due to leakage.

This study validates mass estimation techniques based on changes of the Earth's gravitational potential expressed in spherical harmonics. A closed-loop validation procedure based on synthetic Earth gravity modelling is applied on simulated mass distributions. Specific focus is on the leakage properties introduced by isotropic and anisotropic smoothing techniques on the inferred mass.

The results of this study show that the use of filter techniques can introduce significant leakage effects leading to a loss of signal of almost 70% under extreme circumstances. Furthermore, the smoothing filters introduce distortions so that often the inferred mass distribution has little in common with the spatial extent

of the simulated mass. Previously not very well known, the performance of the mass recovery depends on the geographic location with better recovery for masses located at higher geographic latitude.

Keywords: *Space gravity, spatial and spectral leakage, validation, synthetic Earth gravity modelling, isotropic and anisotropic filters, GRACE*

Acknowledgements

First of all I would like to express the best gratitude to my supervisor, Assoc. Prof Michael Kuhn, for his encouragement, guidance, support and supervision throughout this PhD study. I am indebted to him not only for scientific supervision, but also for his understanding, help, and friendship. I am also grateful to my co-supervisor, Assoc. Prof Joseph Awange, particularly for his support and advices.

I acknowledge Curtin University for Curtin Strategic International Research Scholarship (CSIRS) award, the Department of Spatial Sciences and the Institute of Geoscience Research (TIGeR) for the funding of my PhD scholarship. In addition, I would like to thank Oliver Baur and Michael Kuhn for providing me the routines for mass estimate calculation, also Jürgen Kusche and R. Rietbroek for the information and routine to extract the DDK filter.

Thanks are also extended to all current and former members of Western Australian Centre for Geodesy, especially Mick Filmer, Neda Darbeheshti, Sten Claessens, David Belton, Kevin Fleming and Christian Hirt for their friendship and help on different stages of this research. In general I would like to thank all staff at the Department of Spatial Sciences, who have contributed to the enjoyable working environment.

Finally, I would like to thank my husband Iing for his love and support for me to finish up this PhD. I am also grateful to our son, Zaidan, who always cheers my days up. I am truly indebted to my parents Nono and Atik for their support and practical assistance, especially over the last two years.

Table of Contents

List of Figures

List of Tables

List of Acronyms

CHAMP	Challenging Mini-satellite Payload	1
CNES	Centre National d'Etudes Spatiales	2
CODATA	Committee on Data for Science and Technology	11
EGM	Earth Gravitational Model	30
EWH	Equivalent Water Height	109
FGM	Forward Gravity Modelling	3
GBVP	Geodetic Boundary Value Problem	15
GFZ	Geo Forschungs Zentrum (Postdam)	2
GGM	Global Geopotential Model	15
GNSS	Global Navigation Satellite System	31
GOCE	Gravity Field and Steady-State Ocean Circulation Explorer	1
GPS	Global Positioning System	25
GRACE	Gravity Recovery and Climate Experiment	1
ITG	Institute of Theoretical Geodesy	2
JPL	Jet Propulsion Laboratory	2
MASCONS	Mass Concentrations	7
PAGEOS	Passive Geodetic Satellite	24
SDS	Science Data System	2
SEGM	Synthetic Earth Gravity Model	4
SHC	Spherical Harmonic Coefficients	15
SST	Satellite-to-Satellite Tracking	24
TWS	Terrestrial Water Storage	46
US NRC	the United States National Research Council	2
UTCSR	University of Texas Centre for Space Research	2

List of Symbols

b	parameter that characterises the smoothing process	58
C_{lm}, S_{lm}	gravity field SHC / Stokes coefficients	54
$\bar{C}_{lm}, \bar{S}_{lm}$	fully normalized gravity field SHC	15
$\bar{c}_{lm}$	changes of the gravitational potential	50
D	spatial-scale (half wavelength given in km)	15
$D\phi$	spatial-scale (half wavelength given in km) along a parallel	15
dm	infinitesimal small mass element	12
dv	infinitesimal small volume element	12
ΔN	vertical separation between two equipotential surfaces	13
$\Delta C_{lm}, \Delta S_{lm}$	time-variable SHC	52
$\Delta\kappa$	change in surface density	52
δg	gravity disturbance	19
Δg	gravity anomaly	19
ΔV	potential differences between two equipotential surfaces	14
d^o	ocean depth	36
$\vec{F}$	gravitational force	10
G	Newton's gravitational constant	10
g	magnitude of local gravity acceleration	14
$\vec{g}$	gravitational acceleration or gravitational attraction	12
γ	mean gravity (on reference ellipsoid)	18
$\bar{h}_{lm}$	height coefficient	49
h^t	topographic height	36
k_l	load Love number	49

Chapter 1

Introduction

1.1 Background

Global observation of both the static and time-variable part of the Earth's gravity field has been significantly improved with the launch of the three dedicated satellite missions Challenging Mini-satellite Payload (CHAMP), Gravity Recovery and Climate Experiment (GRACE) and Gravity Field and Steady-State Ocean Circulation Explorer (GOCE). While the CHAMP and GOCE missions are primarily designed to observe the static part of Earth's gravity, the GRACE mission specifically targets the monitoring of temporal changes, which are of primary focus within this study. Since its launch in 2002, GRACE provides monthly solutions (observed approx. every 10 days) of the Earth's gravity field with near-global coverage and with unprecedented accuracy and spatial resolution (e.g., Tapley et al., 2004a,b).

The GRACE mission is specifically designed to monitor changes in the Earth gravity field as a result of mass changes (e.g. mass transport), which in turn are taken as indicators for Earth system changes (e.g., Tapley et al., 2004a,b; Wahr et al., 2004; Ramillien et al., 2004; Chambers, 2006). The success of this mission triggered many new studies in all geoscience areas dealing with geodynamic processes (e.g., Beutler et al., 2003) such as changes in the cryosphere and hydrosphere as well as Earth's crust. As of 2012, the expected mission life-time of GRACE has more than doubled considering a designed life-time of five years (e.g., Chen et al., 2006b). As of today, GRACE is still operational, though with longer

data gaps due to power constraints (see UTCSR, 2013; JPL NASA, 2013; GFZ Postdam, 2013). The extended life-time is now providing an excellent constraint for many global and regional geodynamic processes. As the GRACE mission life-time is expected to end in 2014/2015 (GFZ Postdam, 2013), a GRACE-Follow-On mission has been recommended by the United States National Research Council (US NRC) for launch in the 2016-2020 time frame (Committee on Earth Science and Applications from Space: A Community Assessment and Strategy for the Future, National Research Council, 2007). The new mission is anticipated to operate with improved performances with respect to the current one (e.g., Cazenave and Chen, 2010).

Combined monthly GRACE gravity solutions are mostly provided in form of spherical harmonic representations of the Earth's external gravitational potential (e.g., GRACE Level-2 data). From the start of the mission these solutions have been generated and provided by three major processing centres of the Science Data Centre (SDS) (Cazenave and Chen, 2010): (1) Centre for Space Research University of Texas (UTCSR), (2) GeoForschungsZentrum Potsdam (GFZ) and (3) Jet Propulsion Laboratory (JPL). GRACE gravity field monthly and 10 days solutions are also provided by several other groups. They include the Goddard Space Flight Centre - NASA (Rowlands et al., 2002), the Centre National d'Etudes Spatiales (CNES)(Lemoine et al., 2007b), the Delft Institute of Earth Observation and Space Systems (Klees et al., 2008) and the Institute of Theoretical Geodesy (ITG) at the University of Bonn (Eicker, 2008) .

The time-variable gravity data provided by these processing centres are commonly used to infer changes of the Earth's mass distribution by applying different techniques (see e.g., Awange et al., 2009). Each of these techniques has its advantages and disadvantages in terms of their ability to resolve spatial and/or temporal mass variations (see e.g., Swenson and Wahr, 2002). Of particular interest are spatial and spectral leakage that can adversely affect mass change estimates.

According to Seo and Wilson (2005), the success of inferring mass changes from GRACE data depends on how well the method extracts local mass variation and

reduces errors (i.e., measurement error, leakage error and atmospheric pressure error). This is directly related to the use of filtering and smoothing methods and on how the leakage errors are dealt with (e.g., Baur et al., 2009). In addition, according to Lelgemann and Cui (2003), a good understanding for all possible shortcomings in the data analysis is required in order to avoid an interpretation of 'geodetic observation errors' as physical signals of mass redistributions.

Leakage is introduced in the mass recovery process as the result of spatial averaging and limited spectral resolution for the representation of the gravitational field data (e.g., Chen et al., 2006b). Spectral leakage appears when band-limiting the original signal and high-frequency signals or errors are mapped into lower frequencies so that producing unrealistic low-frequency signals (e.g., Baur et al., 2009). Spatial leakage occurs when spatial filtering (smoothing) is applied on the original signal, causing the recovered signal to spread outside the spatial extent of the original signal (over the whole globe; e.g., Chen et al., 2006d).

This study will assess leakage errors introduced by three main filtering techniques which are all based on the spherical harmonic approach as explained by Wahr et al. (1998). The assessed techniques are: (1) Gaussian isotropic filter (e.g., Wahr et al., 1998); (2) Han's anisotropic filter (e.g., Han et al., 2005a); (3) Kusche's decorrelated-anisotropic (DDK) filter (e.g., Kusche, 2007; Kusche et al., 2009).

1.1.1 Forward Gravity Modelling of Time-variable Gravity

Forward Gravity Modelling (FGM) describes the process of modelling the gravitational signal of a given mass distribution through the evaluation of Newton's volume integral (e.g., Blakely, 1996; Hofmann-Wellenhof and Moritz, 2005). FGM can be categorised into space-domain and spectral-domain techniques (e.g., Kuhn and Seitz, 2005). Space-domain techniques are based on the direct evaluation of Newton's volume integral through integration techniques (e.g., Nagy, 1966; Kuhn, 2003; Heck and Seitz, 2007). Spectral-domain techniques are based on the transformation of Newton's volume integral into the spectral domain using potential series expansions in powers of topographic heights (e.g., Rummel et al., 1988;

Wieczorek and Phillips, 1998; Kuhn and Featherstone, 2005; Hirt and Kuhn, 2012). An alternative procedure, combining space and spectral domain techniques, is given through the computation of gravitational function values on a regular grid followed by a spherical harmonic analysis.

Based on reasonably realistic information of the Earth's mass distribution, FGM can be used to reconstruct the Earth's gravity field as done in the construction of so-called Synthetic Earth Gravity Models (SEGMs) (e.g., Kuhn and Featherstone, 2005). This study will use FGM techniques for the validation of the three methods used to infer mass changes from time-variable gravity observations as listed before. The validation will be based on closed-loop modelling where the gravitational signal of synthetic (e.g. simulated) mass distributions (called here synthetic Earth gravity modelling) are used within the mass estimation techniques considered (e.g., Baur et al., 2009, section 3). The closed-loop check is able to provide information on the correctness of mass estimation techniques, quantify errors, and can help to select the most suitable method for a specific task (see Sections 5.1 and 5.2 for more details). Here, synthetic Earth gravity modelling or the construction of SEGMs is only concerned with gravity changes over time, thus FGM of the static part of the Earth gravity field is outside the scope of this study. However, any static model (e.g., static SEGM) can be made dynamic by considering reasonably realistic mass changes over time (e.g., dynamic SEGM).

Within a closed-loop validation procedure the synthetic gravity signal obtained from synthetic Earth gravity modelling is used as input for the methods used to infer mass variations from time-variable gravity observations. Ultimately, results from the mass estimation methods are then compared to the given (time-variable) mass distribution. Any differences will be attributed to shortcomings of the methods and/or evaluation techniques used.

1.1.2 Gravity Satellite Missions

CHAMP was launched on July 15, 2000 and started a new era of geodetic gravity satellite missions. CHAMP is the first dedicated gravity mission that mostly maps

the static part of the Earth's gravity field (e.g., Reigber et al., 2003). CHAMP also had other tasks such as to observe Earth's magnetic field and atmospheric sounding through radio occultation observations. The CHAMP mission was followed by the GRACE mission, which was launched on March 17, 2002 with slightly different aims from those of CHAMP in mapping the Earth's gravity field. The GRACE satellite mission consists of a satellite pair (twin satellites) flying in the same orbit where precisely measured distance changes between the two satellites act as sensors for spatial gravity changes. Due to its approximately 10-day repeat cycle, GRACE provides both information of the static and time-variable gravity field. The latter is valuable information for studying the dynamics of the Earth including global mass changes. On March 17, 2009, the GOCE satellite mission was launched. The GOCE mission is designed to observe the static part of the Earth's gravity field with an unprecedented geoid accuracy of a few centimetres and minimum resolution of 65 km (e.g., Rummel, 2005; Han et al., 2006b; Hirt and Kuhn, 2012; European Space Agency, 2013).

These three geodetic gravity satellite missions have given a breakthrough in the knowledge of the static Earth's gravity field, and more importantly the time-variable part. The accurate and up-to-date information of time-variable gravity is a significant contribution in the study of the dynamics of the Earth and a new field of *environmental geodesy* (e.g., Awange, 2012). Numerous studies have now shown that GRACE can detect and monitor large-scale ice mass changes (e.g., Velicogna and Wahr, 2006b,a; Chen et al., 2006b,d; Ramillien et al., 2006; Luthcke et al., 2006b; Arendt et al., 2008; Baur et al., 2009; Velicogna, 2009), land hydrology changes (e.g., Swenson and Wahr, 2003; Rodell et al., 2004; Han et al., 2005b; Chen et al., 2005b; Ramillien et al., 2005; Seo and Wilson, 2005; Seo et al., 2006; Frappart et al., 2006; Schmidt et al., 2006; Chen et al., 2007a; Fiedler and Döll, 2007; Klees et al., 2007; Chen et al., 2009b; Han et al., 2009; Brown and Tregoning, 2010; Longuevergne et al., 2010), ocean mass changes (e.g., Nerem et al., 2003; Chambers et al., 2004; Lombard et al., 2007; Morison et al., 2004; Chambers, 2009; Catalão and Sevilla, 2009), and crustal changes due to post-glacial rebound (e.g., Barletta et al., 2008; Barletta and Bordoni, 2009).

Furthermore, studies by Bao et al. (2005); Han et al. (2006a); Chen et al. (2007b); Lemoine et al. (2007a); Panet et al. (2007); Sabadini et al. (2007); de Viron et al. (2008); Migliaccio et al. (2008); Han and Simons (2008); Han et al. (2008); Cannelli et al. (2008); Anjasmara (2008); Anjasmara and Kuhn (2009, 2010); and de Linage et al. (2009) have shown that the GRACE data clearly depicted the effect of the great Sumatra-Andaman earthquake in 2004.

1.1.3 Inferring Mass Changes from Time-Variable Gravity

Gravity changes recorded by the GRACE gravity satellite mission reflect mass changes in the atmosphere, on and/or beneath the Earth's surface. Therefore the gravity satellite mission can be employed to monitor temporal mass changes on a global and regional scale. Various methods have been proposed in order to infer mass changes from time-variable gravity observations. These methods can be divided into two main categories:

1. techniques that employ GRACE level-1 data (original K-band observations, e.g. distance changes) (e.g., Han et al., 2005a; Rowlands et al., 2005),
2. techniques that employ GRACE level-2 data (gravity potential changes) (e.g., Wahr et al., 1998; Swenson and Wahr, 2002; Swenson et al., 2003).

This study focuses on mass recovery technique that employ GRACE level-2 data. For level-2 data, currently the simplest and most popular method was proposed by Wahr et al. (1998), which implicitly assumes that all mass changes occur on a mass layer on the Earth's surface (see Chapter 4). This assumption allows for a direct inversion of potential changes into *surface* mass changes. This assumption is justified as mass changes close to the Earth's surface can be approximated by surface layers.

Fundamentally, based on Wahr et al. (1998), various alternative methods have been proposed (e.g., Swenson and Wahr, 2006) applying various filtering techniques in order to enhance the accuracy of the mass change estimates. Furthermore, the above techniques usually try to suppress high-frequency errors by

some data smoothing, having direct impact on the magnitude as well as spatial distribution of the recovered mass changes.

A different approach is followed by Lemoine et al. (2007b) through the introduction of so-called mass concentrations (mascons). In an attempt to recover the local mass flux, this technique uses the range rate (e.g., level-1 data) and other data to directly estimate surface mass changes represented as point or concentrated masses (e.g., Rowlands et al., 2005; Klosko et al., 2009; Luthcke et al., 2006b; Klees et al., 2008). This is supposed to provide a better localized recovery, but is also depending on the applied constraint and imposed correlation among the local mass changes (e.g., Luthcke et al., 2006a, 2008).

1.2 Research Objectives

The main objective of this study is to validate methods used to infer mass changes from time-variable gravity observations. Particular focus will be on the methods that apply filtering techniques (isotropic and non-isotropic) on spherical harmonic coefficients of the Earth's external gravitational potential (Stokes coefficients given by e.g., GRACE level-2 data). The validation will be performed in order to gain general information on the most suitable method to infer mass changes from time-variable gravity and in particular to study the impact of leakage (spatial and spectral) on mass estimates. In order to achieve these goals, synthetic Earth gravity modelling will be applied on both simplistic mass distributions and realistic mass changes. The latter will be based on GRACE-derived linear mass changes assumed to be error-free within the synthetic Earth gravity modelling.

The research objectives will be accomplished through the following steps:

1 Review of existing methods to infer mass changes from time-variable gravity observations with a particular view on satellite gravity measurements (e.g., GRACE data).

2 Development of reasonably realistic mass change models to be used in the closed-loop validation procedure. In this study global mass changes will be based on GRACE-derived linear mass changes.

3 Simulation of (time-variable) gravity observations applying synthetic Earth gravity modelling on the mass changes developed in step 2. These simulated gravity observations are self-consistent with the given mass distribution.

4 Implementation and validation of existing techniques used to infer mass changes from time-variable gravity observations. This will be done by employing the simulated time-variable gravity observations within the selected techniques.

5 Analysis of the validation results through comparison to the given (time-variable) mass changes. Particular focus will be on spatial and spectral leakage as a result of filtering the simulated (time-variable) gravity observations.

1.3 Significance

This study is significant to provide improved mass change estimates and ultimately better quantify global and regional environmental changes. This is important for both the scientific as well as the wider community.

Improved mass change information will be beneficial for studying the dynamics of the Earth such as monitoring of large water sheds, ice melt, post-glacial rebound and even the impact of large earthquakes. Moreover, improved global mass transport information provides valuable contributions for a better and more reliable understanding of causes and effects of global climate change (e.g., Leuliette et al., 2002; Nerem et al., 2003; Chambers et al., 2004; Ramillien et al., 2006; Chen et al., 2006a; Velicogna and Wahr, 2006a).

This study will also be significant as no comprehensive validation of proposed and used mass change estimation techniques has been done so far. Furthermore,

no standard procedure for testing the correctness of each method exists so far. Therefore, it is of great importance to provide such standards, which will be the main outcome of the proposed research.

1.4 Thesis Outline

This thesis comprises seven chapters. Chapter 2 essentially presents the theoretical background of the Earth's gravity field and its generating mass distribution. The fundamental theory of potential of the Earth, gravitational force, spherical harmonic and static and time-variable gravity are summarized. At the end of the chapter, the relation of the Earth's gravity field and its generating mass distribution is presented, i.e., Newton's integral.

Chapter 3 reviews the fundamentals of gravity field modelling, including an overview on the construction of SEGMs and FGM. Techniques of inferring mass changes from time-variable gravity are discussed in Chapter 4. However, only the techniques that are significant to the intended study are presented. Some of the smoothing procedures that are used in this thesis are also reviewed.

Chapter 5 details the validation procedure including routines and software that are used in this study. Results from different validation scenarios using simple simulated disc masses are presented. A further validation using more realistic mass distributions, which are derived from GRACE satellite data, is performed and presented in Chapter 6, where visual and numerical analysis of the validation results are discussed.

A summary of the most important results and an itemized overview of the main conclusions of the study are presented in Chapter 7. Furthermore, an outlook and recommendation for future research related to this study is also presented in this chapter.

Chapter 2

Earth's Gravity Field and Mass Distribution

Determination of the gravity field of the Earth is one of the major goals of geodesy (e.g., Vaníček and Krakiwsky, 1986). This chapter presents the theoretical background of Earth's gravity field modelling and shows how mass distributions used in this thesis are generated. An overview of fundamental theories and techniques of gravity field modelling (i.e. Earth's potential, gravitational force, static and time-variable gravity) is presented, with detailed coverage referred to standard text books (e.g., Torge (1989, 2001); Heiskanen and Moritz (1967); and Hofmann-Wellenhof and Moritz (2005)). Fundamental relations between the Earth's gravity field and its generating mass distribution is thereafter presented in Section 2.1.

2.1 Gravity Field of the Earth

2.1.1 Gravitational Force and Acceleration

Newton's law of universal gravitation introduces the fundamental concept of gravitation, which in its simplest form describes the relationship between the gravitational force $\vec{F}$ and two point masses m_1 and m_2 (see Figure 2.1) expressed by the relation (e.g., Heiskanen and Moritz, 1967; Hofmann-Wellenhof and Moritz, 2005; Torge, 1989, 2001; Kaula, 2000):

$$\vec{F}_{12} = G\frac{m_1 m_2}{L^2}\hat{\ell} = -\vec{F}_{21}, \tag{2.1}$$

where G is Newton's gravitational constant and $L = |\vec{L}|$ is the Euclidean distance between the two point masses m_1 and m_2, commonly termed as the attracting

mass and the attracted mass, respectively, $\vec{L}$ is the vector connecting m_1 and m_2, and $\hat{\ell} = \dfrac{\vec{L}}{L}$ a unit vector in the direction of $\vec{L}$. Often, the gravitational force is expressed as a negative force in order to identify the force F_{21} that acts on the attracted mass m_2 in the direction of the attracting mass m_1 (see Figure 2.1). In this study, Newton's gravitational constant has been set to $G = 6.67384 \times 10^{-11}\mathrm{m}^3\mathrm{kg}^{-1}\mathrm{s}^{-2}$ in accordance with the recommendation of the 2010 Committee on Data for Science and Technology (CODATA; Mohr et al. (2012)).

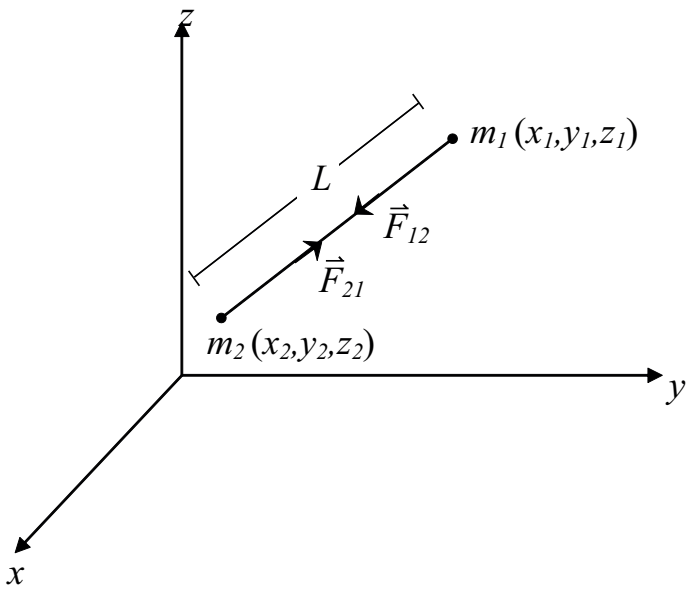

Figure 2.1: Gravitational forces $\vec{F}_{12}$ and $\vec{F}_{21}$ between two generating point masses m_1 and m_2.

In order to describe the gravitational field of one point mass (e.g., m_1 the attracting mass), the attracted mass is set to unity. This reduces the relation in Equation (2.1) to

$$\vec{g}_{12} = G\frac{m}{L^2}\hat{\ell} = -\vec{g}_{21}, \tag{2.2}$$

representing the gravitational acceleration vector (or gravitational attraction) caused by the attracting mass $m = m_1$ at any location in space separated by the distance L. In vector form, Equation (2.2) represents the gravitational field of a

point mass, e.g., the gravitational acceleration vector at any point in space.

While the simple Equation (2.1) and Equation (2.2) only hold for point masses (or spheres with radial-symmetric density distribution), they have to be replaced by integrals over any arbitrary spatial mass distribution. Therefore, in case of a more complex mass distribution (e.g., for the Earth's mass distribution), the gravitational acceleration $\vec{g}$ can be obtained by evaluating Newton's volume integral for the gravitational acceleration in vectorial form

$$\vec{g} = G \iiint\limits_{mass} \frac{\hat{\ell}}{L^2} dm = G \iiint\limits_{volume} \frac{\rho}{L^2} \hat{\ell} \, dv \tag{2.3}$$

which holds for any arbitrary mass distribution. The integration is taken over all infinitesimal small mass elements dm (e.g., point masses) frequently expressed by infinitesimal small volume elements dv multiplied by the corresponding mass density ρ (see e.g., Heiskanen and Moritz, 1967).

2.1.2 Gravitational Potential

The gravitational potential (V) of a point mass is defined as

$$V = \int_{\infty}^{\vec{L}} < \vec{g}, d\vec{L} > \tag{2.4}$$

which is the work that must be done by gravitation in order to move a unit mass from infinity ($V = 0$) to a point with distance L from the attracting mass m. In Equation (2.4), $< \vec{g}, d\vec{L} >$ stands for the scalar product between $\vec{g}$ and $d\vec{L}$ an infinitesimal change in direction of $\vec{L}$. Inserting $\vec{g} = \vec{g}_{21}$ (from Equation (2.2)) into Equation (2.4) yields

$$V = \int_{\infty}^{\vec{L}} < G\frac{m}{L^2}\hat{\ell}, d\vec{L} > \; = G\frac{m}{L} \quad \text{with} \quad \lim_{L\to\infty} V = 0. \tag{2.5}$$

Equation (2.5) represents the gravitational potential of the point mass m at a location separated by the Euclidian distance L.

While Equation (2.5) only holds for point masses (or sphere with radial-symmetric density distribution), again, the simplistic formula has to be replaced by an integral over all infinitesimal mass elements of any arbitrarily shaped body (e.g., Heiskanen and Moritz, 1967). For a more complex mass distribution (e.g., for the Earth's mass distribution), the simple formula has to be replaced by integrals over the entire mass distribution. Applying this to Equation 2.4 yields Newton's volume integral for the gravitational potential given by

$$V = G \iiint_{mass} \frac{dm}{L} = G \iiint_{volume} \frac{\rho}{L} dv. \tag{2.6}$$

Similar to the gravitational acceleration (see Equation (2.3)), the volume integral above is taken over all infinitesimal small mass elements dm (e.g., point masses) or replaced by infinitesimal small volume elements dv multiplied by the corresponding mass density ρ.

2.1.3 Equipotential Surface and Plumbline

Geometrically, a gravity field (gravitational and centrifugal field) can be described by its surfaces of constant gravity potential (e.g., Torge, 1989); also known as equipotential surfaces or level surfaces (see Figure 2.2). The properties of the Earth's gravity field are closely related to the so called figure of the Earth (e.g., Burša and Pěč, 1988), which is given by the geoid, i.e., the equipotential surface that most closely coincides with the undisturbed mean sea level.

The gravity field lines that are always orthogonal on the equipotential surfaces are called plumblines (orthogonal trajectories). The direction of the gravity force $\vec{F}$ or acceleration $\vec{g}$ is given through the tangent along the plumbline running through the point of interest. The vertical separation ΔN between two equipotential surfaces measured along the plumbline is given in first order approximation by Bruns formula (e.g., Heiskanen and Moritz, 1967)

$$\Delta N = \frac{\Delta V}{g}, \tag{2.7}$$

where $\Delta V = V_2 - V_1$ is the potential difference between the two equipotential surfaces and g is the magnitude of the local gravity acceleration, $\vec{g}$.

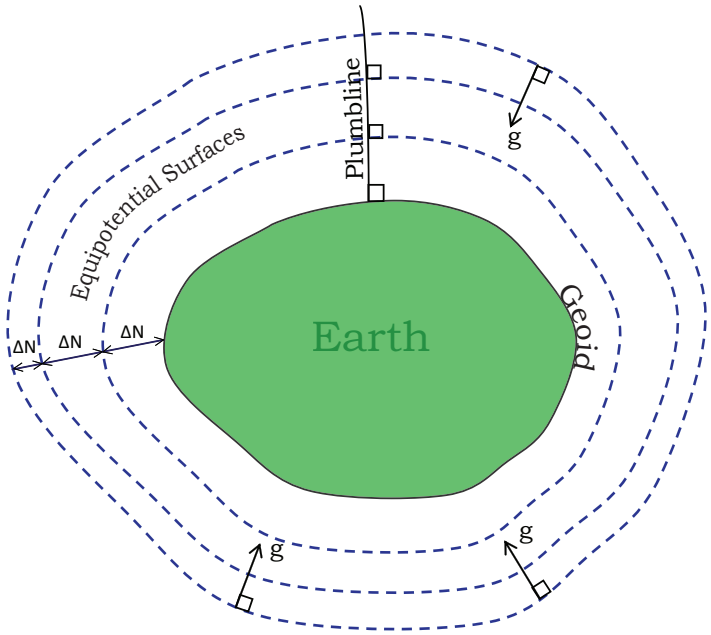

Figure 2.2: Equipotential surfaces and plumb lines near the Earth's surface. [adapted from Torge (2001)]

2.1.4 Spherical Harmonic Representation of the Earth's Gravitational Field

According to Heiskanen and Moritz (1967), the Earth's gravitational potential (V) at any point on or exterior to the Earth's surface (approximated by a mean sphere of radius R, e.g. $r \geqslant R$) can be expressed by an infinite spherical harmonic series. For the point of interest specified through the geocentric radius (r), geographic latitude (ϕ) and longitude (λ), the Earth's exterior potential is given by

$$V(\phi, \lambda, r) = \frac{GM}{R} \sum_{l=0}^{\infty} \sum_{m=0}^{l} \left(\frac{R}{r}\right)^{l+1} \bar{P}_{lm}(\sin\phi)\left[\bar{C}_{lm}\cos m\lambda + \bar{S}_{lm}\sin m\lambda\right], \quad (2.8)$$

with the fully normalized Legendre functions $\bar{P}_{lm}$ of degree l and order m, Newton's gravitational constant G, the total mass of the Earth M, the mean Earth

radius R, and the fully normalized spherical harmonic coefficients (SHC, also called Stokes coefficients) $\bar{C}_{lm}$ and $\bar{S}_{lm}$ (dimensionless). For practical evaluation, the infinite series is truncated at the maximum resolvable degree l_{max}, which corresponds to a spatial resolution that is equivalent to the spatial extension of tesseral harmonic elements (Torge, 1989) on the sphere with mean radius R. "Tessera" means a tile, i.e., the sphere is divided into compartments in which the function values are alternatively positive and negative, somewhat like a chess board (see Figure 2.3). The fixed spatial extent D of these surface elements along meridians and the equator is given by the relation

$$D = \frac{\pi R}{l_{max}}[\text{km}], \tag{2.9}$$

which represents the half-wavelength (expressed as spatial distance in km) of a sin-wave on the sphere with l_{max} waves. Following the principle of meridian convergence the spatial extent of the surface elements along a parallel is not constant but varies depending on the geographic latitude with the lowest resolution along the equator and increased resolution towards the poles. In order to account for the meridian convergence Equation (2.9) changes to

$$D_\phi = \frac{\pi R}{l_{max}} \cos\phi[\text{km}]. \tag{2.10}$$

In geodesy, the knowledge of the Earth's gravity field is important for the determination of the Earth's physical shape the geoid (i.e., figure of the Earth). This objective is accomplished by solving the geodetic boundary value problem (GBVP), which allows the determination of the geoid from gravity measurements given upon its surface (e.g., Heiskanen and Moritz, 1967; Torge, 2001). Global models of the Earth's gravitational potential are commonly called Global Geopotential Models (GGMs; see Torge (2001)) . They are usually given through the fully normalized spherical harmonic coefficients $\bar{C}_{lm}$ and $\bar{S}_{lm}$ for all degrees and orders from $l = 2$ up to $l = l_{max}$. The actual values of the coefficients are commonly determined from observational data (e.g., satellite, airborne, terrestrial and marine gravity data).

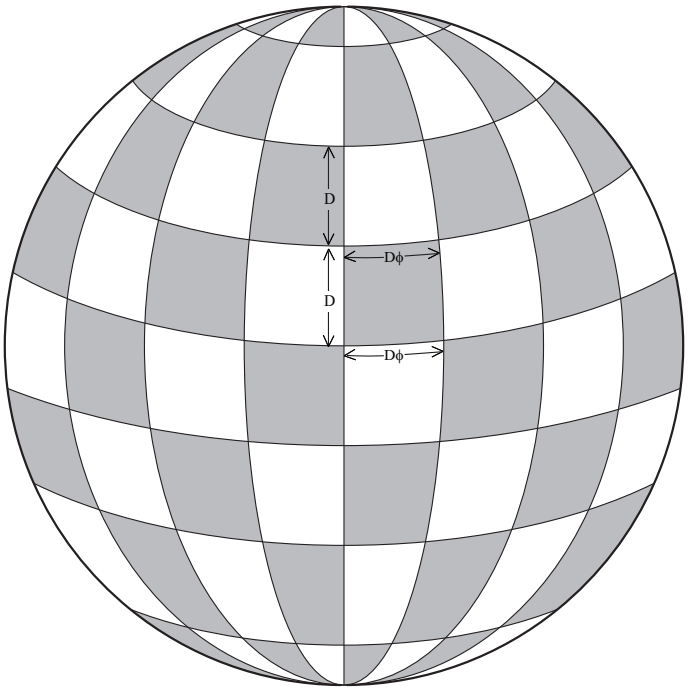

Figure 2.3: Geometrical representation of tesseral spherical harmonics.

Based on the observational data available, three classes of GGMs can be distinguished (e.g., Torge, 2001): (1) satellite-only GGMs, (2) combined GGMs and (3) tailored GGMs. Satellite-only GGMs are derived solely from the analysis of the orbits of artificial Earth satellites whereas combined GGMs are derived from the combination of satellite orbit data, airborne gravimetry data, land and ship track gravity observations, and marine gravity anomalies derived from satellite radar altimetry. While the GGMs have generally a global view, tailored GGMs are developed with a regional focus in order to better approximate the gravity field over a particular area of interest (e.g., based on high-resolution gravity observations). Such models are constructed by adjusting a satellite-only or combined GGM using gravity data that optimally have not been used before to better reproduce high resolution gravity field signatures in the region of interest (e.g., higher degree coefficients produce results that are only valid over the region of interest).

2.1.5 Spectral Properties of the Earth's Gravity Field

Typical wavelength ranges and their corresponding spectral resolution on a sphere are given in Table 2.1. The table provides the maximum resolvable spherical harmonic degree l and related spatial resolution (given by the half-wavelength) expressed either by the spatial distance D (see Equation (2.9)) or the spherical distance ψ, representing a geographic longitude interval ($\Delta\lambda$) for east-west section at the equator.

Table 2.1: Typical wavelength ranges in which the gravity field is represented (adapted from Reigber (1989)). Both spherical and spatial distances are given as half-wavelength.

Wavelength Ranges				
	long	medium	short	very short
l	< 5	< 36	< 200	>200
ψ°	$> 45^\circ$	$> 5^\circ$	$> 1^\circ$	$< 1^\circ$
D [km]	> 5000	> 500	> 100	< 100

According to Table 2.1, long wavelengths or low frequency constituents of the Earth's gravity field relate to the first few spherical harmonic degrees (e.g., $l < 5$) representing spatial signatures larger than ≈ 5000 km. Medium wavelength ranges relate to spherical harmonic degrees between 5 and 36 representing spatial signatures between 500 km and 5000 km. Spherical harmonic degrees between 36 and 200 relate to the short wavelength ranges represented by spatial signatures between 100 km and 500 km. Smaller spatial signatures (e.g., < 100 km) are given by spherical harmonic degrees larger than 200 and represent the very short wavelength range.

Currently, the long, medium to short wavelength ranges of the Earth gravity field are obtained from satellite observations including the most recent dedicated gravity missions CHAMP, GRACE and GOCE. These are the wavelength ranges of most interest within this thesis. The very short wavelength ranges are commonly obtained from airborne, marine and terrestrial gravity data.

2.1.6 Meissl Scheme

The Meissl scheme represents spectral relations between quantities of the Earth's gravity field. These relations are provided for the disturbance potential ($T = V - U$), where U is a reference normal potential (e.g., from a reference sphere or ellipsoid), and its first and second radial derivatives. Based on a spherical harmonic representation of the disturbance potential in the form as given in Equation (2.8), it can be shown that the scheme is based on a set of eigenvalue connections between gravity quantities given at the Earth's surface and at a given altitude above the Earth's surface (e.g., Rummel and van Gelderen, 1995). The scheme provides a general insight in how different gravity field quantities are coupled to the disturbance potential, or to any other gravity field quantity (see Figure 2.4). Hereby the eigenvalues represent degree-dependent factors to be applied to the corresponding spherical harmonic coefficients. The gravity quantities of interest are mainly potential differences and geoid heights, gravity anomalies and disturbances (first derivatives of T) deflections of the vertical (first horizontal derivatives of T), and gravity gradients (second derivatives of T).

Assuming the fully normalized SHC $\bar{C}_{lm}$ and $\bar{S}_{lm}$ are related to the disturbing potential T, then the geoid heights N (measured above the adopted reference sphere) are obtained by applying Bruns formula (see Equation (2.7)), which is given by

$$N(\phi,\lambda) = \frac{T(\phi,\lambda)}{\gamma} = R\sum_{l=2}^{L}\sum_{m=0}^{l}\bar{P}_{lm}(\sin\phi)\left[\bar{C}_{lm}\cos m\lambda + \bar{S}_{lm}\sin m\lambda\right], \quad (2.11)$$

where $\gamma = \dfrac{GM}{R^2}$ is the gravity of the reference sphere with total mass of the Earth

M. Applying the factor $-\dfrac{(l+1)}{R}$ as given in Meissl's scheme (see Figure 2.4) yields the gravity disturbance

$$\delta g(\phi,\lambda) = \gamma \sum_{l=2}^{L}(l+1) \sum_{m=0}^{l} \bar{P}_{lm}(\sin\phi)\left[\bar{C}_{lm}\cos m\lambda + \bar{S}_{lm}\sin m\lambda\right], \tag{2.12}$$

and the gravity anomaly is given by

$$\Delta g(\phi,\lambda) = \gamma \sum_{l=2}^{L}(l-1) \sum_{m=0}^{l} \bar{P}_{lm}(\sin\phi)\left[\bar{C}_{lm}(t)\cos m\lambda + \bar{S}_{lm}(t)\sin m\lambda\right]. \tag{2.13}$$

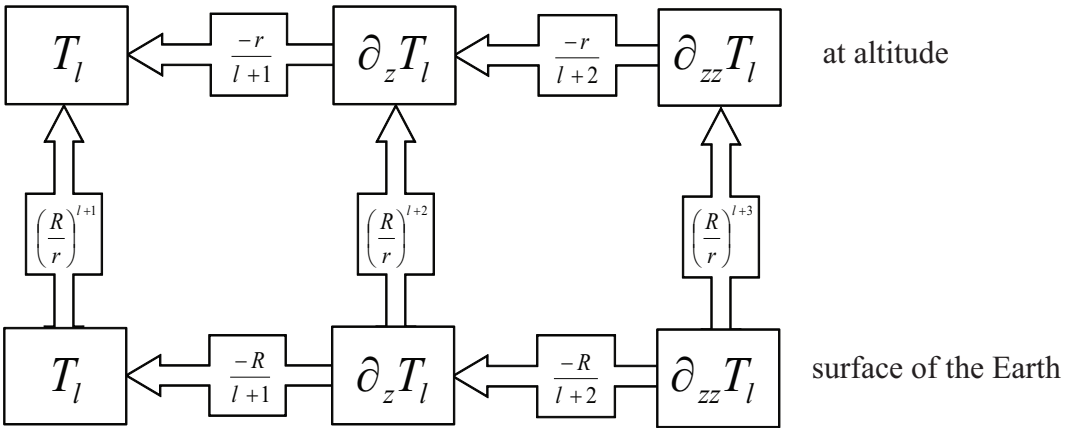

Figure 2.4: Meissl scheme: Eigenvalues (spherical symbols) per degree l, connecting the disturbance potential T and its first and second radial derivatives, at the Earth's surface and at altitude. The arrows indicate the direction for which the eigenvalues apply [adapted from Rummel and van Gelderen (1995)].

Apart from dealing with the disturbing potential T, Meissl's scheme can be applied to the gravitational potential caused by any mass distribution such as anomalous masses or (small) mass changes on or close to the Earth's surface. The latter will be the major focus within this thesis.

2.2 Static and Time-variable Gravity Field

Static gravity treats the Earth's gravity field as steady-state or invariable with time, even though it has small temporal variations (e.g., Biro, 1983; Dickey et al., 1997; Dickey, 2001). The static gravity field is also known as the mean gravity field, as it is either determined and/or assumed to represent the gravity field as an average over time. The assumption of static gravity is violated by many geophysical processes (e.g., Dickey et al., 1997) causing changes of the Earth's mass distribution and in turn the Earth's gravity field on a wide range of time scales from hours to millions of years and spatial scales from localized to global dimensions (e.g., Cazenave and Nerem, 2002). Figure 2.5 provides an overview of major geophysical processes that cause time-variable gravity changes and their respective temporal and spatial scales.

In this thesis, the static gravity field defined as average over time is subtracted from time-variable models of the Earth's external gravitational potential as given by the GRACE satellite mission. Using a spherical harmonic representation (Equation (2.8)) this will result in the use of residual spherical harmonic coefficients (see Chapter 4), which provide an enhanced view of the time-variable part of the Earth's gravity field.

Time-variable gravity considers the Earth's gravity field as changing over time. This view is based on the fact that the Earth's mass distribution is constantly changing over time (e.g., Cazenave and Nerem, 2002). According to Newton's law of gravitation (see Equation (2.1)), any mass change produces a gravity change. Therefore, time-variable gravity provides indirect information on mass changes over time. In this study, time-variable gravity refers mainly to short-term gravity variations of months to several years, which are the result of mass re-distribution in the atmosphere, oceans, hydrosphere, cryosphere and within the Earth crust, or of mass exchange between these components (e.g., Dickey et al., 1997; Wahr et al., 1998; Rummel, 2005).

The magnitudes of these short-term variations of the Earth's gravity field are very small, usually well below 1 mGal ($1 \cdot 10^{-5}$ ms^2), which is less than one-millionth of Earth's gravity at its surface (see Table 2.2). Time periods of these processes range from short periodic (sudden events, sub-daily, daily, seasonal and annual) to long periodic and secular events (e.g., Biro, 1983; Rummel, 2005). To observe the broad range of time-variable gravity, relatively dense temporal and spatial coverage and highly accurate measurements are necessary. To some extent, this can be provided for a global coverage by space techniques (e.g., Dickey et al., 1997), such as the gravity satellite missions (CHAMP, GRACE and GOCE).

2.3 Spatial and Temporal Variations of the Earth's Gravity Field

As outlined above, spatial and temporal variations of the Earth's gravity field are the result of an ever changing mass distribution within the Earth and on or above its surface (e.g., Wahr et al., 1998; Rummel, 2005). Conversely, the Earth's gravity field reflects the composition, structure and change of the planet's mass distribution, including the redistribution of atmosphere and water masses (e.g., Tapley et al., 2004a). While the composition and structure of the solid Earth is changing by processes that generally occur within longer periods (see Figure 2.5), Chen et al. (2005a) argue that for periods of several years or shorter, the main driving forces behind temporal variations of the Earth's gravity field originate from the atmosphere, ocean and continental water storage (in liquid and solid form).

According to Lambert et al. (1995), the geodynamic processes that cause changes in gravity can be specified in terms of their principal frequencies (periods) and spatial scales (wavelengths) (see Figure 2.5). The processes influencing the gravity field are composite of primary and secondary effects; e.g. one process can be triggered by another process. For instance, sea level change can be constituted by ice-mass melting (e.g., Ivins, 2009; Bamber et al., 2009; Rignot et al., 2011; Jacob et al., 2012), changes in land hydrology (e.g., Gornitz et al., 1997; Wada et al., 2010; Konikow, 2011) and post-glacial rebound (e.g., Peltier, 1998, 1999,

2009; Paulson et al., 2007). The processes occurring within periods of longer than 100 years generally appear as secular variations with rates of $\leq$10 μGal (see Table 2.2).

Table 2.2: Time variable gravity field and its scientific requirements. The '?' symbol shows that the respective magnitudes are not yet well known [adapted from Beutler et al. (2003)].

Geodynamic Effect	Magnitude		Spatial Resolution (km)	Main Periods
	Geoid (mm)	Gravity (μgal)		
Tides (oceans, solid earth)	100-150		50-5000	Diurnal, semi-diurnal, semi-monthly
Atmosphere (Inverted Barometer (IB), Non Inverted Barometer (NIB), vertical integration)	15		200-2000	Annual, seasonal, diurnal, others
Oceans (Sea level, currents)	10-15		100-2000	Seasonal, secular
Hydrology (snow, rain, run-off, precipitation, evaporation, reservoir, ground water)		10	10-1000	Diurnal to annual
Post-glacial rebound		10	1000-10000	Secular
Polar ice and glaciers		5	100 -1000	Secular
Solid Earth				
-Earthquakes	0.5		10 - 100	Single events
-Volcanism	0.5		10 - 100	Single events
-Tectonics	?		$>$ 500	Secular
-Core and Mantle	?		$>$ 500	Secular

Figure 2.5 shows that Earth's gravity changes are caused by geodynamic processes that occur over short-term to long-term periods covering spatial scales from few kilometres to thousands of kilometres. The effect (magnitude) of these geodynamic processes in terms of gravity and geoid height according to their spatial and temporal resolution, as given in e.g., Rummel et al. (2002), are presented in Table 2.2. In addition, Table 2.2 also shows the requirements for the spatial and temporal resolutions that are needed to detect various geodynamic processes from gravity measurements.

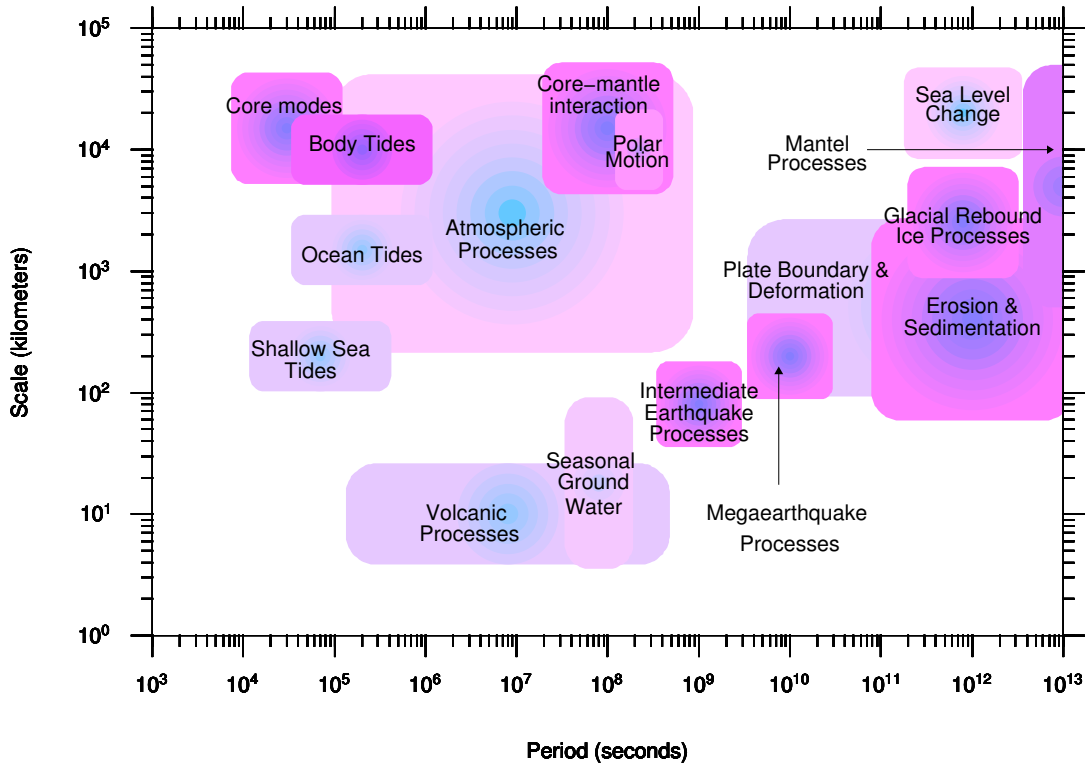

Figure 2.5: Mass redistribution on and beneath the Earth's surface and their respective spatial and temporal scales [adapted from Cazenave and Nerem (2002)].

2.4 Determination of the Earth's Gravity Field from Satellite Observations

The advantage of satellite space techniques over terrestrial or airborne observation techniques is their ability to monitor static and time-variable parts of the Earth's gravity field on a global as well as regional scale. With dedicated satellite missions, it is now possible to obtain gravity field information with homogeneous quality without the limitations of geographic or geopolitical boundaries (e.g., Dickey et al., 1997).

Since the launch of Sputnik in 1957, artificial satellites have been used for geodetic purposes such as positioning and Earth's gravity field determination (e.g., Nerem et al., 1995; Torge, 2001; Hofmann-Wellenhof and Moritz, 2005). Concerning the recovery of the Earth's gravity field, various space techniques can be used, ranging from tracking of satellite orbits, satellite-to-satellite tracking (SST) to combination of SST with satellite gradiometry. The latter two are the techniques used in the recent dedicated gravity field missions CHAMP, GRACE and GOCE.

2.4.1 Tracking Satellite Orbit

The analysis of satellite orbit perturbations, which reflects varying (mostly gravitational) forces acting on the satellite, can be used to determine global gravity field models by inversion techniques (e.g., Balmino, 2001). Various methods have been developed to collect the information of satellite orbit perturbations, primarily through tracking the satellite's orbit from monitoring stations located on the Earth's surface.

Tracking satellite orbits between 1958 and 1970 was done by optical-photographic observation, such as BC4 cameras of the Passive Geodetic Satellite (PAGEOS) (e.g., Mancini, 1971; Swanson and Yeager, 1971). Laser ranging and altimetry as well as Doppler positioning methods were developed in the 1970s (e.g., Kouba, 1983); for example, using the TRANSIT system (e.g., Black et al., 1980; Black,

1990). These methods not only refined satellite orbit observation techniques, but also increased the accuracy of the data, which made it possible to measure geodynamic phenomena such as crustal deformation. The development and implementation of NAVSTAR Global Positioning System (GPS) in the mid-1980s considerably improved SST methods through precise orbit monitoring. However, using these conventional orbit tracking techniques, the accuracy needed specifically for geodetic purposes e.g. mGal-level for gravity and mm-level for geoid height were yet to be achieved. This shortcoming has been overcome with the implementation of dedicated gravity field monitoring missions using SST techniques.

2.4.2 Satellite-to-Satellite Tracking

To map the gravity field with space techniques, two broad categories of dedicated gravity satellite missions can be considered: gravity gradiometry, which measures the differences in acceleration of two masses within the same spacecraft; and SST, which utilizes differential tracking of two satellites (e.g., Dickey et al., 1997; Rummel et al., 2002). Figure 2.6 illustrates the different SST concepts, which are described in more detail below.

Based on SST, a new era of dedicated gravity satellite missions began with the launch of the CHAMP satellite mission in July 2000. This mission adopted high-low SST (Figure 2.6a) using GPS and on-board accelerometers combined with a low-altitude and near polar orbit (e.g., Reigber et al., 2003). GRACE is the second dedicated gravity satellite mission, launched in March 2002, that was designed to map the Earth's gravity field with an expected lifetime of five years (e.g., Tapley et al., 2004a; Wahr et al., 2004; Kusche and Schrama, 2005; Fengler et al., 2006; Hinderer et al., 2006). The mission was extended until early 2010 (e.g., Chen et al., 2006b) but is still operational until today. GRACE measures the Earth's gravity field using the low-low SST mode (Figure 2.6b) with two satellites flying in tandem (approximately 220 km apart) tracked by GPS. Variations in gravity are indirectly obtained through the measurement of the changing distance between

the two satellites using a very precise K-band microwave ranging system. The GRACE mission looks at both the static and the time-variable part of the Earth's gravity field whereas, CHAMP mostly is concerned with the static field.

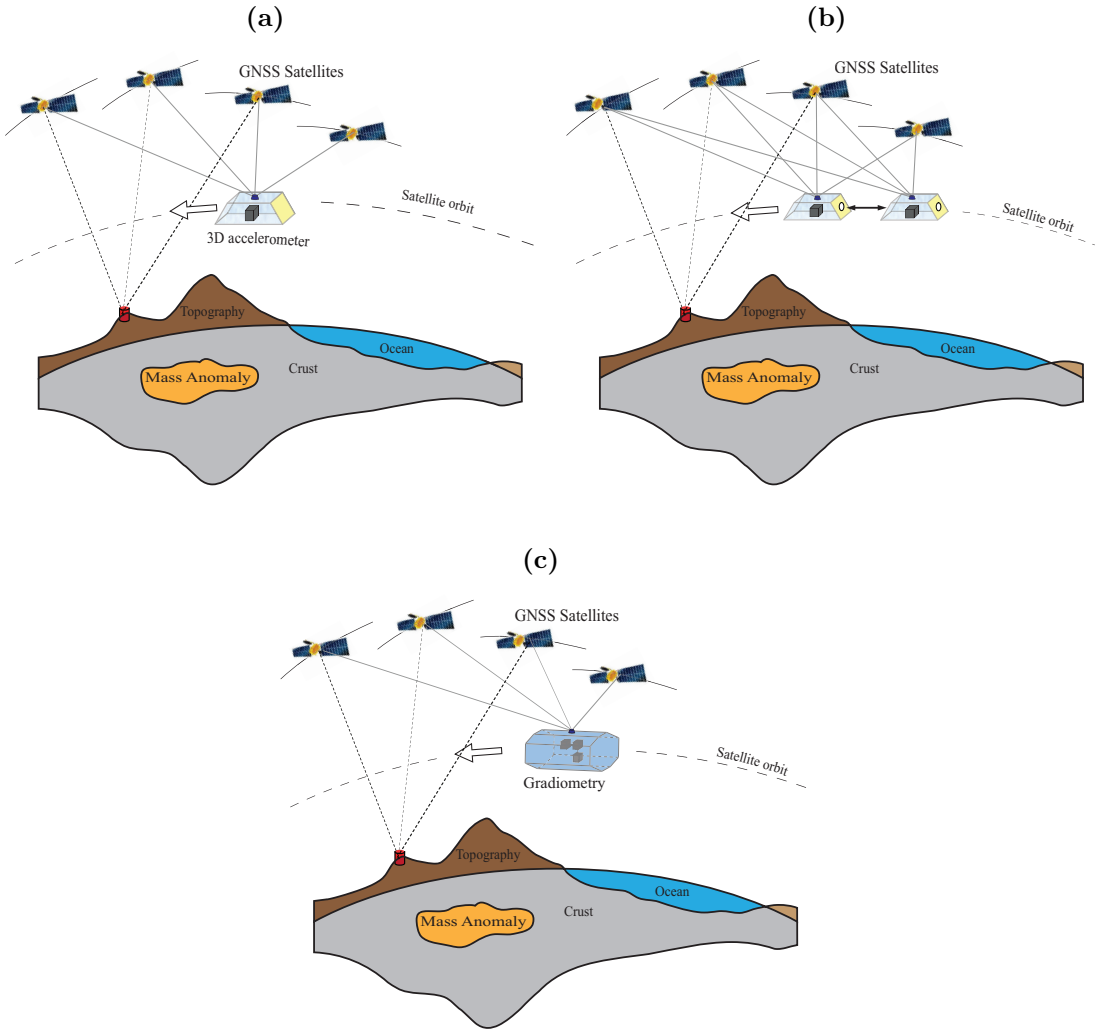

Figure 2.6: Concept of satellite-to-satellite tracking: (a) in the high-low mode (SST-*hl*), (b) in the low-low mode (SST-*ll*), (c) satellite gradiometry combined with SST-*hl* (adapted from Rummel et al. (2002)).

Gravity gradiometry combined with SST (Figure 2.6c) is realized by the GOCE satellite mission launched in March 2009 (e.g., European Space Agency, 2013). This mission is designed to observe the static gravity field of the Earth with an unprecedented geoid accuracy of several centimetres and a maximum resolution of 65 km (e.g., Rummel, 2005; Han et al., 2005a). The GOCE satellite is equipped with an on board gradiometer to measure the Earth's gravity gradient tensor, and

GPS receivers to determine its precise orbit.

With the implementation of the dedicated gravity satellite mission, particularly GRACE and GOCE, the knowledge of the global gravity field and its temporal variation has been and still will be improving considerably. The remaining commission errors in gravity and geoid height with respect to various spatial scales as presented by Rummel (2005) are summarized in Table 2.3.

Table 2.3: Improved geoid and gravity commission errors after GRACE and GOCE [adapted from Rummel (2005)].

Geoid (mm)	Gravity (mgal)	Spatial scale (km)	
45	2.0	200	time-variable gravity
10	0.2	100	
1	0.03	65	static gravity

2.5 Chapter Summary

This chapter has summarized the fundamental concept of the Earth's gravity field and its relations to the mass distributions within and on the Earth's surface. The basic concept of the Earth's gravitational potential and spherical harmonic representation of the gravity field was presented in the first part of the chapter. To give an idea of the resolution of gravity field data, information on spectral properties of Earth's gravity data and corresponding spatial signatures has been presented. The concept of determination of the Earth's gravity field from satellite observations was briefly discussed. Overall, it has been demonstrated that the knowledge of the static and time-variable part of the Earth's gravity field has been improved considerably with the introduction of the dedicated gravity satellite missions CHAMP, GRACE and GOCE.

Chapter 3

Synthetic Earth Gravity Modelling

Many techniques have been developed with the aim to model, describe or recover parameters of the Earth's gravity field (Heiskanen and Moritz, 1967; Vaníček and Krakiwsky, 1986; Torge, 1989) termed here as Earth gravity modelling techniques. Techniques to construct a synthetic Earth Gravity Model (SEGM) are, instead, summarized here under the term synthetic Earth gravity modelling techniques. While many of these techniques are identical to classical Earth Gravity modelling techniques their aim is different in that they are employed to provide a synthetic description of the Earth's gravity field (e.g., Haagmans, 2000; Claessens, 2002; Ågren, 2004; Kuhn and Featherstone, 2005; Baran et al., 2006; Tsoulis and Kuhn, 2007; Fellner et al., 2012; Bagherbandi and Sjöberg, 2012). The primary aim is not to describe the real gravity field but to simulate it. While the synthetic model can be rather realistic, it is generally sufficient if it is only reasonably realistic.

The purpose of SEGMs is for testing different theories and methods applied in Earth gravity field modelling (e.g., geoid determination and downward continuation) (e.g., Pail, 2000; Kuhn and Featherstone, 2003; Ågren, 2004). The advantage of synthetic Earth gravity modelling is the ability to construct targeted parameters of the Earth gravity field that are self-consistent with the respective data used. As such, synthetic Earth gravity modelling is well suited to validate methods to infer mass changes from satellite gravity measurements, which is the aim of this thesis.

Similar to the construction of SEGMs, synthetic Earth gravity modelling can be based on observations (effects modelling), mass sources within the Earth's interior (source modelling) or a combination of them (hybrid modelling). This chapter provides theoretical and practical aspects of these techniques with particular focus on source modelling based on principles of forward gravity modelling. In addition this chapter presents an overview on the construction of SEGMs.

3.1 Synthetic Earth Gravity Models

An SEGM generates self-consistent gravity field parameters based on a realistic-as-possible representation of the Earth's gravity field (e.g., Kuhn and Featherstone, 2003; Tsoulis and Kuhn, 2007). With different techniques and purposes, several studies to develop SEGMs have been performed. As summarized in Pail (2000) and Baran et al. (2006), based on the techniques used SEGMs can be categorized into three different types, namely: Effects Model SEGMs, Source Model SEGMs and Hybrid Model SEGMs.

3.1.1 Effects Model SEGMs

Effects model SEGMs use observed gravity field information and do not make any assumptions about the mass-density distribution inside the Earth. Furthermore, these models usually treat the observed gravity parameter as error-free or apply a pre-defined error model. Effects model SEGMs are not suitable to study the interior of the Earth as they only model the external gravity field, thus are not defined inside the Earth's masses. Effects model SEGMs have been developed and applied by e.g., Tziavos (1996); Nóvak et al. (2001) and Featherstone (2002).

3.1.2 Source Model SEGMs

In contrast to effects model SEGMs, source model SEGMs are constructed by considering the mass-density distribution of the Earth. The information of the Earth's interior mass-density distribution is used to generate Earth gravity by

forward gravity modelling based on Newton's law of gravitation. Source model SEGMs are a good tool to help to understand geophysical and geodetic phenomena, particularly those that are related to the Earth's mass redistribution (i.e., mass transports within, on and above the surface of the Earth)

Vermeer (1995) implemented the source model approach by developing a geopotential model using point masses. A global source model SEGM based on known mass distributions of the Earth's topography and crust has been developed by Kuhn and Featherstone (2003). This model has been further refined by the inclusion of information on the Earth's mantle (Kuhn and Featherstone, 2005). Tsoulis (2004) has developed two Earth gravity models based on the analysis of global crustal data. A global source model SEGM based on known topography and simulated masses in the Earth's crust and mantle has been developed by Fellner et al. (2012) and was applied to the study of orthometric heights in Fellner (2011).

3.1.3 Hybrid Model SEGMs

Hybrid model SEGMs combine both the effects and source model approaches. Often the combination is done by using an effects model such as an existing GGM to model the long-wavelength information and a source model for the higher-frequency gravity signals. This ensures that the SEGM is rather realistic but also contains some high frequency signals (e.g., Baran et al., 2006).

Hybrid model SEGMs were developed and further studied by Rummel et al. (1988); Pail (2000); Haagmans (2000); Claessens (2002); Baran et al. (2006). Both Pail (2000) and Haagmans (2000) modelled globally distributed point masses combined with low-frequency gravity signals from Earth Gravitational Model 1996 (EGM96; e.g., Lemoine et al., 1998). Baran et al. (2006) combined EGM96 with high-resolution topography information to construct a hybrid SEGM over Australia.

3.2 Fundamentals of Synthetic Earth Gravity Modelling

The determination of the so-called figure of the Earth, the geoid, is a main task within geodesy. Therefore, Earth gravity modelling is ubiquitous in geodesy (e.g., Heiskanen and Moritz, 1967; Torge, 1989) as is synthetic Earth gravity modelling when aiming to construct SEGMs. Both Earth gravity and synthetic Earth gravity modelling can be done through effects modelling based on observational data, source modelling based on mass sources or hybrid modelling, a combination of effects and source modelling. With respect to the construction of an SEGM these are the corresponding modelling techniques to construct an effects model SEGM, source model SEGM or hybrid model SEGM (see Section 3.1).

3.2.1 Effects Modelling

Effects modelling is based on observational data of the Earth gravity field, most dominantly gravity observations. In this context, the observations are taken to either directly model or to derive other parameters of the Earth's gravity field. For example, gravity observations can be used directly to model the variation of Earth gravity or to derive parameters of the anomalous gravity field such as gravity anomalies or geoid heights. Some of the common observations in Earth gravity modelling are gravity, deflections of the vertical and geoid heights through the difference of GNSS-derived ellipsoidal heights and levelled heights. In the concept of synthetic Earth gravity modelling, the observational data are often taken as error-free or assumed to follow a pre-defined error model so to obtain a reasonably realistic representation of the Earth's gravity field with known error characteristics (e.g., Featherstone, 2002).

Probably the most commonly used technique in relation to effects modelling is the representation of the Earth's gravity field through a spherical harmonic series describing the external potential or other derived parameters (see Equation (2.8), Equation (2.11), Equation (2.12), Equation (2.13) and Chapter 2). Here, the observational data (mostly gravity) are used to derive the respective spherical

harmonic coefficients. As observational data are usually given on or above the Earth's surface, the spherical harmonic modelling approach in particular and effects modelling in general are only suited to model the Earth's external gravity field. This shortcoming can only be removed when modelling the sources of the Earth gravity field directly as is done by source modelling (see Section 3.2.2).

3.2.2 Source Modelling

Modelling the Earth's gravity field through its generating sources, e.g., its mass distribution, is done by source modelling. This employs forward gravity modelling techniques to be able to derive the gravitational effect or any other gravity field related parameter from the given mass sources. Importantly, source modelling can be used to model both the external and internal gravity field of the Earth. The latter is possible as the generating mass sources are assumed to be known or obtain from geological or seismological information. In the context of synthetic Earth gravity modelling it is sufficient to only use a reasonably realistic mass distribution instead of the real one, which probably will never be exactly known. Quite differently with effects modelling, in source modelling the used mass sources are either taken as error-free or assumed to follow a pre-defined error model.

Source modelling is directly based on forward gravity modelling, thus the evaluation of Newton's volume integral (Equation (2.3) and Equation (2.6) for the gravitational attraction and potential, respectively). This can be done in both the space and spectral domains (e.g., Kuhn and Seitz, 2005). The former is based on the direct evaluation of Newton's volume integral while the latter transforms Newton's volume integral into spherical harmonic series (cf. Section 3.3).

3.2.3 Hybrid Modelling

Combining both effects and source modelling is done by hybrid modelling, which unites the characteristics of both modelling techniques in one. Involving effects modelling ensures that synthetic Earth gravity modelling includes characteristics

of the observed (real) Earth gravity field while source modelling provides the opportunity to model inside the Earth's masses and to augment observational data with forward gravity modelled effects. This is frequently done for local to regional synthetic Earth gravity modelling employing global gravity models of the Earth's external potential and local or regional higher-resolution mass information to model the higher-frequency constituents of the Earth's gravity field (e.g., Baran et al., 2006). Hybrid modelling is also used when constraining mass models as to fit given observational data (e.g., Fellner, 2011; Fellner et al., 2012). In this case, the mass model may not be realistic but generates a gravity signal on or above the Earth's surface that is reasonably realistic.

3.3 Forward Gravity Modelling

The fundamental approach used in source modelling is forward gravity modelling (FGM). Based on a given mass distributions, FGM derives the generated gravitational signal by evaluating Newton's volume integral. If the mass density distribution is that of the Earth, FGM can be used to recover the Earth's gravity field. Based on the evaluation of Newton's volume integral, FGM can be used to derive any Earth gravity field related parameter outside, on its surface and inside its masses.

FGM techniques are frequently used in geophysics and geodesy to model the gravitational effect of the topographic masses (e.g Heiskanen and Moritz, 1967; Torge, 1989). While both have the aim to remove the gravitational effect of the topographic masses there is a difference in the respective views (e.g., Hackney and Featherstone, 2003; Kuhn et al., 2009). In geophysics, the gravitational effect of the topographic masses is removed so to enhance the gravitational signal, present in the Bouguer gravity anomaly, of deeper seated mass anomalies. In geodesy instead, the gravitational effect of the topographic masses is removed (1) to remove all masses outside the geoid surface or (2) to obtain smoother residuals of smaller amplitude (e.g., gravity anomalies).

Methods used for FGM can be categorized into space and spectral domain tech-

niques (e.g., Kuhn and Seitz, 2005). Space domain techniques are based on the direct evaluation of Newton's volume integral through various integration techniques (e.g., Nagy, 1966; Forsberg, 1984; Nagy et al., 2000; Smith et al., 2000; Kuhn, 2003; Heck and Seitz, 2007; Hirt, 2010; D'Urso, 2012; Tsoulis, 2012). Spectral domain techniques are based on the transformation of Newton's volume integral into the spectral domain using spherical harmonic series of powers of the mass vertical extensions of height or depth (e.g., Rummel et al., 1988; Wieczorek and Phillips, 1998; Ramillien, 2002; Kuhn, 2003; Wieczorek, 2007; Hirt and Kuhn, 2012) measured with respect to a given reference sphere (cf. Figure 3.1). While this study is mostly based on spectral domain techniques, information on commonly used space domain techniques is provided for completeness.

3.3.1 FGM in the Spectral Domain

In this approach, the formula derivation starts with the fundamental form of Newton's volume integral for the gravitational potential (see Equation (2.6)). Following the approach taken in Kuhn and Featherstone (2002), the gravitational potential $V(\Omega, r)$ at point $P(\Omega, r)$ located on or above the mean sphere with radius R is expressed by

$$V(\Omega, r) = \sum_{l=0}^{l_{\max}} \left(\frac{R}{r}\right)^{l+1} \sum_{m=-l}^{l} \bar{V}_{lm} \bar{Y}_{lm}(\Omega), \tag{3.1}$$

with the fully normalized SHC $\bar{V}_{lm}$, and the surface spherical harmonics are

$$\bar{Y}_{lm}(\Omega) = \begin{cases} \bar{P}_{lm}(\cos\theta)\cos m\lambda & m \geq 0 \\ \bar{P}_{l|m|}(\cos\theta)\sin|m|\lambda & m < 0 \end{cases} \tag{3.2}$$

$\bar{P}_{lm}$ denotes the fully normalized associated Legendre functions of the first kind for degree l and order m (e.g., Heiskanen and Moritz, 1967). $\Omega(\theta, \lambda)$ denotes the coordinate pair of spherical longitude λ and co-latitude θ, and r is the radial distance measured from the geo-centre to the point $P(\Omega, r)$.

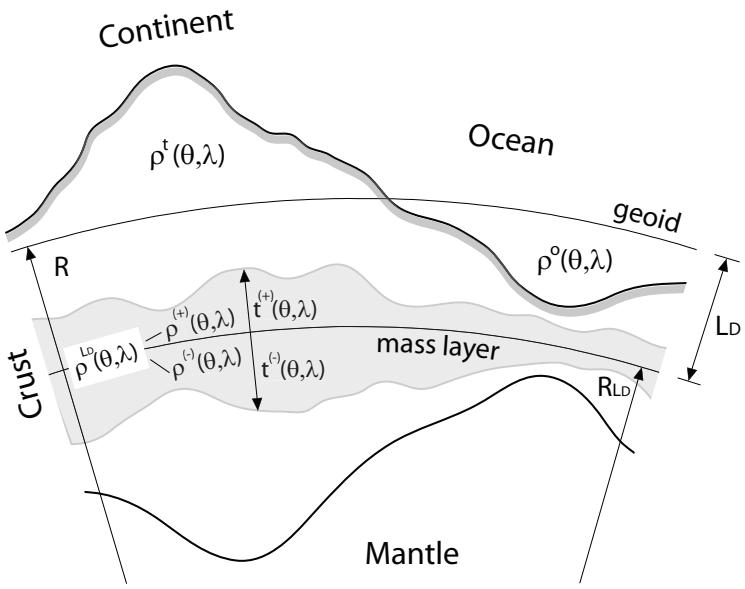

Figure 3.1: Mass layer within the Earth's crust [adapted form Kuhn and Featherstone (2002)]

A relation between the given mass distribution and the spherical harmonic coefficients $\bar{V}_{lm}$ in Equation (3.1) can be found by replacing the inverse distance in Newton's volume integral through a series of Legendre polynomials and expansion of the height/depth ($t^{(\pm)}$ in Figure 3.1) into a binomial series. The fully normalized SHC are given by an infinite sum of SHC, $\bar{\kappa}_{p,lm}$ representing surface density functions (Ramillien, 2002; Kuhn and Featherstone, 2003)

$$\bar{V}_{lm} = \mu_l \left(\frac{R_L}{R}\right)^{l+2} \sum_{p=1}^{\infty} \frac{\Gamma(l+3)}{p!\Gamma(l+4-p)} \bar{\kappa}_{p,lm} \tag{3.3}$$

with the factor

$$\mu_l = \frac{4\pi G R}{2l+1} \tag{3.4}$$

and the fully normalized SHC, $\bar{\kappa}_{p,lm}$, related to the surface density functions $\kappa_p(\Omega)$ via

$$\kappa_p(\Omega) = \rho(\Omega)\frac{t^{(\pm)^p}(\Omega)}{{R_L}^{p-1}} = \sum_{l=0}^{l_{max}} \sum_{m=-l}^{l} \bar{\kappa}_{p,lm} Y_{lm}(\Omega), \qquad p \in N^+. \tag{3.5}$$

In the above relation, the actual mass distribution used has been described as a spherical layer with a laterally variable mass density $\rho(\Omega)$ and vertical extensions above ($t^{(+)}(\Omega) > 0$) or below ($t^{-}(\Omega) < 0$) the mean sphere of radius R_{L_D}. While Equation (3.3) holds for any mass distribution the height/depth functions $t^{(\pm)}(\Omega)$ and density $\rho(\Omega)$ can be replaced by the topographic height $h^t(\Omega)$ and density $\rho^t(\Omega)$ and ocean depth $d^o(\Omega)$ and density $\rho^o(\Omega)$ when dealing with topographic and bathymetric masses, respectively (see Figure 3.1 and Section 3.3.3).

As Equation (3.3) depends on surface density functions (see Equation (3.5)), it is important to include more than one term (e.g., $p > 1$) in order to model the third dimension of the mass distribution considered. According to Wieczorek (2007), the first term $p = 1$ corresponds to the effect of a spherical shell and terms $p > 1$ can be interpreted as terrain corrections, thus adding the third dimension. Hirt and Kuhn (2012) have shown that terms up to 7^{th} power are required to model gravitational effects of the most rugged topography over the Himalayan with a mGal-level precision. Truncating to only third power gives rise to maximum truncation errors exceeding 100 mGal when evaluating Equation (3.1) on the sphere (e.g., $r = R_{L_D} = R$).

It is important to mention that the coefficients $\bar{V}_{lm}$ given by Equation (3.3) differ from other derivations (e.g., Rummel et al., 1988; Wieczorek and Phillips, 1998; Wieczorek, 2007; Hirt and Kuhn, 2012) in that they are not dimensionless but carry the dimension of potential. The difference is given by the factor $\frac{GM}{R}$. This is also the reason why Equation (3.3) depends only on the mass density of the considered mass distribution and not on the mean density of the Earth.

The explicit formulae for the spherical harmonic coefficients given by Equation (3.3) are provided in Section 3.3.3 and Section 3.3.4 for the gravitational potential of the topographic, ocean water and compensation masses.

3.3.2 Effect of Spherical Mass Distributions

In spherical approximation, all mass density distributions can be expressed as deviations $t^{(+)}(\Omega)$ above and $t^{(-)}(\Omega)$ below a mean sphere at depth L_D, i.e., with the radius $R_{L_D} = R - L_D$. In the following, the superscripts (+) and (-) denote parameters that apply to masses respectively located above and below the mean sphere with radius R_{L_D} (see Figure 3.1).

The gravitational potential V at point $P(\Omega, r)$ is given by Newton's volume integral (cf. Equation (2.6))

$$V^{(\pm)}(\Omega, r) = G \iiint_v \frac{\rho^{(\pm)}(\Omega')}{L(\Omega, r, \Omega', r')} dv' \tag{3.6}$$

for the radial distance, r, the spherical volume element $dv = r^2 \sin(\theta)\, d\lambda\, d\theta\, dr$, the gravitational constant G, and the Euclidean distance (e.g., Heiskanen and Moritz, 1967)

$$L(\Omega, r, \Omega', r') = \sqrt{r^2 + r'^2 - 2rr' \cos\psi}$$

with $\cos\psi = \cos\theta\cos\theta' + \sin\theta\sin\theta'\cos(\lambda' - \lambda)$. By replacing the inverse distance in Equation (3.6) by a series of Legendre polynomials (e.g., Heiskanen and Moritz, 1967), Newton's integral can be expressed by (see also Equation (3.1))

$$V^{(\pm)}(\Omega, r) = \sum_{l=0}^{l_{max}} \left(\frac{R}{r}\right)^{l+1} \sum_{m=-l}^{l} \bar{V}_{lm}^{(\pm)} \bar{Y}_{lm}(\Omega). \tag{3.7}$$

$\bar{V}_{lm}^{(\pm)}$ are the fully normalized spherical harmonic coefficients and the surface spherical harmonics are given by Equation (3.2). For a laterally variable density distribution $\rho^{(\pm)}(\Omega)$, the fully normalized spherical harmonic coefficients are

$$\bar{V}_{lm}^{(\pm)} = \mu_l \left(\frac{R_{L_D}}{R}\right)^{l+2} \sum_{p=1}^{\infty} \bar{\kappa} p_{lm}^{*\,(\pm)} \tag{3.8}$$

where

$$\bar{\kappa} p_{lm}^{*\,(\pm)} = (\pm 1)^p \frac{\Gamma(l+3)}{p!\Gamma(l+4-p)} \bar{\kappa} p_{lm}^{(\pm)}, \qquad p \in N^+ \tag{3.9}$$

with the fully normalized spherical harmonic coefficients $\bar{\kappa}p^{\pm}_{lm}$ of the surface density functions (see Equation (3.5))

$$\bar{\kappa}p^{(\pm)} = \rho^{(\pm)}(\Omega)\frac{t^{(\pm)^p}}{{R_L}^{p-1}}, \qquad p \in N^+ \tag{3.10}$$

and the factor μ_l given by Equation (3.4).

3.3.3 Effect of Topographic and Ocean Masses

Following the general approach in the previous section, the topographic and oceanic masses can be expressed as deviation from the mean sphere with radius R. Introducing the topographic height $h^t(\Omega)$ and ocean depth $d^o(\Omega)$ (see Figure 3.1) in Equation (3.10) yields κp^t and κp^o and the spherical harmonic coefficients (given for $p \leq 3$) are

$$\bar{V}^t_{lm} = \mu_l \left[\bar{\kappa}1^t_{lm} + \frac{l+2}{2}\left(\bar{\kappa}2^t_{lm} + \frac{l+1}{3}\bar{\kappa}3^t_{lm}\right)\right] \tag{3.11}$$

$$\bar{V}^o_{lm} = \mu_l \left[\bar{\kappa}1^o_{lm} + \frac{l+2}{2}\left(-\bar{\kappa}2^o_{lm} + \frac{l+1}{3}\bar{\kappa}3^o_{lm}\right)\right]. \tag{3.12}$$

3.3.4 Effect of Compensation Masses

For any kind of compensation masses below the mean sphere with radius R (e.g., geoid in spherical approximation), only the upward-continuation factor $\left(\frac{R_{L_D}}{R}\right)^{l+2}$ has to be considered for the attenuation of energy of the spherical harmonic coefficients when evaluating the gravitational potential through Equation (3.1). The explicit formula (given for $p \leq 3$) is given by

$$\bar{V}^{(\pm)}_{lm} = \mu\left(\frac{R_{L_D}}{R}\right)^{l+2}\left[\bar{\kappa}1^{(\pm)}_{lm} + \frac{l+2}{2}\left(\pm\bar{\kappa}2^{(\pm)}_{lm} + \frac{l+1}{3}\bar{\kappa}3^{(\pm)}_{lm}\right)\right]. \tag{3.13}$$

3.3.5 Extended Meissl Scheme for FGM

As explained earlier in Section 2.1.6, different gravity field parameters (e.g., geoid height N and gravity disturbance δg) can be derived from the gravitational potential using Meissl's spectral scheme (e.g., Rummel and van Gelderen, 1995).

Here, Meissl's scheme is extended for forward gravity modelling by including the spectral relation between the mass distribution (e.g., κp^*_{lm}) and potential (e.g., V_{lm}). (e.g., Kuhn and Featherstone, 2002). Table 3.1 shows the extended Meissl's scheme, where the relation between κp^*_{lm} and V_{lm} (see Equation (3.9)) is included in the left column and upper row of the scheme. The grey shaded part of Table 3.1 is the original Meissl scheme as given by Figure 2.4 in Chapter 2.

Table 3.1: The extended Meissl spectral scheme for FGM (from Kuhn and Featherstone (2002)).

	κp^*_{lm}	V_{lm}	N_{lm}	δg_{lm}
κp^*_{lm}	1	$\left[\mu_l \left(\frac{R_{L_D}}{R}\right)^{l+2}\right]^{-1}$	$\left[\frac{\mu_l}{\gamma} \left(\frac{R_{L_D}}{R}\right)^{l+2}\right]^{-1}$	$\left[\frac{-(l+1)\mu_l}{R} \left(\frac{R_{L_D}}{R}\right)^{l+2}\right]^{-1}$
V_{lm}	$\mu_l \left(\frac{R_{L_D}}{R}\right)^{l+2}$	1	$\left[\frac{1}{\gamma}\right]^{-1}$	$\left[-\frac{l+1}{R}\right]^{-1}$
N_{lm}	$\frac{\mu_l}{\gamma} \left(\frac{R_{L_D}}{R}\right)^{l+2}$	$\frac{1}{\gamma}$	1	$\left[-\frac{\gamma(l+1)}{R}\right]^{-1}$
δg_{lm}	$\frac{-(l+1)\mu_l}{R} \left(\frac{R_{L_D}}{R}\right)^{l+2}$	$-\frac{l+1}{R}$	$-\frac{\gamma(l+1)}{R}$	1

3.3.6 FGM in the space domain

Newton's volume integral (Equation (2.6)) can be solved analytically with closed formulae for simple, discrete mass elements or evaluated numerically for any arbitrary mass distribution. The latter has to be applied when dealing with the Earth's mass distribution, which is too complex to provide a closed solution for Newton's volume integral. Numerical integration techniques can be based on either standard algorithms such as based on the Gaussian quadrature rule (e.g., Hildebrand, 1974) or on so-called *discretised* numerical integration (e.g., Kuhn, 2003; Kuhn et al., 2009). The latter approach combines analytical solutions for discrete mass elements with numerical integration techniques. In this case Newton's volume integral is replaced by a summation over the gravitational effect generated by a series of discrete mass elements such as point masses, prisms, polyhedrons or tesseroids (e.g. Nagy, 1966; Forsberg, 1984; Nagy et al., 2000; Smith et al., 2000; Kuhn, 2003; Heck and Seitz, 2007; Hirt, 2010; D'Urso, 2012;

Tsoulis, 2012). Following the *discretised* numerical integration approach, Newton's volume integral for the gravitational potential (Equation (2.6)) is replaced by the summation

$$V(\phi, \lambda, r) = \sum_{l=1}^{N} \delta V_i(\phi, \lambda, r, \phi_i, \lambda_i, r_i), \tag{3.14}$$

where $\delta V_i(\phi, \lambda, r, \phi_i \lambda_i, r_i)$ is the effect on the gravitational potential at the evaluation point (ϕ, λ, r) of the mass element i located at (ϕ_i, λ_i, r_i). The summation in Equation (3.14) is done over all N discrete mass element that are used to describe (approximately) the given mass distribution (e.g., of the Earth).

The discretised numerical integration is commonly used in Earth gravity modelling. Basically, any geometrical body with a regular shape and size can be used as a mass element. A single point mass is often used in FGM as it is the simplest mass body, thus relatively simple formulae can be used (e.g., Barthelmes and Kautzleben, 1983; Barthelmes et al., 1991; Barthelmes and Dietrich, 1991; Vermeer, 1995; Claessens and Featherstone, 2001, etc.). Other commonly used regular shaped mass bodies are tesseroids, prisms and polyhedra. In the following, brief summaries of discretised numerical integration using tesseroids and prisms are given.

Discretised numerical integration using tesseroids

The term "tesseroid" was probably first introduced by Anderson (1976). It is a spherically shaped mass block (Figure 3.2) that describes the volume element in spherical coordinates. This kind of geometrical body is appropriate to be used for global applications where the Earth's curvature has to be considered. The gravitational potential generated by a tesseroid (spherical volume element) can be derived from Newton's volume integral (Equation (2.6)) by the following formula

$$V(\Omega, r) = G \iiint_{v_{Tess}} \frac{\rho}{L(\Omega, r, \Omega', r')} dv \tag{3.15}$$

where v_{Tess} is the volume of the tesseroid, $dv = r^2 \cos\phi d\lambda d\phi dr$ is the infinitesimal spherical volume element, r is the radial distance measured from the Earth's centre to the evaluation point $P(\Omega, r)$, $L(\Omega, r, \Omega', r')$ is the Euclidean distance between the evaluation point (Ω, r) and the source point Ω', r' and Ω is the coordinate pair of latitude and longitude (ϕ, λ). In Equation (3.15), ρ denotes the density, which is considered constant within the tesseroid. To evaluate Equation 3.15, a series expansion of the integrand around the mid-point $P_0(\phi_0 = (\phi_1 + \phi_2)/2, \lambda_0 = (\lambda_1 + \lambda_2)/2, r_0 = (r_1 + r_2)/2)$ can be introduced and subsequently piece-wise integrated (e.g., Seitz and Heck, 2003). This yields,

$$V(\Omega, r) = G\rho(\Omega')r_0 \frac{\cos\psi_0(\Omega, r, \Omega', r')}{\sqrt{C}} \Delta\lambda\Delta\phi\Delta r + O^2(\Delta\lambda, \Delta\phi, \Delta r) \qquad (3.16)$$

with the constant $C = l_0^2/r_0^2$ and $l_0 = 2\pi \sin(\psi_0/2)$, where ψ_0 is the spherical distance between mid-point P_0 of the tesseroid and computation point $P(\Omega', r')$ (e.g., Heiskanen and Moritz, 1967) and $\Delta\phi = \phi_2 - \phi_1, \Delta\lambda = \lambda_2 - \lambda_1, \Delta r = r_2 - r_1$.

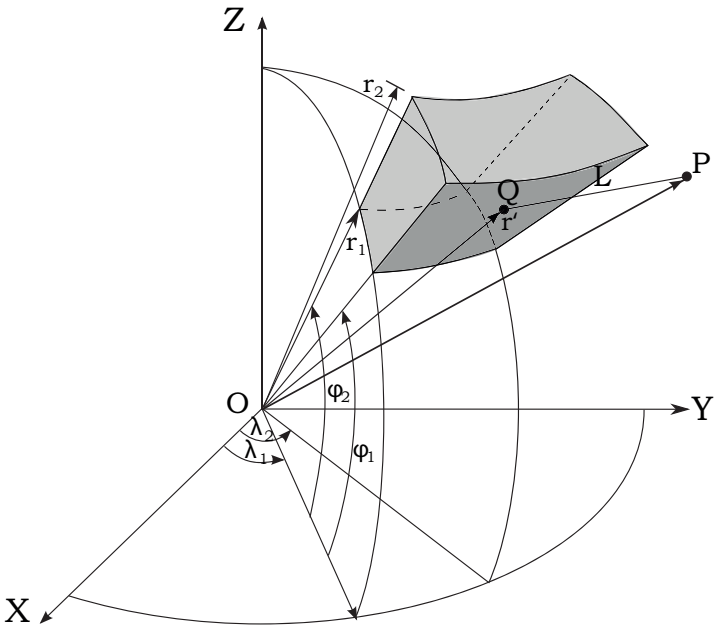

Figure 3.2: Geometry of a tesseroid (spherical volume element) [from Kuhn and Seitz (2005)]. The coordinates X, Y, Z refer to a global 3D Cartesian coordinate system.

Discretised numerical integration using prisms

For local gravity field studies, where a flat-Earth approximation is adequate, or regional and global studies where spherical mass elements are approximated, a right rectangular parallelepiped (prism) is commonly used as a mass element for FGM (e.g., Mader, 1951; Nagy, 1966; Tsoulis, 1999; Nagy et al., 2000; Smith et al., 2000; Tsoulis, 2000; Kuhn and Seitz, 2005; Heck and Seitz, 2007; Fellner, 2011; Grombein et al., 2013). The gravitational potential generated by a prism can be derived from Newton's volume integral (Equation (2.6)) by the following formula

$$V(\Omega, r) = G \iiint_{v_{Prism}} \frac{\rho}{L(\Omega, r, \Omega', r')} dv \tag{3.17}$$

where v_{Prism} is the volume of the prism and $dv = dxdydz$ is the infinitesimal volume element

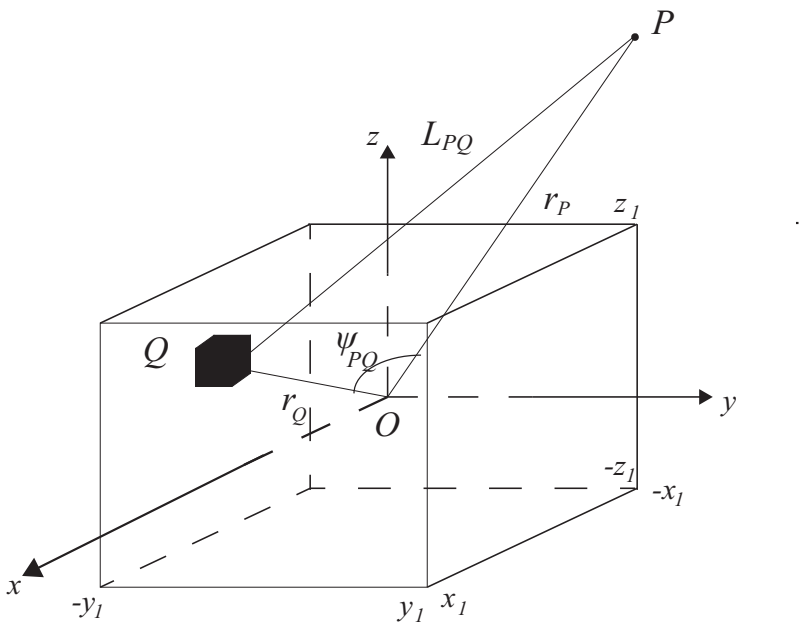

Figure 3.3: Geometry of a right rectangular prism. The origin of the coordinate system is placed in the centre of the prism. (adapted from Tsoulis (1999))

Based on the prism's dimension illustrated in Figure 3.3, Newton's integral, Equation (2.6) can be solved using the following formula (e.g., Nagy et al., 2000)

$$\begin{aligned}\frac{1}{G\rho}V &= \left|\left|\left| xy\ln\left(\frac{z+L}{L_z}\right) + yz\ln\left(\frac{y+L}{L_y}\right) + yx\ln\left(\frac{x+L}{L_x}\right) - \right.\right.\right. \\ &\quad -\frac{1}{2}x^2\arctan\frac{yz}{Lx} - \frac{1}{2}y^2\arctan\frac{xz}{Ly} - \\ &\quad \left.\left.\left. -\frac{1}{2}z^2\arctan\frac{xy}{Lx}\right|_{-x_1}^{x_1}\right|_{-y_1}^{y_1}\right|_{-z_1}^{z_1}\end{aligned} \tag{3.18}$$

with the auxiliary quantities

$$L = \sqrt{x^2+y^2+z^2} \tag{3.19}$$

$$L_x = \sqrt{y^2+z^2} \quad L_y = \sqrt{x^2+z^2} \quad L_z = \sqrt{x^2+y^2}. \tag{3.20}$$

3.4 Chapter Summary

Fundamentals of SEGMs and forward gravity modelling were presented in this chapter. Based on the techniques to construct SEGMs, three different types of SEGMs, i.e., sorce model SEGMs, effects model SEGMs and hybrid model SEGMs were briefly discussed. The concept of synthetic gravity modelling called here synthetic Earth gravity modellling, which is important for this study, was outlined. This concept follows that of SEGMs by distinguishing between effects, source and hybrid modelling. As synthetic Earth gravity modelling is based on FGM principles, techniques applied in the space and spectral domains have been presented.

Chapter 4

Inferring Mass Changes from Gravity Changes

Spatial and temporal gravity changes detected from space (e.g. by the GRACE mission) reflect mass re-distributions (or mass transports) in space and time. Many studies have been performed (e.g., Tapley et al., 2004a; Wahr et al., 2004; Andersen and Hinderer, 2005; Han et al., 2005a; Rowlands et al., 2005) that show that the GRACE mission is capable to observe large-scale (e.g., few hundred kilometres in extension) mass redistributions within the Earth system. According to Chao (2005), temporal changes of Earth gravity or simply termed as time-variable gravity is the sum of the gravitational signals originating from all geophysical sources at work at any given time.

This chapter first presents some examples on the use of GRACE time-variable gravity observations for the detection of mass changes over the cryosphere, hydrological changes over land and mass changes in the Earth's interior. This is followed by the main focus, the presentation of techniques commonly used to infer mass changes from time-variable gravity with a specific view on the technique proposed by Wahr et al. (1998). The chapter closes by presenting the smoothing procedures used in this thesis. These are the Gaussian isotropic smoothing and and non-isotropic smoothing according to Han et al. (2005b), Kusche (2007) and Kusche et al. (2009).

4.1 Detecting Mass Changes from GRACE Time-variable Gravity

Changes in Earth's gravity field can be used to study processes involving changes in the Earth's mass distribution (e.g., Wahr et al., 2004). This corresponds to an inverse gravimetric problem which is known to be not unique (e.g., Moritz, 1990). According to Ramillien et al. (2004), the GRACE time-variable gravity can be useful to detect changes as a result of surface and deep currents in the oceans, change in soil and ground water storage on land, mass changes of the ice sheets and glaciers (cryosphere), air and water vapor mass change within the atmosphere and variation of mass within the solid part of the Earth. A study by Fengler et al. (2006) shows that GRACE time-variable gravity is also capable of sensing signals related to high-frequency geophysical, geodetic, magnetic and oceanographic phenomena. In the following, examples of different studies that utilize the capability of GRACE data to detect mass changes will be briefly summarized.

4.1.1 Mass Changes over the Cryosphere

Numerous studies have shown that GRACE can detect and monitor large-scale ice mass changes. In particular, the study of mass balance over polar ice sheets (Greenland and Antarctica) is substantially improved by GRACE gravity mass change estimates as they directly measure the mass variation or redistribution (e.g. Cazenave and Chen, 2010). "Secular" mass rates over the Greenland and Antarctica ice sheets could already be derived from a few years of GRACE time-variable gravity data. From GRACE data alone, studies have shown the significant mass losses in East Greenland and West Antarctica (e.g., Velicogna and Wahr, 2006b,a; Chen et al., 2006b,d; Ramillien et al., 2006; Luthcke et al., 2006b; Arendt et al., 2008; Baur et al., 2009; Velicogna, 2009).

The extended lifetime of the GRACE mission means that increasingly more data are available to provide a significantly improved constraint on present-day ice loss. The new estimates from 6-7 years of GRACE data indicate that Antarctica

is losing ice at 220-246 Gt/year during the period 2006-2009 (e.g. Wouters et al., 2008; Cazenave et al., 2009; Peltier, 2009; Velicogna, 2009; Chen et al., 2009a). The majority of ice loss is from West-Antarctica, particularly in Amundsen Sea and Antarctic peninsula. Over Greenland, a study by Velicogna (2009) shows a rate of ice loss of 267-286 Gt/year during 2006-2009.

Apart from its capability for detecting the mass variation of large ice sheets, GRACE also provides estimates of mass rates of mountain glaciers (e.g., Tamisiea et al., 2005; Chen et al., 2006a; Arendt et al., 2008; Luthcke et al., 2008). Over the Alaskan glacier complex, a study by Chen et al. (2006a) shows the significant amount of mass loss of 101 $\pm$ 22 Gt/year (between April 2002 - November 2005), whereas Luthcke et al. (2008), based on GRACE mascon solutions, estimate a loss of 71 $\pm$ 6 Gt/yr (July 2003 - July 2008).

4.1.2 Hydrological Mass Changes

Hinderer et al. (2006) showed that seasonal changes in the gravity field detected by GRACE include large scale continental hydrological cycles. Inter-annual gravity changes from GRACE also have been studied by Andersen and Hinderer (2005) in relation to changes in terrestrial water storage (TWS). Schmidt et al. (2006), state that the time-variable gravity field measured by GRACE has provided a novel data source for measuring the variation of continental water storage from space, even though it only has a limited spatial resolution. A series of studies of regional to continental scales using GRACE gravity estimates have been successfully performed to detect land hydrology changes (e.g., Swenson and Wahr, 2003; Rodell et al., 2004; Han et al., 2005b; Chen et al., 2005b; Ramillien et al., 2005; Seo and Wilson, 2005; Seo et al., 2006; Frappart et al., 2006; Schmidt et al., 2006; Chen et al., 2007a; Fiedler and Döll, 2007; Klees et al., 2007; Chen et al., 2009b; Han et al., 2009; Brown and Tregoning, 2010; Longuevergne et al., 2010) and ocean mass changes (e.g., Nerem et al., 2003; Chambers et al., 2004; Lombard et al., 2007; Morison et al., 2004; Chambers, 2009; Catalão and Sevilla, 2009).

Over the Amazon basin, a study by Chen et al. (2009b) detected the signature

of the 2005 extreme drought in the Amazon basin, the 2002-2003 El-Ninõ event and abnormal warming of the northern tropical Atlantic Ocean. In their study, Swenson and Wahr (2009) found a significant TWS minimum over Lake Victoria which apparently is related to the drought in this region in 2005.

4.1.3 Mass Changes in the Earth's Interior

Some research has been performed to investigate the potential of GRACE time-variable gravity for understanding solid Earth processes. Studies by Bao et al. (2005); Han et al. (2006a); Ogawa and Heki (2007); Chen et al. (2007b); Lemoine et al. (2007a); Panet et al. (2007); Sabadini et al. (2007); de Viron et al. (2008); Migliaccio et al. (2008); Han and Simons (2008); Han et al. (2008); Cannelli et al. (2008); Anjasmara (2008); Anjasmara and Kuhn (2009, 2010); and de Linage et al. (2009) have shown that the GRACE data clearly depicted the effect of the great 2004 Sumatra-Andaman earthquake.

Following the melting of ice loads during the last glacial maximum some 20,000 years ago, a large isostatic adjustment of the Earth's crust and mantle (called post-glacial rebound, PGR) is also happening. This process generates secular gravity field changes which can be detected by GRACE by its extended period of collecting time-variable gravity data. Paulson et al. (2007) used GRACE and other geological observations to refine PGR modelling and constrain upper and lower mantle viscosity. Studies by Barletta et al. (2008); Barletta and Bordoni (2009) also show that GRACE is able to detect crustal changes due to post-glacial rebound.

4.2 Techniques to Infer Mass Changes from Time-variable Gravity

In Chapter 3 it has been shown that the Earth gravity field is generated by the gravitational effect of its mass distribution such as masses inside the Earth, on its surface and its atmosphere. The fundamental relation between the mass distribution and its generated gravitational effects is provided by Newton's vol-

ume integral (see Equation (2.6)). According to Newton's law of gravitation any change in gravity is directly related to a change in the generating mass distribution. This is the fundamental property used when inferring mass changes from time-variable gravity such as observed by the GRACE mission.

If the mass distribution and/or changes in the mass distribution are known the corresponding gravitational effect is directly obtained by applying forward gravity modelling techniques, e.g. the evaluation of Newton's volume integral (see Chapter 3). Inversion techniques have to be used when deriving mass changes from time-variable gravity. In this regard, Newton's integral represents an integral equation that has to be solved for the unknown mass distribution. As will be shown in this chapter, the inversion is not-unique and requires some external constraints such as the spatial extent of the mass distribution (e.g., Moritz, 1990). Techniques used in this thesis are based on the assumption that mass changes are surface mass changes only, e.g. given by a surface mass layer.

4.2.1 Relation between Gravity and Surface Mass Changes

One of the drawbacks of inferring mass changes from time-variable gravity is the non-unique solution of the gravitational inverse problem. It states that the external gravity field, even if completely and exactly known, cannot uniquely determine the density distribution of the body that produces the gravity field (e.g., Chao, 2005). This is a natural character of the gravity field that obeys the Laplace equation (e.g., Hofmann-Wellenhof and Moritz, 2005). One possibility to mitigate this problem for Earth gravity is to introduce the constraint that all mass changes are represented by surface mass changes on the Earth's surface.

The uniqueness problem of the gravitational inversion for satellite application has been examined by Chao (2005) using spherical harmonic representations of the gravitational signal. Chao (2005) proved that using a 2-D spherical shell without radial dependency, the gravitational inversion for the (surface) density function is unique. This assumption is applicable for many geophysical processes of the Earth that happen on or close to the Earth's surface. Therefore, by assuming the

density redistribution is concentrated in a thin layer on the Earth's surface, the inversion of time-variable gravity to mass changes is unique (e.g., there is only one mass layer that can produce the given gravity signal).

The unique relation between the gravitational potential and the generating surface masses is given in the spectral domain by the first term of Equation (3.3) and setting $R_{L_D} = R$. The relation is given between the respective spherical harmonic coefficients of the gravitational potential $\bar{V}_{lm}$ and the surface density $\bar{\kappa}_{lm}$ (e.g., Kuhn and Featherstone, 2002, eq. 4)

$$\bar{V}_{lm} = \frac{4\pi GR}{2l+1}\bar{\kappa}_{lm}. \tag{4.1}$$

In Equation (4.1) the spherical harmonic coefficients $\bar{\kappa}_{lm}$ are that of the laterally variable surface density function $\kappa(\Omega) = \rho(\Omega)h(\Omega)$. For a constant density (e.g. $\rho = \rho_w = 1000\ kg/m^3$) the relation is given in the spectral domain by

$$\bar{V}_{lm} = \frac{4\pi GR\rho}{2l+1}\bar{h}_{lm} \tag{4.2}$$

for the spherical harmonic coefficients $\bar{h}_{lm}$ of the laterally variable height function $h(\Omega)$.

The relations given by Equation (4.1) and Equation (4.2) hold for a rigid Earth while for an elastic Earth the Love numbers k_l have to be introduced changing the relation to

$$\bar{V}_{lm} = \frac{4\pi GR}{2l+1}(1+k_l)\bar{\kappa}_{lm} \tag{4.3}$$

for the surface density coefficients $\bar{\kappa}_{lm}$ and

$$\bar{V}_{lm} = \frac{4\pi GR\rho}{2l+1}(1+k_l)\bar{h}_{lm} \tag{4.4}$$

for the height coefficients $\bar{h}_{lm}$.

Solving Equation (4.3) and Equation (4.4) for κ_{lm} and h_{lm} yields

$$\bar{\kappa}_{lm} = \frac{2l+1}{4\pi GR(1+k_l)}\bar{V}_{lm} \tag{4.5}$$

and

$$\bar{h}_{lm} = \frac{2l+1}{4\pi GR\rho(1+k_l)}\bar{V}_{lm}, \tag{4.6}$$

respectively. Based on the spherical harmonic coefficients given in Equation (4.5) and Equation (4.6), the corresponding lateral variable functions in the space domain are obtained by the evaluation of

$$\kappa(\Omega) = \frac{1}{4\pi GR}\sum_{l=0}^{l_{max}}\sum_{m=-l}^{l}\frac{2l+1}{(1+k_l)}\bar{V}_{lm}\bar{Y}_{lm} \tag{4.7}$$

for the surface density function and

$$h(\Omega) = \frac{1}{4\pi GR\rho}\sum_{l=0}^{L_{max}}\sum_{m=-l}^{l}\frac{2l+1}{(1+k_l)}\bar{V}_{lm}\bar{Y}_{lm} \tag{4.8}$$

for the height function, where the fully normalized surface spherical harmonics $\bar{Y}_{lm}$ are given by Equation (3.2).

In Equation (4.5) and Equation (4.6) or Equation (4.7) and Equation (4.8) the factor $(2l+1)$ causes an increased amplification of errors for higher degree terms. This property is the main reason for the introduction of filtering techniques to dampen higher-frequency noise as will be explained in Section 4.3.

While the spherical harmonic coefficients $\bar{V}_{lm}$ used above are not dimensionless but have the unit of potential often the dimensionless coefficients $\bar{c}_{lm}$ are used. The relation between $\bar{V}_{lm}$ and $\bar{c}_{lm}$ is given by (e.g., Heiskanen and Moritz, 1967)

$$\bar{V}_{lm} = \frac{GM}{R}\bar{c}_{lm}. \tag{4.9}$$

Introducing Equation (4.9) into Equation (4.5) and Equation (4.6) yields

$$\bar{\kappa}_{lm} = \frac{(2l+1)GM}{4\pi GR^2(1+k_l)}\bar{c}_{lm} \tag{4.10}$$

and

$$\bar{h}_{lm} = \frac{(2l+1)GM}{4\pi GR^2\rho(1+k_l)}\bar{c}_{lm}. \tag{4.11}$$

Introducing the total mass of the Earth

$$M = \frac{4}{3}\pi R^3 \rho_{ave} \tag{4.12}$$

with the average density and radius of the Earth ρ_{ave} and R respectively yields

$$\bar{\kappa}_{lm} = \frac{R\rho_{ave}}{3}\frac{(2l+1)}{(1+k_l)}\bar{c}_{lm} \tag{4.13}$$

and

$$\bar{h}_{lm} = \frac{R\rho_{ave}}{3\rho}\frac{(2l+1)}{(1+k_l)}\bar{c}_{lm}. \tag{4.14}$$

Finally, the evaluation formulae (see Equation (4.7) and Equation (4.8)) for the laterally variable functions $\kappa(\Omega)$ and $h(\Omega)$ in the space domain are now given by (e.g. Wahr et al., 1998, eq. 14)

$$\kappa(\Omega) = \frac{R\rho_{ave}}{3}\sum_{l=0}^{l_{max}}\sum_{m=-l}^{l}\frac{2l+1}{(1+k_l)}\bar{c}_{lm}\bar{Y}_{lm} \tag{4.15}$$

and

$$h(\Omega) = \frac{R\rho_{ave}}{3}\sum_{l=0}^{l_{max}}\sum_{m=-l}^{l}\frac{2l+1}{(1+k_l)}\bar{c}_{lm}\bar{Y}_{lm} = \frac{\kappa(\Omega)}{\rho} \tag{4.16}$$

with the surface spherical harmonics $\bar{Y}_{lm}$ given by Equation (3.2) and $\rho_{ave} = \rho =$ constant.

4.2.2 Surface Mass Change Estimates According to Wahr et al. (1998)

Fundamental to this study is the surface mass change estimation technique developed by Wahr et al. (1998). Currently, this technique is probably most commonly used to derive surface mass change estimates from time-variable gravity observations of the GRACE mission (e.g., Swenson and Wahr, 2002; Swenson et al., 2003; Swenson and Wahr, 2003; Baur et al., 2009). The method is based on the same relation between the spectral representations of changes in the gravitational potential and a lateral variable surface density (or height) function as presented in Chapter 3, however, with the difference, that the technique of Wahr et al. (1998)

only considers surface mass density changes whereas the technique presented in Chapter 3 is based on the general case of a 3D mass density distribution. Because of the importance of this technique, this chapter provides a summary of the main development steps.

Wahr et al. (1998) showed that a local change in surface mass density, $\Delta\kappa(\Omega)$, can be related to the change in gravitational potential, given by the corresponding changes in spherical harmonic coefficients (time-variable SHC) ΔC_{lm} and ΔS_{lm} (see Equation (4.17) and Equation (4.18) below). Like in the previous chapter, the fundamental assumption is that the 3D density distribution, $\Delta\rho(r,\Omega)$, is concentrated to a thin layer with the surface mass density given by

$$\Delta\kappa(\Omega) = \int\limits_{\text{thin layer}} \Delta\rho(r,\Omega)dr. \tag{4.17}$$

Based on Equation (4.17) the relation between (surface) mass density changes and changes of the gravitational potential expressed in the spectral domain are given by

$$\begin{aligned}\begin{Bmatrix} \Delta C_{lm} \\ \Delta S_{lm} \end{Bmatrix} &= \frac{3}{4\pi R\rho_{ave}(2l+1)} \int \Delta\rho(r,\Omega)\bar{P}_{lm}(\cos\phi) \\ &\times \left(\frac{r}{R}\right)^{n+2} \begin{Bmatrix} \cos(m\lambda) \\ \sin(m\lambda) \end{Bmatrix} \sin\phi \; d\phi \; d\lambda \; dr\end{aligned} \tag{4.18}$$

with ρ_{ave} being the average density of the Earth (e.g., $\rho_{ave} = 5517kg/m^3$).

The relation above holds for a rigid Earth, thus it provides the direct gravitational effect of the surface mass changes without the elastic deformation of the solid Earth due to the surface mass load changes. To account for this, Equation (4.19) and Equation (4.20), respectively, show the direct gravitational effect as well as the indirect gravitational effect due to elastic deformation of the solid Earth. The total change in the Earth's gravitational potential is expressed by the sum of the

corresponding spherical harmonic coefficients.

$$\left\{ \begin{array}{c} \Delta C_{lm} \\ \Delta S_{lm} \end{array} \right\}_{\text{surf mass}} = \frac{3}{4\pi R \rho_{ave}(2l+1)} \int \Delta\sigma(\phi,\lambda) \times \bar{P}_{nm}(\cos\phi) \left\{ \begin{array}{c} \cos(m\lambda) \\ \sin(m\lambda) \end{array} \right\} \sin\phi \; d\phi \; d\lambda \tag{4.19}$$

$$\left\{ \begin{array}{c} \Delta C_{lm} \\ \Delta S_{lm} \end{array} \right\}_{\text{elastic E}} = \frac{3k_l}{4\pi R \rho_{ave}(2l+1)} \int \Delta\kappa(\Omega) \times \bar{P}_{lm}(\cos\phi) \left\{ \begin{array}{c} \cos(m\lambda) \\ \sin(m\lambda) \end{array} \right\} \sin\phi \; d\phi \; d\lambda. \tag{4.20}$$

Equation (4.20) includes the Love numbers k_l representing the elastic response of the Earth due to the changing surface mass loads, where for $l = 1$ it is assumed that the origin of the coordinate system is the centre of figure of the solid Earth not including the oceans. The Love numbers are taken from Wahr et al. (1998) and given in Table 4.1.

Table 4.1: Elastic Love numbers taken from Wahr et al. (1998)

l	k_l	l	k_l
0	+0.000	12	-0.064
1	+0.027	15	-0.058
2	-0.303	20	-0.051
3	-0.194	30	-0.040
4	-0.132	40	-0.033
5	-0.104	50	-0.027
6	-0.089	70	-0.020
7	-0.081	100	-0.014
8	-0.076	150	-0.010
9	-0.072	200	-0.007
10	-0.069		

Combining Equation (4.19) and Equation (4.20) yields the final relation between laterally variable surface mass density changes and corresponding changes in the gravitational potential.

$$\Delta\kappa(\Omega) = \frac{R\rho_{ave}}{3}\sum_{l=0}^{\infty}\sum_{m=0}^{l}\frac{(2l+1)}{(1+k_l)}\bar{P}_{lm}\cos(\phi)\{\Delta C_{lm}\cos m\lambda + \Delta S_{lm}\sin m\lambda\} \quad (4.21)$$

The spherical harmonic evaluation formula above is identical with the relation given by Equation (4.15)) when combining the coefficients ΔC_{lm} and ΔS_{lm} to $\bar{c}_{lm}$. The corresponding spectral relation between changes of the gravitational potential $\bar{c}_{lm}$ and surface mass density $\bar{\kappa}_{lm}$ and height $\bar{h}_{lm}$ is given by Equation (4.15) and Equation (4.16), respectively.

4.3 Filtering techniques

The GRACE-derived high-degree coeficients C_{lm} and S_{lm} (e.g. Stokes coefficients) are dominated by errors that are related to the near-polar orbit ground track (e.g., Wahr et al., 1998; Chen et al., 2005a). These so called correlation errors (because they imply correlations in the gravity field coefficients) present in the GRACE monthly solution as linear features (i.e. stripes) are generally oriented north to south (the orientation of the satellite ground tracks) (e.g., Swenson and Wahr, 2006). This error reflects a weakness in the GRACE recovery of the cross-track gravity signal (e.g., Wahr et al., 2004).

Apart from the correlated errors, any observation error is amplified due to the $(2l+1)$-factor in the spectral relation between gravitational potential and surface mass density changes (see Equation (4.18)). Therefore, higher degree coefficients of the surface density or height functions (see Equation (4.18)) are increasingly more noisy. In order to reduce the effects of increased noise in the higher-degree coefficients (e.g., correlated and/or amplified errors), spatial filtering (e.g., averaging or smoothing) is a common tool applied to the GRACE-derived surface mass changes.

Methods to smooth the GRACE data have been proposed by several authors. Based on GRACE-derived Stokes coefficients, these methods include but are not limited to: Gaussian isotropic filter (e.g., Wahr et al., 1998), anisotropic filter (e.g., Han et al., 2005c; Kusche, 2007; Kusche et al., 2009; Zhang et al., 2009), optimal filters based on a priori estimates of signal and measurement error variances (e.g., Swenson and Wahr, 2002; Seo and Wilson, 2005), global optimized variance-dependent smoothing (e.g., Chen et al., 2006c), spectral-domain filtering (e.g., Swenson and Wahr, 2006) and empirical orthogonal functions (e.g., Schrama et al., 2007).

Isotropic filtering, also known as Gaussian isotropic filter or Gaussian isotropic smoothing, was introduced by Wahr et al. (1998) and is based on Jekeli's Gaussian averaging function (e.g., Jekeli, 1981). This function was constructed to improve the estimates of the Earth's gravity field to compensate for the poorly known, short-wavelength components of the spherical harmonic coefficients. Today, this is a common method to reduce the high-frequency noise in the GRACE-derived gravity data (e.g., Wahr et al., 1998; Chen et al., 2005a) for global and regional (e.g. large scale) applications. For local (e.g. small scale) applications, e.g., small river basins, the Gaussian smoothing is less appropriate. According to Chen et al. (2006c), this is due to two main limitations of the method; namely, (i) an increased leakage associated error as the effective radius increases and (ii) Gaussian smoothing that only assigns isotropic weights in the spatial domain or only degree-dependent weights in the spectral domain. The leakage error arises from the limited range of GRACE spherical harmonics which are not corrupted by noise (e.g., Seo et al., 2006) and which falsify the spatial interpretation of the gravity field anomaly.

Shum et al. (2004) as cited in Han et al. (2005c) also argue that isotropic smoothing is not optimal for GRACE level-2 products as they inherit the spherical harmonic degree-dependent and order-dependent error characteristics associated with the high inclination of the GRACE orbit. Han et al. (2005c) introduced a non-isotropic filter that has a degree-dependent and order-dependent spectrum. Applying the non-isotropic filter yields improved correlation of the smoothed

GRACE gravity field, which also improves the resolution with higher latitude (e.g., due to the meridian convergence; Figure 2.3).

The global optimized variance-dependent smoothing method proposed by Chen et al. (2006c) is assumed to be more effective in recovering global surface mass changes from GRACE time-variable gravity compared to Gaussian smoothing. This method maximizes the variance ratio of mass changes over the land relative to the ocean and also produces lower levels of leakage associated with a limited range of spherical harmonics and improved spatial resolution. Like the non-isotropic filtering introduced by Han et al. (2005c), the method also assigns the degree and order dependent weights differently.

Due to different levels of errors for some local regions, it is also important to treat the error in specific regions differently. Swenson and Wahr (2002) and Swenson et al. (2003) proposed a method to minimize the sum of satellite errors and leakage errors through the construction of an optimal averaging kernel for each region. As stated in Swenson and Wahr (2002), there are four methods for constructing the averaging kernel; namely, choosing an exact (block) average, Gaussian convolution, the use of Lagrange multipliers, and minimization of the sum of satellite and leakage errors.

Some studies have investigated how to choose the most optimal smoothing radius (e.g., Chen et al., 2005a; King et al., 2006). Chen et al. (2005a) point out that the effective smoothing radius may be studied from two approaches. The first approach is based on the comparison of the GRACE results with estimates from advanced geophysical models. In this case, the model prediction acts as a "ground truth" to evaluate at what spatial radius GRACE yields the best agreement with the model. The second approach is based on the selection of an optimum smoothing radius that can be examined from the representation of some residuals over the ocean as the GRACE level-2 data have been de-aliased from oceanic influences. From their study, Chen et al. (2005a) concluded that a 800 and 600 km Gaussian smoothing radius can efficiently remove the high-frequency errors from GRACE-estimated global mass changes and geoid height changes, respectively.

Spatial averaging or smoothing was constructed to compensate the poorly known, short wavelength spherical harmonics to improve the estimates of the Earth's gravity field (e.g., Wahr et al., 1998). According to (Wahr et al., 1998) spatial averages of the surface mass density can be obtained through the following spatial average function

$$\overline{\Delta\kappa}(\theta,\lambda) = \int \sin\theta' d\theta' d\lambda' \Delta\kappa(\theta',\lambda') W(\theta,\lambda,\theta',\lambda') \tag{4.22}$$

where $W(\theta,\lambda,\theta',\lambda')$ is an averaging function and θ is co-latitude. In terms of the SHC ΔC_{lm} and ΔS_{lm}, recoverable from satellite observations, the above formula can be expanded as

$$\begin{aligned}
\overline{\Delta\kappa}(\theta,\lambda) &= \frac{R\rho_{ave}}{12\pi} \sum_{l,m} \tilde{P}_{lm}(\cos\theta) \sum_{l',m'} \frac{2l'+1}{1+k_{l'}} \\
&\times \Big[\Big(\Delta C_{l'm'} W_{lmc}^{l'm'c} + \Delta S_{l'm'} W_{lmc}^{l'm's} \cos(m\lambda) \Big) \\
&+ \Big(\Delta C_{l'm'} W_{lms}^{l'm'c} + \Delta S_{l'm'} W_{lms}^{l'm's} \sin(m\lambda) \Big) \Big]
\end{aligned} \tag{4.23}$$

where

$$\begin{aligned}
\begin{Bmatrix} W_{lmc}^{l'm'c} \\ W_{lmc}^{l'm's} \\ W_{lms}^{l'm'c} \\ W_{lms}^{l'm's} \end{Bmatrix} &= \int \sin\theta d\theta d\lambda \int \sin\theta' d\theta' d\lambda' \times \begin{Bmatrix} \cos m'\lambda' \cos m\lambda \\ \cos m'\lambda' \sin m\lambda \\ \sin m'\lambda' \cos m\lambda \\ \sin m'\lambda' \sin m\lambda \end{Bmatrix} \\
&\times W(\theta,\lambda,\theta',\lambda') \tilde{P}_{lm}(\cos\theta) \tilde{P}_{l'm'}(\cos\theta').
\end{aligned} \tag{4.24}$$

For spatial averaging over large regions, the values for $W_{lms}^{l'm's}$, $W_{lmc}^{l'm's}$, $W_{lms}^{l'm'c}$ and $W_{lmc}^{l'm'c}$ are small for large l, m, l', m', so that the contributions to $\overline{\Delta\kappa}$ from the poorly known ΔC_{lm} and ΔS_{lm} for large values of l', m', tend to be small.

If W is defined such that it depends only on the angle between (θ,λ) and (θ',λ'), e.g. $W = W(\psi)$, then the two equations above can be reduced to

$$\begin{aligned}
\overline{\Delta\kappa}(\theta,\lambda) &= \frac{R\rho_{ave}\pi}{3} \sum_{l,m} \frac{2l+1}{1+k_l} W_l \tilde{P}_{lm}(\cos\theta) \\
&\times \Big[\Delta C_{lm} \cos(m\lambda) + \Delta S_{lm} \sin(m\lambda) \Big]
\end{aligned} \tag{4.25}$$

where

$$W_l = \int_0^{\pi} W(\psi) P_l(\cos\psi) \sin\psi d\psi \tag{4.26}$$

and where $P_l = \tilde{P}_{lm=0}/\sqrt{2l+1}$ are the Legendre polynomials.

In Equations above ψ is the angle (spherical distance) between the two points (θ, λ) and (θ', λ') given by

$$\cos\psi = \cos\theta\cos\theta' + \sin\theta\sin\theta'\cos(\lambda - \lambda'). \tag{4.27}$$

The value for the weighting factor, W, can be obtained through different techniques. The filtering techniques considered in this study are: Gaussian isotropic filter (e.g., Wahr et al., 1998), Han's anisotropic filter (e.g., Han et al., 2005c), and Kusche's de-correlated anisotropc filter (e.g., Kusche, 2007; Kusche et al., 2009). These have been chosen to have three different types of filters. All three filters will be described in more detail in the following sub-chapters.

4.3.1 Gaussian Isotropic Smoothing

Jekeli (1981) introduced the Gaussian mean to be used as a weighting function to produce a mean gravity field. The Gaussian mean takes its name from the bell-shaped normal (Gaussian) probability density function, which is the approximate weighting function $W(\psi)$, for a small ψ, e.g.

$$\begin{aligned} W(\psi) &= e^{-b(1-\cos\psi)} \quad , \quad b > 0 \quad , \quad 0 \le \psi \le \pi \\ &\cong e^{-\frac{b}{2}\psi^2} \quad , \quad \text{small } \psi \end{aligned} \tag{4.28}$$

"b" is a dimensionless parameter that characterises the smoothing process. And since

$$\frac{1}{4\pi}\iint_{\sigma} W(\psi) d\sigma = \frac{1}{2b}(1 - e^{2b}), \tag{4.29}$$

then, by dividing Equation (4.28) with (4.29), Equation (4.28) becomes

$$W(\psi) = \frac{b}{2\pi}\frac{e^{[-b(1-\cos\psi)]}}{1 - 2e^{-2b}} \tag{4.30}$$

with specific choice of b

$$b = \frac{\ln(2)}{(1 - \cos(r_g/R))} \tag{4.31}$$

σ represents a unit sphere ($0 \leq \lambda < 2\pi,\ 0 \leq \theta \leq \pi$). r_g is the distance on the Earth at which W has dropped to half of its value at ψ=0 ($r_g = R\psi$), r_g then refers to as Gaussian averaging radius. The degree-dependent weighting coefficients, W_l (filter coefficients) can be computed by the recursive relations Jekeli (1981)

$$\begin{aligned} W_0 &= \frac{1}{2\pi} \\ W_1 &= \frac{1}{2\pi}\left[\frac{1+e^{-2b}}{1-e^{-2b}} - \frac{1}{b}\right] \\ W_{l+1} &= -\frac{2l+1}{b}W_l + W_{l-1}. \end{aligned} \tag{4.32}$$

Figure 4.1 shows different Gaussian isotropic weighting functions for the radii r_g=250 km, r_g=500 km, and r_g=750 km and their south-north and west-east profiles across the centre of each filters. It can be seen that for the Gaussian filter, due to the isotropic behaviour, the south-north and west-east profiles are identical. The figure also shows that for an increased averaging radius, the original value of the signal will be increasingly altered by the weighting function. Figure 4.2 displays the spectra for different Gaussian filters (r_g=250 km, r_g=500 km, and r_g=750 km).

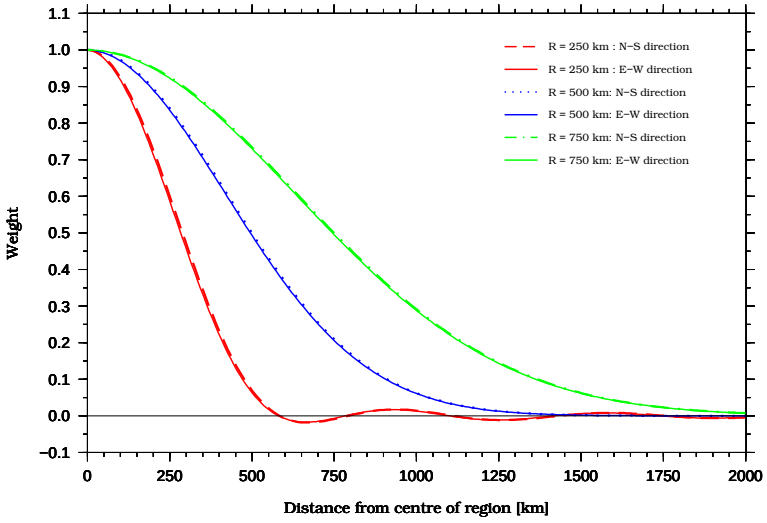

Figure 4.1: Gaussian averaging functions for smoothing radii r_g=250 km, r_g=500 kn and r_g=750 km. The smoothing kernel is centred at $\phi = 0°$, $\lambda = 180°$, the west-east and south-north distance is measured along the equator and along the meridian, respectively.

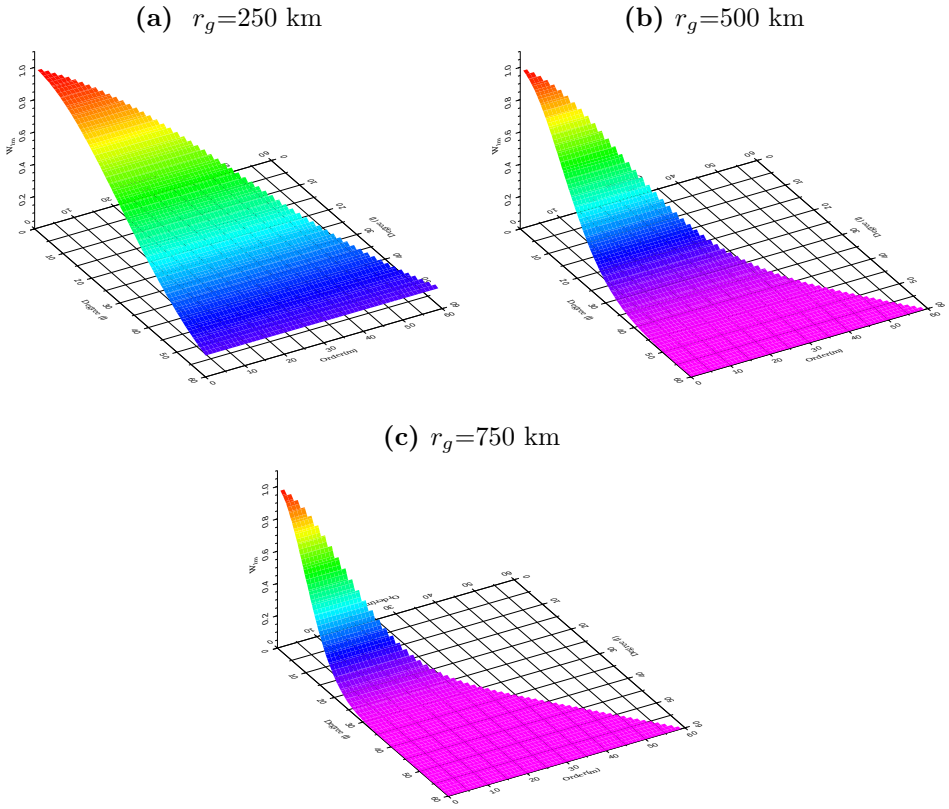

Figure 4.2: Selected spectra for Gaussian isotropic filters with different averaging radii (a) r_g=250 km ; (b) r_g=500 km; (c) r_g=750 km.

Introducing the degree-dependent filter coefficients W_l for Gaussian smoothing (e.g., Jekeli, 1981) in the above relation enables the reduction of high-frequency errors. The relation for $\kappa(\Omega)$ (see Equation (4.15) and (4.16)) changes to (e.g., Wahr et al., 1998, eq.14)

$$\kappa_s(\Omega) = \frac{2\pi R\rho_{ave}}{3} \sum_{l=0}^{L_{max}} \sum_{m=-l}^{l} \frac{2l+1}{1+k_l} W_l \bar{c}_{lm} \bar{Y}_{lm}. \tag{4.33}$$

The factor 2π is equal to $\frac{1}{W_0}$ and is the result of introducing spatial averages. Depending on the chosen filter the coefficients can be changed accordingly. Introducing the relation

$$W_l = \frac{1}{2\pi} + \delta W_l \tag{4.34}$$

with

$$\delta W_l = W_l - \frac{1}{2\pi} \tag{4.35}$$

the effect of the filter on the recovery of $\kappa_s(\Omega)$ can be studied through the relation

$$\tilde{\kappa}_s(\Omega) = \kappa(\Omega) + \delta\kappa_s(\Omega) = \frac{2\pi R\rho_{ave}}{3} \sum_{l=0}^{L_{max}} \sum_{m=-l}^{l} \frac{2l+1}{1+k_l} \left(\frac{1}{2\pi} + \delta W_l \right) \bar{c}_{lm} \bar{Y}_{lm} \quad (4.36)$$

with

$$\delta\kappa_s(\Omega) = \frac{2\pi R\rho_{ave}}{3} \sum_{l=0}^{N_{max}} \sum_{m=-l}^{n} \frac{2l+1}{1+k_l} \delta W_l \bar{c}_{lm} \bar{Y}_{lm}. \quad (4.37)$$

Introducing only the errors $\delta\bar{c}_{lm}$ in $\bar{c}_{lm}$ yields the relation

$$\tilde{\kappa}_c(\Omega) = \kappa(\Omega) + \delta\kappa_c(\Omega) = \frac{R\rho_{ave}}{3} \sum_{L=0}^{N_{max}} \sum_{m=-l}^{n} \frac{2l+1}{1+k_l} (\bar{c}_{lm} + \delta\bar{c}_{lm}) \bar{Y}_{lm}. \quad (4.38)$$

The effect of the errors can be studied through the relation

$$\delta\kappa_c(\Omega) = \frac{R\rho_{ave}}{3} \sum_{l=0}^{L_{max}} \sum_{m=-l}^{n} \frac{2l+1}{1+k_l} \delta\bar{c}_{lm} \bar{Y}_{lm}. \quad (4.39)$$

The combined effect on the recovery of $\kappa(\Omega)$ from errors and filtering can be studied through the relation

$$\begin{aligned} \delta\kappa_{c,s}(\Omega) &= \kappa_c(\Omega) + \kappa_s(\Omega) \\ &= \frac{2\pi R\rho_{ave}}{3} \sum_{n=0}^{N_{max}} \sum_{m=-n}^{n} \frac{2n+1}{1+k_n} \\ &\times \left[\frac{1}{2\pi} (\bar{c}_{nm} + \delta\bar{c}_{nm}) + \delta W_n \delta\bar{c}_{nm} \right] \bar{Y}_{nm}. \end{aligned} \quad (4.40)$$

4.3.2 Gaussian Anisotropic Smoothing

An anisotropic averaging function has been introduced by Han et al. (2005b). This filtering technique applies a Gaussian weight matrix, but instead of depending only on the degree of the spherical harmonic coefficients the averaging filter coefficients of the weighting function also depend on the order. The research by Han et al. (2005b) showed that the filter increases GRACE gravity signals with significant resolution in latitude and the same resolution in the longitude without reducing the accuracy as compared to the conventional Gaussian filter.

According to Han et al. (2005b), degree and order dependent filter coefficient are appropriate for GRACE level 2 data and are obtained through

$$W_{lm} = W_l(r_{1/2}(m)) \tag{4.41}$$

$$r_{1/2}(m) = \frac{r_1 - r_0}{m_1} m + r_0 \tag{4.42}$$

where r_0 and r_1 are the averaging radii, respectively, applied for zonal harmonics ($m = 0$) and for order m_1 harmonics ($m = m_1$).

Figure 4.3 shows different anisotropic Gaussian weighting functions for the radii combinations $r_0 = 250$ km, $r_1 = 500$ km; $r_0 = 500$ km, $r_1 = 1000$ km; and $r_0 = 750$ km, $r_1 = 1500$ km and their south-north and west-east profiles across the centre of each filters. It can be seen that, different to the Gaussian isotropic filter, the anisotropic filter has smaller dimension along the south-north direction yielding higher spatial resolution in latidue than in longitude directions. Figure 4.4 displays the spectra for different Han's anisotropic filters ($r_0 = 250$ km, $r_1 = 500$ km; $r_0 = 500$ km, $r_1 = 1000$ km; and $r_0 = 750$ km, $r_1 = 1500$ km). The figure shows that the anisotropic filter can effectively pass the higher degree and and lower order coefficients and reject undesired higher order coefficients.

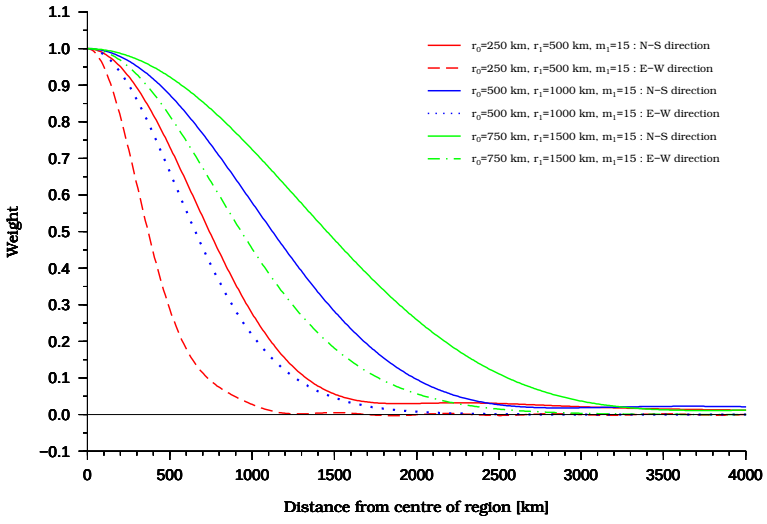

Figure 4.3: Anisotropic Gaussian average functions for the smoothing radii applied for order harmonic $m_1 = 15$. The smoothing kernel is centred at $\phi = 0°$, $\lambda = 180°$, the west-east and south-north distance is measured along the equator and along the centre meridian respectively.

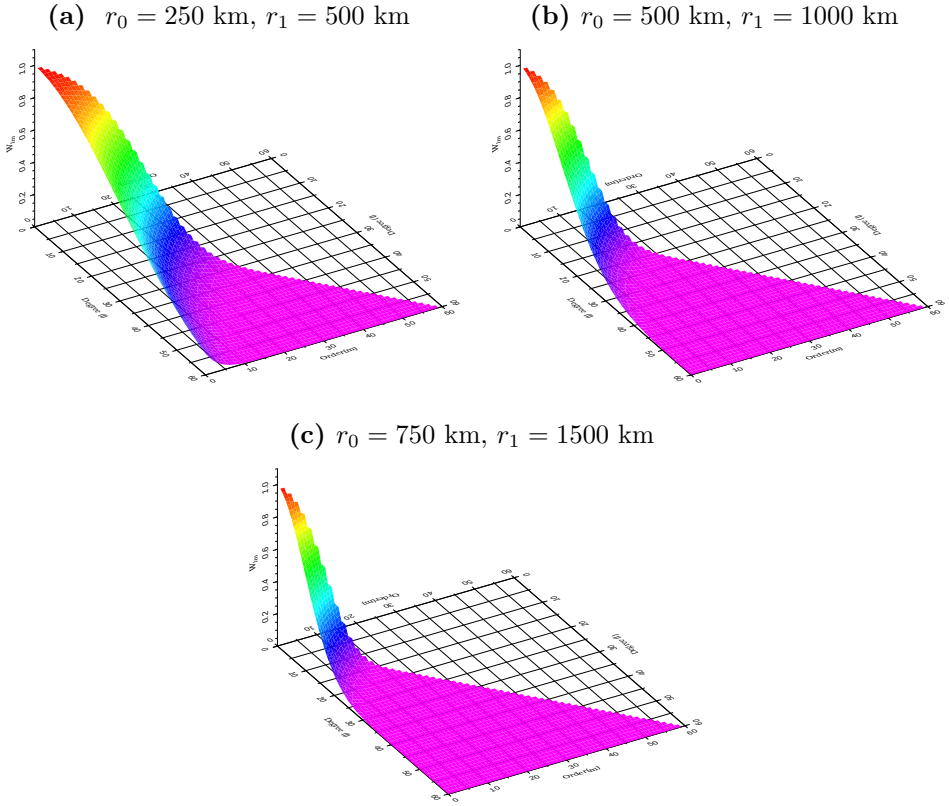

Figure 4.4: Selected spectra for Han's anisotropic filter (a) with averaging radii $r_0 = 250$ km, $r_1 = 500$ km, and $m_1 = 15$; (b) with averaging radii $r_0 = 500$ km, $r_1 = 1000$ km, and $m_1 = 15$; (c) with averaging radii $r_0 = 750$ km, $r_1 = 1500$ km, and $m_1 = 15$.

4.3.3 De-correlated and Anisotopic Smoothing

Kusche (2007) introduced a method for de-correlating and anisotropically smoothing of the gravity field. Here, a brief summary of the developed filter will be presented. Full information of the method can be found in Kusche (2007) and Kusche et al. (2009).

According to Kusche (2007), and based on the smoothing parameter a, each spherical harmonic coefficient ($\kappa_{lmn} = c^{\kappa}_{lm}$ for $q = 0$ and $\kappa_{lmq} = s^{\kappa}_{lm}$ for $q = 1$) of the surface mass anomaly $\sigma(\Omega)$ (or any functional of gravity change) can be

de-correlated and smoothed in the following way

$$\kappa_{lmq}^{filt} = \sum_{l'=l_{min}}^{l_{max}} \sum_{m'=0}^{l'} \sum_{q'=0}^{1} w_{lmq}^{l'm'q'}(a)\kappa_{l'm'q'}, \tag{4.43}$$

where l and m are harmonic degree and order, and the surface mass anomaly coefficients κ_{lmq} are obtained from GRACE geopotential coefficients (e.g. Wahr et al., 1998) by

$$\sigma_{lmq} = \frac{2\rho_e}{3\rho_w(1+k_l')}\left(1+\frac{1}{2}\right)\delta x_{lmq}, \tag{4.44}$$

where ρ_e and ρ_w are average density of solid Eath and sea-water respectively, k_l' is the load Love number of degree l, and $\delta x_{lmq} = x_{lmq} - \bar{x}_{lmq}$ are residual coefficients between the GRACE geopotential coefficients x_{lmq} and the long-time average of geopotential coefficients $\bar{x}_{lmq}$. l_{min} and l_{max} are the minimum and maximum spherical harmonic degrees considered. $w_{lmq}^{l'm'q'}(a)$ is the matrix of de-correlation coefficients W_a with the continuous non-negative parameter a that controls the degree of smoothness. Following probabilistic inverse principles yields the de-correlation coefficient matrix (see Kusche, 2007)

$$\begin{aligned} W_a &= (E^{-1} + aS^{-1})^{-1}E^{-1} \\ &= (I + (a-a')WES^{-1})W_{a'}. \end{aligned} \tag{4.45}$$

When E^{-1} equals the GRACE normal equation matrix and S^{-1} equals the regularization matrix, the filter is equivalent to the common (quadratic) constraint of GRACE solutions. The advantage of this method compared to Gaussian and other filtering methods is the ability to de-correlate the coefficients. The drawback is, because of the full matrix approach, that the number of filter coefficients n_K can be quite large when l_{max} is large e.g. $n_K = ((l_{max}+1)^2 - l_{min}^2)^2$.

Table 4.2 presents an overview of the smoothing properties of the three developed filter versions, namely DDK1, DDK2, and DDK3. These are given in terms of the corresponding smoothing radius of an approximately equivalent Gaussian filter.

Table 4.2: Smoothing characteristics of three de-correlation filters used in Kusche et al. (2009).

De-correlation filter	Corresponding Gaussian radius (km)		Parameter a and p
	Acc. to Kusche (2007)	Acc to $\omega_l = \frac{1}{2}$	Acc. to Kusche (2007)
DDK1	1,350	530	$a = 1 \times 10^{14}, p = 4$
DDK2	900	340	$a = 1 \times 10^{13}, p = 4$
DDK3	660	240	$a = 1 \times 10^{12}, p = 4$

Figure 4.5 shows the different de-correlation weighting functions DDK1, DDK2 and DDK3 and their south-north and west-east profiles across the centre of each filter. It can be seen that the de-correlation filters have smaller dimension along the south-north direction yielding higher spatial resolution in latitude than in longitude. Figure 4.6 displays the spectra for the de-correlated anisotropic filters DDK1, DDK2 and DDK3. Like for Han's anisotropic filter, the figure shows that the de-correlated anisotropic filters can effectively pass the higher degree and lower order coefficients and reject undesired higher order coefficients.

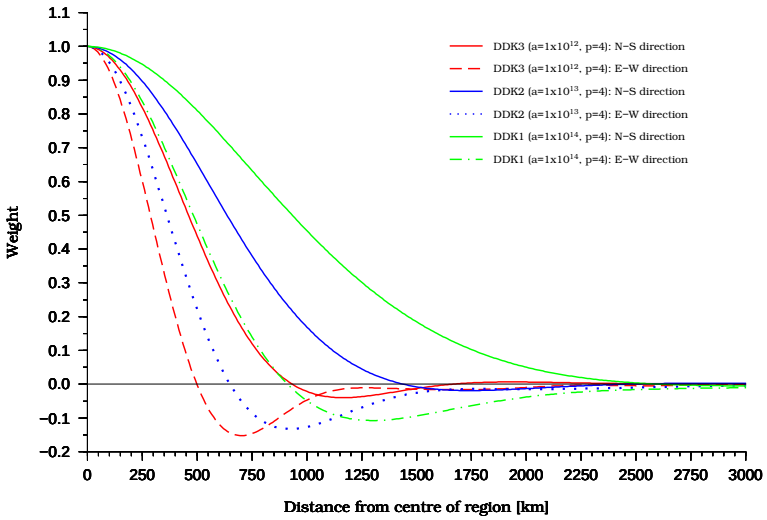

Figure 4.5: Kusche's de-correlated anisotropic smoothing with different parameters. The smoothing kernel is centred at $\phi = 0°$, $\lambda = 180°$, the west-east and south-north distance is measured along the equator and along the centre meridian respectively.

(a) DDK3: $a = 1 \times 10^{12}$ and $p = 4$ **(b)** DDK2: $a = 1 \times 10^{13}$ and $p = 4$

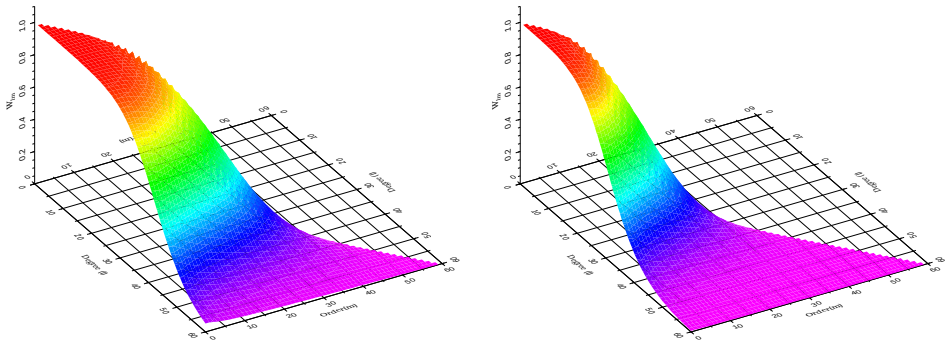

(c) DDK1: $a = 1 \times 10^{14}$ and $p = 4$

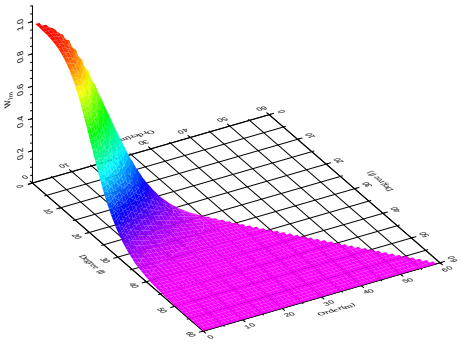

Figure 4.6: Selected spectra of Kusche's de-correlated, anisotropic filters (a) DDK3 with $a = 1 \times 10^{12}$ and $p = 4$; (b) DDK2 with $a = 1 \times 10^{13}$ and $p = 4$; (c) DDK1 with $a = 1 \times 10^{14}$ and $p = 4$.

4.4 Chapter Summary

This chapter provided an overview of techniques to infer mass changes from time-variable gravity derived from the GRACE satellite mission. The use of GRACE time-variable gravity observations for the detection of mass changes over the cryosphere, hydrological changes over land and mass changes in the Earth interior were presented in the first part of this chapter. This was followed by the main focus, the presentation of techniques commonly used to infer mass changes from time-variable gravity with the specific view on the technique proposed by Wahr et al. (1998). The chapter closed by a summary of the smoothing procedures used in this thesis, namely: Gaussian isotropic smoothing, Han's anisotropic smoothing and Kusche's de-correlated anisotropic smoothing.

Chapter 5

Validation Using Spherical Disc Masses

This chapter presents the validation results of inferring simulated mass changes from their respective Stokes coefficients using the method introduced by Wahr et al. (1998). Different filtering procedures, namely: (1) Gaussian isotropic filter (e.g., Jekeli, 1981); (2) Han's anisotropic filter (e.g., Han et al., 2005c); and (3) Kusche's de-correlated, anisotropic filter (e.g., Kusche, 2007; Kusche et al., 2009) are applied and examined. The validation is based on a closed-loop procedure using forward gravity modelling to derive the gravitational signal of the respective simulated mass changes (omitting elasticity and loading effects). In this chapter spherical disc masses with various sizes placed at different geographic locations are used. The rather simplistic mass changes allow for a detailed examination of general principles and properties inherent in the mass estimation procedure as well as filtering technique used. Results are mostly analysed in terms of the ability to recover the simulated input masses. In particular this will be quantifying the total mass recovered, spatial and spectral leakage and examines the isotropic/anisotropic properties of the filters introduced by providing west-east and south-north cross-sections of the differences between initial and recovered masses.

5.1 Validation Procedure

The validation procedure employed simulates common processing steps performed to infer mass changes from GRACE-level 2 data. The symbolic work flow of the validation procedure is illustrated in Figure 5.1 and consists of five different steps

.

- **Step 1:**

  Within the first step of the validation procedure simulated mass distributions are developed, which build the input masses. In this chapter spherical disc masses are used as input masses while Chapter 6 uses more realistic mass distributions based on GRACE-derived mass changes. Importantly, the input masses selected are exactly known and assumed to be error-free.

- **Step 2:**

  The simulated mass distributions from step 1 are used to generate [simulate] self-consistent gravity field changes through the application of FGM. The FGM technique used here is based on series expansions for the generating gravitational potential based on surface spherical harmonics. This requires the development of the height of input masses in spherical harmonics (e.g., spherical harmonic analysis) and conversion of spherical harmonic coefficients into Stokes coefficients (see Chapter 3).

- **Step 3:**

  The generated gravity field changes are used as input for the selected mass estimation procedure. These mostly differ by the use of various smoothing filters. Therefore, this step applies different smoothing filters on the Stokes coefficients derived in step 2. The smoothing filters considered here are Gaussian isotropic smoothing, Han's anisotropic smoothing and Kusche's de-correlated anisotropic smoothing (see Chapter 4).

- **Step 4:**

  In this step the filtered Stokes coefficients from step 3 are used to recover again the initial mass distribution. This is done by employing the inversion technique described in Chapter 3, which is based on the conversion of the filtered Stokes coefficients into coefficients representing the height of the recovered mass distribution. The latter coefficients are used to derive the recovered mass on a regular geographic grid through a spherical harmonic synthesis.

- **Step 5:**

  The result obtained from step 4 will be a recovered mass distribution that - if estimated correctly - should match the input mass. Any differences will be the result of shortcomings of the used mass estimation procedure. These differences will be analysed in order to validate the effectiveness of the mass estimation procedure.

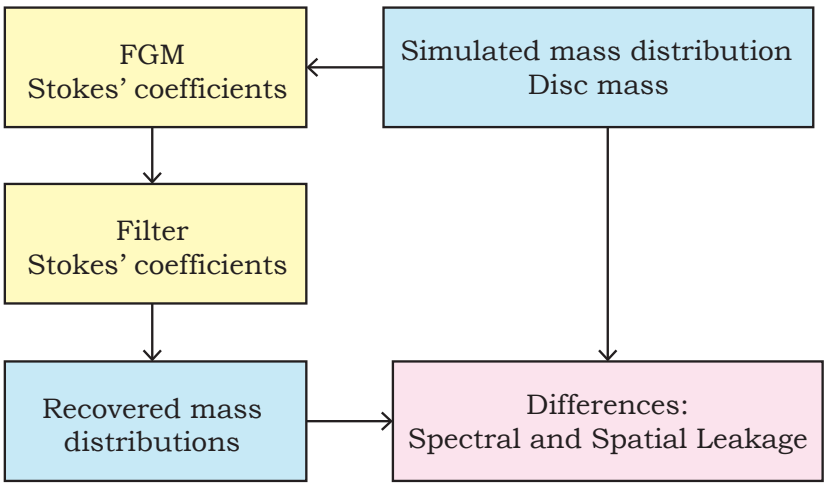

Figure 5.1: Symbolic work flow for the validation process used.

5.2 Routines and Software

The validation procedure described in the previous chapter requires FGM techniques to be applied to the simulated masses in order to derive the generating gravitational potential (e.g., Stokes coefficients). In this study FGM is done in the spectral domain based on series expansions for the generating gravitational potential using surface spherical harmonics (see Chapter 3). This requires the use of spherical harmonic analysis and synthesis. As the maximum spherical harmonic degree considered in this study is $l_{max} = 60$, standard spherical harmonic analysis and synthesis software can be used without the need for numerical optimisation for high and ultra-high degrees (e.g., Holmes, 2003; Wittwer et al., 2008; Balmino et al., 2012).

The spherical harmonic analysis and synthesis routines used in this study are based on software used in Baur et al. (2009) and Kuhn and Seitz (2005). The developed routines have been cross-checked by this software as well as the freely available software SHTools (http://shtools.ipgo.fr/), which revealed negligible differences between the software at the level of the numerical precision.

Apart from the comparison with other software (e.g., external check), the developed routines have been tested through a closed-loop check (see Figure 5.2). This test uses a band-limited spatial signal as input for a spherical harmonic analysis and synthesis using a spherical harmonic degree equivalent to the band-limited input signal. In particular the closed-loop test performs the following steps:

(1) Creation of a band-limited signal in the space domain ($F^l(\lambda, \phi)$). This is achieved by spectral filtering of a space domain signal (which includes all special frequencies). This is done by applying a spherical harmonic analysis and synthesis on a given space domain signal provided by grid values on a regular geographic grid. The space domain signal used here is illustrated in Figure 5.3 and based on global mass changes as detected by GRACE over an 8-year period (see Chapter 6). The grid resolution used is 15 arc minutes and the maximum spherical harmonic degree has been selected to $l_{max} = 60$.

(2) The spectrally filtered space domain signal $F^l(\lambda, \phi)$ now builds the input for a spherical harmonic analysis up to the same degree used to band-limit the space domain signal (see step 1). This results in the spherical harmonic coefficients F^l_{nm}.

(3) The spherical harmonic coefficients F^l_{nm} of the previous step are subjected to a spherical harmonic synthesis up to the same degree used to band-limit the space domain signal (see step 1). The synthesis is performed on the same grid locations (15 arc minute grid) and for the same maximum degree $l_{max} = 60$ as used for the input grid in steps 1 and 2 to form the recovered space domain signal $\tilde{F}^l(\lambda, \phi)$.

(4) The result of the previous step, $\tilde{F}^l(\lambda, \phi)$ is compared to the spectrally filtered space domain signal $F^l(\lambda, \phi)$. Due to the use a maximum spherical harmonic degree that is equivalent to the band-limitation of the input signal any differences are the result of shortcomings of the developed software routines used.

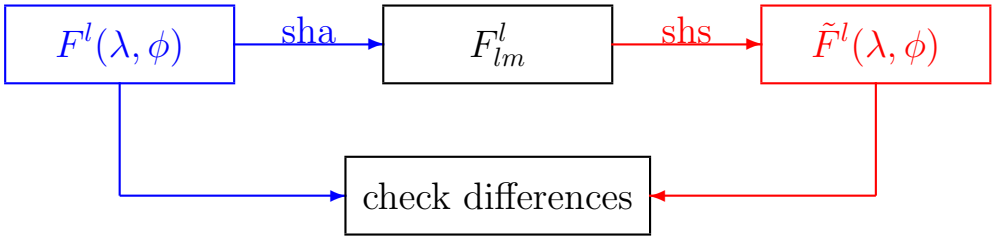

Figure 5.2: Layout of the internal check to test the spherical harmonic analysis and synthesis software used.

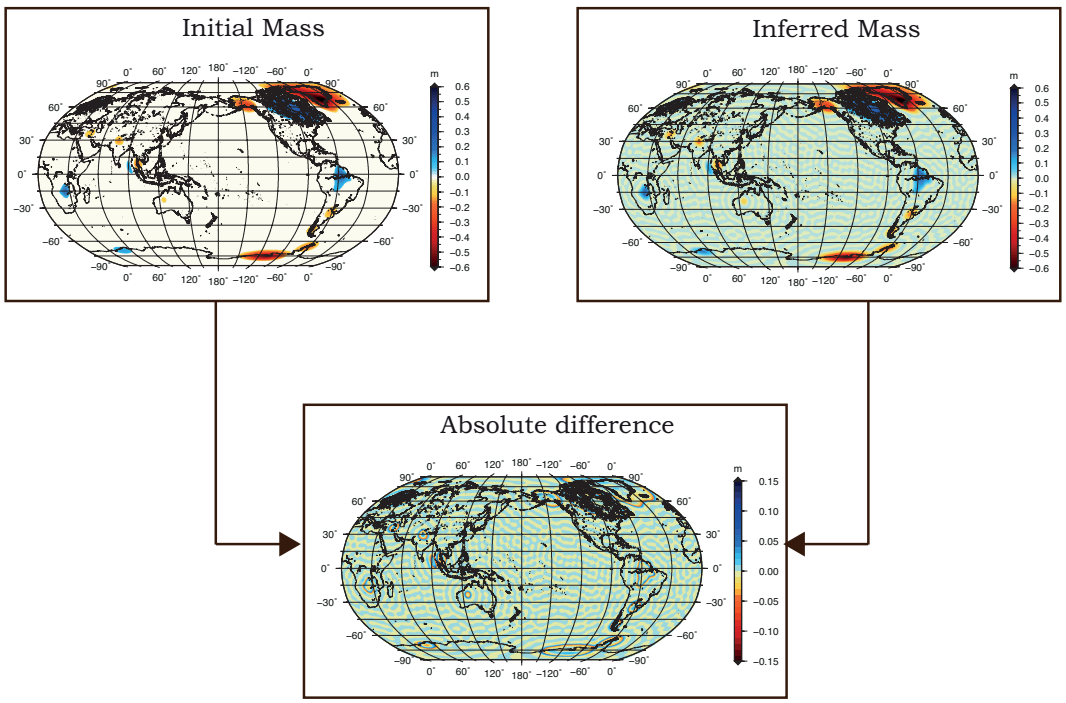

Figure 5.3: Closed-loop check result. Based on global mass changes detected by GRACE over an 8-years period. Displayed is the height of equivalent water volume

Figure 5.3 illustrates both the band-limited input masses and the result of the closed-loop test described above. The test revealed that the differences (e.g., mean differences of -1.047×10^{-7} m) between both are generally at least five orders of magnitudes smaller than the input signal, thus can safely be neglected.

5.3 Input Disc Masses

In the following Section 5.4 and Appendix A, the validation procedure described in Section 5.1 will be applied to simple mass distributions arranged at various locations, in order to validate techniques used to infer mass changes from gravity changes (see Chapter 4). In particular, this will look at leakage properties when applying various filters to the gravity data. As simple mass distributions spherical disc masses with varying size and location have been selected.

Table 5.1: Properties of the simulated disc masses. Note the disc mass estimates (last column) differ slightly due to differences in sampling caused by the geographic grid resolution.

Discs	Lat (ϕ)	Lon (λ)	Radius (°)	Height (m)	Volume (km^3)	Density (kg/m^3)	Mass (Gt)
Disc Ia	70°	320°	10	0.1	388.249	1000	388.249
Disc Ib	70°	320°	5	0.4	389.882	1000	389.882
Disc IIa	0°	180°	10	0.1	388.245	1000	388.245
Disc IIb	0°	180°	5	0.4	391.213	1000	391.213
Disc IIIa	-75°	250°	10	-0.1	-388.449	1000	-388.449
Disc IIIb	-75°	250°	5	-0.4	-389.511	1000	-389.51

Two disc masses with the same total mass but different spherical radii (10° and 5°) have been placed at three locations (see Figure 5.4). This simulates the two cases of (a) a more widely spread mass source and (b) a spatially more concentrated mass source. The three locations have been selected at (1) high northern latitude to simulate ice mass changes over Greenland, (2) the equator to simulate hydrological changes over tropical regions, and (3) at high southern latitude to simulate ice mass changes over Antarctica. Figure 5.4 shows the spatial

distribution of the selected disc masses and Table 5.1 provides information on their size and total mass.

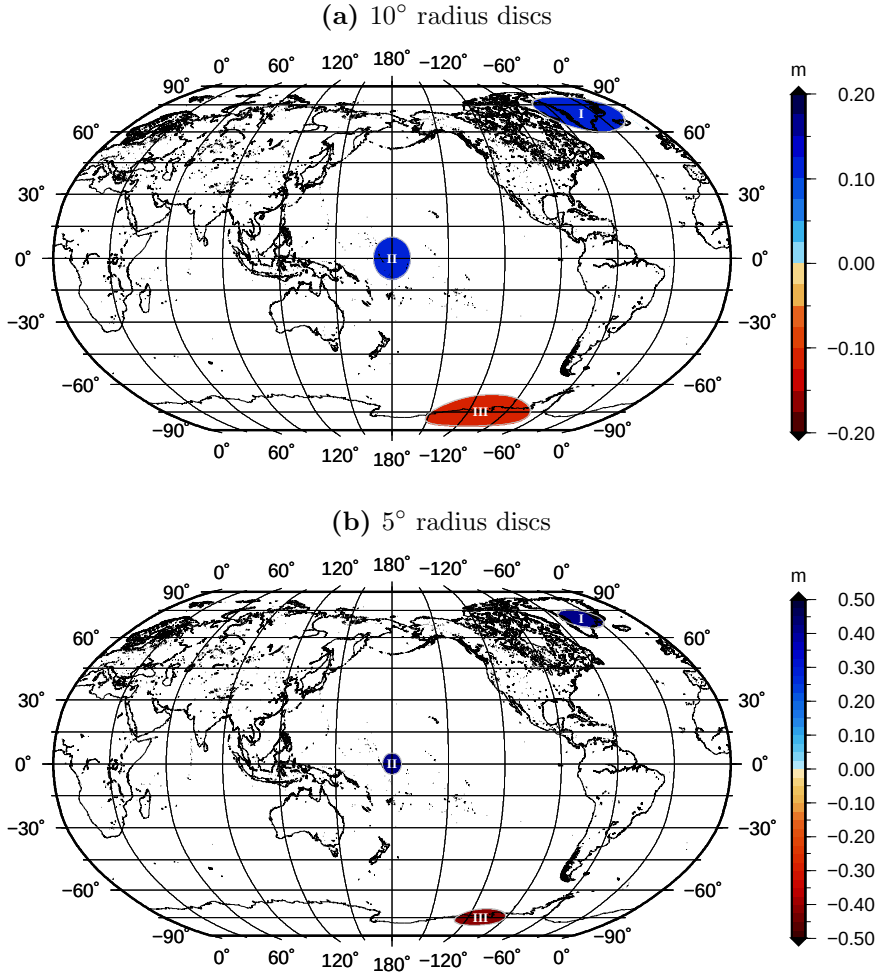

Figure 5.4: Disc masses distribution. Disc I centred at $\phi = 70°$, $\lambda = 320°$; Disc II centred at $\phi = 0°$, $\lambda = 180°$; Disc III centred at $\phi = -75°$, $\lambda = 250°$. Note that the form of the disc masses at higher northern and southern latitude are distorted due to the use of the Robinson map projection.

The magnitude of the total discs masses have been chosen to represent realistic mass changes currently detected by GRACE over a period of 8 years (e.g., Anjasmara and Kuhn, 2009). The geometry of the disc has been chosen to have a vertical boundary at their respective edges so to simulate a jump discontinuity from a constant disc height to a "zero" height outside the disc. This geometry has been selected to provide maximum effects when trying to recover the simulated masses by the use of spherical harmonics, e.g., using periodic functions as basis

functions, which will lead to the well-known Gibbs phenomenon (e.g., Seo and Wilson, 2005).

5.4 Validation Results for Disc Masses Ia and Ib

This chapter provides a complete overview of all validation results obtained for the disc masses Ia and Ib. The disc masses are centred at $\phi = 70°$, $\lambda = 320°$ to simulate ice mass changes over Greenland (see Section 6.3.2). Figure 5.5 shows the location and size of the two disc masses as well as south-north and west-east cross-sections through each. The latter demonstrates the property that disc mass Ia has double the horizontal extension than disc mass Ib but only a fourth of the height. Thus both disc masses have the same total mass but different spatial concentrations.

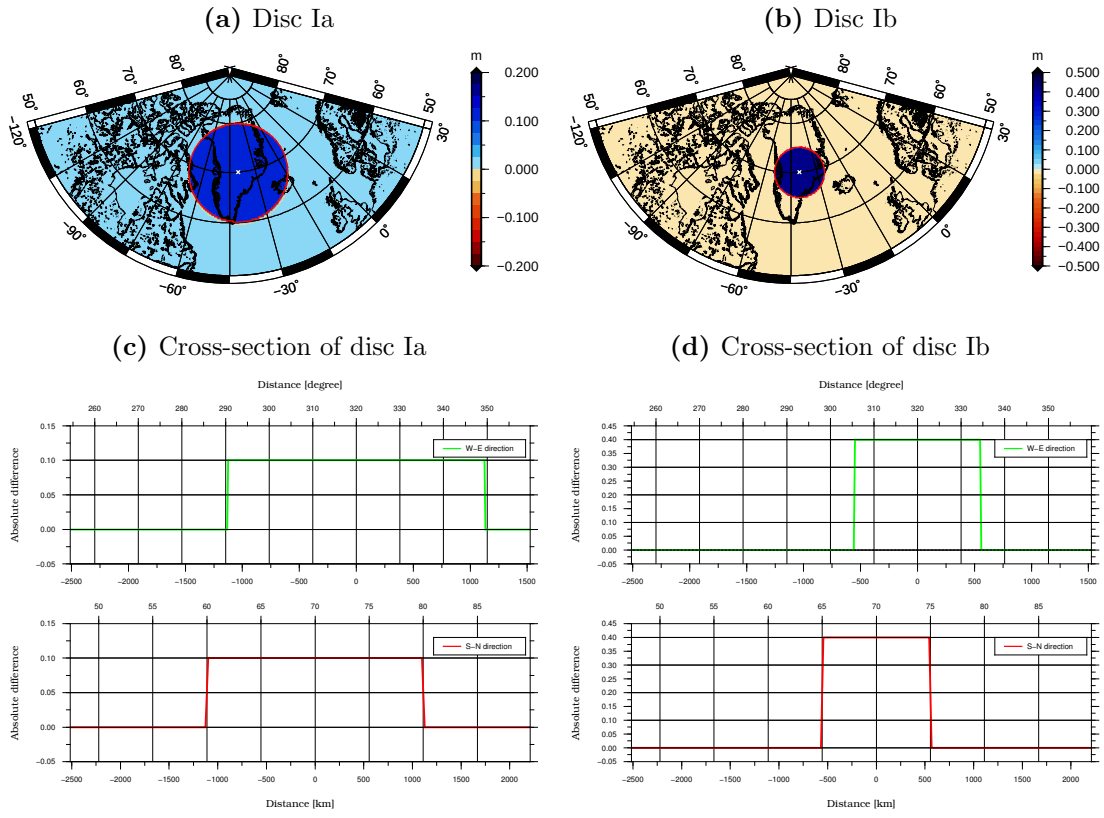

Figure 5.5: Simulated disc masses with radii 10° and 5° centred at $\phi = 70°, \lambda = 320°$ (panels a and b) and west-east and south-north cross-sections (panels c and d).

Using the disc masses as simulated input mass for the validation procedure described in Section 5.1, four scenarios with respect to the filter applied onto the Stokes coefficients will be examined, namely:

(1) No filter
(2) Gaussian isotropic filter
(3) Han's anisotropic filter
(4) Kusche's de-correlated, anisotropic filter

In this Section the properties of the recovered mass distributions for disc masses I will be discussed in detail. As many properties are similar for the disc masses II and III, the results will be provided in the Appendix A.

5.4.1 Results for no filter

Before examining the impact of the smoothing filters no smoothing will be applied to recover the input masses. This will provide information on spectral leakage, the ability to recover the input masses by the use of a band-limited representation using spherical harmonics up to the maximum degree l_{max} (here $l_{max} = 60$). Figure 5.6 shows the recovered disc masses and respective cross-sections in west-east and south-north directions of the initial and recovered masses and the respective differences between both.

The recovered masses as illustrated in Figure 5.6 mostly show the Gibbs phenomenon with larger differences close to the edge of the disc mass demonstrating the inability to model a jump discontinuity via periodic functions (e.g., surface spherical harmonics). The undulating "ripple" pattern over the top of the disc mass (mostly visible in Figure 5.6a) and spreading (radiating) away from the disc mass (visible in both Figure 5.6a and Figure 5.6b) is based on the same principle that a constant function (e.g., constant height) is approximated by periodic functions. While the undulations have a considerable magnitude over the disc mass their magnitude quickly tapers down to a value of effectively zero outside the initial disc masses.

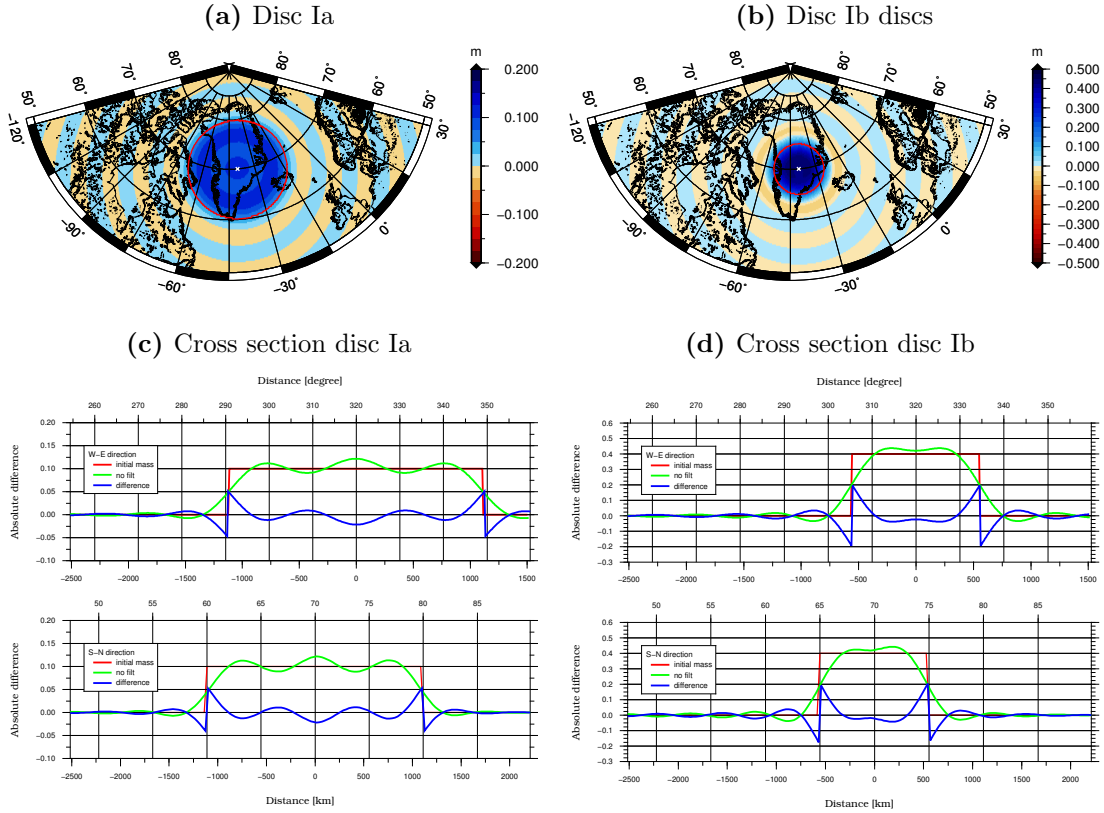

Figure 5.6: Recovered disc masses with radius 10° and 5° centred at $\phi = 70°, \lambda = 320°$ (panels a and b) and west-east and south-north cross-sections (panels c and d). No smoothing filter has been applied. The red circle indicates the spatial extension of the input disc mass.

When comparing the recovered mass within the same spatial limitations of the input disc mass the effect of spectral leakage can be quantified by the portion of mass that spread (leaked) outside. Table 5.2 and Table 5.3 in Section 5.5 show that with no smoothing applied 93.5% of the input mass has been recovered for disc mass Ia and 87.4% for disc mass Ib. Therefore, the spectral leakage can be quantified to 6.5% and 12.6% for disc Ia and Ib, respectively. This means that respectively for disc Ia and Ib, 6.5% and 12.6% of the input mass leaked outside of the area of the original disc due to truncating the spherical harmonic expansion to the maximum degree $l_{max} = 60$. Additional tests have shown (not shown here) that the spectral leakage can be minimized and practically eliminated by increasing the maximum spherical harmonic degree (e.g., $l_{max} > 1000$). It is

interesting to note that for the two disc masses examined spectral leakage is about double when halving the horizontal extension. The further application of smoothing filters will increase the level of mass loss (leakage) where the difference to spectral leakage is attributed to spatial leakage (e.g., impact of the smoothing filter).

5.4.2 Gaussian Isotropic Filter

The next validation scenario uses a Gaussian isotropic filter (see also Chapter 4) to smooth the Stokes coefficients obtained within the validation procedure (see Section 5.1). Three different smoothing radii have been selected and applied in order to examine the recovery of the disc masses. This resulted in the following six smoothing scenarios:

(a) r_g = 125 km / disc radius is 10°
(b) r_g = 125 km / disc radius is 5°
(c) r_g = 250 km / disc radius is 10°
(d) r_g = 250 km / disc radius is 5°
(e) r_g = 500 km / disc radius is 10°
(f) r_g = 500 km / disc radius is 5°

The three smoothing radii 125 km, 250 km and 500 km have been selected to obtain"weak", "medium" and "strong" isotropic smoothing. Examples for the input and recovered masses given as west-east and south-north cross-sections are shown in Figure 5.7 for a smoothing radius of 250 km superimposed on the discs Ia and Ib.

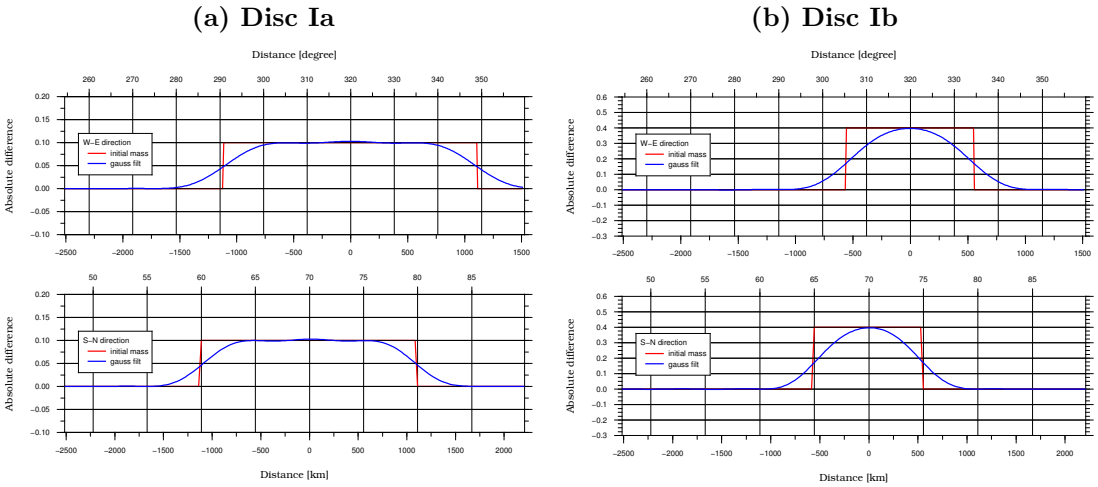

Figure 5.7: West-east (top) and south-north (bottom) cross-sections of the recovered masses for Gaussian isotropic smoothing with a smoothing radius r_g=250 km (blue line) superimposed on disc Ia and disc Ib (red line).

The validation results for all combinations are shown in Figure 5.8 for the recovered masses and in Figure 5.9 for west-east and south-north cross-sections of the differences between the input and recovered masses. Table 5.2 and Table 5.3 in Section 5.5 list the total mass recovered, the total mass loss and the amount of mass loss due to spectral and spatial leakage.

(a) Gaussian isotropic filter for r_g = 125 km and 10° disc

This case examines the application of weak Gaussian isotropic smoothing with a smoothing radius of 125 km to disc mass Ia. Examining Figure 5.8a it can be seen that the recovered mass distribution is quite similar to that in Figure 5.6a when no smoothing has been applied. The recovered mass distribution shows little leakage but the typical Gibbs phenomenon. Table 5.2 confirms that with 90.8% the recovered mass is similar to that when applying no smoothing (e.g., 93.5%). The difference of 2.7% can be interpreted as spatial leakage, the effect of the applied smoothing filter.

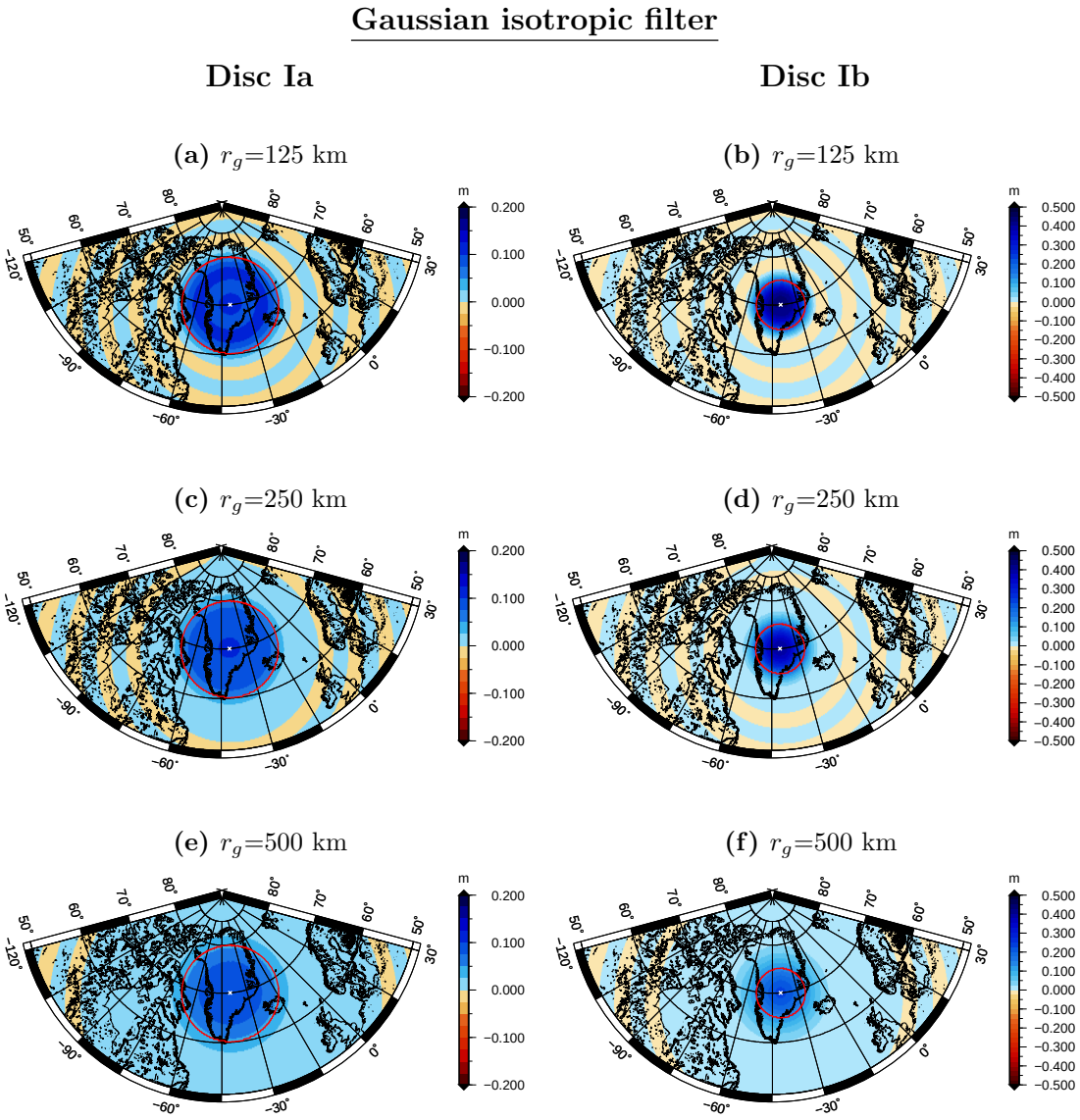

Figure 5.8: Recovered masses for discs Ia and Ib with radii 10° and 5°, respectively, after applying Gaussian isotropic smoothing. The discs are centred at $\phi = 70°, \lambda = 320°$. The red circle indicates the spatial extension of the input disc mass.

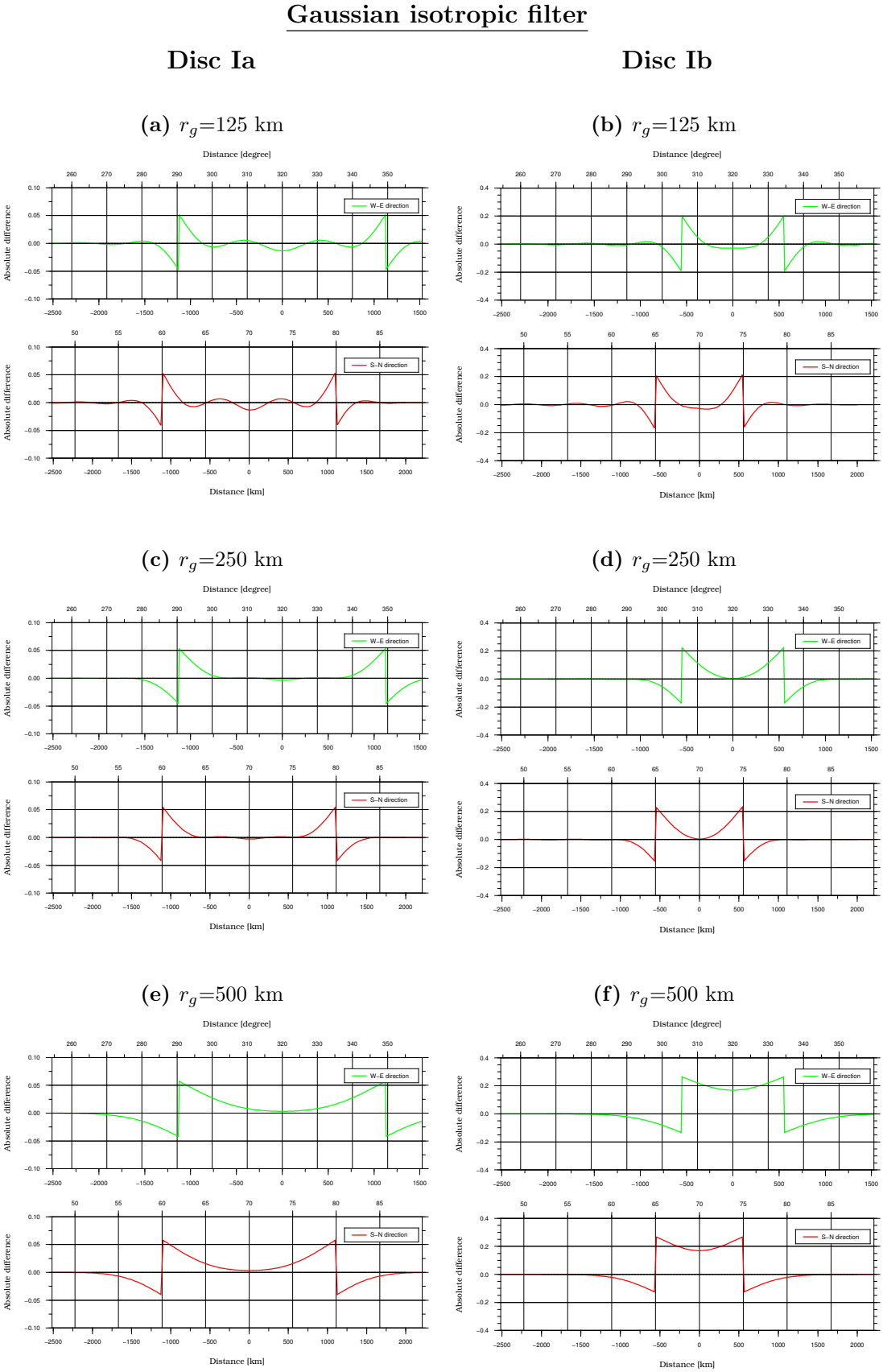

Figure 5.9: West-east (green line) and south-north (red line) cross-sections of the difference between input and recovered masses when applying Gaussian isotropic smoothing.

Figure 5.9a shows the difference between the input and the recovered mass as cross-sections through the centre of the disc in west-east and south-north directions. The differences are mostly dominated by the Gibbs phenomenon with undulations over the disc and larger differences at the edges of the disc. At the disc's edges the differences change from large positive (mass loss) to large negative (mass gain) values and decrease to zero at a distance of about 250 km from the disc. This suggests mass transport (e.g., leakage) mostly from the edges to the outside of the disc due to the combined effect of spectral and spatial leakage. As expected for isotropic smoothing, the differences in the west-east and south-north cross-sections show the same behaviour.

(b) Gaussian isotropic filter for r_g = 125 km and 5° disc

Like scenario (a) above this scenario still examines the application of weak Gaussian isotropic smoothing with a smoothing radius of 125 km but now applied to the spatially more concentrated disc mass Ib. Again, the recovered mass distribution illustrated in Figure 5.8b is quite similar to that when applying no smoothing (see Figure 5.6b). The recovered mass distribution mostly shows the typical Gibbs phenomenon. In this scenario the total mass recovered is 81.9%, which is 5.5% less than recovered with no smoothing applied (see Table 5.3). Again, the difference of 5.5% reflects the effect of spatial leakage, which is about double than in the previous scenario (e.g., 2.7% vs. 5.5%).

Similar to the previous scenario, the differences between input masses and recovered masses illustrated in Figure 5.9b show smaller differences over the disc but larger differences (similar magnitude to scenario (a)) closer to the disc's edges and decrease to zero at the same distance as in scenario (a). Due to the smaller spatial extension of disc mass Ib no undulations are present over the disc. The distance at which the difference at the outside of the disc reach zero is similar to the previous validation scenario. Again, this behaviour suggests mass transport mostly from the disc's edges to the outside of the disc due to the combined effect of spectral and spatial leakage. As expected for isotropic smoothing, the differences

in the west-east and south-north cross-sections show the same behaviour.

(c) Gaussian isotropic filter for r_g = 250 km and 10° disc

Now the scenario is examined where medium Gaussian isotropic smoothing with a smoothing radius of 250 km is applied to the disc mass Ia. The recovered mass distribution is illustrated in Figure 5.8c and shows considerable leakage around the spatial extent of the input masses. This is mostly noticeable by the undulating ring-pattern around the disc mass that now starts with a much increased distance from the disc as compared to scenario (a). This is also confirmed by Table 5.2 indicating that 84.4% of the input mass is recovered. Compared to the recovered mass when applying no smoothing, the increased mass loss is now the result of increased spatial leakage amounting to 9.0%. This means that spatial leakage is now larger than spectral leakage (e.g., 9.0% vs. 6.5% in scenario (a)).

The differences between input masses and recovered masses illustrated in Figure 5.9c now show almost no undulating pattern over the disc (e.g., much reduced magnitude). The largest differences occur again close to the disc's edge now extending about 500 km around the disc before reaching values close to zero. With respect to scenario (a) it can also be noticed that in the same way as mass spreads further away from the disc the increase of the differences from the disc centre towards the disc's edges starts earlier. This is consistent with an increased mass transport from the disc's edges to the outside of the disc with the effect of spatial leakage now being more pronounced. Again, as expected for isotropic smoothing, the differences in the west-east and south-north cross-sections show the same behaviour.

(d) Gaussian isotropic filter for r_g = 250 km and 5° disc

Now medium Gaussian isotropic smoothing with a smoothing radius of 250 km is applied to the spatially more concentrated disc mass Ib. Like in the previous scenario Figure 5.8d shows that for the higher mass concentration leakage

has increased. Again, the undulating ring-pattern around the disc starts with a much increased distance from the disc as compared to scenario (b). This is also confirmed in Table 5.3 by a decreased mass recovered with a level of only 69.6%, which is 12.3% higher than in scenario (b). Again this is the result of increased spatial leakage now at a level of 17.8%, which is considerably larger than spectral leakage (e.g., 17.8% vs. 12.6% in scenario (b)).

The differences illustrated in Figure 5.9d are around zero over the centre of the disc but start to increase just off the centre with maximum values close to the disc's edges. The maximum decreases to values close to zero at a distance now extending about 500 km around the disc. This suggests a much increased mass transport (e.g., leakage) to the outside of the disc not only from the disc's edges but also from parts close to the disc's centre. Again, as expected for isotropic smoothing, the differences in the west-east and south-north cross-sections show the same behaviour.

(e) Gaussian isotropic filter for r_g = 500 km and 10° disc

This scenario applies the strongest Gaussian isotropic smoothing with a smoothing radius of 500 km to disc mass Ia. Now leakage is even further increased with respect to the previous scenarios (a) and (c) as illustrated in Figure 5.8e showing increased masses outside the spatial extent of the input masses. Table 5.2 confirms that the input mass is recovered to only 69.9%, considerably less as in scenario (c), which recovered 84.4%. Considering this fact, the effect of spatial leakage is now the dominating effect as confirmed by 23.6% spatial leakage vs. 6.5% spectral leakage (see Table 5.2).

While the differences over the centre of the disc are still rather small they rapidly increase off the centre towards the disc's edges. Now considerable masses are transported (leaked) from areas close to the disc's centre outside the disc extending to about 1000 km around the disc before reaching values close to zero. Also in this scenario the differences in the west-east and south-north cross-sections show the same behaviour as is expected for isotropic smoothing.

(f) Gaussian isotropic filter for r_g = 500 km and 5° disc

Finally, the last scenario considered applies the strongest Gaussian isotropic smoothing with a smoothing radius of 500 km to the disc mass Ib, which leads to even higher levels of leakage as is illustrated in Figure 5.8f. Increased leakage is manifested in Figure 5.8f by a much increased zone around the spatial extension of the initial disc mass. Table 5.3 confirms this behaviour indicating that only 44.2% of the input mass has been recovered, thus with a level of 43.2%, the spatial leakage is now largely dominating with respect to 12.6% accounting for spectral leakage.

The strong increase of spatial leakage is also documented by the differences illustrated in Figure 5.9f. These differences are no more zero close to the disc's centre and reach very high levels at the disc's edges. As in the previous scenario the differences extend to about 1000 km around the disc before reaching values close to zero. This suggests massive mass transport (e.g., leakage) from all parts of the disc to its outside. This extreme case demonstrates that increased Gaussian isotropic smoothing can introduce massive leakage effects when dealing with spatially rather concentrated mass sources. Also in this scenario the differences in the west-east and south-north cross-sections show the same behaviour as is expected for isotropic smoothing.

5.4.3 Han's anisotropic filter

This validation follows the same layout as that in the previous Section 5.4.2 but - instead of an isotropic filter - it uses an anisotropic smoothing filter with different properties in west-east and south-north directions. The smoothing filter used here is Han's anisotropic filter as introduced in Chapter 4. Again three different degrees of smoothing have been selected as to reflect "weak", "medium" and "strong" anisotropic smoothing. These have been applied to the disc masses Ia and Ib in order to examine their impact on the recovery of the disc masses using the validation procedure described in Section 5.1. The following six validation

scenarios (all using the parameter m_1=15 , see Chapter 4) have been considered:

(a) r_0=125 km, r_1=250 km, disc radius is 10°

(b) r_0=125 km, r_1=250 km, disc radius is 5°

(c) r_0=250 km, r_1=500 km, disc radius is 10°

(d) r_0=250 km, r_1=500 km, disc radius is 5°

(e) r_0=500 km, r_1=1000 km, disc radius is 10°

(f) r_0=500 km, r_1=1000 km, disc radius is 5°

The smoothing radii r_0 and r_1 have been selected to be larger in west-east than in south-north direction (e.g., $r_1 > r_0$) to simulate the standard situation of removing/reducing the so-called striping effect in GRACE data by a stronger smoothing across track (approximately west-east) and a weaker smoothing along track (approximately south-north). Examples for the input and recovered masses in west-east and south-north cross-sections are shown in Figure 5.10 for the smoothing radii r_0=250 km and r_1=500 km superimposed on the discs Ia and Ib geometrical extensions.

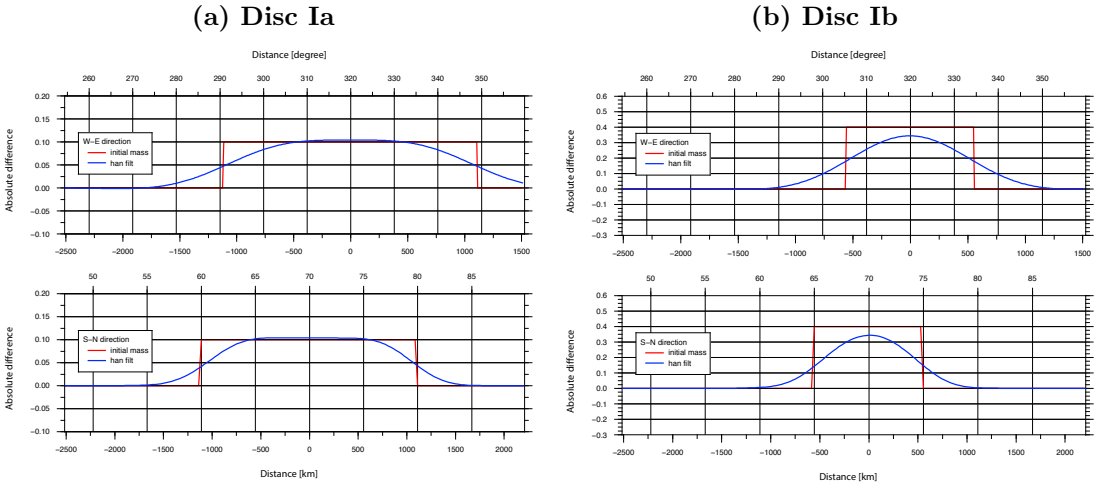

Figure 5.10: West-east (top) and south-north (bottom) cross-sections of the recovered masses for Han's anisotropic smoothing with smoothing radii r_0=250 km and r_1=500 km (blue line) superimposed on disc Ia and disc Ib (red line).

The validation results for all combinations are shown in Figure 5.11 for the recovered mass distributions and in Figure 5.12 for west-east and south-north cross-

section of the differences between the input and recovered masses. Table 5.2 and Table 5.3 in Section 5.5 list the total mass recovered, the total mass loss and the amount of mass loss due to spectral and spatial leakage.

(a) Han's anisotropic filter for r_0=125 km, r_1=250 km and 10° disc

Figure 5.11a shows the recovered mass distribution when applying weak anisotropic smoothing with the smoothing radii r_0=125 km and r_1=250 km onto the disc mass Ia. The recovered mass distribution is very similar to the result obtained through Gaussian isotropic smoothing with a smoothing radius of R = 125 km. The main difference is the undulating "ripple" pattern that now has different patterns in west-east and south-north direction as a result of anisotropic smoothing. Table 5.2 also confirms that the recovered mass distribution is similar to the corresponding isotropic scenario (a), though with a slightly lower total mass recovered (e.g., 88.6% vs. 90.8%). The lower recovery for the anisotropic case as compared to the corresponding isotropic case can be explained by the selection of a higher smoothing in west-east than south-north direction. Comparing the recovered mass with that when no smoothing applied (see also Section 5.4.1) reveals that spatial leakage with 4.9% is still smaller than the spectral leakage of 6.5% (see Table 5.2).

Figure 5.12a shows the difference between the input and the recovered mass in cross-sections through the centre of the disc in west-east and south-north directions. In south-north direction the differences are mostly dominated by the Gibbs phenomenon with undulating differences over the disc and larger differences at the disc's edges. This pattern largely follows the same pattern for isotropic smoothing. In west-east direction the undulating differences are largely reduced and follow more the pattern of isotropic smoothing with a smoothing radius of 250 km (e.g., scenario (c) for Gaussian isotropic smoothing). The difference in smoothing radii used can also be noticed at the distance at which the difference outside the disc reaches zero. With about 500 km the distance is about twice as large as in south-north direction (e.g., 250 km). As for the previous validation

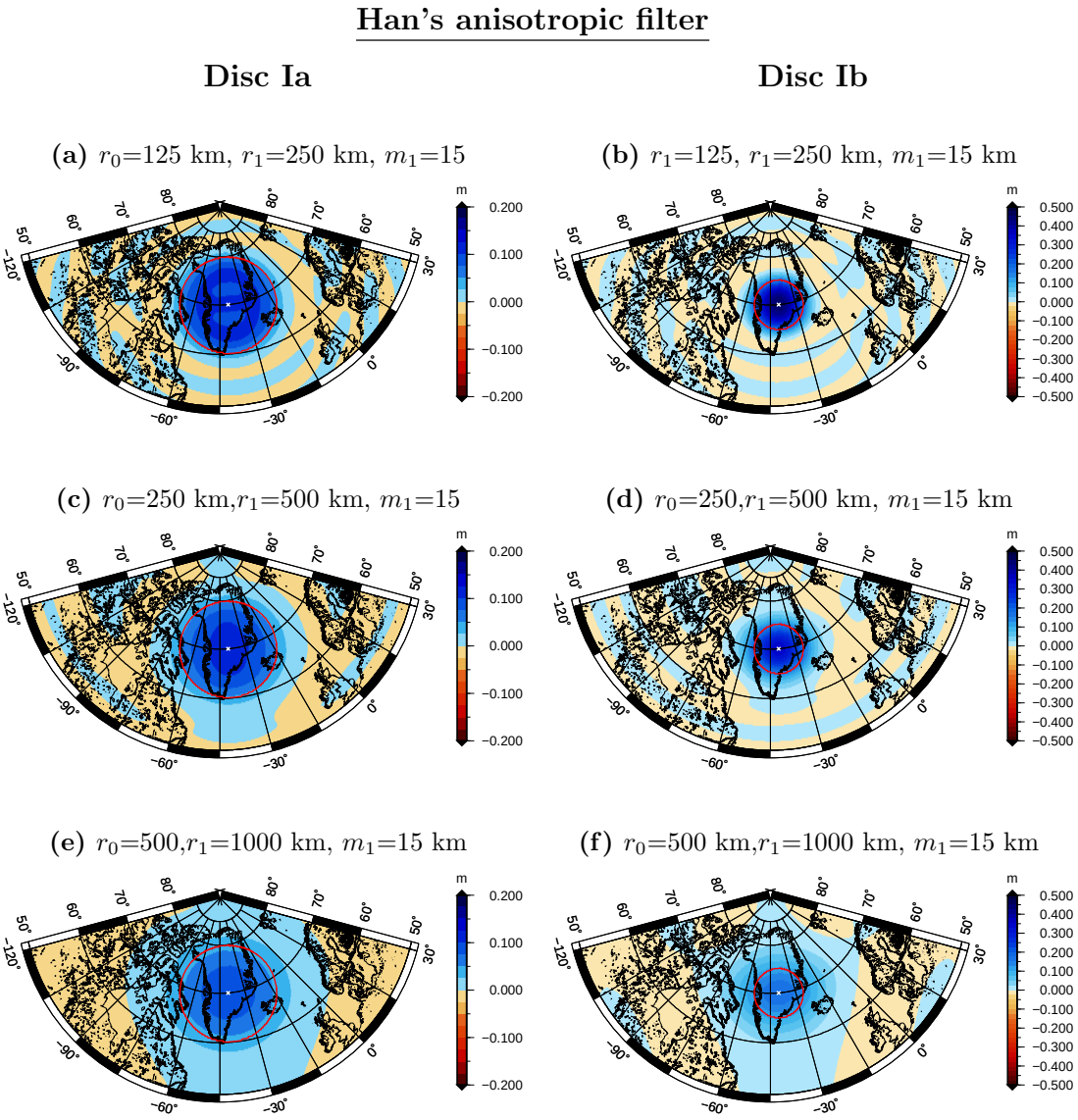

Figure 5.11: Recovered masses for discs Ia and Ib with radii 10° and 5°, respectively, after applying Han's anisotropic smoothing. The discs are centred at $\phi = 70°, \lambda = 320°$. The red circle indicates the spatial extension of the input disc mass.

Disc Ia **Disc Ib**

(a) r_0=125 km, r_1=250 km, m_1=15

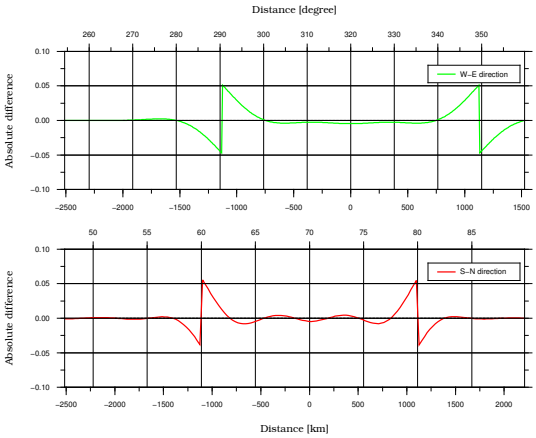

(b) r_0=125 km, r_1=250 km, m_1=15

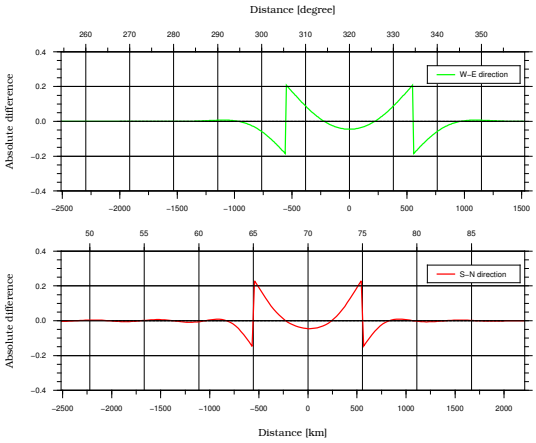

(c) r_0=250 km, r_1=500 km, m_1=15

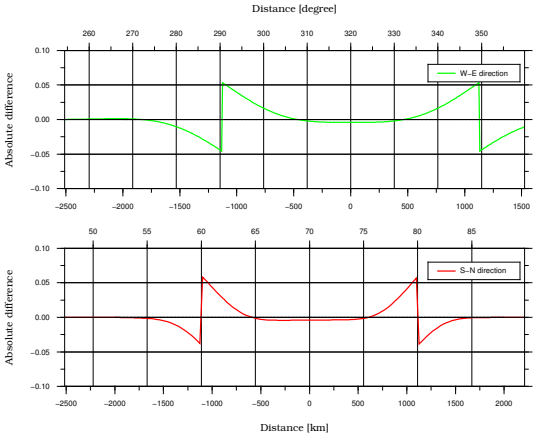

(d) r_0=250 km, r_1=500 km, m_1=15

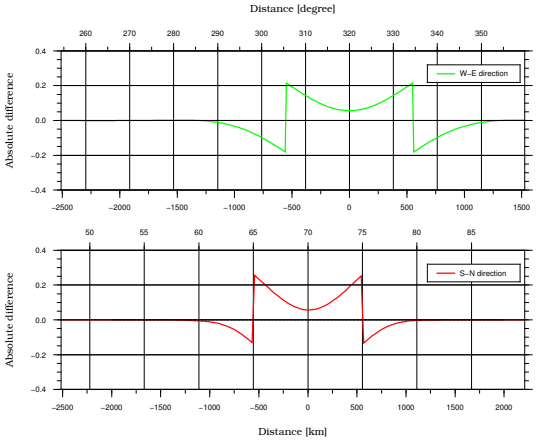

(e) r_0=500 km, r_1=1000 km, m_1=15

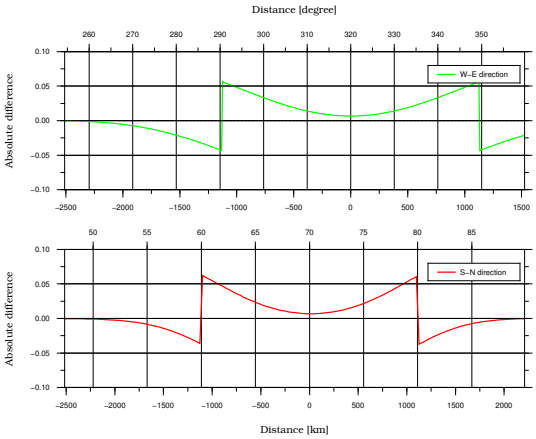

(f) r_0=500 km, r_1=1000 km, m_1=15

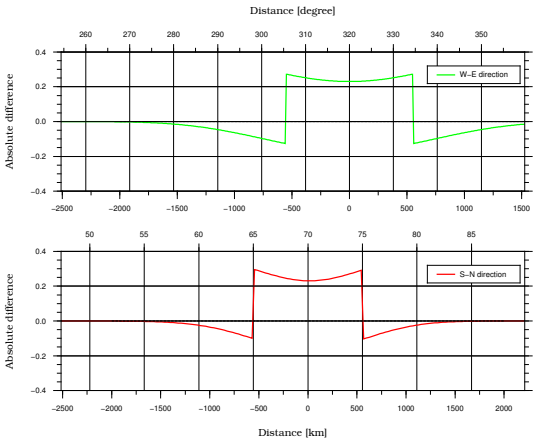

Figure 5.12: West-east (green line) and south-north (red line) cross-sections of the difference between input and recovered masses with Han's anisotropic smoothing.

scenarios, the differences suggest mass transport (e.g., leakage) mostly from the edges to the outside of the disc due to the combined effect of spectral and spatial leakage.

(b) Han's anisotropic filter for r_0 = 125 km, r_1 = 250 km and 5° disc

This validation scenario is equivalent to that above but applied to the spatially more concentrated disc mass Ib. Again the recovered mass distribution illustrated in Figure 5.9b is very similar to the result obtained through Gaussian isotropic smoothing with a smoothing radius of R = 125 km (see scenario (b) for Gaussian isotropic smoothing). Like Figure 5.11a also Figure 5.11b shows a different undulating "ripple" pattern in west-east and south-north direction as a result of anisotropic smoothing (also possibly interfering with the pattern of spectral leakage, e.g., Figure 5.6). With 77.2% the recovered mass is similar to the 81.9% recovered in the corresponding isotropic scenario (b). Again the slightly lower recovery for the anisotropic case can be explained by the selection of a higher smoothing in west-east than south-north direction with respect to isotropic smoothing. In this scenario, spatial and spectral leakage are similar with levels of 10.1% and 12.6% (see Table 5.1). The differences illustrated in Figure 5.12b show the same behaviour as for the corresponding isotropic scenario (b) with the exception of slightly higher magnitudes over the centre as well as at the disc's edges. Again the distance at which the difference outside the disc reaches zero is about twice as large in west-east than south-north direction (e.g., 500 km vs. 250 km). The combined effect of spectral and spatial leakage suggests mass transport (e.g., leakage) mostly from the edges to the outside of the disc.

(c) Han's anisotropic filter for r_0=250 km, r_1=500 km and 10° disc

With medium anisotropic smoothing using the smoothing radii r_0 = 250 km and r_1 = 500 km the spatial pattern of the recovered mass distribution illustrated in Figure 5.11c starts to show considerable differences in west-east and south-north direction. This is now quite different to the corresponding isotropic case

illustrated in Figure 5.8c The total mass recovered is with 80.6% significantly less than for the case of weak anisotropic smoothing (88.6%; scenario (a) above) as well as medium isotropic smoothing (84.4%; scenario (c) of Gaussian isotropic smoothing). The decreased recovery is the result of higher smoothing radii used. Like for the isotropic scenario with medium anisotropic smoothing spatial leakage starts to become more pronounced. In this validation, spatial leakage is now 12.8% as compared to 6.5% spectral leakage (see Table 5.2).

With respect to the corresponding scenario (a) of weak anisotropic smoothing the differences over the centre of the disc have no undulations and are close to zero whereas increased differences occur at the disc's edge (see Figure 5.12c). It also can be noticed that the differences show a slightly different behaviour with a faster increase from the centre to the disc's edge in west-east than south-north direction. At the outside of the disc the distance at which the differences reach zero is about 500 km in north-south and close to 1000 km in west-east direction. This is consistent with an increased mass transport (e.g., leakage) mostly from the edges of the disc to the outside of the disc with the effect of spatial leakage now being more pronounced.

(d) Han's anisotropic filter for r_0=250 km, r_1=500 km and 5°-disc

Figure 5.11d illustrates the recovered mass distribution for the scenario of medium anisotropic smoothing using the smoothing radii $r_0 = 250$ km and $r_1 = 500$ km applied to disc mass Ib. Like for the previous scenario the spatial pattern of the recovered mass distribution now shows considerable differences in west-east and south-north direction as an impact of anisotropic smoothing. Due to the spatially more concentrated mass only 61.0 % has been recovered, which is significantly less than in scenario (c). With 26.4% versus 12.6% spatial leakage is now the dominating contribution to the overall mass loss (see Table 5.1).

The differences illustrated in Figure 5.12d are now always at a higher level than in the previous cases. Over the centre of the disc the differences are significantly different from zero and rapidly increase to reach maximum levels at the disc's

edge. Similarly as in the previous scenario, the distance at which the differences reach zero is about 500 km in south-north and close to 1000 km in west-east direction. Again this is consistent with an increased mass transport (e.g., leakage) from the edges of the disc outside of the disc. Also in this case the differences show a slightly different behaviour in south-north than west-east direction with a faster increase from the centre to the disc's edges as well as slower decrease outside of the disc with respect to the former cross-section.

(e) Han's anisotropic filter for r_0=500 km, r_1=1000 km and 10° disc

Strong anisotropic smoothing with the smoothing radii $r_0 = 500$ km and $r_1 = 1000$ km has been applied to disc Ia. In this scenario the recovered mass distribution shows considerable leakage with a distinct anisotropic pattern between west-east and south-north. In total only 65.1% of the input mass has been recovered leading to a spatial leakage of 28.4%, which is considerably higher than for the scenario (c) of medium anisotropic smoothing. Therefore, spatial leakage is now the most dominating contribution to the total mass loss (see Table 5.2).

The differences illustrated in Figure 5.12e are now always higher than for the medium anisotropic smoothing scenario. Figure 5.12e shows that the differences are relatively small over the centre of the disc but gradually increase towards the disc's edges. The distances at which the differences reach zero is now close to 1000 km in north-south and considerably higher (∼1500 km) in west-east direction. This means considerable mass is transported (leaked) from areas close to the disc's centre outside the disc. The differences in Figure 5.12e now show that there is considerable different behaviour in the west-east and south-north cross-section as expected for anisotropic smoothing.

(f) Han's anisotropic filter for r_0=500 km, r_1=1000 km and 5° disc

Again the last scenario looks at the strongest anisotropic smoothing with smoothing radii of $r_0 = 500$ km and $r_1 = 1000$ km applied to disc mass Ib. In this case

most of the mass is leaked out of the original disc mass as illustrated in Figure 5.11f and numerically confirmed in Table 5.3. Only about a third (35.1%) of the input mass is recovered and the majority has leaked outside of the original disc. Considering a spectral leakage of 12.6% more than half of the original disc mass (52.3%) is lost due to spatial leakage.

The enormous leakage can also be seen in the differences illustrated in Figure 5.12f, which shows already high levels over the disc's centre and increasing further towards the disc's edges, thus indicating most of the initial disc mass is leaked outside of the disc. Similarly as in the previous scenario the distances at which the differences reach zero outside the disc are now close to 1000 km in north-south and 1500 km in west-east direction. Like for strong isotropic smoothing, this also confirms that strong anisotropic smoothing can lead to massive leakage effects when applied to spatially rather concentrated masses (e.g., disc mass Ib). As in the previous scenarios the relative differences illustrated in Figure 5.12f are different for the west-east and south-north cross-sections as expected for anisotropic smoothing.

5.4.4 Kusche's de-correlated anisotropic filter

The third validation is based on Kusche's de-correlated anisotropic filter (Section 4.3.3). Like for the previous validations three different filters have been used representing "weak", "medium" and "strong" de-correlated anisotropic smoothing These have been applied to the disc masses Ia and Ib in order to examine their impact on the recovery of these masses using the validation procedure described in Section 5.1. The following six validation scenarios have been considered:

(a) DDK3: $a = 1 \times 10^{12}$ and $p = 4$, disc radius is 10°
(b) DDK3: $a = 1 \times 10^{12}$ and $p = 4$, disc radius is 5°
(c) DDK2: $a = 1 \times 10^{13}$ and $p = 4$, disc radius is 10°
(d) DDK2: $a = 1 \times 10^{13}$ and $p = 4$, disc radius is 5°
(e) DDK1: $a = 1 \times 10^{14}$ and $p = 4$, disc radius is 10°
(f) DDK1: $a = 1 \times 10^{14}$ and $p = 4$, disc radius is 5°

Again, the anisotropy of the filter has been selected to have stronger smoothing in west-east than in south-north direction. Examples for the input and recovered masses as west-east and south-north cross sections are shown in Figure 5.13 for DDK2 superimposed on the discs Ia and Ib.

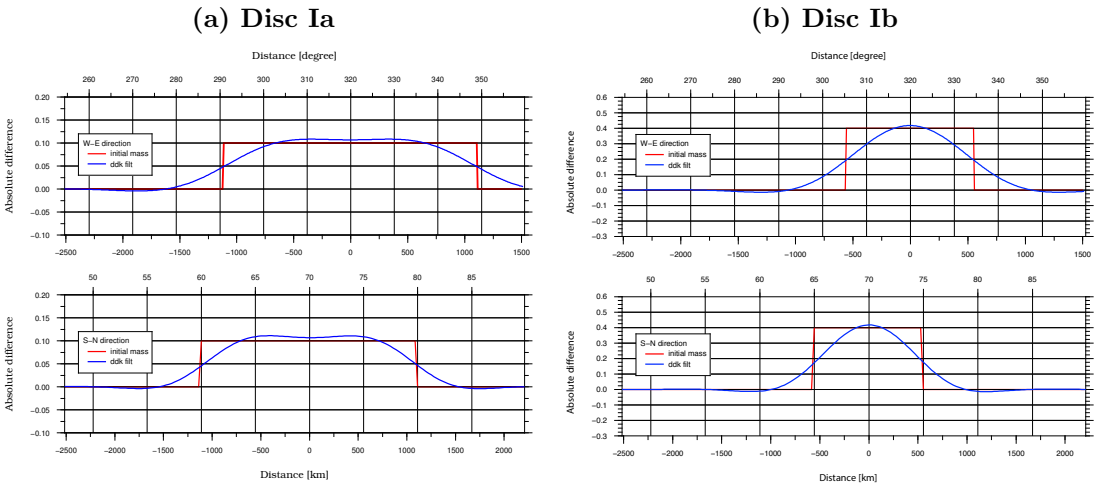

Figure 5.13: West-east (top) and south-north (bottom) sections of recovered masses for Kusche's de-correlated anisotropic filter with parameters $a = 1 \times 10^{13}$ and $p = 4$ (blue line) superimposed on disc Ia and disc Ib (red line).

The validation results for all combinations are shown in Figure 5.14 for the recovered mass distributions and in Figure 5.15 for west-east and south-north cross-sections of the differences between the input and recovered masses. Table 5.2 and Table 5.3 in Section 5.5 list the total mass recovered, the total mass loss and the amount of mass loss due to spectral and spatial leakage.

(a) Kusche's de-correlated anisotropic filter DDK3 and 10° disc

In this validation scenario the DDK3 filter applies weak smoothing onto the disc mass Ia. The recovered mass distribution illustrated in Figure 5.14a is similar to that recovered using no filter (see Figure 5.6). In Figure 5.14a little leakage is visible but the typical Gibbs phenomenon with undulation "ripples" radiating away from the disc mass. In this scenario 90.2% of the initial mass has been

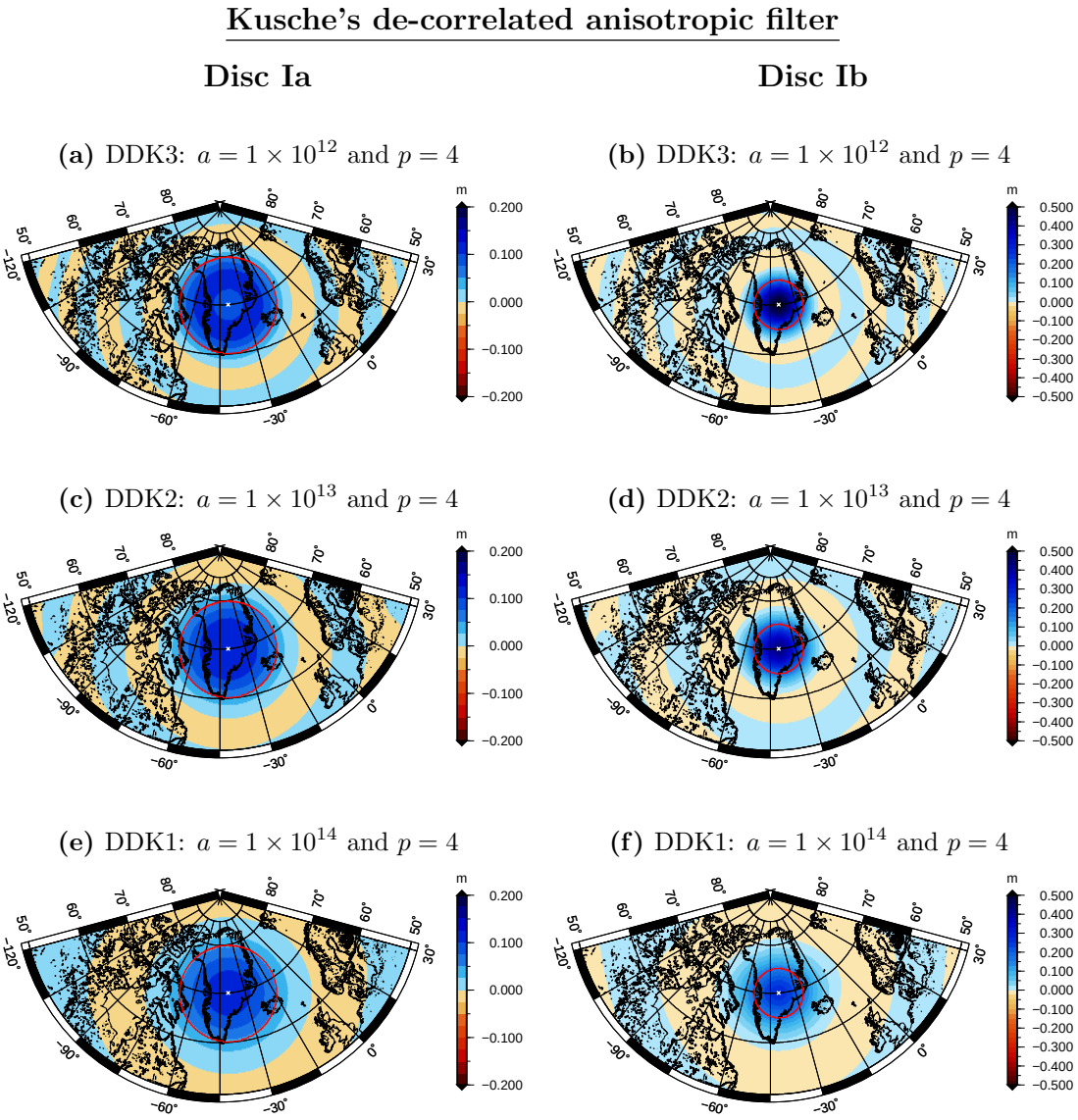

Figure 5.14: Recovered masses for discs Ia and Ib with radii 10° and 5°, respectively after applying Kusche's de-correlated anisotropic filter. The discs are centred at $\phi = 70°, \lambda = 320°$. The red circle indicates the spatial extension of the input disc mass.

Disc Ia **Disc Ib**

(a) DDK3: $a = 1 \times 10^{12}$ and $p = 4$ **(b)** DDK3: $a = 1 \times 10^{12}$ and $p = 4$

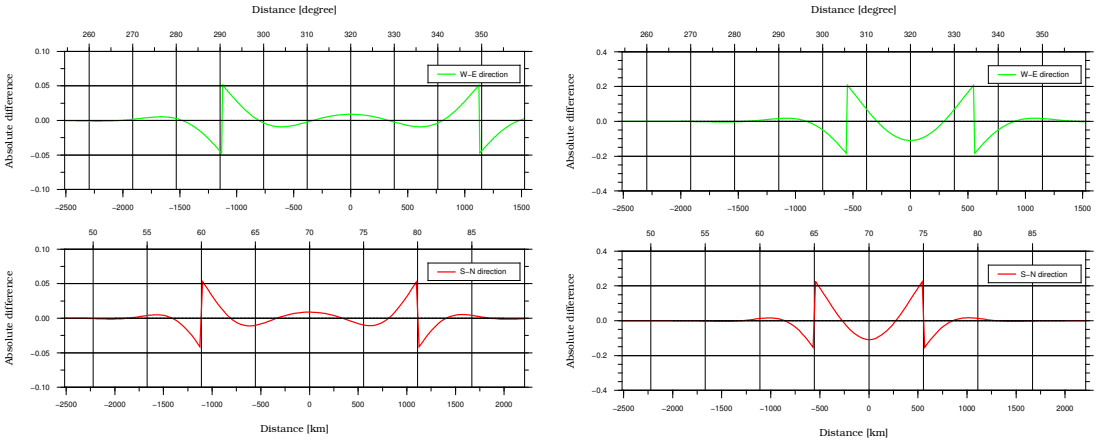

(c) DDK2: $a = 1 \times 10^{13}$ and $p = 4$ **(d)** DDK2: $a = 1 \times 10^{13}$ and $p = 4$

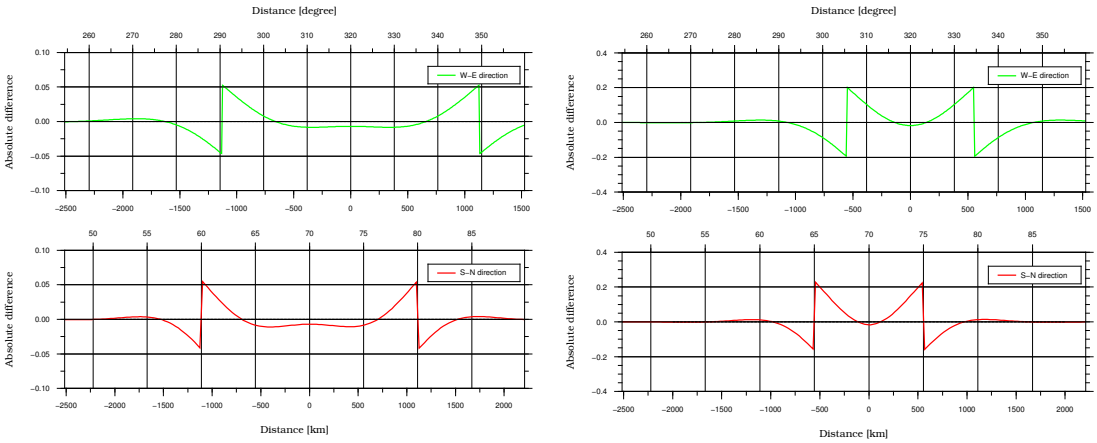

(e) DDK1: $a = 1 \times 10^{14}$ and $p = 4$ **(f)** DDK1: $a = 1 \times 10^{14}$ and $p = 4$

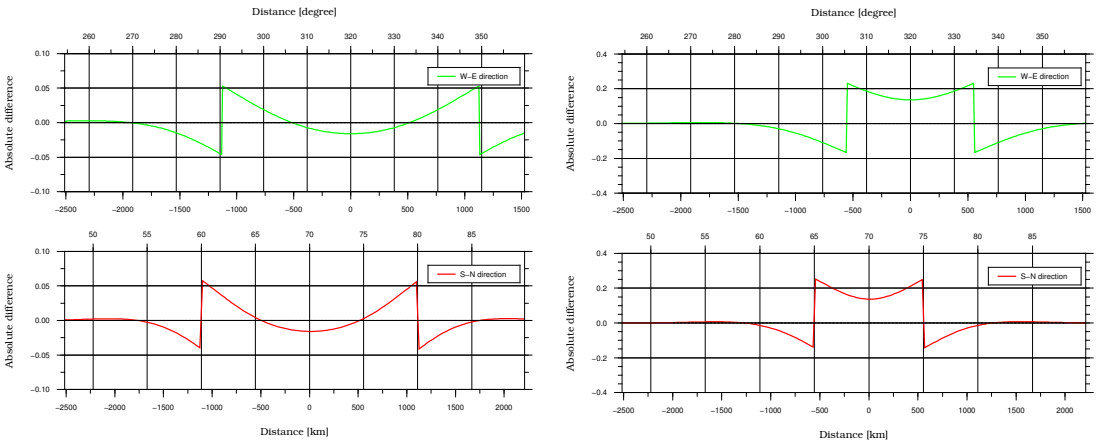

Figure 5.15: West-east (green line) and south-north (red line) cross-sections of the difference between input and recovered masses with Kusche's de-corellated anisotropic smoothing.

recovered (see Table 5.2), which is similar to all previous scenarios when applying no filter (Figure 5.6a), Gaussian isotropic (Figure 5.8a) and Han's anisotropic filter (Figure 5.11a). The mass loss is to a large extent (6.5%) due to spectral leakage and to a minor extent (3.2%) due to spatial leakage as an effect of the introduced filter. For this scenario, the distance at which the differences outside the disc reaches zero is about 400 km in west-east and about 300 km in south-north direction, which is between that of Gaussian isotropic (scenario (a)) and Han's anisotropic filter (scenario (a)). As for all previous validations this suggests mass transport (e.g., leakage) mostly from the disc's edges to the outside of the disc.

(b) Kusche's de-correlated anisotropic filter DDK3 and 5° disc

In this validation the same filter as in the previous scenario is used but applied to disc mass Ib. Again the recovered mass distribution illustrated in Figure 5.14b is similar to that recovered using no filter (see Figure 5.6b), Gaussian isotropic filter (see Figure 5.8b) and Han's anisotropic filter (see Figure 5.11b). Figure 5.14b is dominated by the Gibbs phenomenon and shows only minimal leakage. This is confirmed in Table 5.3 indicating that 81.3% of the original mass has been recovered. In this case a large part of the mass loss is due to spectral leakage (12.6%) and only a smaller part due to spatial leakage (6.0%).

Differences shown in Figure 5.15b exhibit larger magnitudes over the disc's centre and increase towards the disc's edge. The distance at which the differences outside the disc reach zero is slightly larger than in the previous cases. The distances are now about 400 km in west-east and about 300 km in south-north direction. Also for DDK3 filter both cross-sections show a slightly different behaviour in west-east and south-north direction.

(c) Kusche's de-correlated anisotropic filter DDK2 and 10° disc

Through the use of DDK2, this validation applies medium smoothing on disc mass Ia. While the recovered mass distribution illustrated in Figure 5.14c still shows the Gibbs phenomenon and increased leakage around the disc's edges of the original disc mass is visible. Table 5.2 indicates that 86.3% of the input mass is recovered. This indicates that spectral and spatial leakage contribute similarly to the overall mass loss (6.5% versus 7.2%).

The differences illustrated in Figure 5.15c show only minimal undulations over the centre but an elevated level at half of the disc's extension. As in all other cases the differences increase towards the disc's edge. Therefore, both the mass over the centre of the disc and its edge is leaked beyond the disc's initial spatial extent. The distances at which the differences outside the disc reach zero are again slightly larger than in the previous scenarios. The distances are now about 500 km in west-east and about 400 km in south-north direction.

(d) Kusche's de-correlated anisotropic filter DDK2 and 5° disc

Applying medium smoothing through the DDK2 filter on the spatially more concentrated disc mass Ib results in increased leakage around the initial extension of the disc mass (see Figure 5.14d) when compared to the corresponding weak filter. This is confirmed by Table 5.1 with only 71.8% of the initial disc mass recovered. In this case spatial leakage accounts for 15.6%, which is slightly higher than spectral leakage (e.g., 12.6%). Minimum differences are present over the disc's centre as illustrated in Figure 5.15d. The differences gradually increase and reach maximum levels at the disc's edge. This means that considerable mass closer to the disc's edge is leaked well beyond the initial disc mass extension.

(e) Kusche's de-correlated anisotropic filter DDK1 and 10° disc

In this validation DDK1 employs strong smoothing on disc mass Ia. With respect to the previous scenarios much increased leakage beyond the original extension of the disc is now visible, though it reduces fast to a relative low level. This is confirmed by Table 5.2 documenting that still 78.9% of the initial mass is recovered. Now, with 14.7% spatial leakage is larger than spectral leakage (6.5%). However, overall leakage is still considerably smaller when compared to the corresponding strong Gaussian isotropic or Han's anisotropic smoothing. As illustrated in Figure 5.15e, differences are generally small over the disc's centre and increase towards the disc's edge. The distances at which the differences outside the disc reach zero are larger than in the previous scenarios. The distances are about 900 km in west-east and about 600 km in south-north direction. Furthermore, the two cross-sections illustrated in Figure 5.15e differ slightly from each other as expected for anisotropic filters.

(f) Kusche's de-correlated anisotropic filter DDK1 and 5° disc

Finally, as with the remaining validations strong smoothing is applied by the DDK1 filter onto disc mass Ib. This introduces considerable higher leakage beyond the original extension of the disc mass (see Figure 5.14f). Only about half (51.4%) of the input mass is recovered (see Table 5.3) where 36.0 % of the mass is lost due to spatial leakage. However, as with the previous scenarios, while there is considerable leakage for the DDK1 filter this is less than compared to strong Gaussian isotropic and Han's anisotropic smoothing.

This is also confirmed with generally smaller differences as illustrated in Figure 5.15f. Over the disc's centre, differences remain below 50% and increase to the edges of the disc. While this is large, it is considerably less than for strong Gaussian isotropic and Han's anisotropic smoothing. Also in this scenario, the distances at which the differences outside the disc reach zero are about 900 km in west-east and about 600 km in south-north direction. Therefore, the application

of the DDK1 filter introduces leakage that is still considerable but not as strong as the respective isotropic and anisotropic filters used.

5.5 Comparison between Different Filtering Techniques

This Section provides a comparison between validation results based on the simple mass distributions of disc masses. A particular focus is on a comparison between results obtained by the use of the three considered filters. Differences in the recovered mass distributions can directly be attributed to different spatial leakage properties introduced by the used filters. Table 5.2 and Table 5.3 list all results obtained for disc masses with a 10° spherical radius (e.g., Ia, IIa, IIIa) and a 5° spherical radius (e.g., Ib, IIb, IIIb), respectively. In particular Table 5.2 and Table 5.3 list for each validation the total mass recovered, the total mass loss (e.g., combined spectral and spatial leakage) and mass loss due to spectral and spatial leakage. Figure 5.16 and Figure 5.17 illustrate the rate of the recovered masses for disc masses with a 10° spherical radius and a 5° spherical radius, respectively.

Regarding spatial leakage, the results of Section 5.4 and Appendix A have demonstrated that the effect of spatial leakage for each considered filter type is increasing for increased smoothing radii. This means the initial disc mass is spatially spread out more for increased smoothing, as expected. Also for spatially more concentrated masses, e.g., higher jump discontinuity, spectral as well as spatial leakage is increasing. In the validation scenarios considered, the effect of spectral and spatial leakage is approximately double when halving the spatial extension of the disc masses but keeping the total masses the same (e.g., 5° disc masses have 4-times the height of 10° disc masses). While for "weak" smoothing the levels of spectral and spatial leakage are similar for medium to strong smoothing spatial leakage starts to dominate. Especially, for strong smoothing spatial leakage can be very large, often reaching levels over 50%.

While both Han's anisotropic and Kusche's de-correlated anisotropic filters in-

troduce anisotropic behaviour in the recovered mass distribution the effective smoothing radii are different. Han's anisotropic smoothing filter is directly based on varying smoothing radii. Kusche's de-correlated anisotropic filter only shows indirectly the impact of varying smoothing. Results in Appendix A.1.4 suggest that the effective smoothing radii in south-north direction are almost constant and in west-east direction constantly increasing. Information on the effective smoothing radii are obtained through the distances in west-east and south-north direction at which the differences outside the disc reach a level of zero.

An interesting result obtained is the dependency of the recovered mass with respect to geographic latitude. While Gaussian isotropic smoothing shows similar levels of recovery independent of the geographic latitude of the disc mass location, the situation is different for anisotropic filters such as Han's anisotropic and Kusche's de-correlated anisotropic filters. For the latter two cases the recovery is better for disc masses located at higher geographic latitudes and worse for disc masses located at the equator. This may be an effect due to the meridian convergence when using geographic coordinates. The meridian convergence directly depends on the geographic latitude and influences the spatial resolution in west-east direction when using spherical harmonics. As demonstrated in Figure 2.3 (see Chapter 2), the spatial resolution in west-east direction $D\phi$, associated to a particular spherical harmonic degree, increases for higher geographic latitudes. Therefore, this will have a direct impact on the modelling/approximation of mass distributions with spherical harmonics and the use of anisotropic filters that act differently in west-east and south-north directions.

Table 5.2: Validation results: Recovered mass, mass loss and spectral and spatial leakage for disc masses Ia, IIa, and IIIa with 10° spherical radius.

Simulated mass			Recovered Mass		Mass Loss		Spatial Leakage	
			(Gt)	(%)	(Gt)	(%)	(Gt)	(%)
Disc Ia centred at ϕ=70°, λ=320°		Input	388.249	100.000	0.000	0.000	0.000	0.000
		No smoothing	363.052	93.510	25.197*	6.463*	0.000	0.000
	Gauss	r_g=125 km	352.447	90.779	35.802	9.183	10.605	2.720
		r_g=250 km	327.869	84.448	60.380	15.487	35.183	9.024
		r_g=500 km	271.454	69.918	116.795	29.956	91.598	23.494
	Han	r_0=125 km, r_1=250 km	344.044	88.614	44.205	11.338	19.008	4.875
		r_0=250 km, r_1=500 km	313.131	80.652	75.118	19.267	49.921	12.804
		r_0=500 km, r_1=1000 km	252.707	65.089	135.542	34.765	110.345	28.302
	Kusche	DDK3	350.429	90.259	37.820	9.700	12.623	3.238
		DDK2	335.197	86.336	53.052	13.607	27.855	7.144
		DDK1	306.118	78.846	82.131	21.066	56.934	14.603
Disc IIa centered at ϕ=0°, λ=180°		Input	388.245	100.000	0.000	0.000	0.000	0.000
		No smoothing	364.135	93.790	24.110*	6.163*	0.000	0.000
	Gauss	r_g=125 km	353.548	91.063	34.697	8.869	10.587	2.706
		r_g=250 km	328.972	84.733	59.273	15.151	35.163	8.988
		r_g=500 km	272.473	70.181	115.772	29.593	91.662	23.430
	Han	r_0=125 km, r_1=250 km	331.678	85.430	56.567	14.459	32.457	8.297
		r_0=250 km, r_1=500 km	294.804	75.932	93.441	23.885	69.331	17.722
		r_0=500 km, r_1=1000 km	224.797	57.901	163.448	41.780	139.338	35.617
	Kusche	DDK3	336.693	86.722	51.552	13.177	27.442	7.015
		DDK2	306.272	78.886	81.973	20.954	57.863	14.791
		DDK1	247.964	63.868	140.281	35.858	116.171	29.695
Disc IIIa centered at ϕ=-75°, λ=250°		Input	-388.449	100.000	0.000	0.000	0.000	0.000
		No smoothing	-366.140	94.257	-22.309	5.727*	0.000	0.000
	Gauss	r_g=125 km	-355.457	91.507	-32.992	8.470	-10.683	2.743
		r_g=250 km	-330.739	85.143	-57.710	14.816	-35.401	9.089
		r_g=500 km	-274.075	70.556	-114.374	29.363	-92.065	23.636
	Han	r_0=125 km, r_1=250 km	-349.020	89.850	-39.429	10.123	-17.120	4.395
		r_0=250 km, r_1=500 km	-319.017	82.126	-69.432	17.825	-47.123	12.098
		r_0=500 km, r_1=1000 km	-259.432	66.787	-129.017	33.123	-106.708	27.395
	Kusche	DDK3	-354.098	91.157	-34.351	8.819	-12.042	3.092
		DDK2	-339.420	87.378	-49.029	12.587	-26.720	6.860
		DDK1	-311.855	80.282	-76.594	19.664	-54.285	13.937

* Spectral leakage

(a) Gaussian Isotropic Smoothing

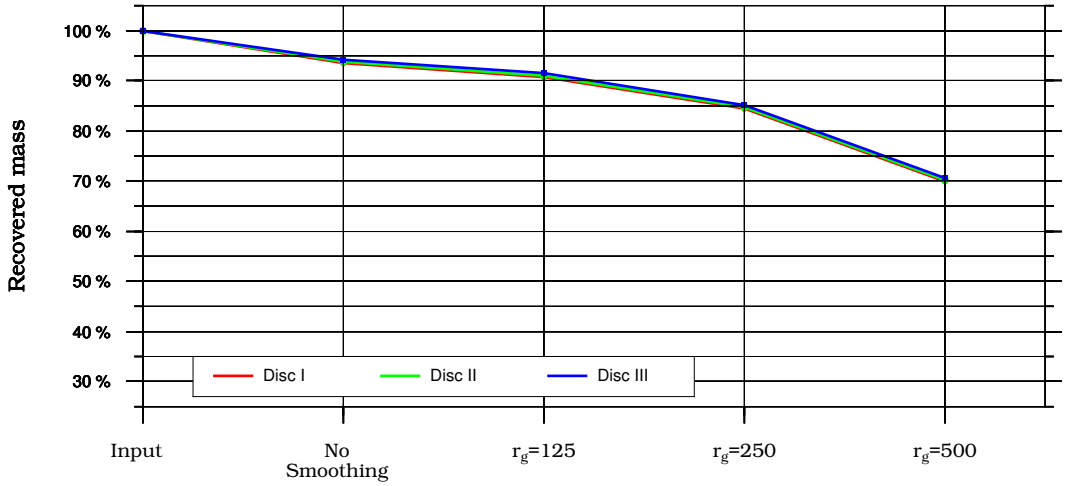

(b) Han's Anisotropic Smoothing

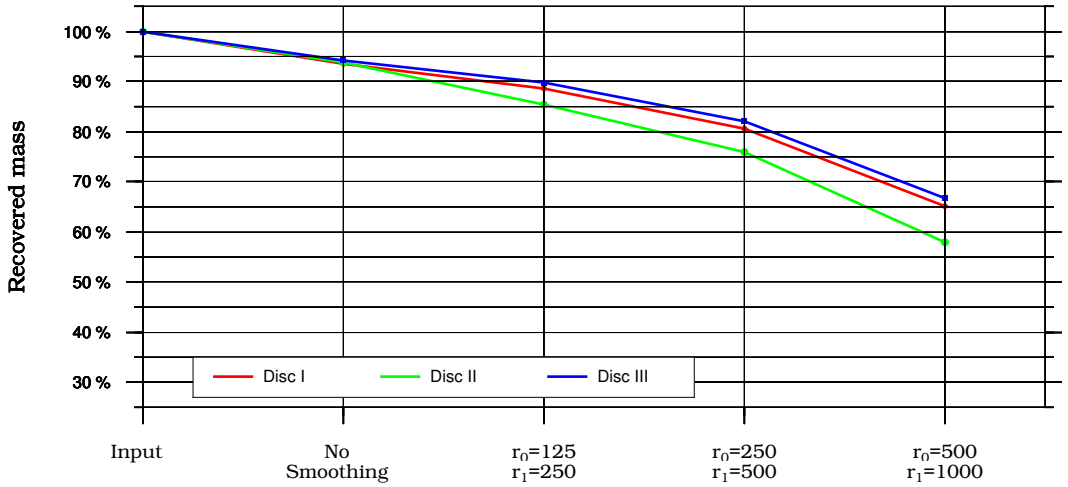

(c) Kusche's de-correlated, Anisotropic Smoothing

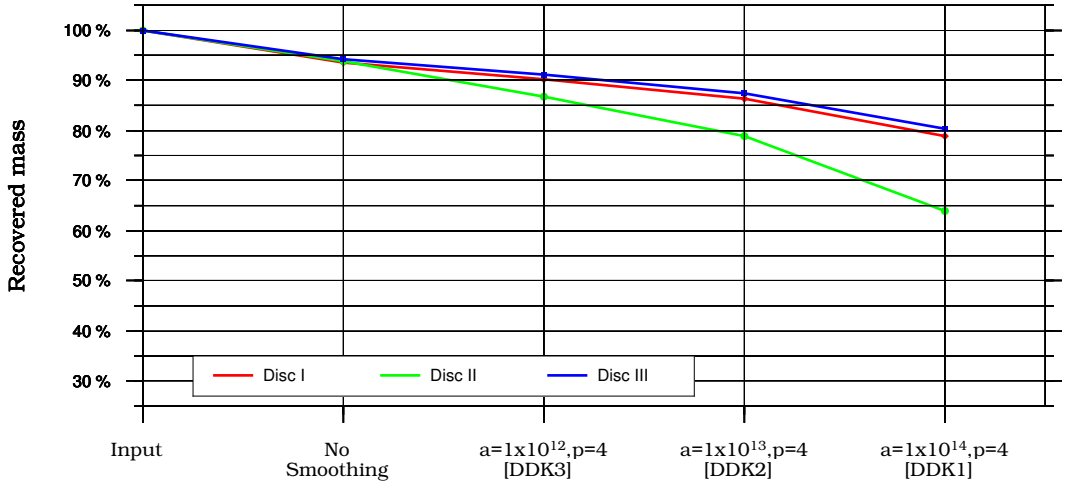

Figure 5.16: Recovered disc masses Ia, IIa and IIIa with 10 ° spherical radius.

Table 5.3: Validation results: Recovered mass, mass loss and spectral and spatial leakage for disc masses Ib, IIb, and IIIb with 5° spherical radius

Simulated mass			Recovered Mass		Mass Loss		Spatial Leakage	
			(Gt)	(%)	(Gt)	(%)	(Gt)	(%)
Disc Ia centred at ϕ=70°, λ=320°		Input	389.882	100.000	0.000	0.000	0.000	0.000
		No smoothing	340.711	87.388	49.171 *	12.612 *	0.000	0.000
	Gauss	r_g=125 km	319.291	81.894	70.591	18.106	21.420	5.494
	Gauss	r_g=250 km	271.321	69.591	118.561	30.409	69.390	17.798
	Gauss	r_g=500 km	172.212	44.170	217.670	55.830	168.499	43.218
	Han	r_0=125 km, r_1=250 km	301.205	77.255	88.677	22.745	39.506	10.133
	Han	r_0=250 km, r_1=500 km	237.779	60.987	152.103	39.013	102.932	26.401
	Han	r_0=500 km,r_1=1000 km	136.717	35.066	253.165	64.934	203.994	52.322
	Kusche	DDK3	317.131	81.340	72.751	18.660	23.580	6.048
	Kusche	DDK2	279.894	71.789	109.988	28.211	60.817	15.599
	Kusche	DDK1	200.189	51.346	189.693	48.654	140.522	36.042
Disc IIb centered at ϕ=0°, λ=180°		Input	391.213	100.000	0.000	0.000	0.000	0.000
		No smoothing	342.383	87.518	48.830*	12.482*	0.000	0.000
	Gauss	r_g=125 km	321.162	82.094	70.051	17.906	21.221	5.424
	Gauss	r_g=250 km	273.346	69.871	117.867	30.129	69.037	17.647
	Gauss	r_g=500 km	173.875	44.445	217.338	55.555	168.508	43.073
	Han	r_0=125 km, r_1=250 km	272.763	69.722	118.450	30.278	69.620	17.796
	Han	r_0=250 km, r_1=500 km	193.460	49.451	197.753	50.549	148.923	38.067
	Han	r_0=500 km, r_1=1000 km	103.212	26.383	288.001	73.617	239.171	61.136
	Kusche	DDK3	279.810	71.524	111.403	28.476	62.573	15.995
	Kusche	DDK2	217.381	55.566	173.832	44.434	125.002	31.952
	Kusche	DDK1	135.767	34.704	255.446	65.296	206.616	52.814
Disc IIIb centered at ϕ=-75°, λ=250°		Input	-389.511	100.000	0.000	0.000	0.000	0.000
		No smoothing	-343.928	88.297	-45.583*	11.703*	0.000	0.000
	Gauss	r_g=125 km	-322.060	82.683	-67.451	17.317	-21.868	5.614
	Gauss	r_g=250 km	-273.480	70.211	-116.031	29.789	-70.448	18.086
	Gauss	r_g=500 km	-173.813	44.623	-215.698	55.377	-170.115	43.674
	Han	r_0=125 km, r_1=250 km	-307.848	79.034	-81.663	20.966	-36.080	9.263
	Han	r_0=250 km, r_1=500 km	-247.102	63.439	-142.409	36.561	-96.826	24.858
	Han	r_0=500 km, r_1=1000 km	-144.952	37.214	-244.559	62.786	-198.976	51.084
	Kusche	DDK3	-320.791	82.357	-68.720	17.643	-23.137	5.940
	Kusche	DDK2	-286.027	73.432	-103.484	26.568	-57.901	14.865
	Kusche	DDK1	-207.955	53.389	-181.556	46.611	-135.973	34.909

* Spectral leakage

(a) Gaussian Isotropic Smoothing

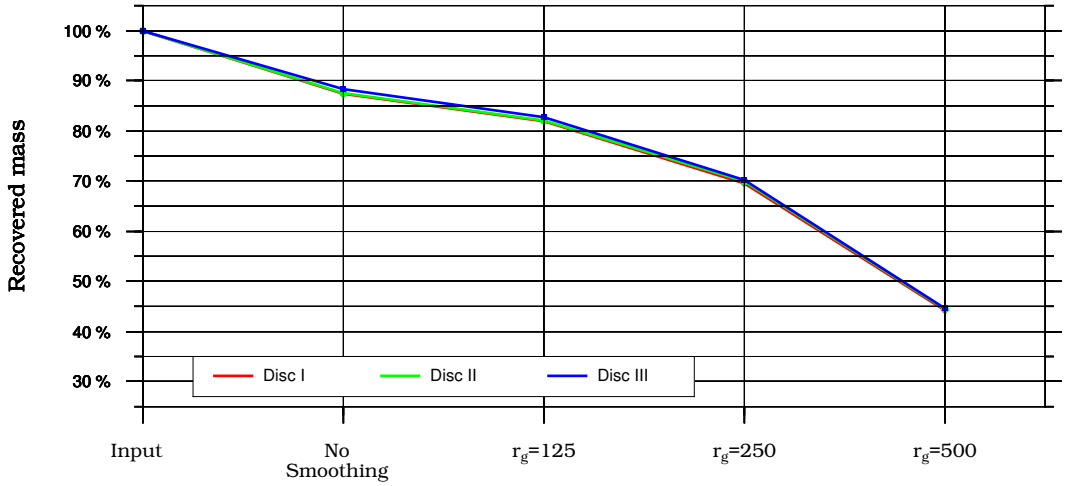

(b) Han's Anisotropic Smoothing

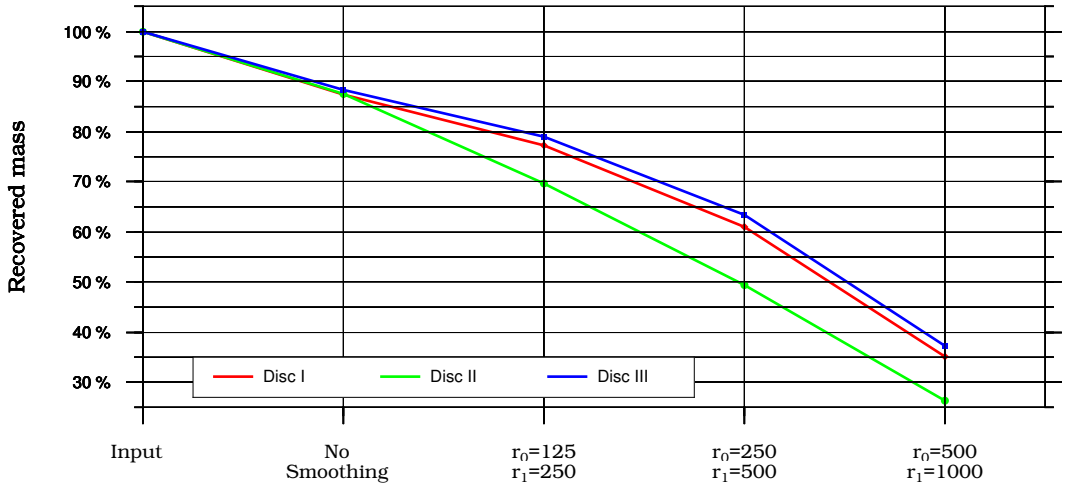

(c) De-correlated, Anisotropic Smoothing

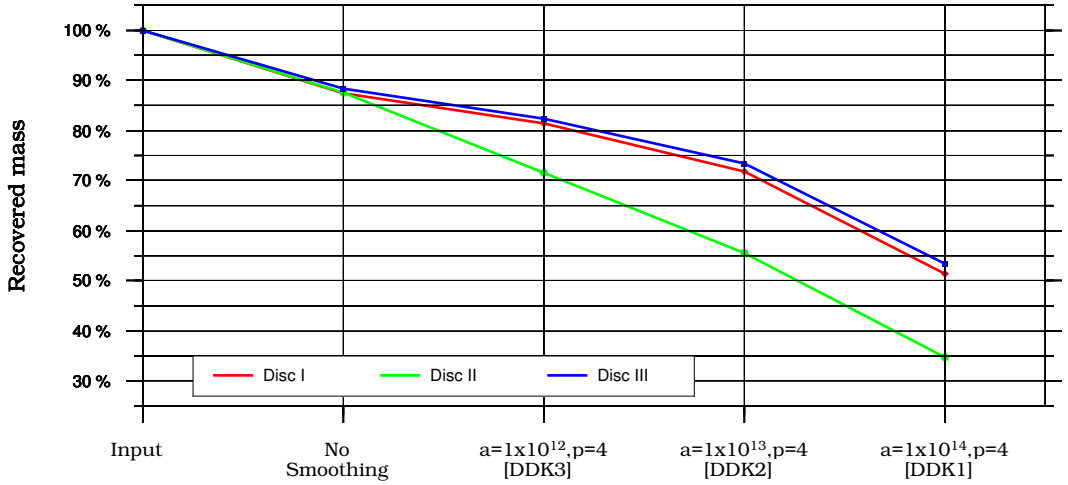

Figure 5.17: Recovered disc masses Ib, IIb and IIIb with 5 ° spherical radius.

For locations at the equator and higher geographic latitude the recovery levels are similar for Gaussian isotropic smoothing and Han's anisotropic smoothing when considering "weak" smoothing only. In this situation the recovered masses are slightly less for Han's anisotropic smoothing due to the larger smoothing radii in west-east direction. This behaviour starts to change when considering medium to strong smoothing with larger differences in recovered mass, again due to the increased smoothing radius used in west-east direction for Han's anisotropic smoothing.

Also for Kusche's de-correlated anisotropic smoothing the recovery level can be considered as comparable to Gaussian isotropic and Han's anisotropic smoothing when considering "weak" smoothing only. However, for locations with higher geographic latitude and considering medium to strong smoothing the recovery level for Kusche's de-correlated anisotropic filter is consistently higher than for Gaussian isotropic and Han's anisotropic smoothing. This may indicate that in these situations smoothing for Kusche's de-correlated anisotropic filter is not as high as for Gaussian isotropic or Han's anisotropic filter.

5.6 Chapter Summary

This chapter presented a validation procedure to examine techniques used to infer mass changes from (time-variable) gravity changes. Simple spherical disc masses with different size and geographic locations have been used as simulated masses within the validation procedure. The disc masses were subjected to a range of smoothing filters. Results for all validation scenarios are presented in terms of the recovered mass distribution and west-east and south-north cross-sections of the differences between input and recovered masses. While all results are described the chapter also provides a comparison between the used smoothing filter.

Chapter 6

Validation Using GRACE-Derived Mass Changes

This chapter presents validation results based on more realistic mass distributions over various geographic locations. The difference to the more simplistic disc masses is mostly in terms of an irregular spatial extension and varying height. The use of more simplistic masses in Chapter 5 revealed general leakage properties as an effect of the smoothing filter and disc mass used within the mass estimation technique of Wahr et al. (1998). Now the same smoothing filter will be applied to more realistic mass distributions. Main focus in this chapter is on the influence of irregularly shaped masses, e.g., the ability to recover the correct spatial distribution (shape).

In particular the simulated mass distributions are subjected to the Gaussian isotropic filter, Han's anisotropic filter and Kusche's de-correlated anisotropic filter (see Chapter 4). For each filter the same smoothing scenarios of "weak", "medium" and "strong" smoothing as introduced in Chapter 5 have been used. This chapter provides only the results of one scenario for each filter as an example. The particular filters chosen are the Gaussian isotropic filter with smoothing radius of r_g = 250 km, Han's anisotropic filter with the smoothing radii r_0=250 km, r_1=500 km and Kusche's de-correlated anisotropic filter DDK3, which have similar smoothing properties. A complete overview of results obtained by applying all filters is given in Appendix B. Furthermore, Table 6.1 and Figure 6.40 in Section 6.4 provide a complete overview regarding the total mass recovered, total mass loss and spectral and spatial leakage for each smoothing filter and each mass

change considered.

6.1 Validation Procedure

The validation procedure employed on the more realistic mass distributions is exactly the same as used in Chapter 5 for the more simplistic disc masses. Figure 6.1 illustrates the validation procedure that differs to that in Section 5.1 only by the simulated mass distributions used as input. The Stokes coefficients of each mass distribution are smoothed with the same smoothing filters, namely Gaussian isotropic smoothing, Han's anisotropic smoothing and Kusche's de-correlated anisotropic smoothing (see Chapter 4). Furthermore, the validation is based on the same software routines to perform spherical harmonic analysis and synthesis as described in Section 5.2.

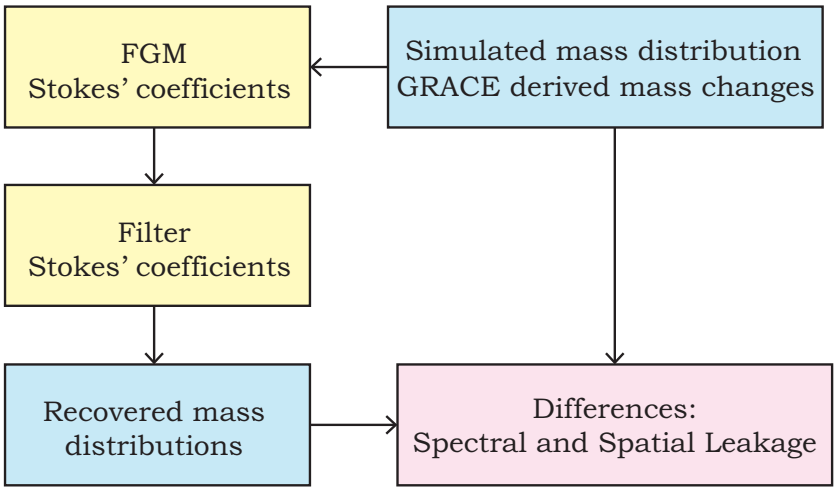

Figure 6.1: Symbolic work flow for the validation process using GRACE-derived mass changes.

6.2 GRACE-Derived Mass Changes

More realistic mass distributions have been obtained from GRACE-derived mass changes over the 8-year period between 2002 and 2010 (see Figure 6.2). These are based on GRACE level-2 RL04 data generated at CSR University of Texas,

Austin. The GRACE data, provided as monthly fully normalized spherical harmonic coefficients sets of the Earth's gravitational potential (Stokes coefficients), have been converted into surface mass changes according to the procedure of Wahr et al. (1998) as described in Chapter 4. In order to suppress high-frequency noise and remove correlated errors, respectively, Gaussian isotropic smoothing with a smoothing radius of $r_g = 500$ km and spectral domain filtering according to Swenson and Wahr (2006) have been applied. This ensures that the input masses used are rather smooth and not contaminated by higher frequency errors that are not further considered in this study. However, as will be seen below, the input masses still contain smaller higher-frequency undulations that are considered as not critical for the results obtained. Moreover it should be mentioned that the use of Gaussian smoothing to derive the simulated input masses is not considered critical as the main focus in this study is on the influence of irregularly shaped masses, e.g., mass distributions with a spatially varying jump discontinuity of the same height.

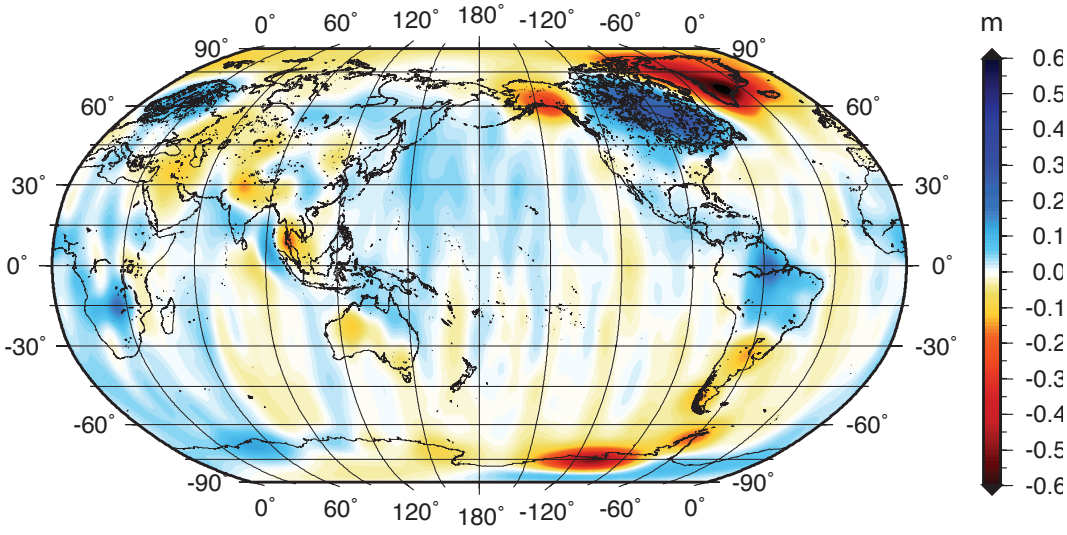

Figure 6.2: Global distribution of mass changes derived from 8 years of GRACE gravity data (2002-2010) transformed into equivalent water height (ewh), showing regions of major mass changes.

Figure 6.2 illustrates the global distribution of mass changes within 8 years used to extract input mass changes for this study. The mass changes are expressed as equivalent water heights (ewh) which is the mass divided by the density of water (e.g., 1,000 kg/m3). The selection of regions is based on the magnitude of the mass changes as to select regions that exhibit largest contemporary mass changes in the cryosphere and hydrosphere (e.g., Anjasmara and Kuhn, 2010; Baur et al., 2012). The spatial extents of the corresponding mass changes have been defined by the ±0.1 m isoline of the equivalent water height and are illustrated in Figure 6.3. Mass changes related to isostatic rebound over North America and Fennoscandia have not been included in this study but mass changes related to the 2004 Sumatra-Andaman earthquake are included. This leads to the following six regions considered:

(1) Alaska - ice mass change
(2) Greenland - ice mass change
(3) Amazon - land hydrology
(4) West Antarctica - ice mass change
(5) Sumatra-Andaman - earthquake
(6) Lake Victoria - land hydrology

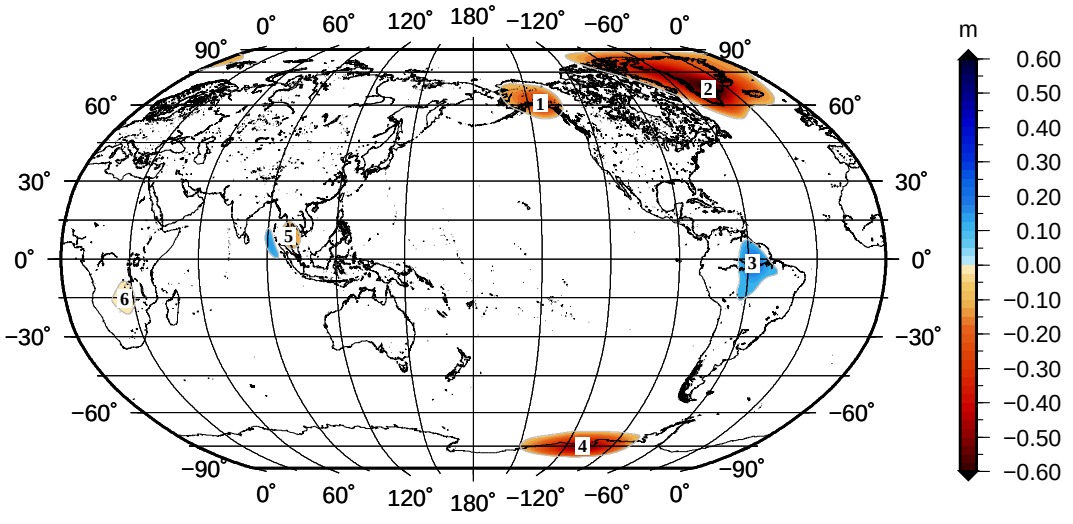

Figure 6.3: Significant mass changes (|equivalent water height| > 0.1 m) highlighted from Figure 6.2.

6.3 Validation Results

This Section provides all validation results obtained for the simulated masses described in the previous Section. Each mass change is used as input mass for the validation procedure described in Section 6.1. Within the validation procedure the masses are subject to the following four smoothing scenarios (see Appendix B for complete overview):

(1) No smoothing
(2) Gaussian isotropic smoothing with smoothing radius of $r_g = 250$ km
(3) Han's anisotropic smoothing with smoothing radii r_0=250 km, r_1=500 km
(4) Kusche's de-correlated anisotropic smoothing with DDK3 filter

The validation results are mostly analysed with respect to properties of the recovered mass distributions. Particular focus is on the spatial distribution (shape) of the recovered mass.

6.3.1 Validation over Alaska

Here, the validation results are obtained by using simulated ice mass changes over Alaska. Figure 6.4 shows the initial mass changes used as input mass for the validation. This simulates wide-spread ice mass loss over Alaska with maximum negative changes of more than 0.3 m (ewh) over the Alaskan glacier region close to the south coast. The total mass change over this area has been set to -372.106 Gt (see Table 6.1). Figure 6.5 illustrates the shape of the input mass distribution and the corresponding recovered mass distribution after application of the smoothing filters considered. The (vertical) shape is illustrated by cross-sections in west-east and south-north direction through the maximum of the mass distribution. Note the small higher-frequency undulations on the original mass which are due to the derivation of the mass from original GRACE data.

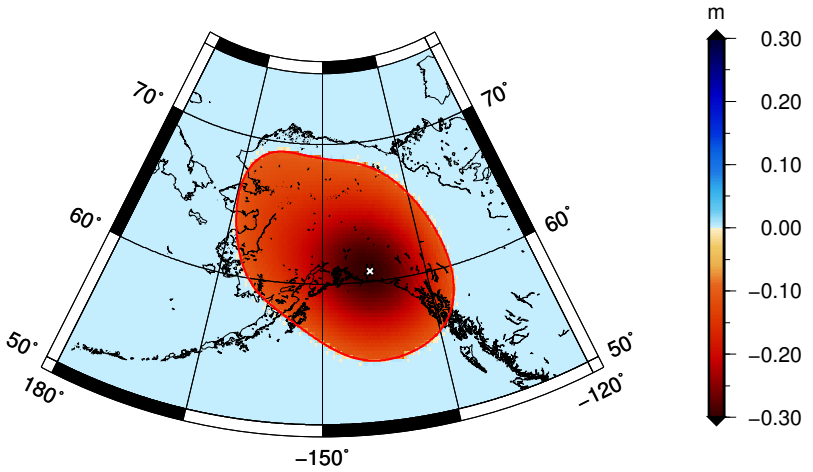

Figure 6.4: Initial mass change over Alaska. The maximum mass change is centred at $\phi = 60.750°$, $\lambda = 217.000°$ (white cross).

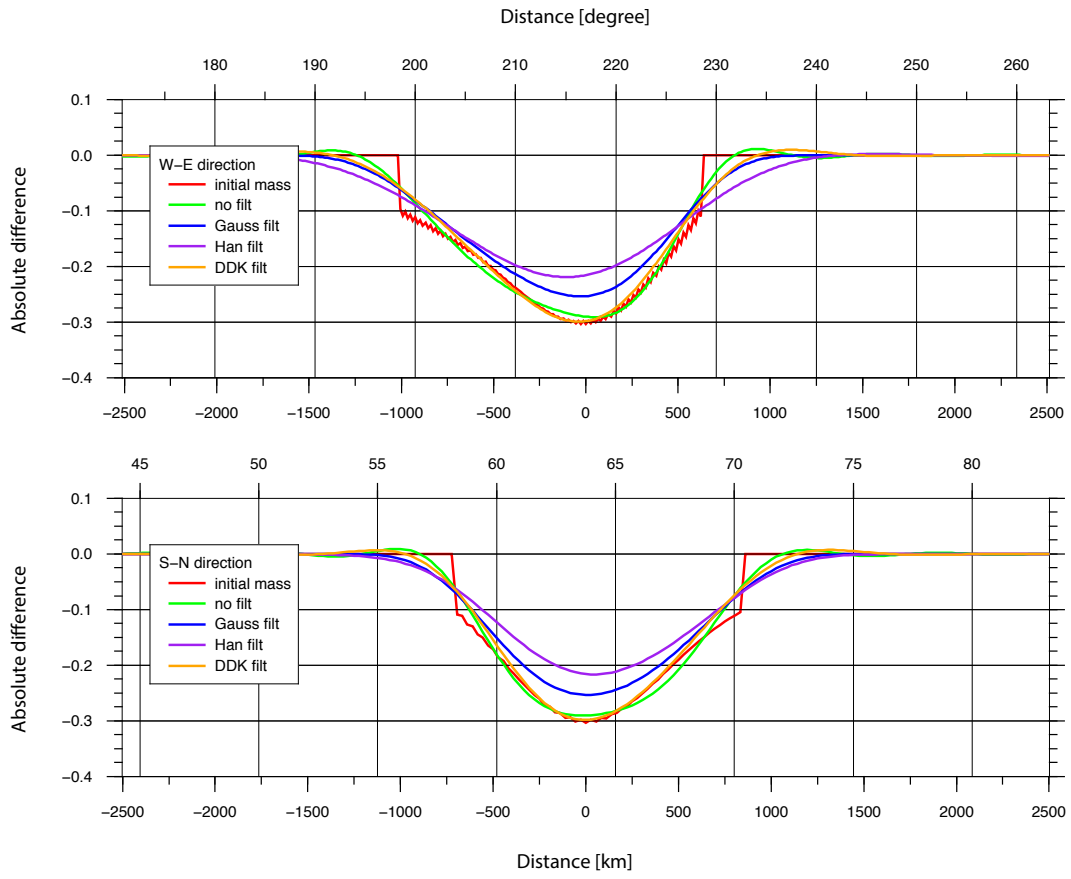

Figure 6.5: Cross-sections of input and recovered masses over Alaska. The smoothing radius for the Gaussian filter is r_g=250 km. Parameters for Han's anisotropic filter are r_0=250 km, r_1=500 km. For de-correlation smoothing, DDK3 is used.

Results for no filter

In this case, no filter has been applied, thus any differences in the recovered mas distribution with respect to the input mass distribution are due to spectral leakage. The recovered mass distribution, illustrated in Figure 6.6, shows a small band around the original mass distribution indicating some mass has leaked outside the spatial extent of the input mass. This area of leakage follows approximately the original -0.1 m isoline and has everywhere the same thickness. This indicates that spectral leakage largely follows the shape of the input mass. Overall, 95.3% of the original mass has been recovered, thus 4.7% of the mass has leaked outside, which is attributed to spectral leakage only.

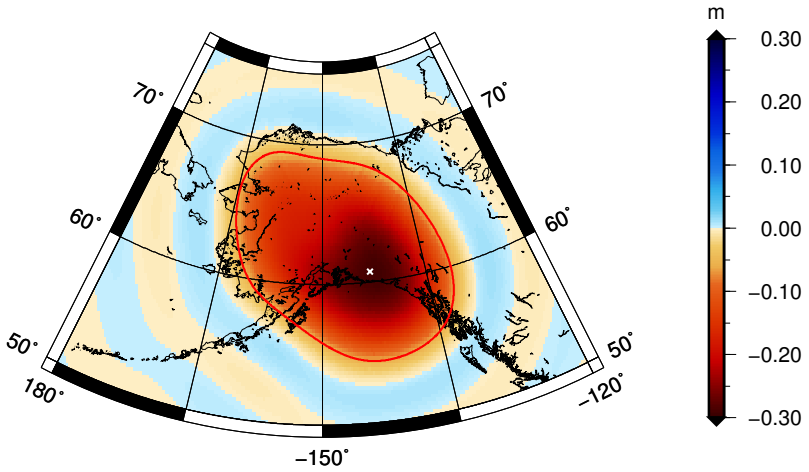

Figure 6.6: Recovered mass over Alaska with no filter applied. The maximum mass change is centred at $\phi = 60.750°$, $\lambda = 217.000°$ (white cross).

Gaussian Isotropic Filter with r_g = 250 km

This validation is based on Gaussian isotropic smoothing with the soothing radius of $r_g = 250$ km. Now the recovered mass distribution illustrated in Figure 6.7 shows much increased leakage around the original mass. This is documented by an increased mass loss when compared to the previous scenario without smoothing. For this scenario only 83.8% of the total mass has been recovered, thus 16.2% of the total mass has leaked outside (see Table 6.1). Considering the same spectral

leakage as in the previous case, spatial leakage accounts for 11.5%, which is due to the smoothing introduced. Apart from increased leakage the recovered mass distribution follows slightly different isolines, e.g., the original -0.1 m isoline does not follow an isoline in the recovered mass distribution. This indicates areas of larger and smaller leakage. For example, it can be seen that leakage is slightly larger towards the east and smaller towards the north-west. This is directly related to the gradient of the original mass, which is much larger towards the east and rather flat towards the north-west.

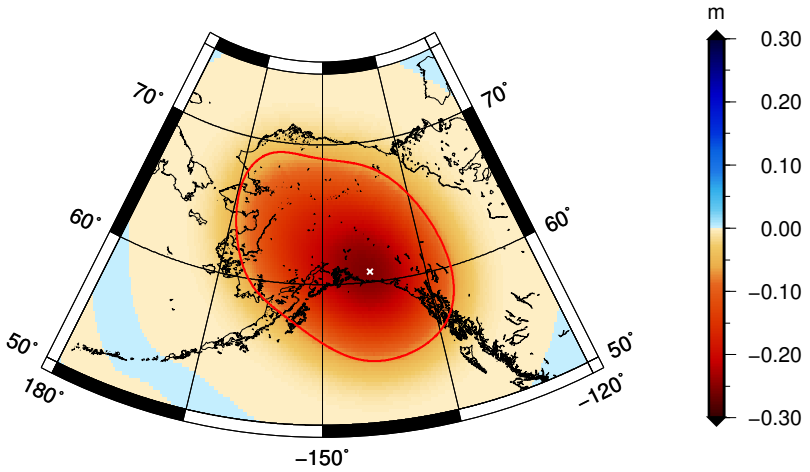

Figure 6.7: Recovered mass over Alaska with Gaussian filter (r_g=250 km). The maximum mass change is centred at $\phi = 60.750°$, $\lambda = 217.000°$ (white cross).

Han's anisotropic filter with r_0=250 km and r_1=500 km

Instead of isotropic filter, this validation is based on Han's anisotropic smoothing with the smoothing radii of r_0= 250 km and r_1 = 500 km. For anisotropic smoothing the asymmetric leakage pattern becomes more visible in the recovered mass distribution as illustrated in Figure 6.8. Leakage is increased in west-east direction as expected for an anisotropic filter. It is now well visible that the recovered mass distribution does not follow anymore the shape of the input mass. Like before, the original -0.1 m isoline does not follow an isoline of the recovered mass distribution. Again maximum leakage effects are towards the east as a result of both increased smoothing and being the area with the highest gradient in the

original mass distribution. The total mass recovered is 76.8% while 18.6% of the mass loss is due to spatial leakage (see Table 6.1).

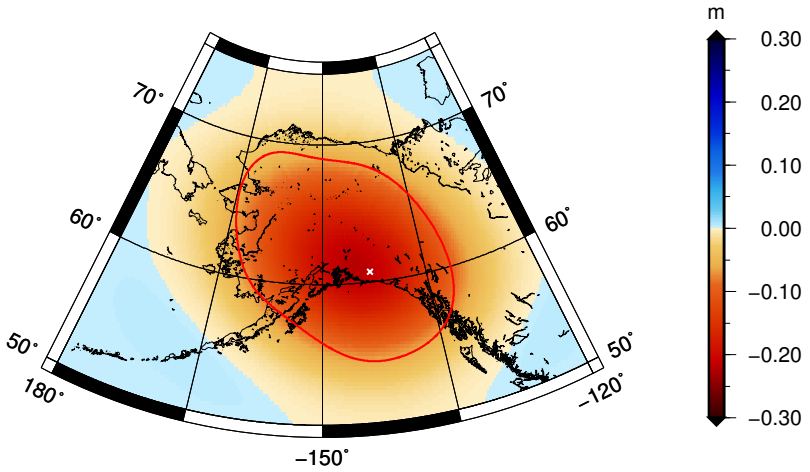

Figure 6.8: Recovered mass over Alaska with Han's anisotropic filter (r_0=250 km, r_1=500 km, m_1=15). The maximum mass change is centred at $\phi = 60.750°$, $\lambda = 217.000°$ (white cross).

Kusche's de-correlated anisotropic filter with DDK3

The last validation considered here is based on Kusche's de-correlated anisotropic smoothing filter DDK3. The recovered mass distribution is illustrated in Figure 6.9. While the area around the original mass influenced by leakage has a similar extension as for Han's anisotropic smoothing the magnitude of the leakage signal is considerably reduced. This is confirmed by 92.0% of the total mass recovered being the highest rate of the three smoothing filters considered (see Table 6.1). In this scenario spatial leakage accounts for only 3.3%. While having a higher recovery rate than for the anisotropic smoothing scenario there is still higher leakage visible towards the east and less leakage towards the north-west. The recovered mass distribution also shows some undulating pattern outside the initial mass, which is not present for the other filters analysed, though it is generally present for all filters when applying weak smoothing (see Appendix B).

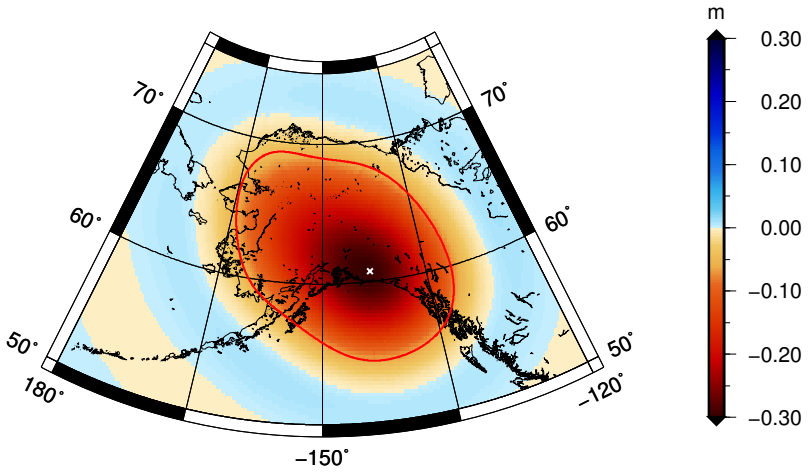

Figure 6.9: Recovered mass over Alaska with Kusche's de-correlated anisotropic filter DDK3. The maximum mass change is centred at $\phi = 60.750°$, $\lambda = 217.000°$ (white cross).

6.3.2 Validation over Greenland

Another scenario of simulated ice mass change is provided by validation results when using simulated ice mass changes over Greenland. Figure 6.10 shows the initial mass changes used as input mass for the validation. Like before, the mass distribution has been obtained from the GRACE-derived mass changes (see Figure 6.1) by extracting all masses contained within the isoline of -0.1 m equivalent water height. This simulates wide-spread ice mass loss over Greenland and Iceland with maximum negative changes of -0.63 m (ewh) close to the south-east coast. With -2,146.6 Gt mass loss, this is the region that has the highest mass change considered in this study (see Table 6.1). Cross-sections in west-east and south-north directions through the maximum of the mass distribution are illustrated in Figure 6.11 and superimposed on the corresponding mass distribution obtained when applying the filter considered. It can be seen that the shape of the filter can almost perfectly match the shape of the input mass (except the edges). Note the small higher-frequency undulations on the original mass distribution which are due to the derivation of the mass from original GRACE data.

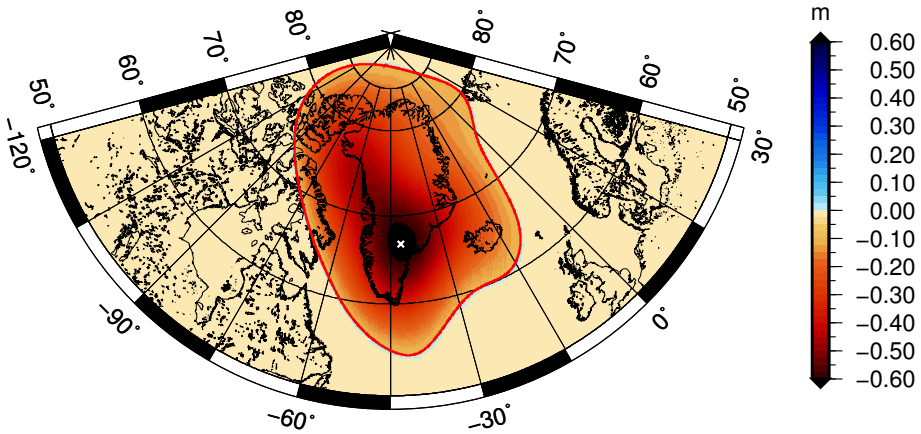

Figure 6.10: Initial mass over Greenland. The maximum mass change is centred at $\phi = 66.750°$, $\lambda = 318.000°$ (white cross).

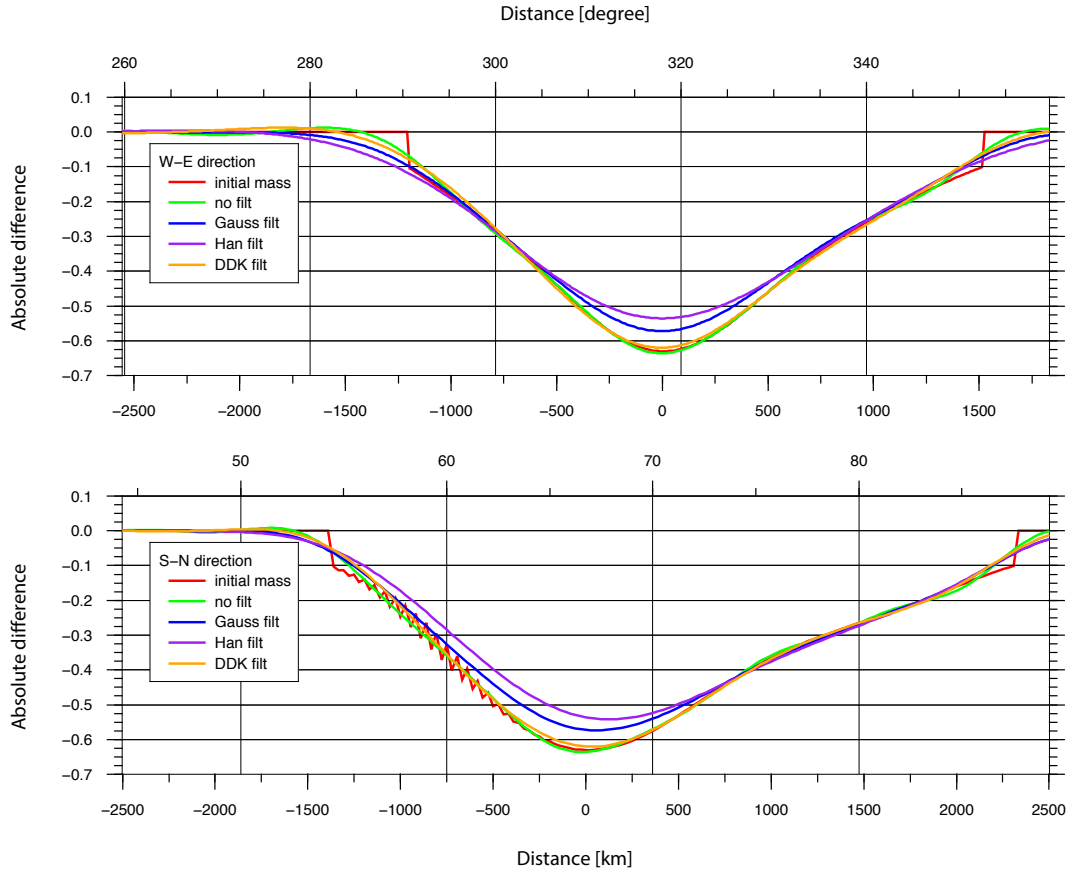

Figure 6.11: Cross-sections of masses over Greenland with different smoothing methods applied. The smoothing radius for Gaussian filter is r_g=250 km. Parameters for Han's anisotropic filter are r_0=250 km, r_1=500 km. For de-correlation anisotropic smoothing, DDK3 is used.

Result for no filter

Like over Alaska, a small band of leakage is visible in the recovered mass distribution (see Figure 6.12) when no smoothing is considered. The band has the same width and follows the -0.1 m isoline of the original mass. The rather small band indicates that most of the mass is recovered, which is confirmed by Table 6.1 indicating that 98.4% of the total mass has been recovered, thus spectral leakage accounts for only 1.6%. The reason for this is the relatively small jump discontinuity (with respect to the magnitude of the signal) and the gradual change of the mass from its edges to the centre. Such a shape can be expressed by a band-limited spherical harmonic expansion with only minimum approximation error as seen in Figure 6.10.

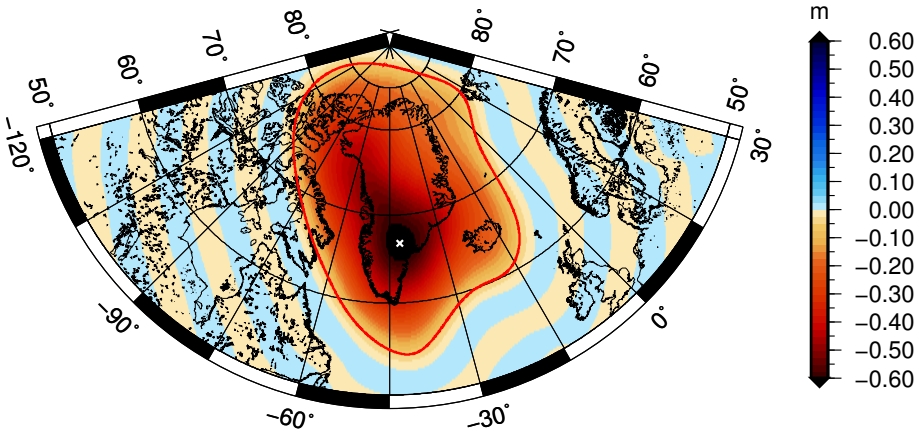

Figure 6.12: Recovered mass over Greenland with no filter applied. The maximum mass change is centred at $\phi = 66.750°$, $\lambda = 318.000°$ (white cross).

Gaussian isotropic filter with $r_g = 250$ km

Using Gaussian isotropic smoothing with the smoothing radius of $r_g = 250$ km slightly increases leakage (see Figure 6.13) with respect to the previous scenario when no smoothing has been applied. Figure 6.13 shows that the leakage band around the input mass has widened. This is also documented by a decrease in total mass recovered reaching a level of 94.1% with spatial leakage accounting for 4.3% (see Table 6.1). Like for the scenario over Alaska, the recovered mass

distribution starts to deviate from the original shape of the input mass. The new isolines do not follow exactly those of the input mass most noticeably visible by the -0.1 m isoline indicating the extension of the input mass. Areas of slightly larger leakage are present on the western and eastern side while leakage is smaller in south-north direction. This is an artefact of the mass distribution's shape that is more elongated in south-north than west-east, thus having larger gradients in west-east direction.

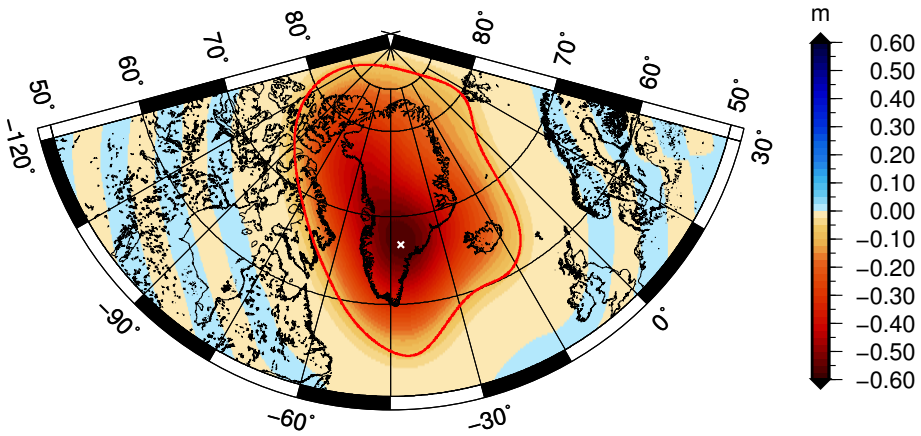

Figure 6.13: Recovered mass over Greenland with Gaussian filter (r_g=250 km). The maximum mass change is centred at $\phi = 66.750°$, $\lambda = 318.000°$ (white cross).

Han's anisotropic filter with r_0=250 km and r_1=500 km

The use of Han's anisotropic smoothing filter with the smoothing radii of r_0=250 km and r_1=500 km further increases leakage in west-east direction when compared to Gaussian isotropic smoothing in the previous scenario. This can be seen in Figure 6.14 showing mostly increased leakage at the western and eastern side of the input mass. This is now the combined effect of the increased smoothing radius in west-east and higher gradients of the mass in the same direction. Furthermore, this behaviour is visible by the increased deviation of the isolines of the recovered mass distribution with respect to that of the input mass, most noticeably for the -0.1 m isoline that indicates the spatial limit of the input mass. The increased leakage is also documented in Table 6.1 with the total mass recovered being 92.5% with 5.9% of the mass loss due to spatial leakage.

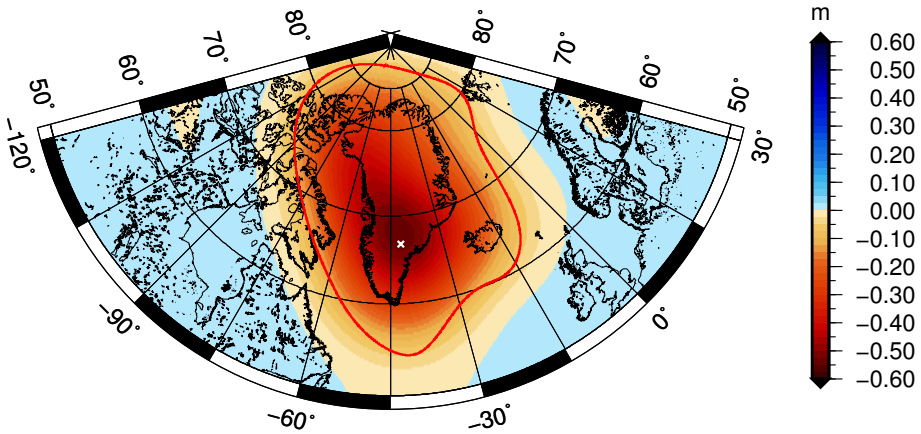

Figure 6.14: Recovered mass over Greenland with Han's anisotropic filter (r_0=250 km, r_1=500 km, m_1=15). The maximum mass change is centred at $\phi = 66.750°$, $\lambda = 318.000°$ (white cross).

Kusche's de-correlated anisotropic filter with DDK3

Figure 6.15 shows the recovered mass distribution when applying Kusche's de-correlated anisotropic smoothing filter DDK3. Similar as for the scenario over Alaska, there is a considerable spatial extent of leakage but with rather low magnitude. This can also be seen in Table 6.1 where the total recovered mass with 97.5% is similar to the case without smoothing, thus spatial leakage is only 0.9%. Even much smaller, this scenario still shows a slight difference in leakage between west-east and south-north. Like for the scenario over Alaska, the recovered mass distribution also shows some undulating pattern outside the initial mass, which is not present for the other analysed filter, though it is generally present for all filters when applying weak smoothing (see Appendix B).

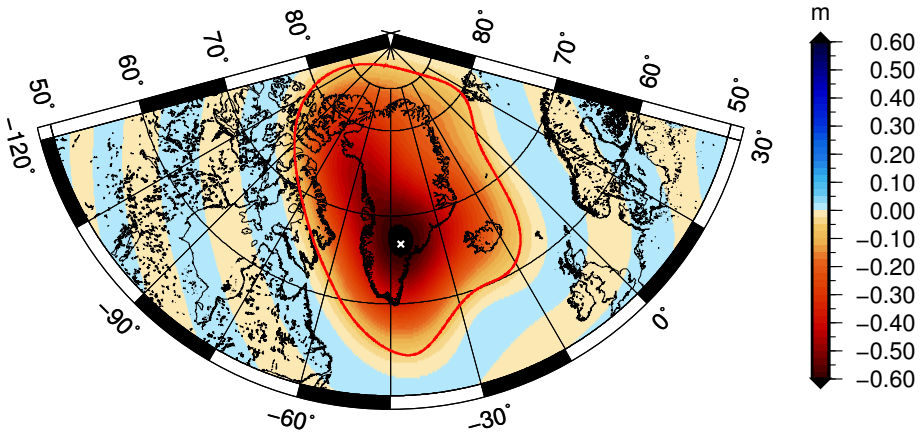

Figure 6.15: Recovered mass over Greenland with de-correlated filter DDK3. The maximum mass change is centred at $\phi = 66.750°$, $\lambda = 318.000°$ (white cross).

6.3.3 Validation over the Amazon Basin

In this section, the validation analyses hydrological changes over parts of the Amazon basin. The initial mass change considered is illustrated in Figure 6.16, which forms the input mass change for the validation. The mass change only covers part of the Amazon basin with maximum changes approximately in the centre of the basin. This simulates some extended mass change over parts of the Amazon basin with maximum changes of 0.2 m ewh. This mass change has a variation between 0.1 m and 0.2 m ewh, thus is rather flat and comparable to a disc with constant height, though with irregular edge. The total mass change over this area has been estimated with 396.9 Gt (see Table 6.1). Figure 6.17 illustrates cross-sections in west-east and south-north direction through the maximum of the mass distribution superimposed on the corresponding recovered mass distribution. It can be noticed that the recovered mass distribution does not match the shape of the input mass as well as in the previous scenario for Greenland.

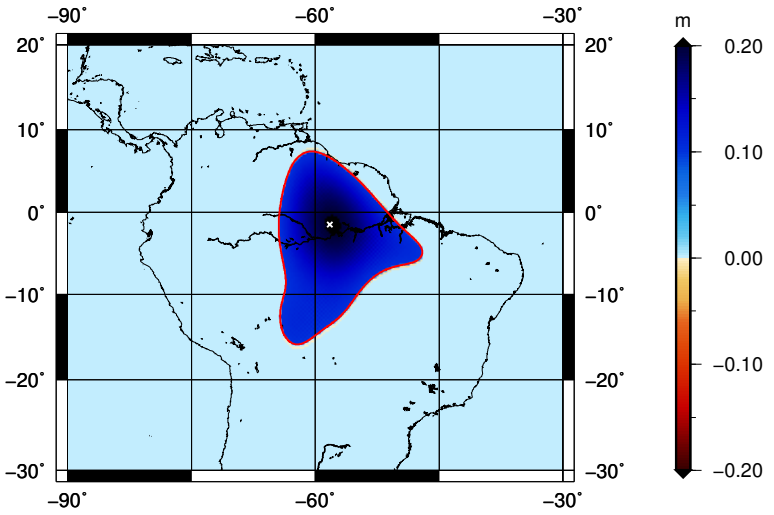

Figure 6.16: Initial mass over the Amazon Basin. The maximum mass change is centred at $\phi = -1.500°$, $\lambda = 301.750°$ (white cross).

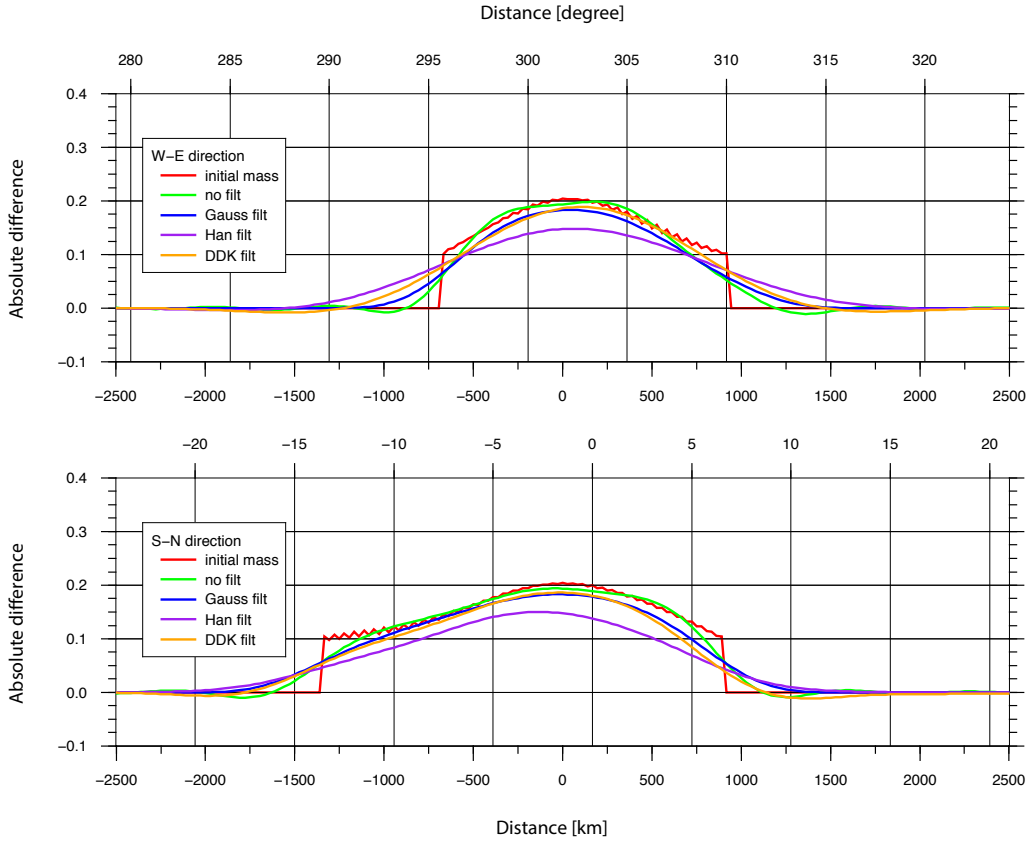

Figure 6.17: Cross-sections of masses over the Amazon Basin with different smoothing methods applied. The smoothing radius for Gaussian filter is r_g=250 km. Parameters for Han's anisotropic filter are r_0=250 km, r_1=500 km. For de-correlation anisotropic smoothing, DDK3 is used.

Result for no filter

Again a small band around the input mass is visible (see Figure 6.18) indicating the effect of spectral leakage when no smoothing filter has been applied. This is rather small but largely follows the original 0.1 m isoline, though with varying thickness. Also visible in Figure 6.18 is the typical Gibbs phenomenon showing as undulating pattern outside the input mass. This is largely due to the fact that the initial mass change has a plateau like shape, thus the jump discontinuity produces a more pronounced Gibbs effects (as is the case for disc masses). According to Table 6.1, 95.0% of the total mass has been recovered, thus spectral leakage is 5.0%.

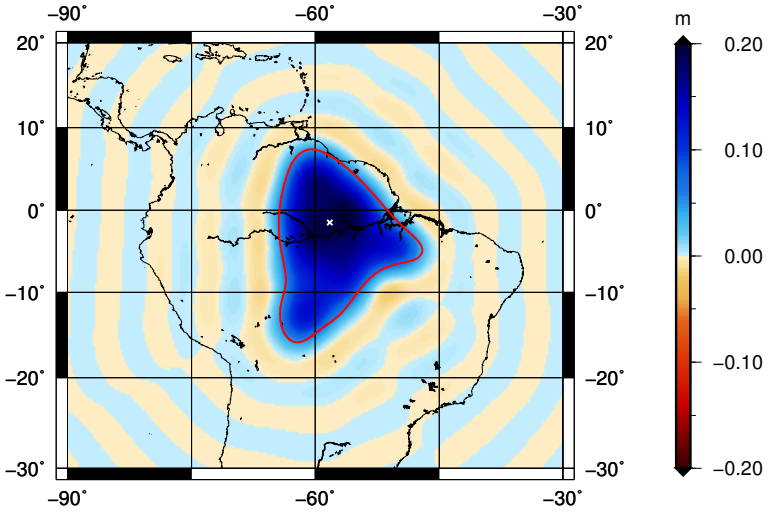

Figure 6.18: Recovered mass over the Amazon Basin with no smoothing applied. The maximum mass change is centred at $\phi = -1.500°$, $\lambda = 301.750°$ (white cross).

Gaussian isotropic filter with $r_g = 250$ km

Applying Gaussian isotropic smoothing with the smoothing radius of $r_g = 250$ km results in stronger leakage as illustrated in Figure 6.19 showing a larger region around the input mass that is affected by leakage. Due to the more irregular shape of the input mass, the shape of the recovered mass shows some larger differences to the input mass, most notably by variations to the 0.1 m isoline of

the input mass (e.g., at the most eastern and southern extent). In this scenario 83.8% of the total mass has been recovered with 11.1% of the mass loss due to spatial leakage (see Table 6.1). Also visible for Gaussian isotropic smoothing is the undulation pattern outside the input mass, though slightly disturbed closer to the input mass.

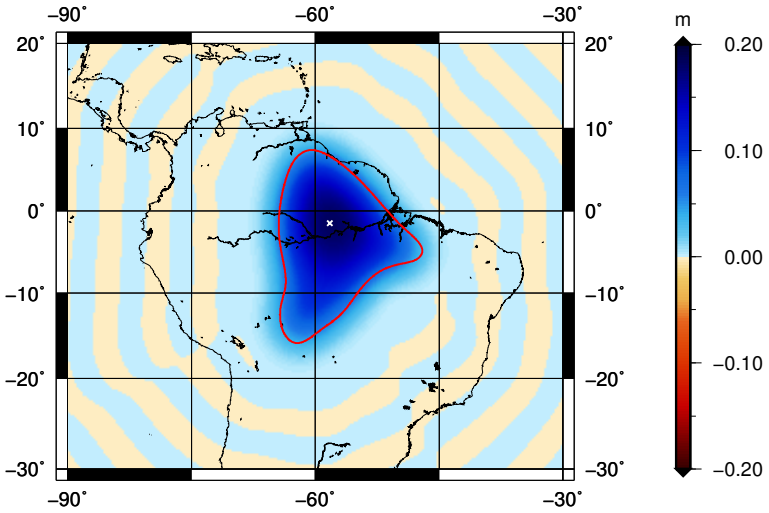

Figure 6.19: Recovered mass over the Amazon Basin with Gaussian filter (r_g=250 km). The maximum mass change is centred at $\phi = -1.500°$, $\lambda = 301.750°$ (white cross).

Han's anisotropic filter with r_0=250 km and r_1=500 km

Applying Han's anisotropic smoothing with the smoothing radii of r_0=250 km and r_1=500 km results in a recovered mass distribution that shows a considerably different shape compared to the input mass (see Figure 6.20). It is noticeable in Figure 6.20 that the recovered mass distribution is less irregular than the input mass and follows more a circular shape, thus sharper bends have been smoothed out. This is in part also due to the anisotropic smoothing filter that changes the input mass which is slightly more elongated in south-north direction into a shape that is elongated more in west-east direction. Furthermore, the undulating pattern around the input mass is considerably disturbed. The total mass recovered is 70.2% with 24.8% of the mass loss due to spatial leakage (see Table 6.1).

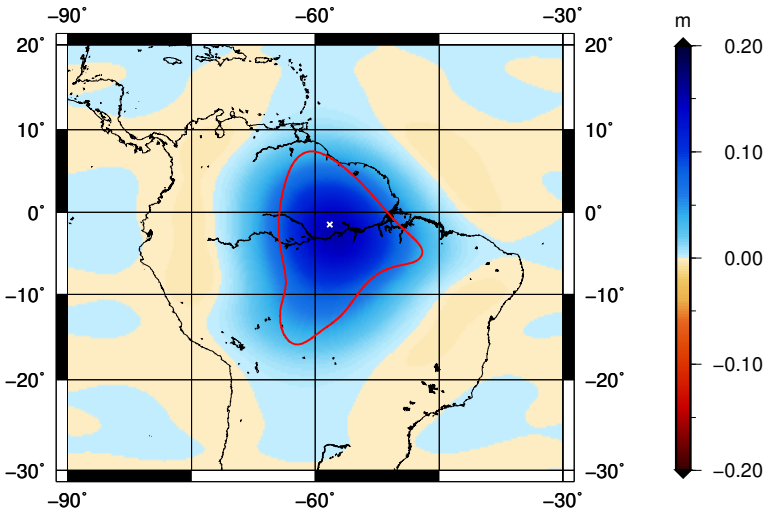

Figure 6.20: Recovered mass over the Amazon Basin with Han's anisotropic filter (r_0=250 km, r_1=500 km, m_1=15). The maximum mass change is centred at $\phi = -1.500°$, $\lambda = 301.750°$ (white cross).

Kusche's de-correlated anisotropic filter with DDK3

Figure 6.21 illustrates the recovered mass distribution when applying Kusche's de-correlated anisotropic smoothing filter DDK3. When compared to the result obtained for Han's anisotropic smoothing the recovered mass distribution illustrated in Figure 6.21 shows a much better resemblance of the input mass shape. However, the zone around the input mass impacted by leakage is slightly larger. Moreover, the area shows anisotropy in that it is larger in west-east than south-north direction. In this scenario the undulating pattern around the initial mass has changed to south-north orientated undulations. The total mass recovered is 84.3%, slightly more than for Gaussian isotropic smoothing. Spectral leakage accounts for 10.7% of the total mass loss (see Table 6.1).

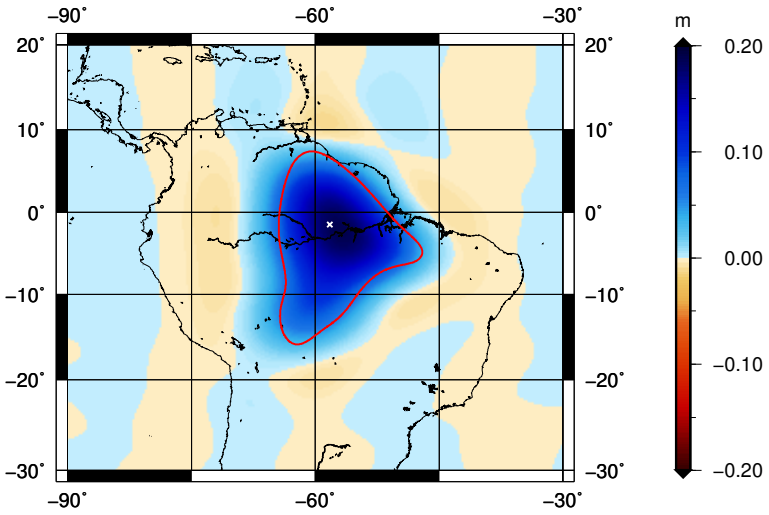

Figure 6.21: Recovered mass over the Amazon Basin with de-correlated filter DDK3. The maximum mass change is centred at $\phi = -1.500°$, $\lambda = 301.750°$ (white cross).

6.3.4 Validation over West-Antarctica

This section provides the validation results obtained for simulated ice mass changes over West-Antarctica. Figure 6.22 shows the initial mass changes used as input mass for the validation which simulates wide-spread ice mass loss along the coast of West-Antarctica with maximum negative changes of -0.51 m ewh, close to the coast of the Amundsen Sea. The total mass change over this area has been estimated to -600.9 Mt (see Table 6.1). Figure 6.22 illustrates the shape of the input mass distribution and the results for the corresponding filters used. The shape is given by cross-sections in west-east and south-north direction through the maximum of the mass distribution superimposed on the corresponding recovered mass distributions. Again it can be noticed that the filters do not match the shape of the input mass as well as for the scenario over Greenland.

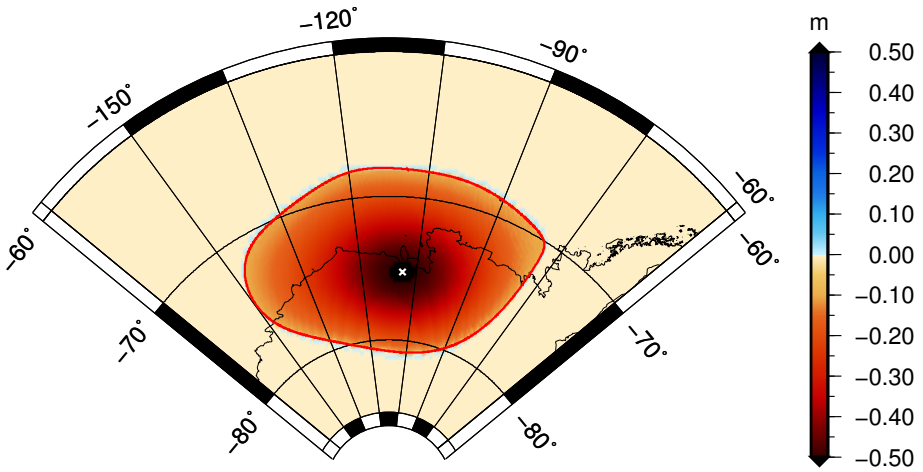

Figure 6.22: Initial mass over West Antarctica. The maximum mass change is centred at $\phi = -75.250°$, $\lambda = 251.250°$ (white cross).

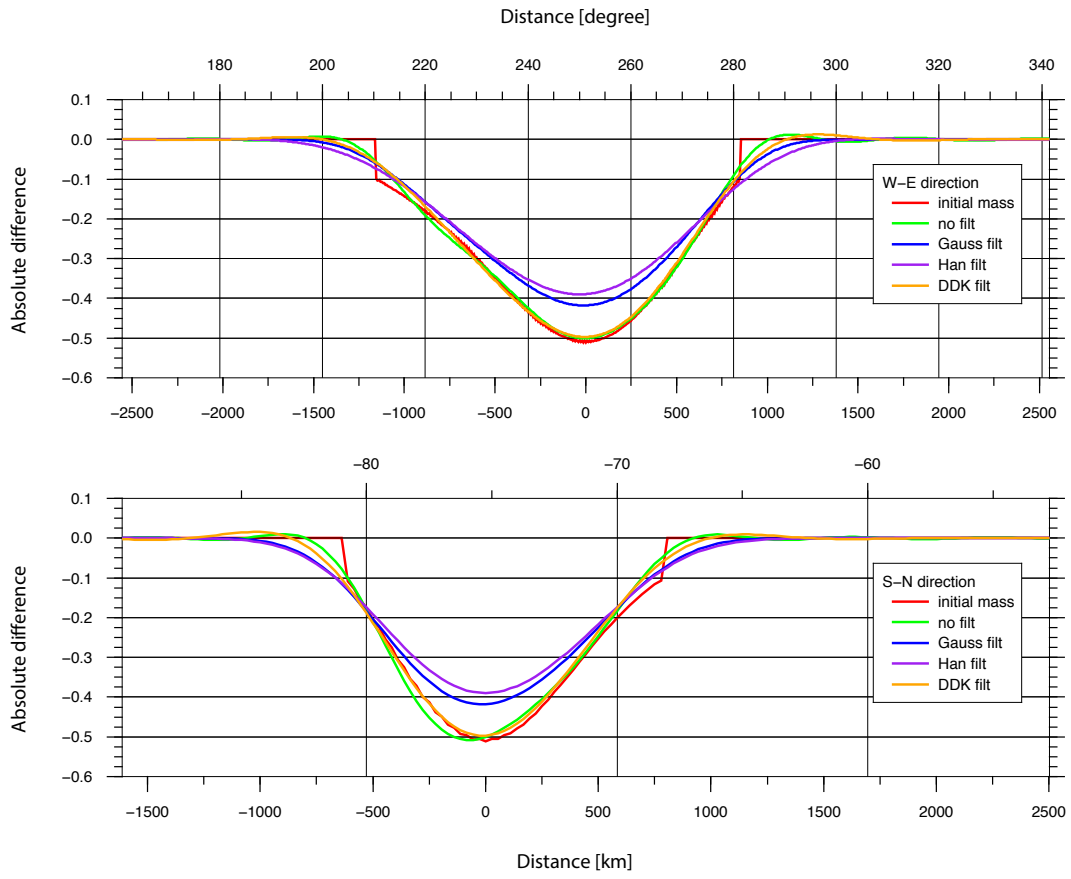

Figure 6.23: Cross-sections of masses over West Antarctica with different smoothing methods applied. The smoothing radius for Gaussian filter is r_g=250 km. Parameters for Han's anisotropic filter are r_0=250 km, r_1=500 km. For de-correlation anisotropic smoothing, DDK3 is used.

Results for no filter

Like over Alaska and Greenland, a small band of leakage is visible in the recovered mass distribution (see Figure 6.24) when no smoothing is considered. However, the band is larger in the southern part at higher southern latitude and smaller in the northern part at lower southern latitude while the west-east extension seems to be balanced. Being similar for the results of a disc mass at high southern latitude (Figure A.10), this may be an artefact of the meridian convergence for locations at high geographic latitude (see Appendix A.2). Table 6.1 shows the total mass recovered as 95.5%, thus spectral leakage accounts for 4.5%.

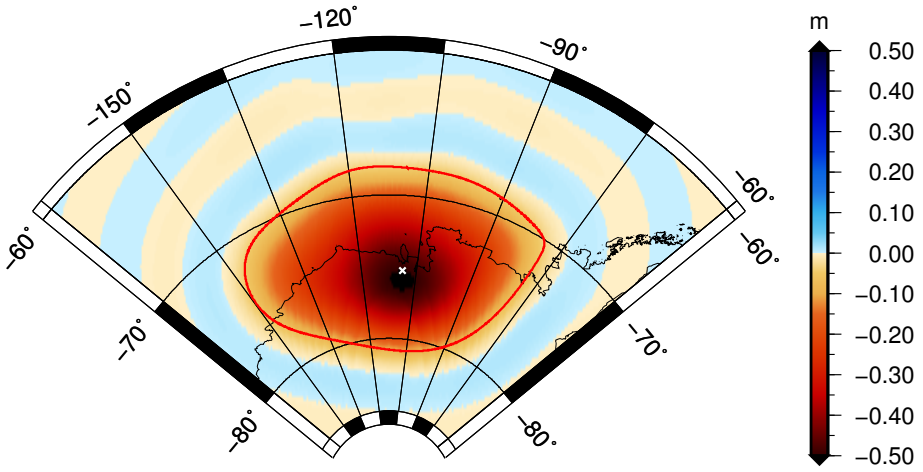

Figure 6.24: Recovered mass over West Antarctica with no smoothing applied. The maximum mass change is centred at $\phi = -75.250°$, $\lambda = 251.250°$ (white cross).

Gaussian isotropic filter with $r_g = 250$ km

Using Gaussian isotropic smoothing with the smoothing radius of $r_g = 250$ km considerably increases the leakage affected area with respect to the previous scenario when no smoothing has been applied as can be seen in Figure 6.25. Like in the previous scenario, there is still some imbalance between the leakage-affected area at the southern and northern end while it is rather balanced in west-east direction. The increased leakage is also documented in a decrease of the total

recovered mass. Table 6.1 shows that 85.8% of the total mass is recovered and 11.1% of the mass lost is due to spatial leakage.

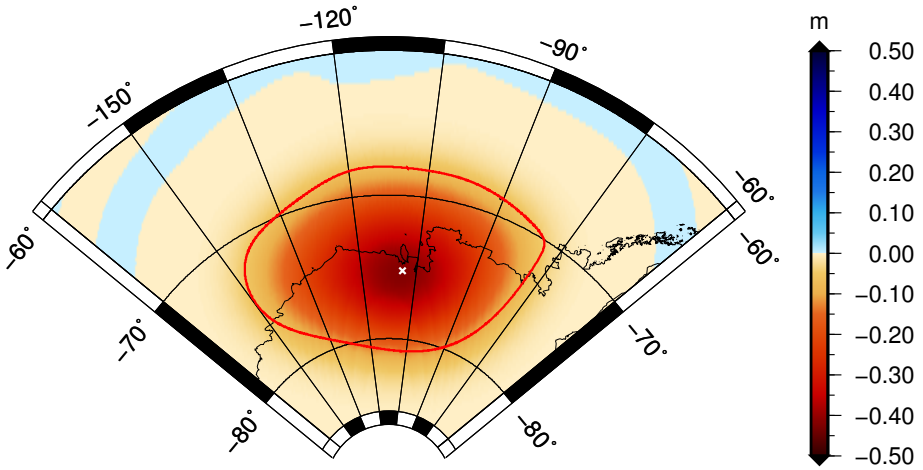

Figure 6.25: Recovered mass over West Antarctica with Gaussian filter (r_g=250 km). The maximum mass change is centred at $\phi = -75.250°$, $\lambda = 251.250°$ (white cross).

Results for Han's anisotropic filter with r_0=250 km and r_1=500 km

In this validation, the use of Han's anisotropic smoothing filter with the smoothing radii of r_0=250 km and r_1=500 km only marginally increases leakage in west-east direction and imbalance in south-north directions remained when compared to Gaussian isotropic smoothing in the previous scenario (see Figure 6.26). Therefore, an increased effect due to the meridian convergence can partly cancel the impact if increased smoothing in west-east direction. According to Table 6.1 the total recovered mass is 83.4% with 12.0% of the mass loss due to spatial leakage.

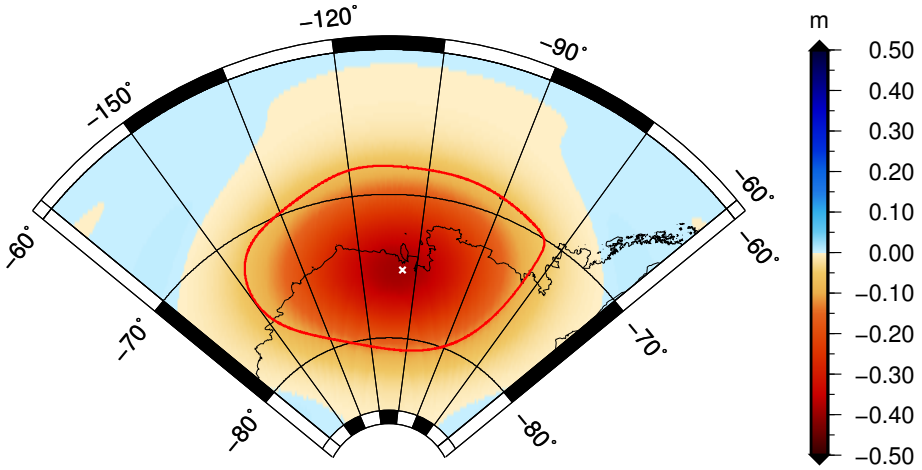

Figure 6.26: Recovered mass over West Antarctica with Han's anisotropic filter (r_0=250 km, r_1=500 km, m_1=15). The maximum mass change is centred at $\phi = -75.250°$, $\lambda = 251.250°$ (white cross).

Kusche's de-correlated anisotropic filter with DDK3

Again, the application of Kusche's de-correlated anisotropic smoothing filter DDK3 results in a rather regular leakage pattern that largely follows the shape of the input. Interestingly, the imbalance in south-north direction present in the previous scenarios has vanished as shown in Figure 6.27. In this case Kusche's de-correlated anisotropic smoothing filter DDK3 introduces considerable leakage (e.g., smoothing) along the edge of the initial mass but largely keeps the shape of the input mass. However, leakage is considerable only in its spatial extent but not in terms of magnitude as confirmed by Table 6.1 showing the total mass recovered to 94.0%, thus only 1.5% of the mass loss is due to spatial leakage.

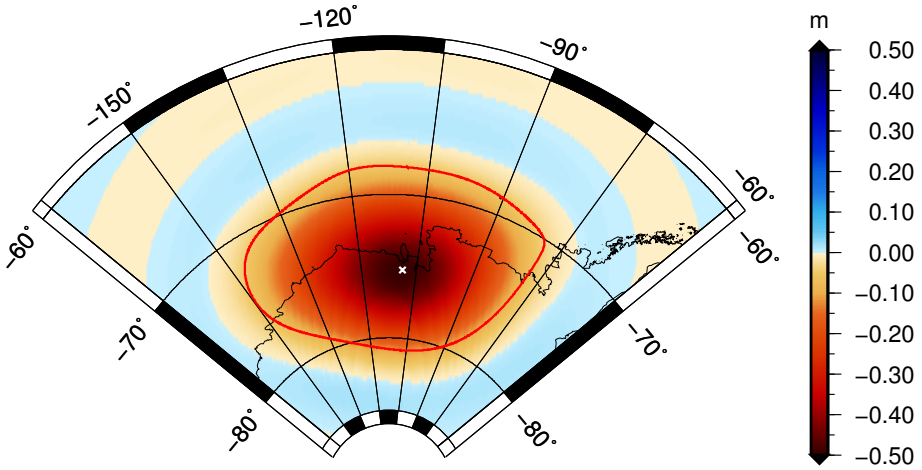

Figure 6.27: Recovered mass over West Antarctica with de-correlated anisotropic filter DDK3. The maximum mass change is centred at $\phi = -75.250°$, $\lambda = 251.250°$ (white cross).

6.3.5 Validation over Sumatra-Andaman

This validation examines mass changes of the Earth's crust as implied by the 2004 Great Sumatra-Andaman earthquake. The mass change considered contains both changes of the Earth's crust due to the earthquake and post-seismic deformations still on-going after several years (e.g., Chen et al., 2007b; Cannelli et al., 2008). The mass change considered is illustrated in Figure 6.28 and is extracted from the GRACE-derived mass changes (see Figure 6.2) by extracting all masses contained within the isolines of ±0.1 m equivalent water height. It shows the typical di-pole structure with a positive mass change over the Indian Ocean and a negative mass change over Thailand. Both mass changes are characterised by almost constant ewh values. With only -56.4 Gt the total mass change is rather small as the larger positive and negative changes partly cancel (see Table 6.1). This mass change has been included due to the following two reasons: (1) as an example of a spatially rather concentrated mass change and (2) region of positive and negative mass changes that are rather close together. Figure 6.29 illustrates cross-sections in west-east and south-north direction through the maximum of the mass distribution superimposed on the corresponding recovered mass distributions. Note that in this case the higher-frequency undulations on the input mass are more pronounced due to the smaller magnitude of the input mass.

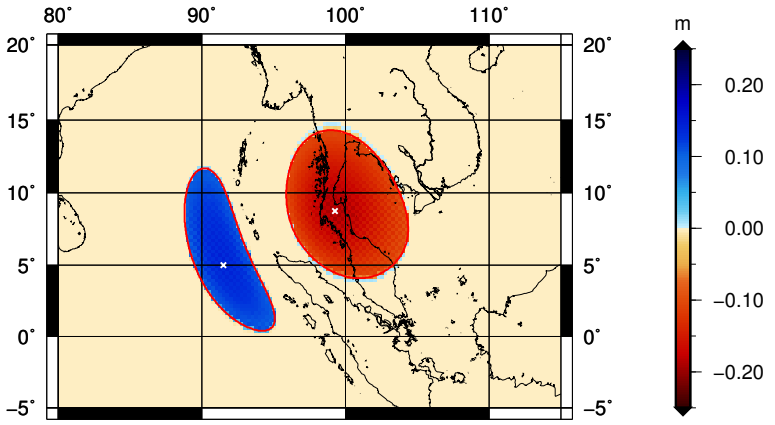

Figure 6.28: Initial mass over Sumatra-Andaman. The maximum mass changes are centred at $\phi = 5.000°$, $\lambda = 91.500°$ and $\phi = 8.750°$, $\lambda = 99.250°$, respectively (white cross).

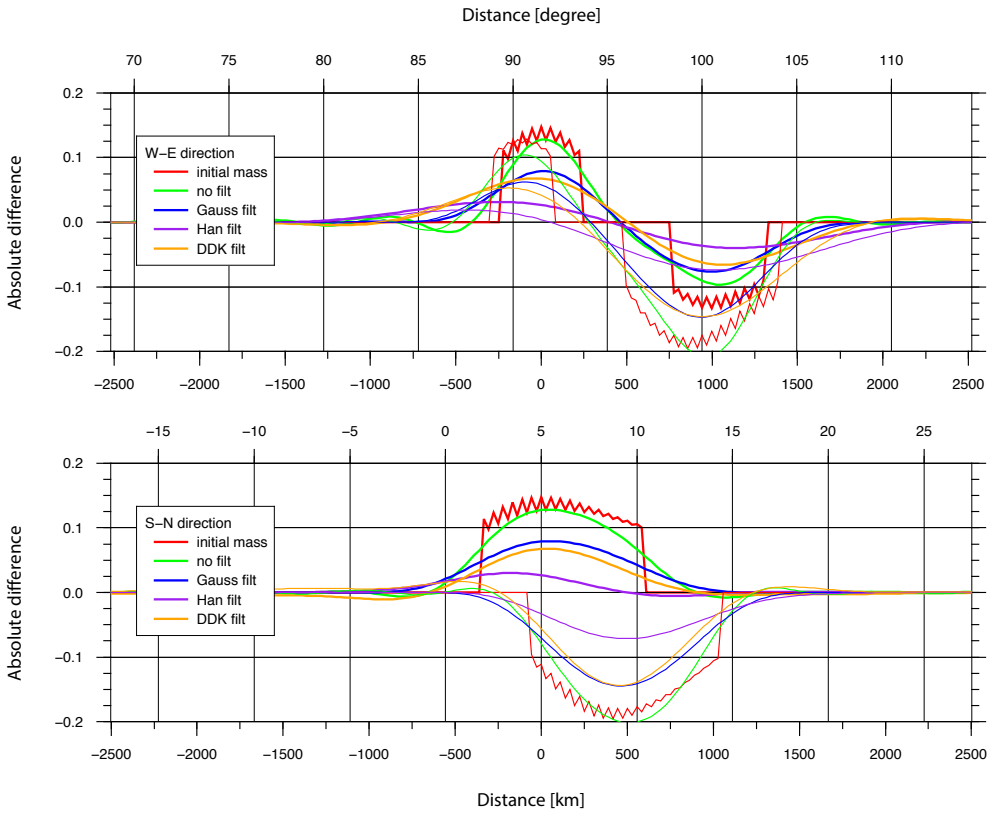

Figure 6.29: Cross-sections of masses over Sumatra-Andaman with different smoothing methods applied. Both cross-sections of the positive and negative mass changes are superimposed. The smoothing radius for Gaussian filter is r_g=250 km. Parameters for Han's anisotropic filter are r_0=250 km, r_1=500 km. For de-correlation anisotropic smoothing, DDK3 is used.

Results for no filter

First a validation without smoothing has been performed in order to estimate the impact of spectral leakage. Figure 6.30 illustrates the recovered mass distribution, which shows for both the positive and negative mass change a band around the input mass indicating the impact of spectral leakage. These bands meet approximately half-way between the two mass changes, thus partly influence each other. Gibbs effects are visible around both mass changes as an undulating pattern. The recovered mass distribution largely follows the shape of the input mass. Overall, with 101.1% more mass is recovered, again showing the impact of two mass changes with opposite sign located close together. In this case spectral leakage has to be examined separately for each mass change.

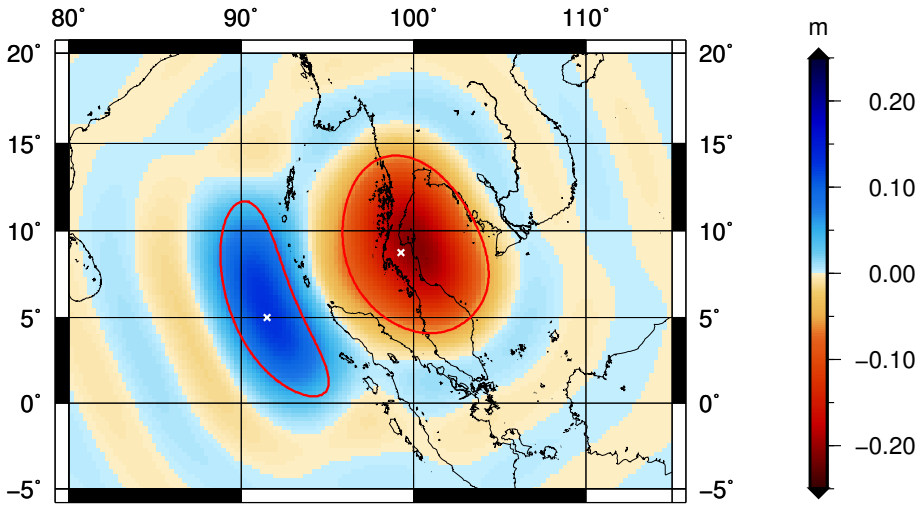

Figure 6.30: Recovered mass over Sumatra-Andaman with no smoothing applied. The maximum mass changes are centred at $\phi = 5.000°$, $\lambda = 91.500°$ and $\phi = 8.750°$, $\lambda = 99.250°$, respectively (white cross).

Gaussian isotropic filter with $r_g = 250$ km

Using Gaussian isotropic smoothing with the smoothing radius of $r_g = 250$ km results in much increased leakage around the original mass as illustrated in Figure 6.31. Around both mass change regions a large area affected by leakage is visible, which largely follows the shape of the input mass. Only between both

mass changes the general behaviour is disturbed by a clear cut between positive and negative change, thus demonstrating their influence on each other. For this scenario only 87.8% of the total mass has been recovered, however, this value has to be taken with care as the two mass changes influence each other.

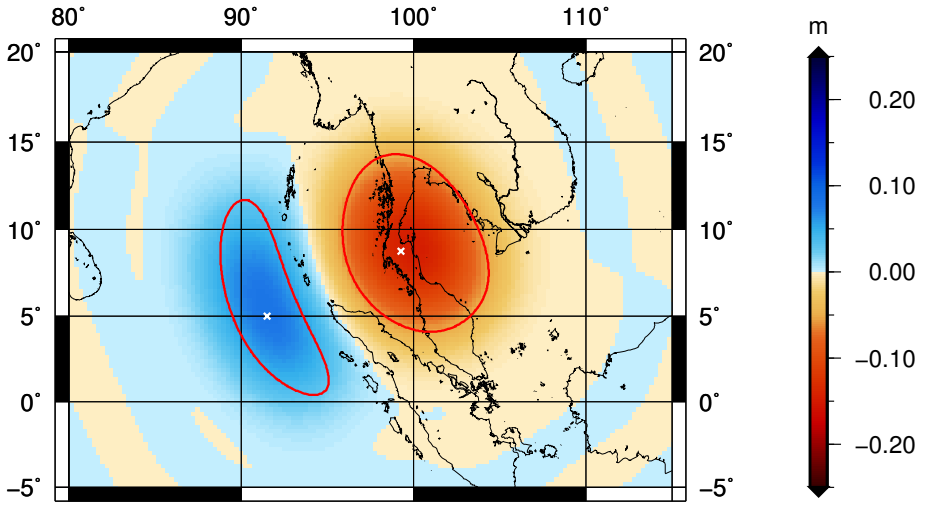

Figure 6.31: Recovered mass over Sumatra-Andaman with Gaussian filter (r_g=250 km). The maximum mass changes are centred at $\phi = 5.000°$, $\lambda = 91.500°$ and $\phi = 8.750°$, $\lambda = 99.250°$respectively. (white cross).

Han's anisotropic filter with r_0=250 km and r_1=500 km

This validation is based on Han's anisotropic smoothing with the smoothing radii of r_0=250 km and r_1=500 km. The recovered mass distribution illustrated in Figure 6.32 shows a clear anisotropic behaviour with much increased leakage in west-east direction compared to in south-north direction. Importantly, the larger negative mass change starts to dominate and partly leaks into the smaller positive mass change and the cut between positive and negative mass changes has moved close to the positive mass change. The total mass recovered is 63.7% (see Table 6.1). Again, this value has to be taken with care as the two mass changes influence each other with the negative change dominating.

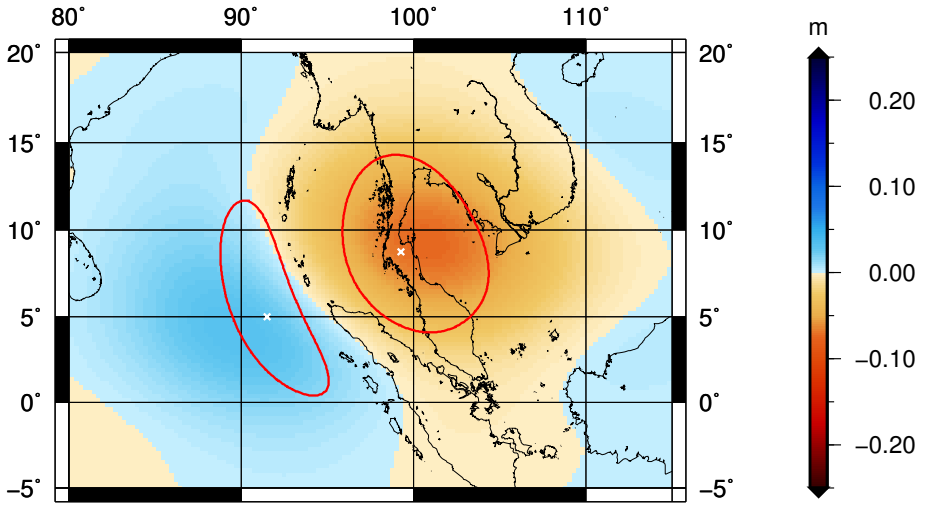

Figure 6.32: Recovered mass over Sumatra-Andaman with Han's anisotropic filter (r_0=250 km, r_1=500 km, m_r1=15). The maximum mass changes are centred at $\phi = 5.000°$, $\lambda = 91.500°$ and $\phi = 8.750°$, $\lambda = 99.250°$, respectively (white cross).

Results for Kusche's de-correlated anisotropic filter with DDK3

This validation considers Kusche's de-correlated anisotropic smoothing filter DDK3. The recovered mass distribution illustrated in Figure 6.33 shows a similar behaviour as that obtained for Gaussian isotropic smoothing. Differences show a slight anisotropic behaviour with increased leakage in west-east direction. Again, it can be seen that the positive and negative mass changes influence each other with the larger negative mass change slightly pushing the cut between positive and negative mass change towards the former. The total mass recovered is 95.4% (see Table 6.1), though this value has to be taken with care as the two mass changes influence each other with the negative change dominating.

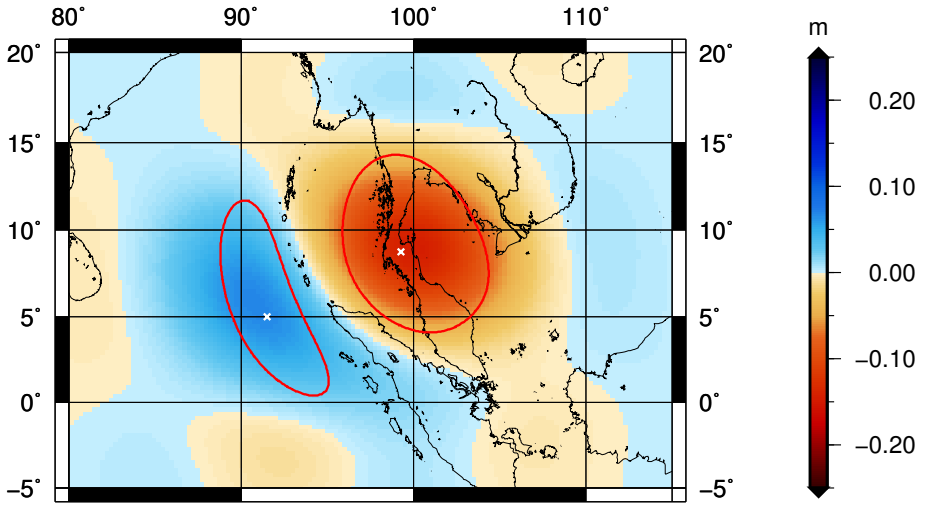

Figure 6.33: Recovered mass over Sumatra-Andaman with de-correlated anisotropic filter DDK3. The maximum mass changes are centred at $\phi = 5.000°$, $\lambda = 91.500°$ and $\phi = 8.750°$, $\lambda = 99.250°$, respectively (white cross).

6.3.6 Validation over Lake Victoria

The last validation is performed over the Lake Victoria region, which includes both lake level and hydrological changes. The initial mass change considered is illustrated in Figure 6.34, which forms the input mass change for the validation procedure. This covers Lake Victoria as well as a large region around it. Like the mass change over the Amazon basin the variation of the mass is rather uniform with values between 0.1 m and 0.2 m ewh. The total mass change over this area has been estimated with 147.4 Gt (see Table 6.1). Cross-sections in west-east and south-north direction through the maximum of the mass distribution superimposed on the corresponding recovered mass distributions are illustrated in Figure 6.35. Like for the Amazon basin, it can be noticed that the filters do not match the shape of the input mass as well as for the scenario over Greenland. Note the undulations on the original mass are due to the derivation of the mass from GRACE data.

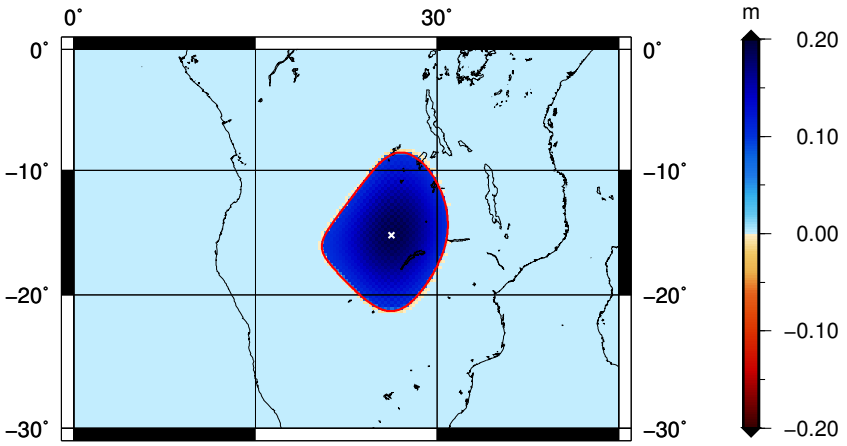

Figure 6.34: Initial mass over Lake Victoria. The maximum mass change is centred at $\phi = -15.250°$, $\lambda = 26.250°$.

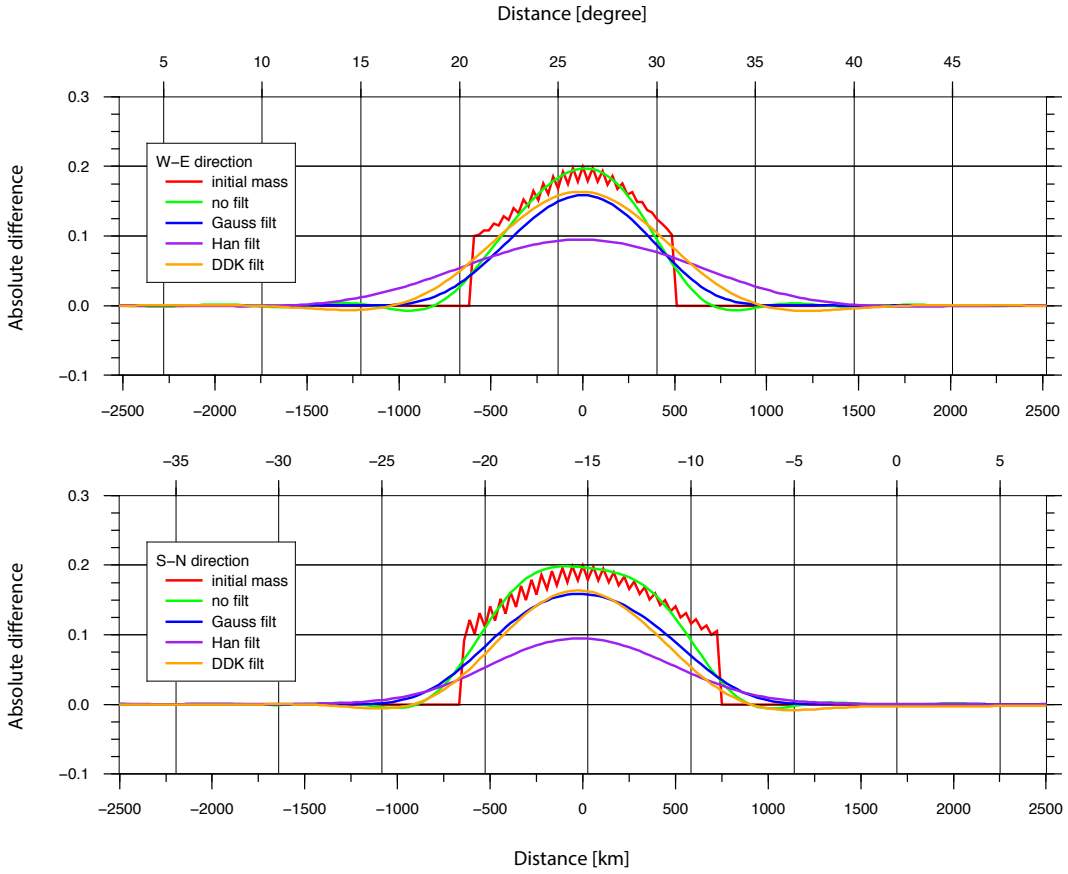

Figure 6.35: Cross-sections of masses over Lake Victoria with different smoothing methods applied. The smoothing radius for Gaussian filter is r_g=250 km. Parameters for Han's anisotropic filter are r_0=250 km, r_1=500 km. For decorrelation anisotropic smoothing, DDK3 is used.

Result for no filter

Like for all other validations a small band around the input mass is visible in the recovered mass distribution (see Figure 6.36) when no smoothing has been applied. This indicates the impact of spectral leakage. The band is rather small and largely follows the original 0.1 m isoline, though with slight variations. Also visible in Figure 6.36 is the typical Gibbs phenomenon showing as undulating pattern outside of the input mass. Like for the mass change over the Amazon basin, this is largely due to the fact that the initial mass change has a plateau-like shape, thus the jump discontinuity produces a more pronounced Gibbs effects (as is also the case for disc masses). The total mass recovered is 90.9%, thus spectral leakage is 9.1% (see Table 6.1).

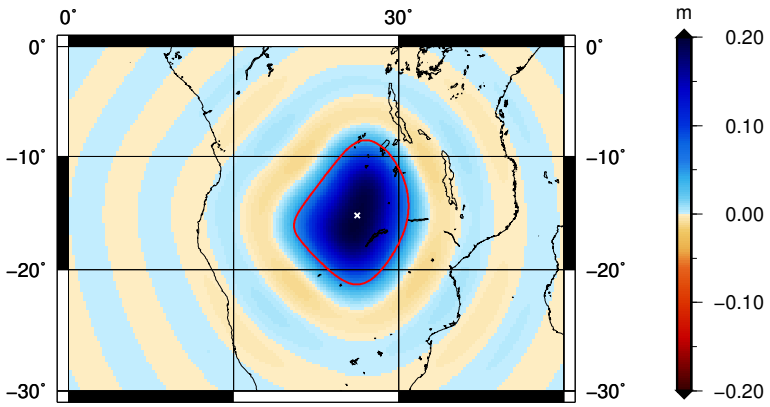

Figure 6.36: Recovered mass over Lake Victoria with no smoothing applied. The maximum mass change is centred at $\phi = -15.250°$, $\lambda = 26.250°$.

Gaussian isotropic filter with $r_g = 250$ km

Figure 6.37 illustrates that the application of Gaussian isotropic smoothing with the smoothing radius of $r_g = 250$ km results in higher leakage. This can be seen by a much increased region around the input mass that is affected by leakage. Furthermore, the recovered mass distribution shows some variation to the initial shape of the input mass most noticeably by the 0.1 m isoline that does not match the isolines of the recovered mass distribution. It can also be noticed that the area

impacted by leakage is slightly larger in west-east than south-north direction. In this scenario 73.1% of the total mass has been recovered with 17.7% of the mass loss due to spatial leakage (see Table 6.1). Also visible for Gaussian isotropic smoothing is the undulation pattern outside the input mass, though starting at a longer distance from the input mass.

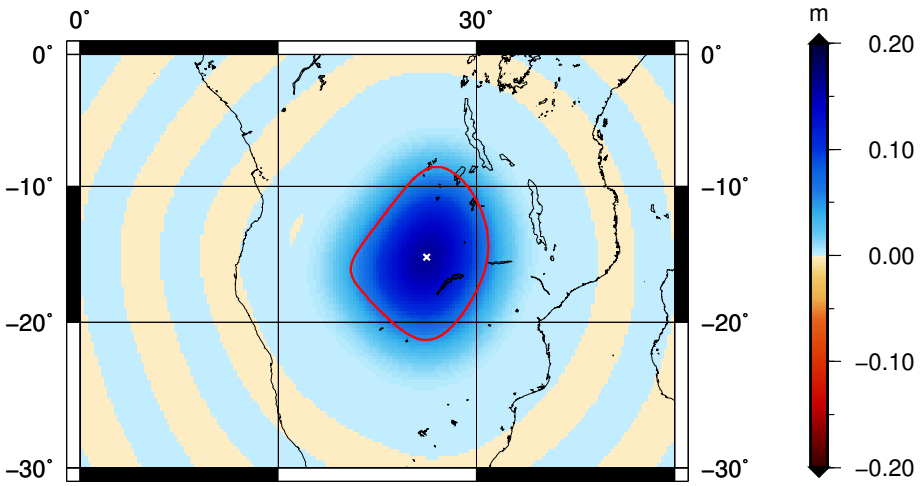

Figure 6.37: Recovered mass over Lake Victoria with Gaussian filter (r_g=250 km). The maximum mass change is centred at $\phi = -15.250°$, $\lambda = 26.250°$.

Han's anisotropic filter with r_0=250 km and r_1=500 km

Like for the validation using a mass change over the Amazon basins, the application of Han's anisotropic smoothing with the smoothing radii of r_0=250 km and r_1=500 km results in a recovered mass distribution that shows a considerably different shape as compared to the input mass (see Figure 6.38). While the input mass had a slightly south-north elongated shape the recovered mass distribution has now a strongly west-east elongated shape. This is due to the anisotropic smoothing filter that impacts most of the mass distribution located close to the equator (e.g., small geographic latitude). Furthermore, the undulating pattern around the input mass is considerably disturbed. The total mass recovered is only 50.7% showing again the large influence of stronger smoothing in west-east directions for locations close to the equator. In this case spectral leakage accounts for 40.2% of the total mass loss (see Table 6.1).

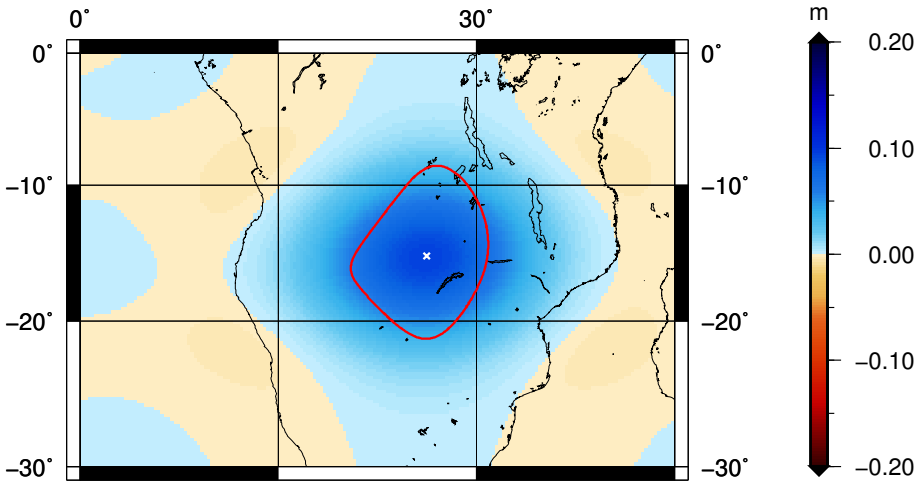

Figure 6.38: Recovered mass over Lake Victoria with Han's anisotropic filter (r_0=250 km, r_1=500 km, m_1=15). The maximum mass change is centred at $\phi = -15.250°$, $\lambda = 26.250°$.

Kusche's de-correlated anisotropic filter with DDK3

This validation applies Kusche's de-correlated anisotropic smoothing filter DDK3. The recovered mass distribution illustrated in Figure 6.39 shows a similar structure as that obtained for Han's anisotropic smoothing (see Figure 6.38). Again, leakage effects dominate in west-east direction, thus largely deform the input mass. The total mass recovered is 75.2%, slightly more than for Gaussian isotropic smoothing. Spectral leakage accounts for 15.7% of the total mass loss (see Table 6.1).

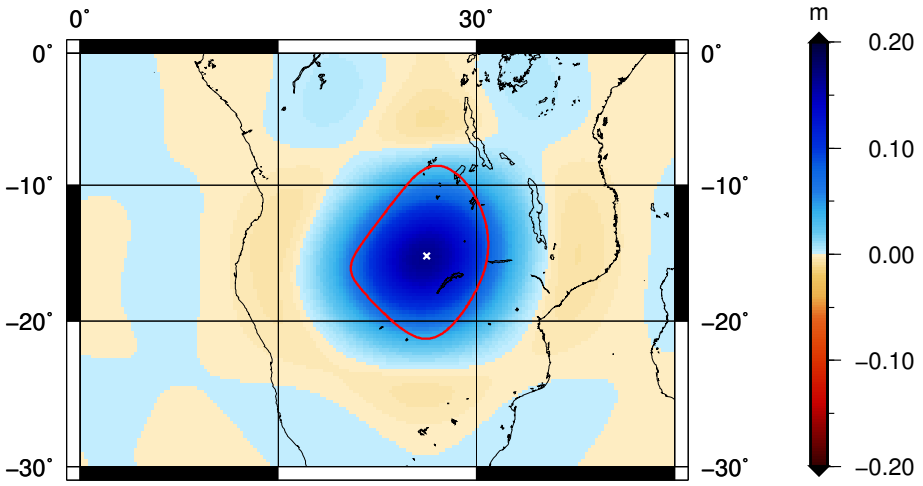

Figure 6.39: Recovered mass over Lake Victoria with Kusche's de-correlated anisotropic filter DDK3. The maximum mass change is centred at $\phi = -15.250°$, $\lambda = 26.250°$.

6.4 Comparisons

In addition to the presentation of all validation results in Section 6.3 and Appendix B, this Section provides a comparison of the results obtained from the application of different filter techniques and mass distributions used. Particular focus will be on the ability of different filters to recover the correct shape of an irregularly shaped mass distribution. This mostly depends on the leakage properties introduced due to the smoothing applied. Less focus is on the total mass recovered as this to some extent depends on the smoothing applied to the input masses. In this case it was Gaussian isotropic smoothing, thus it can be expected that the overall recovery of the total mass is somewhat better for Gaussian isotropic smoothing. However, as will be shown below, this is not always the case.

Table 6.1 provides an overview of all results in terms of the total mass recovered, total mass loss as combined effect of spectral and spatial leakage and mass loss due to spatial leakage only. The latter is considered as the impact of the smoothing filter used. A visual overview of the recovered mass is provided in Figure 6.40.

Table 6.1: Validation results: Recovered total mass, total mass loss and spectral and spatial leakage.

Simulated mass			Recovered Mass		Mass Loss		Spatial Leakage	
			(Gt)	(%)	(Gt)	(%)	(Gt)	(%)
Alaska		Input	-372.106	100.000	0.000	0.000	0.000	0.000
		No smoothing	-354.713	95.326	-17.393	4.674	0.000	0.000
	Gauss	r_g=125 km	-342.21	91.966	-29.896	8.034	-12.503	3.360
	Gauss	r_g=250 km	-311.782	83.788	-60.324	16.212	-42.931	11.537
	Gauss	r_g=500 km	-235.61	63.318	-136.496	36.682	-119.103	32.008
	Han	r_0=125 km, r_1=250 km	-329.603	88.578	-42.503	11.422	-25.110	6.748
	Han	r_0=250 km, r_1=500 km	-285.659	76.768	-86.447	23.232	-69.054	18.558
	Han	r_0=500 km, r_1=1000 km	-196.666	52.852	-175.440	47.148	-158.047	42.474
	Kusche	DDK3	-342.448	92.030	-29.658	7.970	-12.265	3.296
	Kusche	DDK2	-323.397	86.910	-48.709	13.090	-31.316	8.416
	Kusche	DDK1	-265.645	71.390	-106.461	28.610	-89.068	23.936
Greenland		Input	-2146.658	100.000	0.000	0.000	0.000	0.000
		No smoothing	-2113.49	98.455	-33.168	1.545	0.000	0.000
	Gauss	r_g=125 km	-2087.409	97.240	-59.249	2.760	-26.081	1.215
	Gauss	r_g=250 km	-2021.006	94.147	-125.652	5.853	-92.484	4.308
	Gauss	r_g=500 km	-1824.38	84.987	-322.278	15.013	-289.110	13.468
	Han	r_0=125 km, r_1=250 km	-2071.001	96.476	-75.657	3.524	-42.489	1.979
	Han	r_0=250 km, r_1=500 km	-1986.107	92.521	-160.551	7.479	-127.383	5.934
	Han	r_0=500 km, r_1=1000 km	-1753.288	81.675	-393.370	18.325	-360.202	16.780
	Kusche	DDK3	-2094.143	97.554	-52.515	2.446	-19.347	0.901
	Kusche	DDK2	-2070.497	96.452	-76.161	3.548	-42.993	2.003
	Kusche	DDK1	-1992.033	92.797	-154.625	7.203	-121.457	5.658
Amazon Basin		Input	396.876	100.000	0.000	0.000	0.000	0.000
		No smoothing	376.834	94.950	20.042	5.050	0.000	0.000
	Gauss	r_g=125 km	363.546	91.602	33.330	8.398	13.288	3.348
	Gauss	r_g=250 km	332.65	83.817	64.226	16.183	44.184	11.133
	Gauss	r_g=500 km	261.458	65.879	135.418	34.121	115.376	29.071
	Han	r_0=125 km, r_1=250 km	331.816	83.607	65.060	16.393	45.018	11.343
	Han	r_0=250 km, r_1=500 km	278.492	70.171	118.384	29.829	98.342	24.779
	Han	r_0=500 km, r_1=1000 km	194.052	48.895	202.824	51.105	182.782	46.055
	Kusche	DDK3	334.518	84.288	62.358	15.712	42.316	10.662
	Kusche	DDK2	287.237	72.374	109.639	27.626	89.597	22.576
	Kusche	DDK1	215.285	54.245	181.591	45.755	161.549	40.705

Continued on next page

Table 6.1 – *Continued from previous page*

Simulated mass			Recovered Mass		Mass Loss		Spatial Leakage	
			(Gt)	(%)	(Gt)	(%)	(Gt)	(%)
West Antarctica		Input	-600.922	100.000	0.000	0.000	0.000	0.000
		No smoothing	-573.727	95.474	-27.195	4.526	0.000	0.000
	Gauss	r_g=125 km	-557.456	92.767	-43.466	7.233	-16.271	2.708
		r_g=250 km	-515.851	85.843	-85.071	14.157	-57.876	9.631
		r_g=500 km	-401.363	66.791	-199.559	33.209	-172.364	28.683
	Han	r_0=125 km, r_1=250 km	-551.674	91.805	-49.248	8.195	-22.053	3.670
		r_0=250 km, r_1=500 km	-501.411	83.440	-99.511	16.560	-72.316	12.034
		r_0=500 km, r_1=1000 km	-372.359	61.965	-228.563	38.035	-201.368	33.510
	Kusche	DDK3	-564.834	93.995	-36.088	6.005	-8.893	1.480
		DDK2	-549.55	91.451	-51.372	8.549	-24.177	4.023
		DDK1	-479.487	79.792	-121.435	20.208	-94.240	15.683
Sumatra-Andaman		Input	-56.458	100.000	0.000	0.000	0.000	0.000
		No smoothing	-57.067	101.079	0.609	-1.079	0.000	0.000
	Gauss	r_g=125 km	-55.424	98.169	-1.034	1.831	-1.643	2.910
		r_g=250 km	-49.558	87.779	-6.900	12.221	-7.509	13.300
		r_g=500 km	-31.974	56.633	-24.484	43.367	-25.093	44.445
	Han	r_0=125 km, r_1=250 km	-50.885	90.129	-5.573	9.871	-6.182	10.950
		r_0=250 km, r_1=500 km	-35.989	63.745	-20.469	36.255	-21.078	37.334
		r_0=500 km, r_1=1000 km	-19.196	34.000	-37.262	66.000	-37.871	67.078
	Kusche	DDK3	-53.848	95.377	-2.610	4.623	-3.219	5.702
		DDK2	-41.843	74.114	-14.615	25.886	-15.224	26.965
		DDK1	-26.033	46.110	-30.425	53.890	-31.034	54.968
Lake Victoria		Input	147.454	100.000	0.000	0.000	0.000	0.000
		No smoothing	133.996	90.873	13.458	9.127	0.000	0.000
	Gauss	r_g=125 km	126.126	85.536	21.328	14.464	7.870	5.337
		r_g=250 km	107.832	73.129	39.622	26.871	26.164	17.744
		r_g=500 km	68.945	46.757	78.509	53.243	65.051	44.116
	Han	r_0=125 km, r_1=250 km	105.374	71.462	42.080	28.538	28.622	19.411
		r_0=250 km, r_1=500 km	74.753	50.696	72.701	49.304	59.243	40.177
		r_0=500 km, r_1=1000 km	40.881	27.725	106.573	72.275	93.115	63.149
	Kusche	DDK3	110.878	75.195	36.576	24.805	23.118	15.678
		DDK2	86.56	58.703	60.894	41.297	47.436	32.170
		DDK1	54.973	37.281	92.481	62.719	79.023	53.592

(a) Gaussian Isotropic Smoothing

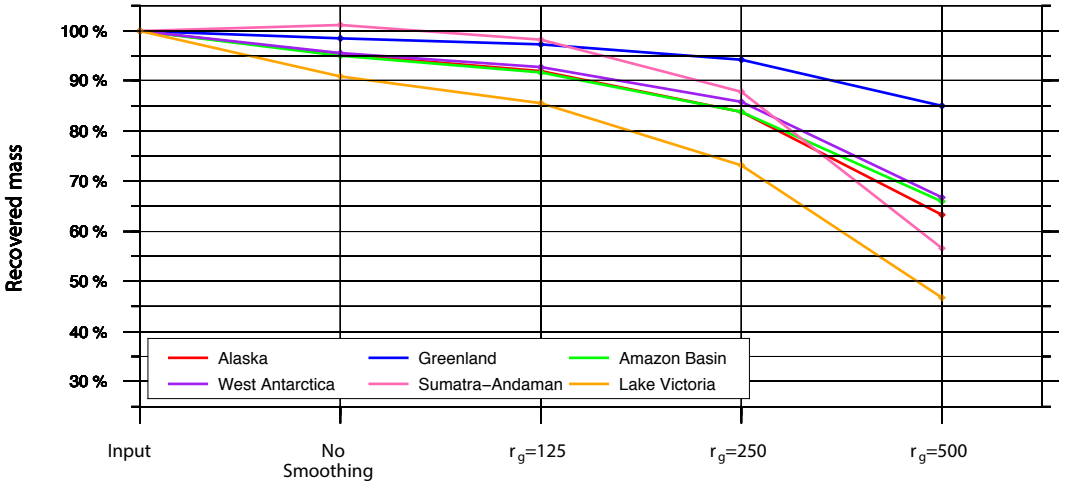

(b) Han's Anisotropic Smoothing

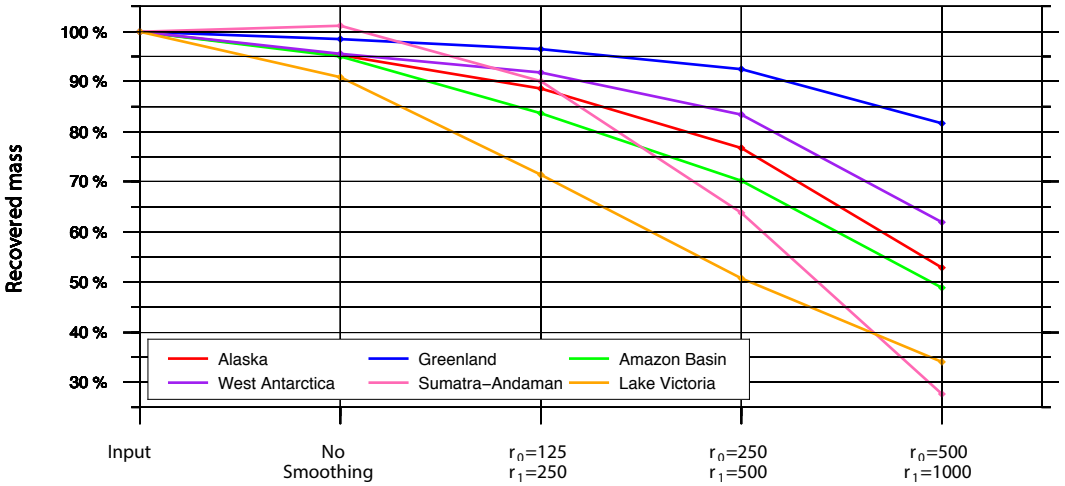

(c) De-correlated, Anisotropic Smoothing

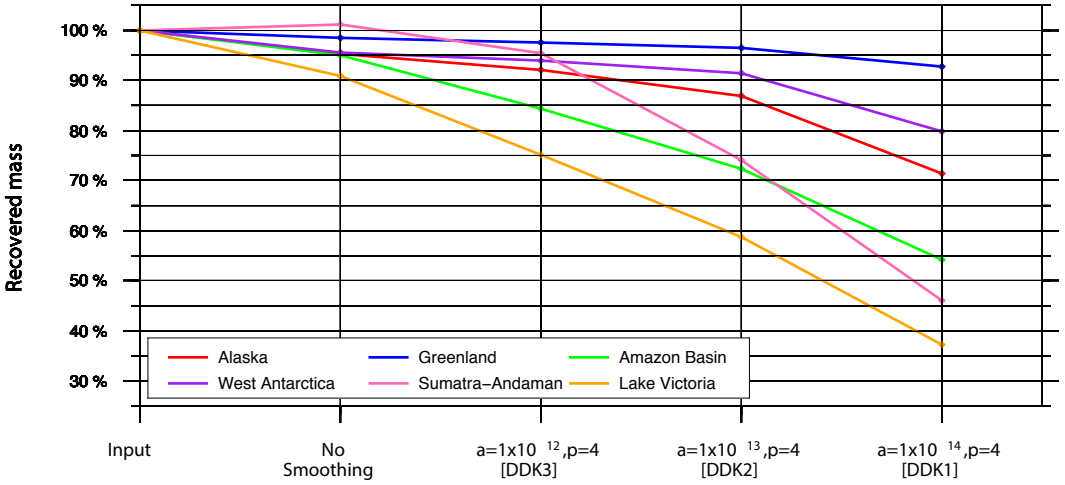

Figure 6.40: Recovered mass of more realistic simulated masses.

The results in terms of the total recovered mass do not confirm that the application of Gaussian isotropic smoothing always results in the best recovery of the total mass but depends on the mass considered. In fact, scrutinizing Table 6.1, this only applies to the simulated mass changes over the Amazon basin, Sumatra-Andaman and Lake Victoria. In the remaining scenarios for Alaska, Greenland and West-Antarctica Kusche's de-correlated anisotropic smoothing filter provides a better recovery. This is independent of the strength of the smoothing used (e.g., weak, medium or strong). Therefore, it seems that Gaussian isotropic smoothing is generally performing better for mass changes that (1) are located close to the equator, (2) don't have a strong variation in height (e.g., plateau like structure), and (3) have a jump discontinuity that is relatively large with respect to the vertical extension of the mass considered.

Regarding the ability to recover the correct shape of an irregularly shaped mass distribution, all filters examined show that the correct shape is generally recovered for weak smoothing but increasingly distorted for medium and strong smoothing. This particularly holds for Han's anisotropic and to a lesser extent for Kusche's de-correlated anisotropic filter. As already seen in Chapter 5 for disc masses, the distortion depends on the geographic location of the mass distribution. Generally, the distortion (mostly in west-east direction) is much larger for masses located close to the equator and smaller for masses located at higher geographic latitude. This behaviour is confirmed by larger distortions for the mass changes over the Amazon basin, Sumatra-Andaman and Lake Victoria and smaller distortions for mass changes over Alaska, Greenland and West-Antarctica. For the latter locations it seems that the impact of anisotropic smoothing (e.g., stronger smoothing in west-east direction) is offset by an increased spatial resolution in west-east direction when using geographic coordinates (e.g., meridian convergence).

The impact of anisotropic smoothing does not only depend on the geographic location of the mass distribution but also on its shape. The impact gets amplified for mass distributions with an elongated shape in orthogonal direction of the strongest smoothing. Therefore, mass distributions with an elongated shape in south-north direction are more influenced by anisotropic smoothing with highest

smoothing in west-east direction. This behaviour is exemplified by the recovery of the mass changes over Sumatra-Andaman where both positive and negative mass changes have a highly elongated shape in south-north direction. In this case the application of strong anisotropic smoothing through Han's anisotropic filter results in the highest distortion in west-east direction and consequently in the lowest recovery of total mass (e.g., only 34.0%).

Comparing the results for Han's anisotropic smoothing filters with Kusche's de-correlated anisotropic filters shows that both introduce some anisotropic behaviour into the recovered mass distribution, though more pronounced for Han's anisotropic smoothing. While introducing anisotropic distortions into the recovered mass distribution Kusche's de-correlated anisotropic filter seems to keep the original shape slightly better but more importantly suppresses more spatial leakage, thus resulting in a better recovery of the total mass.

The Gibbs phenomenon, mostly visible as undulating patterns outside the original mass, is mostly noticeable when either no or weak Gaussian isotropic smoothing is applied. In these cases spectral leakage is the largest contributor, thus introducing the Gibbs phenomenon. As documented by the results, this behaviour starts to change when applying medium to strong Gaussian isotropic or anisotropic smoothing.

Finally, mass changes related to the 2004 Sumatra-Andaman earthquake provide a good example for the influence of two mass changes with opposite signs located close together. These have a direct impact on the shape of the recovered mass distribution. All validation scenarios considered show a disturbance of the recovered mass distribution between the two mass changes (e.g., as a dividing line between positive and negative mass changes).

6.5 Chapter Summary

This chapter presented a validation procedure to examine techniques used to infer mass changes from (time-variable) gravity changes. More realistic mass distributions over various geographic locations have been used as simulated masses within the validation procedure. The more realistic mass distributions have been obtained from GRACE-derived mass changes over the 8-year period between 2002 and 2010. The masses were subjected to a range of smoothing filters. Results for all validation scenarios are presented in terms of the recovered mass distribution and west-east and south-north cross-sections of the differences between input and recovered masses. While all results are described, the chapter also provides a comparison between the used smoothing filters.

Chapter 7

Summary, Conclusions and Recommendations

This chapter provides a summary of the research performed, significant findings obtained, conclusions drawn and gives some recommendations for future work.

7.1 Summary of the Research

The primary aim of this study was to validate existing methods used to infer mass changes from time-variable gravity observations. The methods were limited to techniques that apply spatial smoothing (isotropic and anisotropic) on spherical harmonic coefficients of the Earth's external gravitational potential (e.g., Stokes coefficients given by GRACE level-2 data). Three techniques were considered, which were all based on the approach of Wahr et al. (1998) but differ by the smoothing filter technique used. In particular, Gaussian isotropic smoothing (e.g., Jekeli, 1981) and anisotropic smoothing according to Han et al. (2005b), Kusche (2007) and Kusche et al. (2009) have been used. For each smoothing filter three validation scenarios have been selected representing "weak", "medium" and "strong" smoothing.

The validation procedure chosen is based on forward gravity modelling (FGM) techniques to generate the gravitational signal of simulated mass distributions. It is a closed-loop validation procedure where recovered mass distributions are compared to the simulated input mass (see Chapter 5).

The results of the validation were also intended to gain general information on the most suitable method to infer mass changes from (time-variable) gravity. Within the validation procedure, Synthetic Earth gravity modelling was applied on spherical disc masses and more realistic mass distributions extracted from GRACE gravity observations.

In particular the validation procedure employed performed the following steps:

- First, simulated mass distributions have been developed that form the input for the validation procedure. Two types of input masses have been considered: (1) more simplistic spherical disc masses and (2) more realistic regional mass distributions. For a more ideal case, spherical disc masses have been selected as to study the general properties of the mass estimation techniques examined (see Figure 5.1 in Chapter 5). In this case two disc masses with the same total mass but different spherical radii (10° and 5°) were placed at three different locations (see Figure 5.4). For a more realistic case, simulated regional mass distributions were extracted from GRACE-derived linear mass changes over the 8-year period between 2002 and 2010. The selection of regions was based on the magnitude of the mass change in order to capture the largest contemporary mass changes in the cryosphere and hydrosphere. The spatial extents of these mass changes were defined by the $\pm$ 0.1 m equivalent water height (ewh) isoline. The spatial distribution of the more realistic mass distributions can be seen in Figure 6.3. While the disc masses have a simple regular shape, the more realistic mass changes have been included so as to examine the recovery of mass changes with a more irregular horizontal and vertical extension.

- The simulated mass distributions have been used to generate self-consistent gravity field changes through the application of FGM (see Section 3.3). Here, FGM has been performed in the spectral domain. This created a set of spherical harmonic coefficients of the gravitational potential (e.g., Stokes coefficients) that form the input for the mass estimation techniques considered. For the purpose of validation the simulated mass distributions are assumed to be error-free, thus validation results are not obscured by additional error sources. Impor-

tantly, the so-derived gravitational potential is self-consistent with the given mass distribution, thus is suited to check techniques for the inference of mass changes from gravity changes.

- The simulated mass distributions have been recovered from the Stokes coefficients through the application of the considered mass estimation techniques. For each of the three techniques, four different scenarios with respect to the filters used were applied, namely: (1) No filter; (2) Gaussian isotropic filter; (3) Han's anisotropic filter; and (4) Kusche's de-correlated, anisotropic filter. The validation results using disc masses are provided in Chapter 5 and that using more realistic masses are presented in Chapter 6 and Appendix B.

- Differences between the recovered masses and the input masses are examined. In the closed-loop validation, any differences are due to shortcomings of the mass estimation technique used. Therefore, in this study, the differences form the basis for the general validation of mass estimation techniques, the quantification of spectral and spatial leakage and the analysis of the recovered masses in terms of their spatial distribution. Based on this information significant findings and conclusions are presented in the next section.

7.2 Significant Findings and Conclusions

From the validation results presented and discussed in Chapter 5 and Chapter 6, several significant findings are obtained as well as conclusions drawn. These are summarized below first for the simulated spherical disc masses presented in Chapter 5:

- The Gibbs phenomenon is a dominating feature in the recovered masses for all scenarios considered. This mostly demonstrates the limitations of using band-limited spherical harmonic representations to model signals with jump discontinuities and constant values. The Gibbs phenomenon manifests itself in the recovered masses through undulating (around zero) differences over the disc and spreading out from the disc over the whole globe. Larger differences

occur at the edge of the discs demonstrating the inability to model a jump discontinuity. The Gibbs effect is larger for 5° disc masses (disc Ib, disc IIb and disc IIIb) than for 10° disc masses (disc Ia, disc IIa and disc IIIa), which is due to the higher jump discontinuity of the former.

- As expected, the results confirm that spatial leakage increases for increased smoothing radii. This property holds for all filtering techniques used. For the spatially more concentrated disc masses the effect of spatial leakage is approximately double when halving the spatial extension of the disc masses but keeping the total masses the same (e.g., 5° disc masses have 4-times the height than 10° disc masses). This property holds equally for spectral leakage.

- For "weak" smoothing levels the magnitudes of spectral and spatial leakage are similar, but for "medium" to "strong" smoothing spatial leakage starts to dominate. Especially, for "strong" smoothing, spatial leakage can be very large, often reaching levels of over 50%. In this case, less than half of the input mass is recovered over the area of the input mass and more than half has leaked away. Therefore it is important to consider this property when recovering masses over a spatially limited area (e.g., Baur et al., 2009).

- While both Han's anisotropic and Kusche's de-correlated anisotropic filters introduce anisotropic behaviour in the recovered mass distributions, the effective smoothing radii are different. Han's anisotropic smoothing filter is directly based on the introduction of varying smoothing radii (e.g., different in west-east and south-north). Kusche's de-correlated anisotropic filter only shows indirectly the impact of varying smoothing. From the results in Chapter 5 the range in effective smoothing radii in south-north direction is only about 1/3 of the range in west-east direction (e.g., ∼200 km to 600 km vs. ∼400 km to 1500 km). This confirms the effective smoothing radii given by Kusche et al. (2009) and listed in Table 4.2. In this study, information on the effective smoothing radii is obtained through the distances in west-east and south-north direction at which the differences between input and recovered mass outside the initial disc reach a level of zero.

- One of the important findings of this study is the dependency of the recovered

mass with respect to geographic latitude. While Gaussian isotropic smoothing shows similar levels of recovery, independent of the geographic latitude of the disc mass, the situation is quite different for anisotropic filters such as Han's anisotropic and Kusche's de-correlated anisotropic filters. For these filters, recovery levels are better for disc masses located at higher geographic latitudes and worse for disc masses located at the equator. This may be an effect caused by the meridian convergence when using geographic coordinates. The meridian convergence directly depends on the geographic latitude and influences the spatial resolution in west-east direction when using spherical harmonics. Therefore, effects due to increased smoothing in west-east direction are in part offset by a better approximation of a jump discontinuity due to increased spatial resolution when using spherical harmonics based on geographic coordinates.

Important findings obtained from the validation results using more realistic mass distributions (see Chapter 6) are summarized below:

- The Gibbs phenomenon is not as pronounced for the more realistic mass distributions as for the disc masses. For the former the Gibbs phenomenon is mostly present when applying no or "weak" smoothing, thus it is mostly caused by spectral leakage, which is the dominating impact for these scenarios. For "medium" to "strong" smoothing, the Gibbs phenomenon is less visible, thus is obscured by the dominating effect of spatial leakage.

- Also in case of the more realistic mass distributions, increased smoothing leads to increased spatial leakage. Again this property holds for all filtering techniques used, though the magnitude can vary considerably between techniques and mass distributions considered. In terms of the total recovered mass, the spread is between 97.6% (for "weak" de-correlated anisotropic smoothing over Greenland) and 34.0% (for "strong" anisotropic smoothing over Sumatra-Andaman).

- When considering only the total recovered mass none of the techniques comes out as the optimal technique for all mass distributions and smoothing scenarios.

Instead, in the validation scenarios considered, it is either Gaussian isotropic smoothing or Kusche's de-correlated anisotropic smoothing that obtained the best recovery result. The results suggest that Gaussian isotropic smoothing generally performs better for mass changes that (1) are located close to the equator, (2) do not have a great variation of height (e.g., plateau-like) and (3) have a jump discontinuity that is relatively large with respect to the variation in height. However, this conclusion has to be treated with care and may only apply to the specific cases considered.

- All filter techniques considered largely reproduce the geometrical shape of the input mass in the recovered mass for "weak" smoothing scenarios. This is not any more the case when applying "medium" and "strong" smoothing. For these cases, the original shape of the input mass gets increasingly distorted. In particular, this is a property of anisotropic smoothing with the effect more pronounced for Han's anisotropic smoothing than for Kusche's de-correlated anisotropic smoothing. Like for the disc masses the degree of distortion depends on the geographic location of the mass distribution considered. Also the more realistic mass distributions confirm that distortions are larger for mass distributions closer to the equator (e.g., Amazon Basin, Lake Victoria and Sumatra-Andaman) and smaller for mass distributions at higher geographic latitude (e.g., Alaska, Greenland and West-Antarctica).

- In addition to the last point, the impact of anisotropic smoothing does not only depend on the geographic location of the mass distribution but also on its shape. There is an amplification effect for mass distributions that have an elongated shape in south-north direction. This is exemplified for the recovery of the mass changes related to the great 2004 Sumatra-Andaman earthquake (see the next point below).

- The worst recovery both in terms of total mass recovered and geometrical shape is obtained for the mass changes related to the great 2004 Sumatra-Andaman earthquake. For "strong" anisotropic smoothing only 34% of the total mass is recovered and the recovered geometrical shape has little in common with the input mass distribution. This is a combined effect of anisotropic smoothing

performing worse on mass distributions located close to the equator with an elongated south-north shape and the impact of two mass distributions with alternating sign located close together.

- While both Han's anisotropic and Kusche's de-correlated anisotropic smoothing filters considerably distort the original shape of the input mass distribution, it seems that Kusche's de-correlated anisotropic smoothing filter keeps the original shape slightly better. Apart from this, Kusche's de-correlated anisotropic smoothing filter suppresses better the effect of spatial leakage when compared to Han's anisotropic smoothing filter. While both show similar areas around the input mass affected by leakage, the magnitude is less for Kusche's de-correlated anisotropic smoothing filter, thus leading to better recovery rates.

7.3 Recommendation for Future Work

Based on the concepts used and the results obtained in this study, further research can be performed on similar topics. The list given below provides some ideas in this regard:

1. A land-ocean mask can be applied to the more realistic mass distributions used in this study (e.g., removing any signal over the ocean, see Figure 7.1). In many areas, this is reasonable as the mass change will be confined to land areas only. For example this is the case for mass changes in the cryosphere (e.g., Alaska, Greenland and Antarctica) where the mass change is confined to the ice covered areas only and does not extend over the oceans. The differences to the mass distributions considered in this study will be the introduction of a jump discontinuity that follows the coast lines instead of a particular isoline. This will introduce a jump discontinuity that varies its height with location.

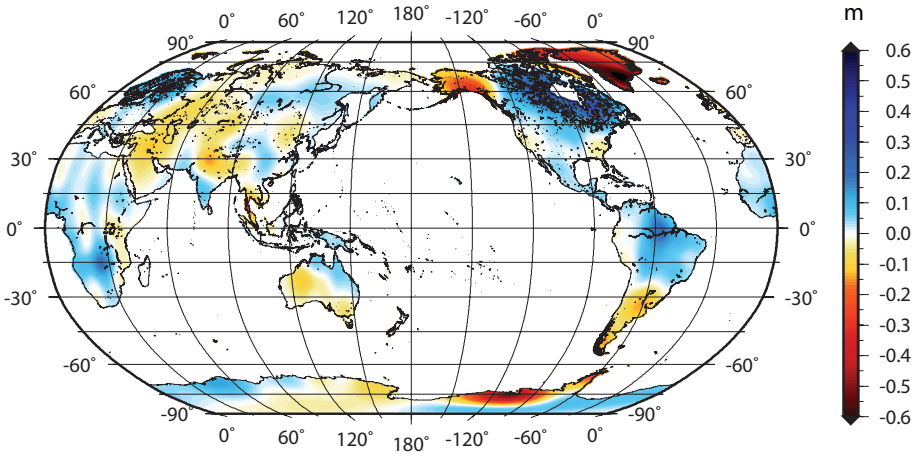

Figure 7.1: Mass changes derived from 8 years GRACE time-variable gravity with all ocean signal removed.

2. Instead of assuming error-free mass distributions as input masses for the validation procedure some error models can be applied so to study the recovery under the presence of errors. In this regard correlated errors in the higher degree Stokes coefficients may be of particular interest producing the stripe-like features in GRACE-derived mass data. A suitable error model for these could be either obtained through the application of the de-correlation technique introduced by Swenson and Wahr (2006) or by the extraction from GRACE time-variable gravity data through the application of the principal component analysis (e.g., Schrama et al., 2007; Anjasmara and Kuhn, 2010).

3. Apart from isotropic and anisotropic smoothing, in the last few years many different filtering techniques have been suggested as outlined in Chapter 4. These techniques include but are not limited to: optimal filters based on a priori estimates of signal and measurement error variances (e.g., Swenson and Wahr, 2002; Seo and Wilson, 2005), global optimized variance-dependent smoothing (e.g., Chen et al., 2006c), spectral-domain filtering (e.g., Swenson and Wahr, 2006) and empirical orthogonal functions (e.g., Schrama et al., 2007). Moreover, combinations of these techniques may also be considered. The concepts and validation procedure of this study can equally be applied to these techniques.

4. Apart from the use of Stokes coefficients (e.g. GRACE level-2 data) other observables can be considered for the mass recovery. Of particular interest would be the use of GRACE level-1 data such as employed by the use of mascons (e.g., Rowlands et al., 2005; Klosko et al., 2009; Luthcke et al., 2006b; Klees et al., 2008). This however, requires different forward modelling techniques as used in this study since the simulated mass changes have to be related to range rate changes between satellites.

5. Finally, another interesting area of study would be the application and validation of GOCE satellite data. While GOCE is designed to observe the static gravity field of the Earth, it is like CHAMP and GRACE based on repeated observations (e.g., satellites on repeat orbits). Furthermore, GOCE is designed to provide Earth gravity field information with an unprecedented geoid accuracy of several centimetres and a minimum resolution of 65 km (e.g., Rummel, 2005; Han et al., 2005a). The final GOCE gravity field models are computed from gravity gradiometer data and orbit solutions (e.g., Floberghagen et al., 2008). As currently the mission already operates for four years (since March 2009), GOCE can also provide time-variable gravity data. A GOCE gravity field model also consists of Stokes coefficients, thus the same techniques used in this study could be applied.

References

Ågren, J. 2004. *Regional Geoid Determination Methods for the Era of Satellite Gravimetry Numerical Investigations Using Synthetic Earth Gravity Models*. Doctoral dissertation, Geodesy, Department of Infrastructure, Royal Institute of Technology.

Andersen, O. and J. Hinderer. 2005. Global inter-annual gravity changes from GRACE: Early results. *Geophysical Research Letters*, 32:L01402. doi:10.1029/2004GL020948.

Anderson, E. 1976. The effect of topography on solutions of Stoke's problem. UNISURV Report S14, University of New South Wales, Kensington, Australia.

Anjasmara, I. M. 2008. *Spatio-temporal analysis of GRACE gravity field variations using the Principal Component Analysis*. Master thesis, Department of Spatial Sciences, Curtin University of Technology.

Anjasmara, I. M. and M. Kuhn. 2009. Revealing the Sumatra-Andaman earthquake's signatures from GRACE time-variable gravity observations. Poster presented at IAG Scientific Assembly. Buenos Aires: International Association of Geodesy.

Anjasmara, I. M. and M. Kuhn. 2010. Analysing Five Years of GRACE Equivalent Water Height Variations Using the Principal Component Analysis. In *Gravity, Geoid and Earth Observations: IAG Symposia*, ed. S. Mertikas, vol. 135, 547–555. International Association of Geodesy Symposia, Berlin: Springer.

Arendt, A. A., S. B. Luthcke, C. F. Larsen, W. Abdalati, W. B. Krabill, and M. J. Beedle. 2008. Validation of high-resolution GRACE mascon estimates

of glacier mass changes in the St Elias Mountaion, Alaska, USA, using aircraft laser altimetry. *Journal of Glaciology*, 54(188):778–787.

Awange, J. 2012. *Environmental Monitoring using GNSS*. Heidelberg, Berlin: Springer.

Awange, J. L., M. A. Sharifi, O. Baur, W. Keller, W. E. Featherstone, and M. Kuhn. 2009. Hydrological monitoring from space: current limitations and future prospects for the GRACE gravimetry mission over Australia. *Journal of Spatial Science*, 53(1):1–14.

Bagherbandi, M. and L. Sjöberg. 2012. A synthetic Earth gravity model based on a topographic-isostatic model. *Studia Geophysica et Geodaetica*, 56:1–21. doi:10.1007/s11200-011-9045-1.

Balmino, G. 2001. New space missions for mapping the Earth's gravity field. *Comptes Rendus de l'Academie des Sciences Series IV Physics*, 2(9):1353C1359. doi:10.1016/S1296-2147(01)01269-0.

Balmino, G., N. Vales, S. Bonvalot, and A. Briais. 2012. Spherical harmonic modelling to ultra-high degree of Bouguer and isostatic anomalies. *Journal of Geodesy*, 86(7):499–520. doi:10.1007/s00190-011-0533-4.

Bamber, J. L., R. E. M. Riva, B. L. A. Vermeersen, and A. M. LeBrocq. 2009. Reassessment of the potential sea-level rise from a collapse of the West Antarctic ice sheet. *Science*, 324(5929):901–903. doi:10.1126/science.1169335.

Bao, L. F., A. Piatanesi, Y. Lu, H. T. Hsu, and X. H. Zhou. 2005. Sumatra tsunami affects observations by GRACE satellites. *EOS Transactions, AGU*, 86:353–356. doi:10.1029/2005EO390002.

Baran, I., M. Kuhn, S. J. Claessens, W. E. Featherstone, S. A. Holmes, and P. Vaníček. 2006. A synthetic earth gravity model designed specifically for testing regional gravimetric geoid determination algorithms. *Journal of Geodesy*, 80:1–16. doi:10.1007/s00190-005-0002-z.

Barletta, V. R. and A. Bordoni. 2009. Clearing observed PGR in GRACE data aimed at global viscosity conversion: Weighted Mass Trends technique. *Geophysical Research Letters*, 36:L02305. doi:10.1029/2008GL036429.

Barletta, V. R., R. Sabadini, and A. Bordoni. 2008. Isolating the PGR signal in the GRACE data: impact on mass balance estimates in Antarctica and Greenland. *Geophysical Journal International*, 172:18–30. doi:10.1111/j.1365-246X.2007.03630.x.

Barthelmes, F. and R. Dietrich. 1991. Use of point masses with optimized positions for the approximation of the gravity field. In *Determination of the Geoid: Present and Future*, eds. R. Rapp and F. Sansò, vol. 106, 484–493. New York: Springer-Verlag.

Barthelmes, F., R. Dietrich, and R. Lehmann. 1991. Representation of the global gravity field by point masses on optimized positions based on recent spherical harmonics expansions. Poster presented at XX General Assembly of the IUGG. Vienna: International Union of Geodesy and Geophysics.

Barthelmes, F. and H. Kautzleben. 1983. A new method of modelling the gravity field of the Earth by point masses. In *Proceedings of the XVIII General Assembly of the IUGG*, 442–448. Hamburg: International Union of Geodesy and Geophysics.

Baur, O., M. Kuhn, and W. E. Featherstone. 2009. GRACE-derived ice-mass variations over Greenland by accounting for leakage effects. *Journal of Geophysical Research*, 114:B06407. doi:10.1029/2008JB006239.

Baur, O., M. Kuhn, and W. E. Featherstone. 2012. Continental mass change from GRACE over 2002-2011 and its impact on sea level. *Journal of Geodesy*, 874(2):117–125. doi:10.1007/s00190-012-0583-2.

Beutler, G., R. Rummel, M. R. Drinkwater, and R. von Steiger, eds. 2003. *Earth gravity field from space - From sensors to Earths sciences*, vol. 17 of *Space Science Series of ISSI*. Dordrecht: Kluwer Academic Publishers.

Biro, P. 1983. *Time variation of height and gravity*. Karlsruhe: Herbert Wichmann Verlag.

Black, H. D. 1990. Early development of transit, the navy navigation satellite system. *Journal of Guidance, Control, and Dynamics*, 13(4):577–585. doi:10.2514/3.25373.

Black, H. D., N. A. G. Leppard, J. C. Blankenburgh, P. G. Sluiter, and D. G. King-Hele. 1980. The transit system, 1977: Performance, plans and potential and discussion. *Phil. Trans. R. Soc. Lond. A*, 294(1410):217–2365. doi:10.1098/rsta.1980.0028.

Blakely, R. J. 1996. *Potential theory in gravity and magnetic applications*. Cambridge: Cambridge University Press.

Brown, N. and P. Tregoning. 2010. Quantifying GRACE data contamination effects on hydrological analysis in the Murray-Darling Basin, Southeast Australia. *Australian Journal of Earth Sciences*, 57:329–335. doi:10.1080/08120091003619241.

Burša, M. and K. Pěč. 1988. *Gravity field and dynamics of the Earth*. Berlin: Springer Verlag.

Cannelli, V., D. Melini, A. Piersanti, and E. Boschi. 2008. Postseismic signature of the 2004 Sumatra earthquake on low-degree gravity harmonics. *Journal of Geophysicsal Research*, 113:B12414. doi:10.1029/2007JB005296.

Catalão, J. and M. Sevilla. 2009. Preliminary observations of global ocean mass variations with GRACE. *Geophysical Research Letters*, 31:L13310. doi:10.1029/2006GL029171.

Cazenave, A. and J. Chen. 2010. Time-variable gravity from space and present-day mass redistribution in theEarth system. *Earth and Planetary Science Letters*, 298(3-4):263–274. doi:10.1016/j.epsl.2010.07.035.

Cazenave, A., S. Guinehut, G. Ramillien, W. Llovel, K. DoMinh, M. Abalin, G. Larnicol, and A. Lombard. 2009. Se level budget over 2003-2008; a reevaluation from satellite altimetry, GRACE and Argodata. *Global Planet Change*, doi:10.1016/j/ gloplacha.2008.10.004.

Cazenave, A. and R. S. Nerem. 2002. Redistributing Earth's mass. *Science*, 297(5582):783–784.

Chambers, D. P. 2006. Observing seasonal steric sea level variations with GRACE and satellite altimetry. *Journal of Geophysical Research*, 111:C03010. doi:10.1029/2005JC002914,.

Chambers, D. P. 2009. Calculating trends from GRACE in the presence of large changes in continental ice storage and ocean mass. *Geophysical Journal International*, 176:415–419. doi:10.1111/j.1365-246X.2008.04012.x.

Chambers, D. P., J. Wahr, and R. Nerem. 2004. Preliminary observations of global ocean mass variations with GRACE. *Geophysical Research Letters*, 31:L13310. doi:10.1029/2006GL029171.

Chao, B. F. 2005. On inversion for mass distribution from global (time-variable) gravity field. *Journal of Geodynamics*, 39(3):223–230. doi:10.1016/j.jog.2004.11.001.

Chen, J., B. Tapley, and C. Wilson. 2006a. Alaskan mountain glacial melting observed by satellite gravimetry. *Earth and Planetary Science Letters*, 248:368–378. doi:10.1126/science.1129007.

Chen, J., C. R. Wilson, and B. D. Tapley. 2005a. Interannual variability of low-degree gravitational change, 1980 to 2002. *Journal of Geodesy*, 78(9):535–543. doi:10.1007/s00190-004-0417-y.

Chen, J. L., M. Rodell, C. R. Wilson, and J. S. Famiglietti. 2005b. Low degree spherical harmonic influences on Gravity Recovery and Climate Experiment (GRACE) water storage estimates. *Geophysical Research Letters*, 32:L14405. doi:10.1029/2005GL022964.

Chen, J. L., C. R.Wilson, D. Blankenship, and B. D. Tapley. 2009a. Accelerated Antarctic ice loss from satellite gravity measurements. *Nature Geoscience*, 2:L14405. doi:10.1038/NGEO694.

Chen, J. L., C. R. Wilson, D. D. Blankenship, and B. D. Tapley. 2006b. Antarctic mass rates from GRACE. *Geophysical Research Letters*, 33:L11502. doi:10.1029/2006GL026369.

Chen, J. L., C. R. Wilson, J. S. Famiglietti, and M. Rodell. 2007a. Attenuation effect on seasonal basin-scale water storage changes from GRACE time-variable gravity. *Journal of Geodesy*, 81:237–245. doi:10.1016/j.epsl.2006.05.039.

Chen, J. L., C. R. Wilson, and K.-W. Seo. 2006c. Optimized smoothing of Gravity Recovery and Climate Experiment (GRACE) time-variable. *Journal of*

Geophysical Research, 111:B06408. doi:10.1029/2005JB004064.

Chen, J. L., C. R. Wilson, and B. D. Tapley. 2006d. Satellite gravity measurements confirm accelerated melting of Greenland ice sheet. *Science*, 313:1958–1960. doi:10.1126/science.1129007.

Chen, J. L., C. R. Wilson, B. D. Tapley, and S. Grand. 2007b. GRACE detects coseismic and postseismic deformation from the Sumatra-Andaman earthquake. *Geophysical Research Letters*, 34:L13302. doi:10.1029/2007GL030356.

Chen, J. L., C. R. Wilson, B. D. Tapley, Z. L. Yang, and G. Y. Niu. 2009b. 2005 drought event in the Amazon River basin as measured by GRACE and estimated by climate models. *Journal of Geophysical Research*, 114:B05404. doi:10.1029/2008JB006056.

Claessens, S. 2002. *A Synthetic Earth Model : Analysis, implementation, validation and application*. Master thesis, Department of Physical, Geometrical and Space Geodesy, Delft University of Technology.

Claessens, S. and W. Featherstone. 2001. Experiences with Point-Mass Gravity Field Modelling in the Perth Region, Western Australia. *Geomatics Research Australasia*, 75:53–86.

Committee on Earth Science and Applications from Space: A Community Assessment and Strategy for the Future, National Research Council. 2007. *Earth Science and Applications from SPACE: National Imperatives for the Next Decade and Beyond*. Washington, D.C., USA: The National Academies Press.

de Linage, C., L. Rivera, J. Hinderer, J.-P. Boy, Y. Rogister, S. Lambotte, and R. Biancale. 2009. Separation of coseismic and postseismic gravity changes for the 2004 Sumatra-Andaman earthquake from 4.6 yr of GRACE observations and modelling of the coseismic change by normal-modes summation. *Geophysical Journal International*, 176:695–714. doi:10.1111/j.1365-246X.2008.04025.x.

de Viron, O., I. Panet, V. Mikhailov, M. van Champ, and M. Diament. 2008. Retrieving earthquake signature in GRACE gravity solutions. *Geophysical*

Journal International, 174:14–20. doi:10.1111/j.1365-246X.2008.03807.x.

Dickey, J. O. 2001. Time variable gravity : An emerging frontier in interdisciplinary geodesy. In *Gravity, Geoid and Geodynamics 2000*, ed. M. G. Sideris, vol. 123, 1–5. International Association of Geodesy Symposia, Berlin: Springer.

Dickey, J. O., C. R. Bentley, R. Bilham, J. A. Carton, R. J. Eanes, T. A. Herring, W. M. Kaula, G. S. E. Lagerloef, S. Rojstaczer, W. H. F. Smith, H. M. van den Dool, J. M. Wahr, and M. T. Zuber. 1997. *Satellite gravity and the geosphere: Contributions to the study of the solid Earth and its fluid envelopes*. Washington, D.C.: National Academic Press.

D'Urso, M. 2012. On the evaluation of the gravity effects of polyhedral bodies and a consistent treatment of related singularities. *Journal of Geodesy*, 87(3):239=2548. doi:10.1007/s00190-012-0592-1.

Eicker, A. 2008. *Gravity field refinement by radial basis functions from in-situ satellite data*. Doctoral dissertation, Univ Bonn.

European Space Agency. 2013. Gravity field and steady-state ocean circulation mission. http://www.esa.int/esaLP/LPgoce.html (accessed 1 April, 2013).

Featherstone, W. E. 2002. Tests of two forms of Stokes's integral using a Synthetic Gravity Field based on Spherical Harmonics. In *Geodesy - The Challenge for the Third Millenium*, eds. E. Grafarend, F. Krumm, and V. Schwarze, 163–171. Berlin: Springer.

Fellner, J. J. 2011. *Numerical Study on Orthometric Heights Using a Synthetic Earth Gravity Model*. Phd thesis, Department of Spatial Sciences, Curtin University.

Fellner, J. J., M. Kuhn, and W. E. Featherstone. 2012. Development of a Synthetic Earth Gravity Model by 3D mass optimisation based on forward modelling. *Earth Planets Space*, 64(1):2–12. doi:10.5047/eps.2011.07.012.

Fengler, M. J., W. Freeden, A. Kohlhaas, V. Michel, and T. Peters. 2006. Wavelet modeling of regional and temporal variations of the Earth's gravitational potential observed by GRACE. *Journal of Geodesy*, 81(1):5–15. doi:10.1007/s00190-006-0040-1.

Fiedler, K. and P. Döll. 2007. Global modelling of continental water storage changes: sensitivity to different climate data sets. *Advances in Geosciences*, 11(1):63–68.

Floberghagen, R., M. Drinkwater, R. Haagmans, and M. Kern. 2008. GOCE's Measurements of the Gravity Field and Beyond. *ESA Bulletin*, 133:24–31.

Forsberg, R. 1984. Study of terrain reduction, density anomalies and geophysical inversion methods in gravity field modelling. Tech. Rep. 5, Department of Geodetic Science and Surveying, The Ohio State University, Colombus.

Frappart, F., G. Ramillien, S. Biancamaria, N. M. Mognard, and A. Cazenave. 2006. Evolution of high-latitude snow mass derived from the GRACE gravimetry mission (2002-2004). *Geophysical research Letters*, 33:L02501. doi:10.1029/2005GL024778.

GFZ Postdam. 2013. The GRACE mission. http://www.gfz-potsdam.de/pb1/op/grace/ (accessed March 2013).

Gornitz, V., C. Rosenzweig, and D. Hillel. 1997. Effects of anthropogenic intervention in the land hydrologic cycle on global sea level rise. *Global and Planetary Change*, 14(3-4):147–161. doi:10.1016/S0921-8181(96)00008-2.

Grombein, T., K. Seitz, and B. Heck. 2013. Optimized formulas for the gravitational field of a tesseroid. *Journal of Geodesy*, 87(7):645–660. doi:10.1007/s00190-013-0636-1.

Haagmans, R. 2000. A synthetic Earth for use in geodesy. *Journal of Geodesy*, 74:503–511. doi:10.1007/s001900000112.

Hackney, R. and W. E. Featherstone. 2003. Geodetic versus geophysical perspectives of the 'gravity anomaly'. *Geophysical Journal International*, 154(1):35–43. doi:10.1046/j.1365-246X.2003.01941.x.

Han, S.-C., H. Kim, I.-Y. Yeo, P. Yeh, T. Oki, K.-W. Seo, D. Alsdorf, and S. B. Luthcke. 2009. Dynamics of surface water storage in the Amazon inferred from measurements of inter-satellite distance change. *Geophysical Research Letters*, 36:L09403. doi:10.1029/2009GL037910.

Han, S.-C., J. Sauber, S. Luthcke, C. Ji, and F. Pollitz. 2008. Implica-

tions of postseismic gravity change following the great 2004 Sumatra-Andaman earthquake from the regional harmonic analysis of GRACE intersatellite tracking data. *Journal of Geophysical Research*, 113:B11413. doi:10.1029/2008JB005705.

Han, S.-C., C. K. Shum, M. Bevis, C. Ji, and C.-Y. Kuo. 2006a. Crustal dilatation observed by GRACE after the 2004 Sumatra-Andaman earthquake. *Science*, 313(5787):658–662. doi:10.1126/science.1128661.

Han, S.-C., C. K. Shum, and A. Braun. 2005a. High-resolution continental water storage recovery from low-low satellite-to-satellite tracking. *Journal of Geodynamics*, 39(1):11–28. doi:10.1016/j.jog.2004.08.002.

Han, S.-C., C. K. Shum, and C. Jekeli. 2006b. Precise estimation of in situ geopotential differences from GRACE low-low satellite-to-satellite tracking and accelerometer data. *Journal of Geophysical Research*, 111:B04411. doi:10.1029/2005JB003719.

Han, S.-C., C. K. Shum, C. Jekeli, and D. Alsdorf. 2005b. Improved estimation of terrestrial water storage changes from GRACE. *Geophysical Research Letters*, 32:L07302. doi:10.1029/2005GL022382.

Han, S.-C., C. K. Shum, C. Jekeli, C.-Y. Kuo, C. Wilson, and K.-W. Seo. 2005c. Non-isotropic filtering of GRACE temporal gravity for geophysical signal enhancement. *Geophysical Journal International*, 163:18–25. doi:10.1111/j.1365-246X.2005.02756.

Han, S.-C. and F. J. Simons. 2008. Spatiospectral localization of global geopotential fields from GRACE reveals the coseismic gravity change due to the 2004 Sumatra-Andaman earthquake. *Journal of Geophysical Research*, 113:B01405. doi:10.1029/2007JB004927.

Heck, B. and K. Seitz. 2007. A comparison of the tesseroid, prism and point-mass approaches for mass reductions in gravity field modelling. *Journal of Geodesy*, 81(2):121–136. doi:10.1007/s00190-006-0094-0.

Heiskanen, W. A. and H. Moritz. 1967. *Physical Geodesy*. San Francisco: W. H. Freeman and Company.

Hildebrand, F. 1974. *Introduction to numerical analysis*. New York: McGraw-Hill.

Hinderer, J., O. Andersen, F. Lemoine, D. Crossley, and J.-P. Boy. 2006. Seasonal changes in the European gravity field from GRACE: A comparison with superconducting gravimeters and hydrology model predictions. *Journal of Geodynamics*, 41(1-3):59–68. doi:10.1016/j.jog.2005.08.037.

Hirt, C. 2010. Prediction of vertical deflections from high-degree spherical harmonic synthesis and residual terrain model data. *Journal of Geodesy*, 84(3):179–190.

Hirt, C. and M. Kuhn. 2012. Evaluation of high-degree series expansions of the topographic potential to higher-order powers. *Journal of Geophysical Research: Solid Earth*, 117(B12). doi:10.1029/2012JB009492.

Hofmann-Wellenhof, B. and H. Moritz. 2005. *Physical Geodesy*. Vienna: Springer.

Holmes, S. 2003. *High Degree Spherical Harmonic Synthesis: New Algorithms and Applications*. Doctoral dissertation, Geodesy, Perth, WA.

Ivins, E. R. 2009. Ice sheet stability and sea level rise. *Science*, 324:888–889. doi:10.1126/science.1173958.

Jacob, T., J. Wahr, W. T. Pfeffer, and S. Swenson. 2012. Recent contributions of glaciers and ice caps to sea level rise. *Nature*, 482:514–518. doi:10.1038/nature10847.

Jekeli, C. 1981. Alternative methods to smooth the Earth's gravity field. Tech. Rep. 327, Dept. of Geod. Sci. and Surv., Ohio State Univ., Columbus.

JPL NASA. 2013. GRACE: Gravity Recovery and Climate Experiment. http://podaac.jpl.nasa.gov/grace/ (accessed March, 2013).

Kaula, W. M. 2000. *Theory of satellite Geodesy: Applications of Satellites to Geodesy*. New York: Dover Publications, Inc.

King, M., P. Moore, P. Clarke, and D. Lavallée. 2006. Choice of optimal averaging radii for temporal GRACE gravity solutions, a comparison with GPS and satellite altimetry. *Geophysical Journal International*, 166:1–11. doi:10.1111/j.1365-246X.2006.03017.x.

Klees, R., E. A. Revtova, B. C. Gunter, P. Ditmar, E. Oudman, H. C. Winsemius, and H. H. G. Savenije. 2008. The design of an optimal filter for monthly GRACE gravity models. *Geophysical Journal International*, 175:417–432. doi:10.1111/j.1365-246X.2008.03922.x.

Klees, R., E. A. Zapreeva, H. C. Winsemius, and H. H. G. Savenije. 2007. The bias in GRACE estimates of continental water storage variations. *Hydrology and Earth System Sciences Discussions*, 3:3557–3594. doi:10.5194/hess-11-1227-2007.

Klosko, S., S. D. Rowlands, F. Lutchke, D. Lemoine, Chinn, and M. Rodell. 2009. Evaluation and validation of mascon recovery using GRACE KBRR data with independent mass flux estimates in the Mississippi basin. *Journal of Geodesy*, 83(9):817–827. doi:10.1007/s00190-009-0301-x.

Konikow, L. F. 2011. Contribution of global groundwater depletion since 1900 to sea-level rise. *Geophysical Research Letters*, 38(17):L17401. doi:10.1029/2011GL048604.

Kouba, J. 1983. A review of Geodetic and Geodynamic satellite DOPPLER positioning. *Reviews of Geophysics and Space Physics*, 21(1):27–40.

Kuhn, M. 2003. Geoid determination with density hypotheses from isostatic models and geological information. *Journal of Geodesy*, 77(1-2):50–65. doi:10.1007/s00190-002-0297-y.

Kuhn, M., W. Featherstone, and J. Kirby. 2009. Complete spherical Bouguer gravity anomalies over Australia. *Australian Journal of Earth Sciences*, 56(2):209–219. doi:10.1080/08120090802547041.

Kuhn, M. and W. E. Featherstone. 2002. On the optimal spatial resolution of crustal mass distributions for forward gravity field modeling. In *Gravity and Geoid 2002*, ed. I. N. Tziavos, 195–200. 3rd Meeting of the International Gravity and Geoid Commission.

Kuhn, M. and W. E. Featherstone. 2003. On the construction of a Synthetic Earth Gravity Model (SEGM). In *3rd Meeting of the International Gravity and Geoid Commission*, ed. I. N. Tziavos, 189–195. Thessaloniki, Greece.

Kuhn, M. and W. E. Featherstone. 2005. Construction of a Synthetic Earth Gravity Model by Forward Gravity Modelling. In *A Window on the Future of Geodesy*, ed. F. Sansó, vol. 128, 350–355. International Association of Geodesy Symposia. doi:10.1007/3-540-27432-4_60.

Kuhn, M. and K. Seitz. 2005. Comparison of Newton's integral in the space and frequency domains. In *A Window on the Future of Geodesy*, ed. F. Sansó, vol. 128, 386–391. International Association of Geodesy Symposia. doi:10.1007/3-540-27432-4_66.

Kusche, J. 2007. Approximate decorrelation and non-isotropic smoothing of time-variable GRACE-type gravity field models. *Journal of Geodesy*, 81(11):733–749. doi:10.1007/s00190-007-0143-3.

Kusche, J., R. Schmidt, S. Petrovic, and R. Rietbroek. 2009. Decorrelated GRACE time-variable gravity solutions by GFZ and their validation using a hydrological model. *Journal of Geodesy*, 83:903–913. doi:10.1007/s00190-009-0308-3.

Kusche, J. and E. J. O. Schrama. 2005. Surface mass redistribution inversion from global GPS deformation and Gravity Recovery and Climate Experiment (GRACE) gravity data. *Journal of Geophysical Research*, 110:B09409. doi:10.1029/2004JB003556.

Lambert, A., T. S. James, J. O. Liard, and N. Courtier. 1995. The role and capability of absolute gravity measurements in determining the temporal variations in the Earth's gravity field. In *Global Gravity and Its Temporal Variations*, eds. R. H. Rapp, A. Cazenave, and R. S. Nerem, vol. 116, 20–29. International Association of Geodesy Symposia, Berlin: Springer.

Lelgemann, D. and C. Cui. 2003. Analytical versus numerical integration in Satellite Geodesy. In *Geodesy - The Challenge of the* 3^{rd} *Millennium*, eds. E. Grafarend, F. Krumm, and V. Schwarz, 269–278. Berlin: Springer.

Lemoine, F., S. Kenyon, J. Factor, R. Trimmer, N. Pavlis, D. Chinn, C. Cox, S. Klosko, S. Luthcke, M. Torrence, Y. Wang, R. Williamson, E. Pavlis, R. Rapp, and T. Olson. 1998. The development of the joint NASA GSFC and the National Imagery and Mapping Agency (NIMA) geopotential model

EGM96. Tech. Rep. NASAITP-1998-206861, Goddard Space Flight Centre, Greenbelt.

Lemoine, F. G., S. Bruisma, S. Loyer, R. Biancale, J.-C. Marty, F. Perosanz, and G. Balmino. 2007a. Temporal gravity field models inferred from GRACE data. *Advances in Space Research*, 39:1620–1629. doi:10.1016/j.asr.2007.03.062.

Lemoine, F. G., S. B. Luthcke, D. D. Rowlands, D. S. Chinn, S. M. Klosko, and C. M. Cox. 2007b. The use of mascons to reslove time-variable gravity from GRACE. In *Dynamic Planet: Monitoring and Understanding a Dynamic Planet with Geodetic and Oceanographic Tools*, eds. P. Tregoning and C. Rizos, vol. 130, 231–236. International Association of Geodesy Symposia, Berlin: Springer. doi:10.1007/978-3-540-49350-1_35.

Leuliette, E. W., R. S. Nerem, and G. L. Russell. 2002. Detecting time variations in gravity associated with climate change. *Journal of Geophysical Research*, 107:2112. doi:10.1029/2001JB000404.

Lombard, A., D. Garcia, G. Ramillien, A. Cazenave, R. Biancale, J. M. Lemoine, F. Flechtner, R. Schmidt, and M. Ishii. 2007. Estimation of steric sea level variations from combined GRACE and Jason-1 data. *Earth and Planetary Science Letters*, 254:194–202. doi:10.1016/j.epsl.2006.11.035, provided by the Smithsonian/NASA Astrophysics Data System.

Longuevergne, L., B. R. Scanlon, and C. R. Wilson. 2010. GRACE Hydrological estimates for small basins: Evaluating processing approaches on the High Plains Aquifer, USA. *Water Resources Research*, W11517. doi:10.1029/2009WR008564.

Luthcke, S. B., A. Arendt, D. Rowlands, J. McCarthy, and C. Larsen. 2008. Recent glacier mass changes in the Gulf of Alaska region from GRACE mascon solutions. *Journal Glaciology*, 54:767–777.

Luthcke, S. B., D. D. Rowlands, F. G. Lemoine, S. M. Klosko, D. Chinn, and J. J. McCarthy. 2006a. Monthly spherical harmonic gravity field solutions determined from GRACE inter-satellite range-rate data alone. *Geophysical Research Letters*, 33:L02402. doi:10.1029/2005GL024846.

Luthcke, S. B., H. J. Zwally, W. Abdalati, D. D. Rowlands, R. D. Ray, R. S. Nerem, F. G. Lemoine, S. M. Klosko, J. J. McCarthy, and D. Chinn. 2006b. Recent Greenland ice mass loss by drainage system from satellite gravity observations. *Science*, 314:1286–1289. doi:10.1126/science.1130776.

Mader, K. 1951. Das Newtonsche Raumpotential prismatischer Körper und seine Ableitung bis zur dritten Ordnung. *Österreichische Zeitschrift für Vermessungswesen*, Sonderheft 11.

Mancini, A. 1971. Satellite geodesy: data acquisition. *Eos, Transactions American Geophysical Union*, 52(3):IUGG34?IUGG37. doi:10.1029/EO052i003pIU034.

Migliaccio, F., M. Reguzzoni, F. Sansò, G. D. Via, and R. Sabadini. 2008. Detecting geophysical signals in gravity satellite missions. *Geophysical Journal International*, 172:56–66. doi:10.1111/j.1365-246X.2007.03600.x.

Mohr, P. J., B. N. Taylor, and D. B. Newell. 2012. CODATA recommended values of the fundamental physiscal constants: 2010. *Reviews of Modern Physics*, 84:1527–1605. doi:10.1103/RevModPhys.84.1527.

Morison, J., J. Wahr, R. Kwok, and C. Peralta-Ferriz. 2004. Recent trends in Artic Ocean mass distribution revealed by GRACE. *Earth and Planetary Science Letters*, 228:281–297. doi:10.1029/2006GL029016.

Moritz, H. 1990. *The figure of the Earth: Theoretical geodesy and the Earth's interior*. Karlsruhe: Wichmann.

Nagy, D. 1966. The gravitational attraction of a right rectangular prism. *Geophysics*, 31(2):362–371. doi:10.1190/1.1439779.

Nagy, D., G. Papp, and J. Benedek. 2000. The gravitational potential and its derivatives for the prism. *Journal of Geodesy*, 74(7):552–560. doi:10.1007/s001900000116.

Nerem, R. S., C. Jekeli, and W. M. Kaula. 1995. Gravity field determination and characteristics: Retrospective and prospective. *Journal of Geophysical Research*, 100(B8):15,053–15,074. doi:10.1029/94JB03257.

Nerem, R. S., J. Wahr, and E. W. Leuliette. 2003. Measuring the distribution

of ocean mass using GRACE. *Space Science Reviews*, 108(1-2):331–344. doi:10.1023/A:1026275310832.

Nóvak, P., P. Vaníček, M. Véronneau, S. Holmes, and W. Featherstone. 2001. On the accuracy of modified Stokes's integration in high-frequency gravimetric geoid determination. *Journal of Geodesy*, 74(11):644–654. doi:10.1007/s001900000126.

Ogawa, R. and K. Heki. 2007. Slow post seismic recovery of geoid depression formed by the 2004 Sumatra-Andaman earthquake by mantle water diffusion. *Geophysical Research Letters*, 34:L06313. doi:10.1029/2007GL029340.

Pail, R. 2000. *Synthetic global gravity model for planetary bodies and applications in satellite gravity gradiometry*. Doctoral dissertation, Institut für Navigation, Graz : Geodastische Inst. der Techn. Univ.

Panet, I., Mikhailov, M. Diament, F. Pollitz, G. King, O. de Viron, M. Holschneider, R. Biancale, and J.-M. Lemoine. 2007. Coseismic and post-seismic signatures of the Sumatra 2004 Decenber and 2005 March earthquakes in GRACE satellite gravity . *Geophysical Journal International*, 171:177–190. doi:10.1111/j.1365-246X.2007.03525.x.

Paulson, A., S. Zhong, and J. Wahr. 2007. Inference of mantle viscosity from GRACE and relative sea level data . *Geophysical Journal International*, 171(2):497–508. doi:10.1111/j.1365-246X.2007.03556.x.

Peltier, W. 1998. Postglacial variations in the level of the sea: implications for climate dynamics and solid-Earth geophysics. *Reviews of Geophysics*, 36(4):603–689. doi:10.1029/98RG02638.

Peltier, W. 1999. Global sea level rise and glacial isostatic adjustment. *Global and Planetary Change*, 20(2-3):93–123. doi:10.1016/S0921-8181(98)00066-6.

Peltier, W. 2009. Closure of the budget of globalsealevelriseover the GRACE era: the importance and magnitudes of the requiredcorrections for globalglacial-isostaticadjustment. *Quaternary Science Reviews*, 28(17-18):1658?1674. doi:10.1016/j.quascirev.2009.04.004.

Ramillien, G. 2002. Gravity/magnetic potential of uneven shell topography. *Journal of Geodesy*, 76(3):139–149. doi:10.1007/s00190-002-0193-5.

Ramillien, G., A. Cazenave, and O. Brunau. 2004. Global time variations of hydrologycal signals from GRACE satellite gravimetry. *Geophysical Journal International*, 158:813–826. doi:10.1111/j.1365-246X.2004.02328.x.

Ramillien, G., F. Frappart, A. Cazenave, and A. Güntner. 2005. Time variations of land water storage from an inversion of 2 years of GRACE geoids [rapid communication]. *Earth and Planetary Science Letters*, 235(1-2):283–301. doi:10.1016/j.epsl.2005.04.005.

Ramillien, G., A. Lombard, A. Cazenave, E. Ivins, R. Remy, and R. Biancale. 2006. Interannual variations of the mass balance of the Antarctica and Greenland ice sheets from GRACE. *Global and Planetary Change*, 53(3):198–208. doi:10.1016/j.gloplacha.2006.06.003.

Reigber, C. 1989. Gravity field recovery from satellite tracking data. In *Theory of satellite geodesy and gravity field determination*, ed. Sansò, F. and Rummel, R. Berlin: Springer-Verlag. doi:10.1007/BFb0010552.

Reigber, C., G. Balmino, P. Schwintzer, R. Biancale, A. Bode, J. Lemoine, R. König, S. Loyer, K. H. Neumayer, J. C. Marty, F. Barthelmes, F. Perosanz, and S. Y. Zhu. 2003. Global gravity field recovery using solely GPS tracking and accelerometer data from CHAMP. In *Earth gravity field from space - From sensors to Earth sciences*, eds. G. Beutler, R. Rummel, M. R. Drinkwater, and R. v. Steiger. Dordrecht: Kluwer Academic Publisher. doi:10.1023/A:1026217713133.

Rignot, E., I. Velicogna, M. R. van den Broeke, A. Monaghan, and J. T. M. Lenaerts. 2011. Acceleration of the contribution of the Greenland and Antarctic ice sheets to sea level rise. *Geophysical Research Letters*, 38(5):L05503. doi:10.1029/2011GL046583.

Rodell, M., J. S. Famiglietti, J. Chen, S. I. Seneviratne, P. Viterbo, S. Holl, and C. R. Wilson. 2004. Basin scale estimates of evapotranspiration using GRACE and other observations. *Geophysical Research Letters*, 31:L20504. doi:10.1029/2004GL020873.

Rowlands, D. D., S. B. Luthcke, S. M. Klosko, F. G. R. Lemoine, D. S. Chinn, J. J. McCarthy, C. M. Cox, and O. B. Anderson. 2005. Re-

solving mass flux at high spatial and temporal resolution using GRACE inter satellite measurements. *Geophysical Research Letters*, 32:L04310. doi:10.1029/2004GL021908.

Rowlands, D. D., R. D. Ray, D. S. Chinn, and F. G. Lemoine. 2002. Short-arc analysis in intersatellite tracking data in a gravity mapping mission. *Journal of Geodesy*, 76(6):307–316. doi:10.1007/s00190-002-0255-8.

Rummel, R. 2005. Geoid and gravity in Earth sciences - An overview. *Earth, Moon, and Planets*, 94(1-2):3–11. doi:10.1007/s11038-005-3755-8.

Rummel, R., G. Balmino, J. Johannessen, P. Visser, and P. L. Woodworth. 2002. Dedicated gravity field missions - principles and aims. *Journal of Geodynamics*, 33(1-2):2–30. doi:10.1016/S0264-3707(01)00050-3.

Rummel, R., R. H. Rapp, and H. Sünkel. 1988. Comparisons of global topographic/isostatic models to the earth's observed gravity field. Tech. Rep. 388, Dept Geod Sci and Surv, Ohio State University, Columbus.

Rummel, R. and M. van Gelderen. 1995. Meissl scheme - spectral characteristics of physical geodesy. *Manuscripta Geodaetica*, 20:379–385.

Sabadini, R., R. E. M. Riva, and G. Dalla Via. 2007. Coseismic rotation changes from the 2004 Sumatra earthquake: the effects of Earth's compressibility versus earthquake induced topography. *Geophysical Journal International*, 171:231–243. doi:10.1111/j.1365-246X.2007.03495.x.

Schmidt, R., P. Schwintzer, F. Flechtner, C. Reigber, A. Güntner, P. Döll, G. Ramillien, A. Cazenave, S. Petrovic, H. Jochmann, and J. Wünsch. 2006. GRACE observations of changes in continental water storage. *Global and Planetary Change*, 50:112–126. doi:10.1016/j.gloplacha.2004.11.018.

Schrama, E. J. O., B. Wouters, and D. A. Lavallée. 2007. Signal and noise in Gravity Recovery and Climate Experiment (GRACE) observed surface mass variations. *Journal of Geophysical Research*, 112:B08407. doi:10.1029/2006JB004882.

Seitz, K. and B. Heck. 2003. Efficient calculation of topographic reductions by the use of tesseroids. In *EGS - AGU - EUG Joint Assembly*, 9336. Provided by the SAO/NASA Astrophysics Data System.

Seo, K.-W. and C. R. Wilson. 2005. Simulated estimation of hydrological loads from GRACE. *Journal of Geodesy*, 78(7-8):442–456. doi:10.1007/s00190-004-0410-5.

Seo, K.-W., C. R. Wilson, J. S. Famiglietti, J. L. Chen, and M. Rodell. 2006. Terrestrial water mass load changes from Gravity Recovery and Climate Experiment (GRACE). *Water Resources Research*, 42:W05417. doi:10.1029/2005WR004255.

Shum, C. K., S.-C. Han, C. Kuo, K. Seo, and C. Wilson. 2004. Assessment of GRACE time-variable gravity observables: a new filtering technique to enhance signal spatial resolutions. In *American Geophysical Union (AGU) Fall Meeting*. San Francisco, USA.

Smith, D., D. Robertson, and D. Milbert. 2000. Gravitational attraction of local crustal masses in spherical coordinates. *Journal of Geodesy*, 74(11-12):783–795. doi:10.1007/s001900000142.

Swanson, L. W. and J. A. Yeager. 1971. A new world geodetic network. *The Polar Record*, 15(99):863–870.

Swenson, S. and J. Wahr. 2002. Methods for inferring regional surface-mass anomalies from gravity recovery and climate experiment (GRACE) measurements of time-variable gravity. *Journal of Geophysical Research*, 107(B9):2193. doi:10.1029/2001JB000576.

Swenson, S. and J. Wahr. 2003. Monitoring changes in continental water storage with GRACE. *Space Science Reviews*, 108(1):345–354. doi:10.1023/A:1026135627671.

Swenson, S. and J. Wahr. 2006. Post-processing removal of correlated errors in GRACE data. *Geophysical Research Letters*, 33:L08402. doi:10.1029/2005GL025285.

Swenson, S. and J. Wahr. 2009. Monitoring the water balance of Lake Victoria, East Africa from space. *Journal of Hydrology*, 370:163–176. doi:10.1016/j.jhydrol.2009.03.008.

Swenson, S., J. Wahr, and P. Milly. 2003. Estimated accuracies of regional water storage variations inferred from the gravity recovery and

climate experiment (GRACE). *Water Resources Research*, 39(8):1223. doi:10.1029/2002WR001808.

Tamisiea, M., E. Leuliette, J. Davis, and J. Mitrovica. 2005. Constraining hydrological and cryospheric mass flux in southeastern Alaska using space-based gravity measurements. *Geophysical Research Letters*, 32:L20501. doi:10.1029/2005GL023961.

Tapley, B. D., S. Bettadpur, J. C. Ries, P. F. Thompson, and M. M. Watkins. 2004a. GRACE measurements of mass variability in the Earth system. *Science*, 305:503–505. doi:10.1126/science.1099192.

Tapley, B. D., S. Bettadpur, M. Watkins, and C. Reigber. 2004b. The gravity recovery and climate experiment: Mission overview and early results. *Geophysical Research Letters*, 31:L09607. doi:10.1029/2004GL019920.

Torge, W. 1989. *Gravimetry*. Berlin: Walter de Gruyter.

Torge, W. 2001. *Geodesy*. 3rd ed. Berlin: Walter de Gruyter.

Tsoulis, D. 1999. *Analytical and numerical methods in gravity field modelling of ideal and real masses*. PhD Thesis, Technische Universität, München, Germany.

Tsoulis, D. 2000. A note on the gravitational field of the right rectangular prism. *Bollettino di geodesia e scienze affini*, 59:21–35.

Tsoulis, D. 2004. Two Earth gravity models from the analysis of global crustal data. *Zeitschrift für Geodäsie, Geoinformation und Landmanagement*, 129:311–316.

Tsoulis, D. 2012. Analytical computation of the full gravity tensor of a homogeneous arbitrarily shaped polyhedral source using line integrals. *Geophysics*, 77:F1–F11.

Tsoulis, D. and M. Kuhn. 2007. Recent developments in synthetic Earth gravity models in view of the availability of digital terrain and crustal databases of global coverage and increased resolution. In *Proceedings of the 1st International Symposium of the International Gravity Field Service*, ed. Kiliçoğlu, A. and Forsberg, R., vol. 18, 354–359. Ankara: Harita Genel Komutanliği.

Tziavos, I. N. 1996. Comparisons of spectral techniques for geoid computations over large regions. *Journal of Geodesy*, 70:357–373. doi:10.1007/BF00868188.

UTCSR. 2013. Gravity recovery and climate experiment homepage. http://www.csr.utexas.edu/grace/ (accessed March,2013).

Vaníček, P. and E. J. Krakiwsky. 1986. *Geodesy : the Concepts*. 2nd ed. Amsterdam: Elsevier.

Velicogna, I. 2009. Increasing rates of ice mass loss from the Greenland and Antarctic ice sheets revealed by GRACE. *Geophysical Research Letters*, 36:L19503. doi:10.1029/2009GL040222.

Velicogna, I. and J. Wahr. 2006a. Acceleration of Greenland ice mass loss in spring 2004. *Nature*, 443:329–331. doi:10.1038/nature05168.

Velicogna, I. and J. Wahr. 2006b. Measurements of Time-Variable Gravity Show Mass Loss in Antarctica. *Science*, 311:1754–1756. doi:10.1126/science.1123785.

Vermeer, M. 1995. Mass point geopotential modelling using fast spectral techniques; historical overview, toolbox description, numerical experiment. *Manuscripta Geodatica*, 20:362–378.

Wada, Y., L. P. H. van Beek, C. M. van Kempen, J. W. T. M. Reckman, S. Vasak, and M. F. P. Bierkens. 2010. Global depletion of groundwater resources. *Geophysical Research Letters*, 37(20):L20402. doi:10.1029/2010GL044571.

Wahr, J., M. Molenaar, and F. Bryan. 1998. Time-variability of the Earth's gravity field: Hydrological and oceanic effects and their possible detection using GRACE. *Journal of Geophysical Research*, 103:30,205 –30,230. doi:10.1029/98JB02844.

Wahr, J., S. Swenson, V. Zlotnicki, and I. Velicogna. 2004. Time-variable gravity from GRACE: First result. *Geophysical Research Letters*, 31:L11501. doi:10.1029/2004GL019779.

Wieczorek, M. 2007. 10.05 - Gravity and Topography of the Terrestrial Planets. In *Treatise on Geophysics*, ed. E. in Chief:Gerald Schubert, 165 – 206.

Amsterdam: Elsevier. doi:10.1016/B978-044452748-6.00156-5.

Wieczorek, M. and R. Phillips. 1998. Potential anomalies on a sphere: applications to the thickness of the lunar crust. *Journal of Geophysical Research*, 103(E1):1715–1724. doi:10.1029/97JE03136.

Wittwer, T., R. Klees, K. Seitz, and B. Heck. 2008. Ultra-high degree spherical harmonic analysis and synthesis using extended-range arithmetic. *Journal of Geodesy*, 82(4-5):223–229. doi:10.1007/s00190-007-0172-y.

Wouters, B., D. Chambers, and E. Schrama. 2008. GRACE observes small-scale mass loss in Greenland. *Geophysical Research Letters*, 35:L20501. doi:10.1029/2008GL034816.

Zhang, Z.-Z., B. F. Chao, Y. Lu, and H.-T. Hsu. 2009. An effective filtering for GRACE time-variable gravity: Fan filter. *Geophysical Research Letters*, 36:L17311. doi:10.1029/2009GL039459.

Appendix A

Results from simple mass discs

Appendix A provides a complete overview of the validation results obtained for disc masses IIa, IIb, IIIa and IIIb (see Section 5.3). As the validation results are very similar to that for disc masses Ia and Ib presented in Section 5.4, their description will be kept brief here with mostly focusing on differences.

A.1 Validation Results for Disc Masses IIa and IIb

This section provides the validation results obtained for the disc masses IIa and IIb (see Section 5.3) that simulate mass changes at the equator such as hydrological changes in the Earth's tropical regions. Both disc masses are centred at $\phi = 0°$, $\lambda = 180°$ (see Figure A.1) and have the same total mass but differ by their respective horizontal extent. Figure A.1 illustrates that disc mass IIa has double the spatial extension (spherical radius of 10°) than disc mass IIb (spherical radius of 5°). Again, these extensions have been selected to model spatially more wide spread and more concentrated mass changes.

Using these disc masses as simulated input mass for the validation procedure the same four scenarios as for disc masses Ia and Ib with respect to the filter of the Stokes coefficients will be examined (see Section 5.4):

(1) No filter
(2) Gaussian isotropic filter
(3) Han's anisotropic filter
(4) Kusche's de-correlated, anisotropic filter

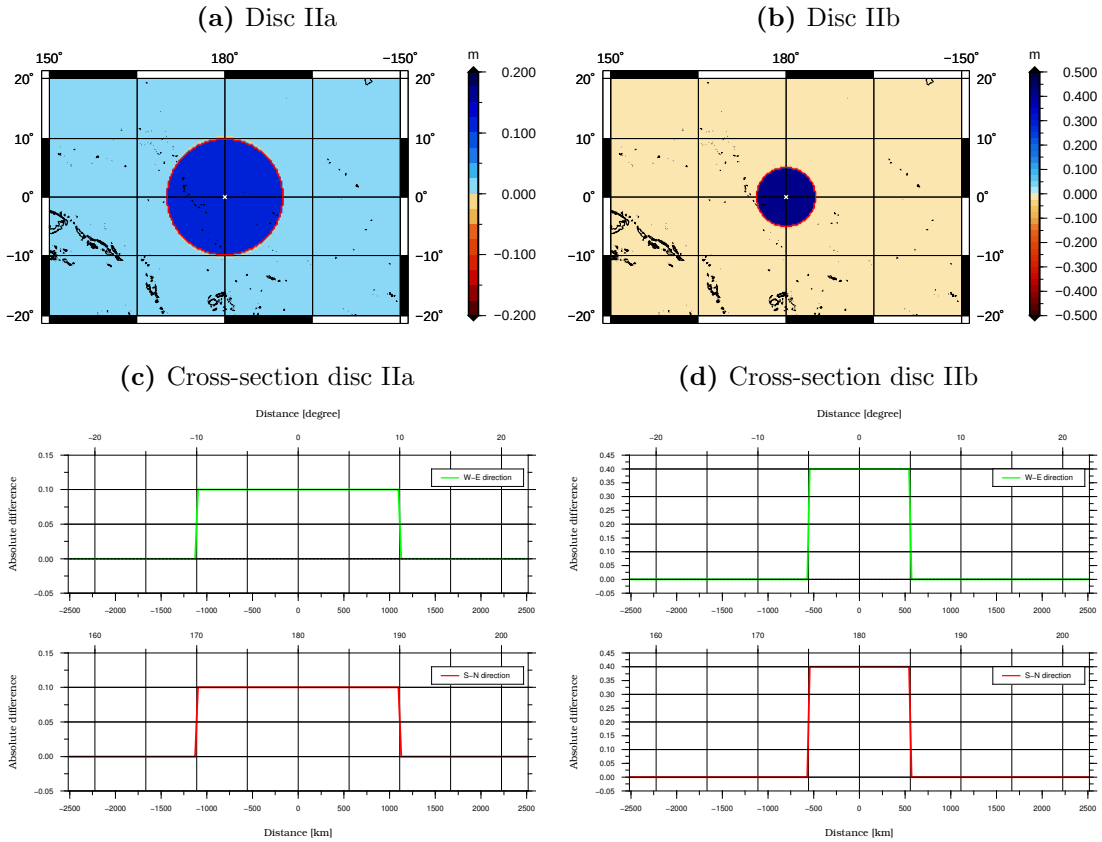

Figure A.1: Simulated disc masses IIa and IIb with radii 10° and 5°, respectively, centred at $\phi = 0°, \lambda = 180°$ (panels a and b) and west-east and south-north cross sections (panels c and d).

A.1.1 Results for no filter

As for disc masses Ia and Ib the first case examined is the recovery of the input masses without applying any filter to the Stokes coefficients. As discussed in Section 5.4, this will provide information on the ability to recover the input masses by the use of a band-limited representation using spherical harmonic expansions up to the maximum degree $l_{max} = 60$. Figure A.2 shows the recovered disc masses IIa and IIb and respective cross-sections in west-east and south-north directions of the recovered masses and the difference between the input and recovered masses.

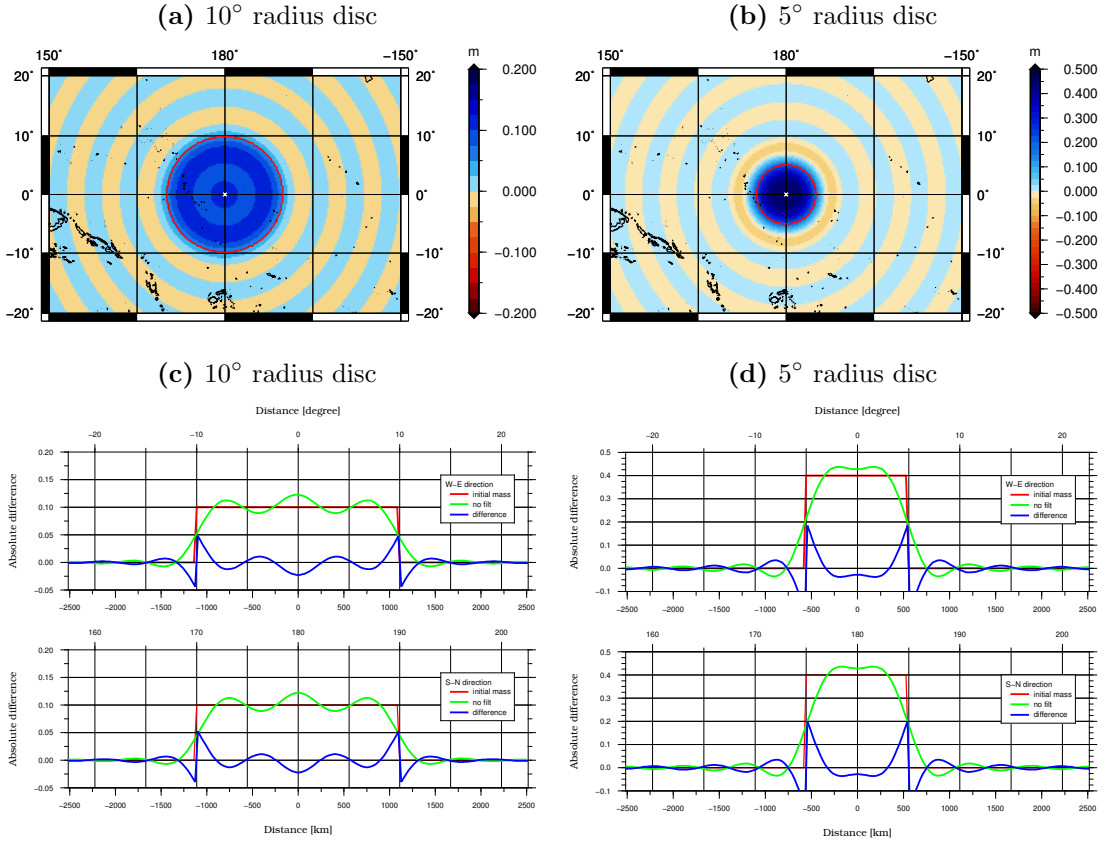

Figure A.2: Recovered disc masses with radii 10° and 5° centred at $\phi = 0°, \lambda = 180°$ (panels a and b) and west-east and south-north cross sections (panels c and d). No smoothing filter has been applied. The red circle indicates the spatial extension of the input disc mass.

As for disc masses Ia and Ib, the Gibbs phenomenon is the dominating feature in the recovered masses (see Figure A.2) with undulating differences over the disc and radiating away from the disc. Larger differences occur at the edge of the discs demonstrating the inability to model a jump discontinuity via a band limited spherical harmonic representation based on periodic base functions. The Gibbs effect is larger for disc mass IIb than for IIa due to the higher jump discontinuity for the former. While the undulations have a considerable magnitude over the disc mass their magnitude quickly decreases to a value of effectively zero but spread over the whole globe.

Quantifying spectral leakage by the difference in input mass and the recovered

mass within the same spatial extent as the input mass reveals 6.2% and 12.5% spectral leakage for disc mass IIa and IIb, respectively. This means mass has leaked away from the input mass and only 93.8% and 87.5% of the input mass has been recovered for disc mass IIa and IIb, respectively (see Table 5.2 and Table 5.3 in Section 5.5). Higher spectral leakage for disc IIb confirms the larger differences visible in Figure A.2.

A.1.2 Gaussian Isotropic Filter

This validation uses again the Gaussian isotropic filter to smooth the Stokes coefficients within the validation procedure (see Section 5.1). As for disc masses Ia and Ib the same filter radii are used to form the same six scenarios referring here to "weak" smoothing using $r_g = 125$ km, "medium" smoothing using $r_g = 250$ km and "strong" smoothing using $r_g = 500$ km:

(a) $r_g = 125$ km / disc radius is 10°
(b) $r_g = 125$ km / disc radius is 5°
(c) $r_g = 250$ km / disc radius is 10°
(d) $r_g = 250$ km / disc radius is 5°
(e) $r_g = 500$ km / disc radius is 10°
(f) $r_g = 500$ km / disc radius is 5°

Examples for the input and recovered mass distributions given as west-east and south-north cross-sections are provided by Figure 5.7 in Section 5.4.2.

Figure A.3 and Figure A.4 summarize all validation results for the recovered masses and for west-east and south-north cross-sections of the difference between the input and recovered masses. Statistical values for the recovered masses and the differences to the input masses are listed in Table 5.2 and Table 5.3 in Section 5.5. The results are very similar to the scenario of applying Gaussian isotropic filters to disc masses Ia and Ib (see Section 5.4.2). Therefore, here only the main features are briefly presented and any differences highlighted.

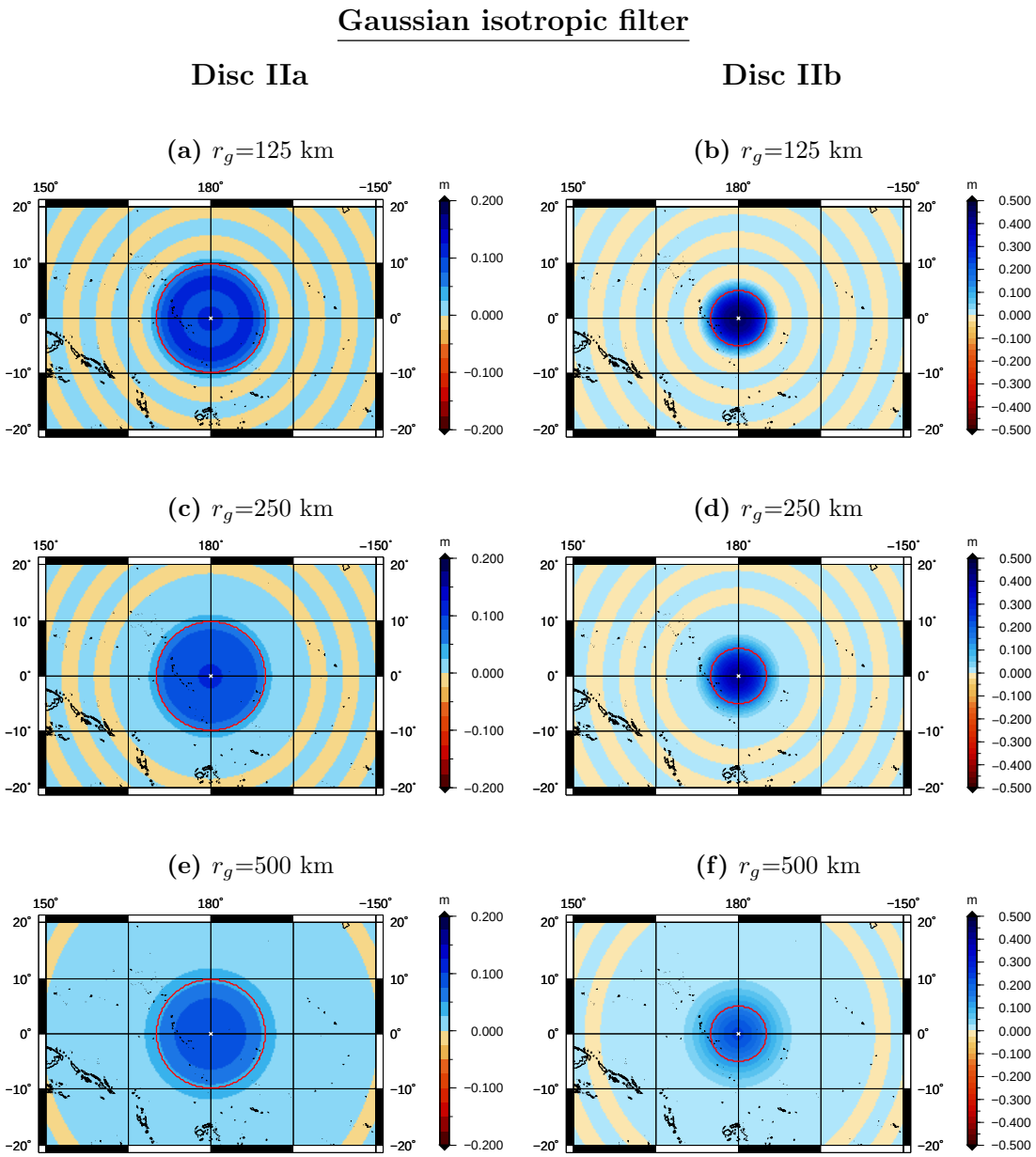

Figure A.3: Recovered masses for discs IIa and II with radii 10° and 5°, respectively, after applying Gaussian isotropic smoothing. The discs are centred at $\phi = 0°, \lambda = 180°$. The red circle indicates the spatial extension of the input disc mass.

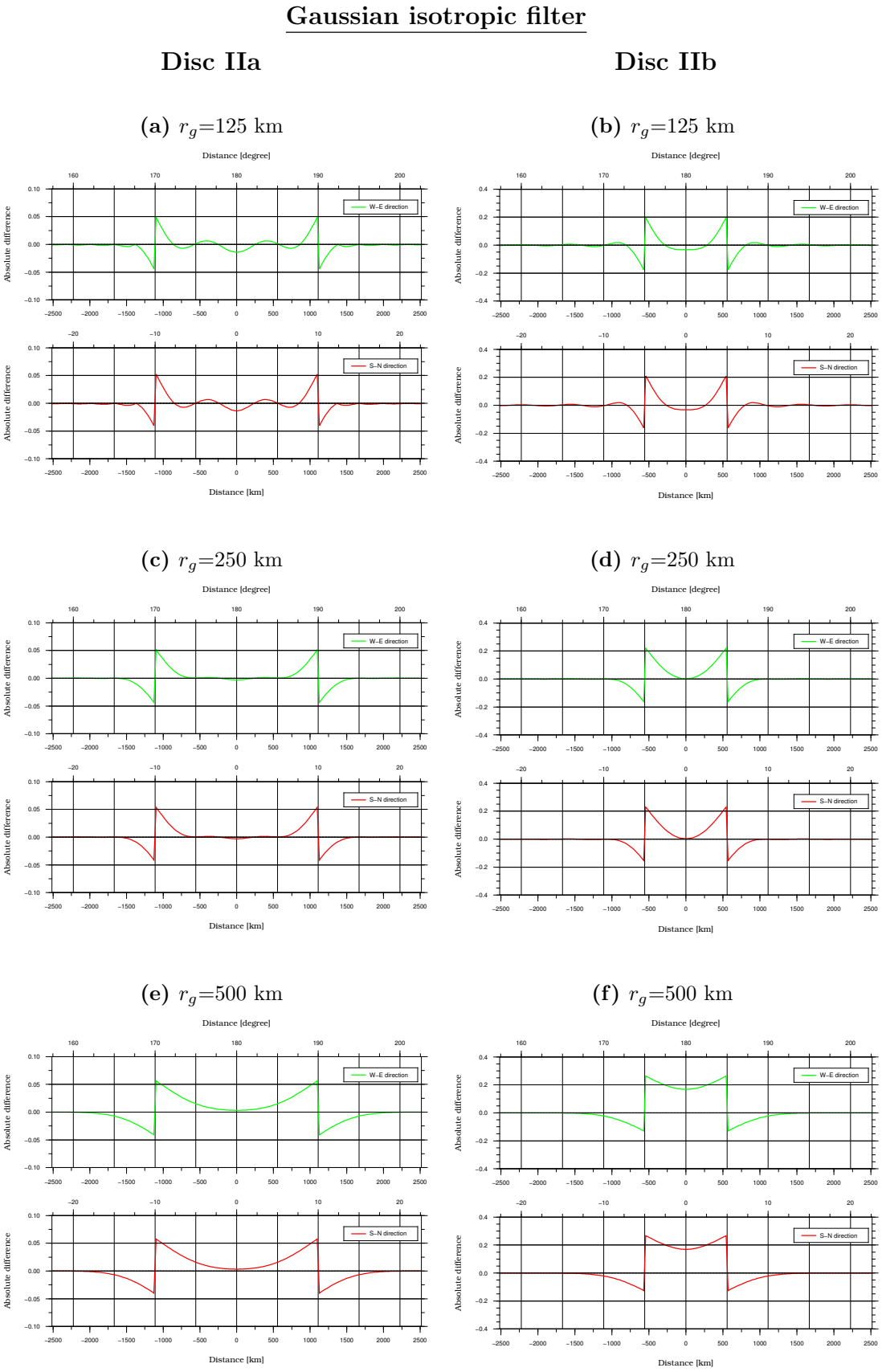

Figure A.4: West-east (green line) and south-north (red line) cross-sections of difference between the input and recovered masses when applying Gaussian isotropic smoothing.

(a) Gaussian isotropic filter for r_g = 125 km and 10° disc

Validation results for weak Gaussian isotropic smoothing applied to disc mass IIa are illustrated in Figure A.3a. Like for the scenario without smoothing, the recovered mass distribution mostly shows the Gibbs phenomenon with largest differences at the disc's edge (see Figure A.4a). Leakage is small with 91.2% of the total mass recovered and spatial leakage contributes with 2.8% (see Table 5.2 in Section 5.5). Like results for weak Gaussian isotropic smoothing applied to disc mass Ia (see Section 5.4.2) differences show the same behaviour in west-east and south-north direction as expected for an isotropic filter.

(b) Gaussian isotropic filter for r_g = 125 km and 5° disc

Similar results are obtained when applying the same filter onto disc mass IIb, though leakage is increased. The recovered mass distribution illustrated in Figure A.3b shows again the Gibbs phenomenon with smaller differences over the centre of the disc and large differences at the disc's edge (see Figure A.4b). The magnitude of the differences is almost identical to the scenario of weak Gaussian smoothing applied to disc mass Ib (see Section 5.4.2). The total mass recovered is 82.1%, which results in a contribution due to spatial leakage of 5.4% (see Table 5.3 in Section 5.5). Like for the previous scenario, the behaviour of the differences is the same in west-east and south-north direction.

(c) Gaussian isotropic filter for r_g = 250 km to 10° radius disc

Leakage has increased when applying medium Gaussian isotropic filter to disc mass IIa as illustrated in Figure A.3c. Compared to scenario (a) the distinct undulating pattern by the Gibbs phenomenon starts at a longer distance from the original disc mass. Now 84.7% of the original mass is recovered while 9.1% is due to spatial leakage (see Table 5.2 in Section 5.5). The differences illustrated in Figure A.4c indicate that the mass over the centre of the disc is almost unchanged, whereas larger mass loss occurs around the disc's edges. Again the same behaviour

of the differences in west-east and south-north direction are visible.

(d) Gaussian isotropic filter for r_g = 250 km and 5° disc

Further increased leakage is present when applying the same filter to the spatially more concentrated disc mass IIb. This is the same behaviour as observed in scenario (d) for the application of medium Gaussian isotropic smoothing to the disc mass Ib (see Section 5.4.2). Again there is almost no mass change over the centre of the disc mass but largely reduced towards the disc's edge. In this scenario spatial leakage accounts for 17.6% and only 69.9% of the initial mass is recovered. Again the same behaviour of the differences in west-east and south-north direction is visible.

(e) Gaussian isotropic filter for r_g = 500 km and 10° disc

Leakage dominates the recovered mass distribution when applying strong Gaussian isotropic smoothing to disc mass IIa as illustrated in Figure A.3e. The undulating pattern around the disc has been considerably pushed away from the disc's original extension. Now mass loss starts immediately over the disc's centre and increases quickly towards the disc's edge (see Figure A.4e). With 70.2% considerably less mass is recovered when compared to the previous scenarios. Spatial leakage accounts now for 23.6% (see Table 5.2 in Section 5.5). This is a similar level as obtained for the application of the same filter to disc mass Ia (see also Section 5.4.2).

(f) Gaussian isotropic filter for r_g = 500 km and 5° disc

Applying strong Gaussian isotropic smoothing to disc mass IIb now results in leakage effects that spread over a considerable distance from the disc's original edge (see Figure A.3f). The differences illustrated in Figure A.3f document that the leaked mass originates from all parts of the disc, though largest differences occur at the disc's edge, thus most mass is leaked from the disc's edges. In this

scenario only 44.4% of the original mass is recovered while 43.1% account for spatial leakage. Again this is a similar level as obtained for the application of the same filter to disc mass Ia (see also Section 5.4.2).

A.1.3 Han's anisotropic filter

Disc masses IIa and IIb are now subjected to the same anisotropic filter as applied to disc masses Ia and Ib (see Section 5.4.3). Han's anisotropic filter is used with three different degrees of smoothing by varying the filter radii in west-east and south-north direction. Again, the three degrees of smoothing are referred to as "weak", "medium" and "strong" anisotropic smoothing. Like in Section 5.4.3, this selection results in six different validation scenarios all using the parameter m_1=15:

(a) r_0=125 km, r_1=250 km, disc radius is 10°
(b) r_0=125 km, r_1=250 km, disc radius is 5°
(c) r_0=250 km, r_1=500 km, disc radius is 10°
(d) r_0=250 km, r_1=500 km, disc radius is 5°
(e) r_0=500 km, r_1=1000 km, disc radius is 10°
(f) r_0=500 km, r_1=1000 km, disc radius is 5°

Examples for the input and recovered mass distributions given as west-east and south-north cross-sections are provided by Figure 5.10 in Section 5.4.3.

The validation results for the six scenarios are shown in Figure A.5 for the recovered mass distributions and in Figure A.6 for west-east and south-north cross-sections of the differences between the input and recovered masses. Statistical values for the recovered masses and the differences to the input masses are listed in Table 5.2 and Table 5.3 in Section 5.5. Results are generally similar to the case of applying Han's anisotropic filter to disc masses Ia and Ib (see Section 5.4.3). Therefore, here only the main features are briefly presented and differences highlighted.

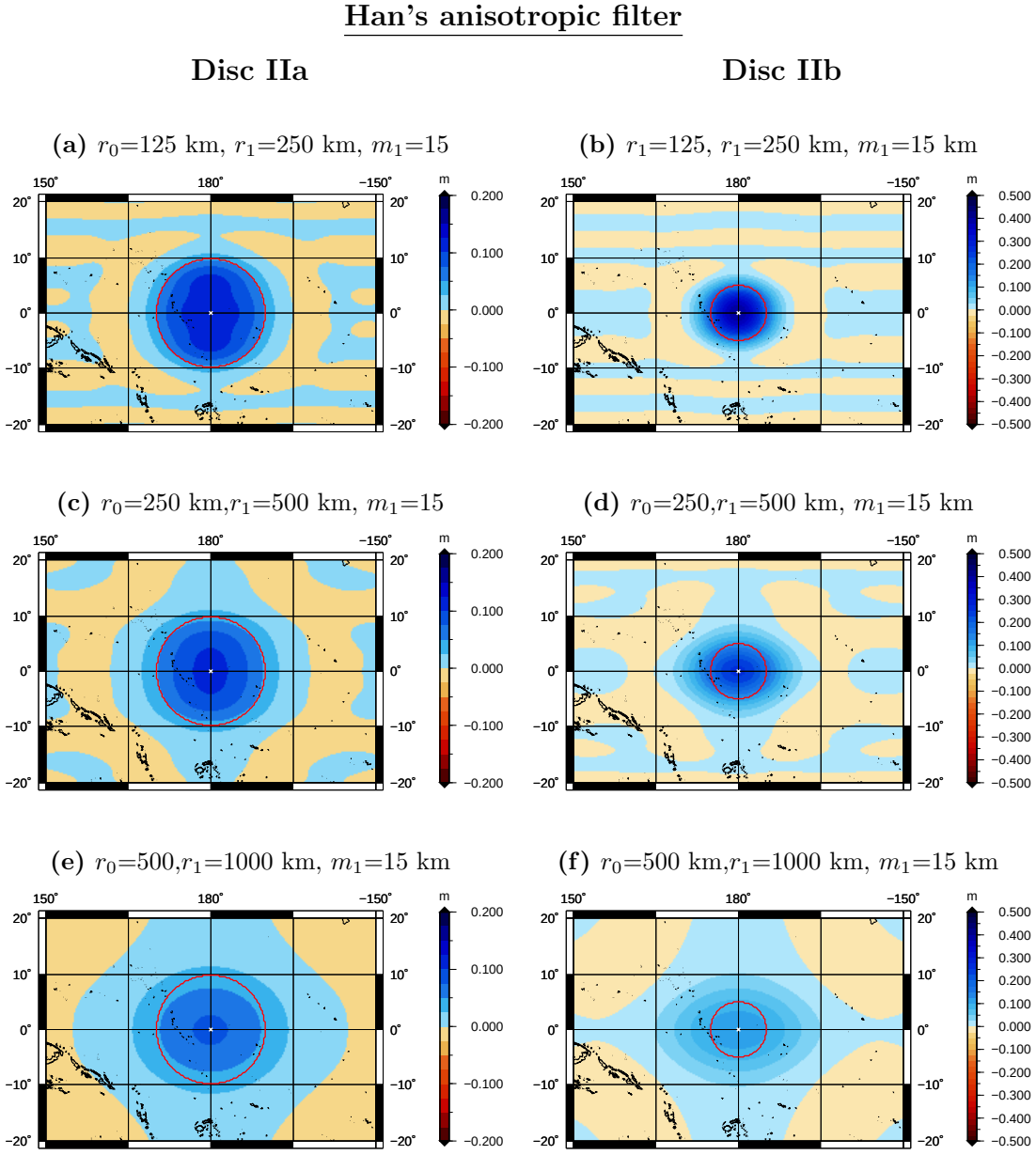

Figure A.5: Recovered masses for discs IIa and IIb with radii 10° and 5°,respectively, after applying Han's anisotropic filter. The discs are centred at $\phi = 0°, \lambda = 180°$. The red circle indicates the spatial extension of the input disc mass.

Disc IIa **Disc IIb**

(a) r_0=125 km, r_1=250 km, m_1=15 **(b)** r_0=125 km, r_1=250 km, m_1=15

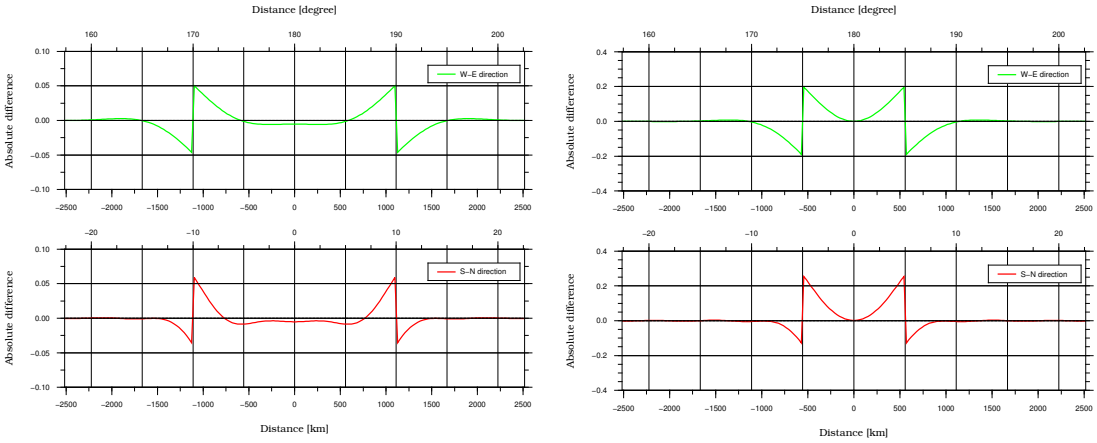

(c) r_0=250 km, r_1=500 km, m_1=15 **(d)** r_0=250 km, r_1=500 km, m_1=15

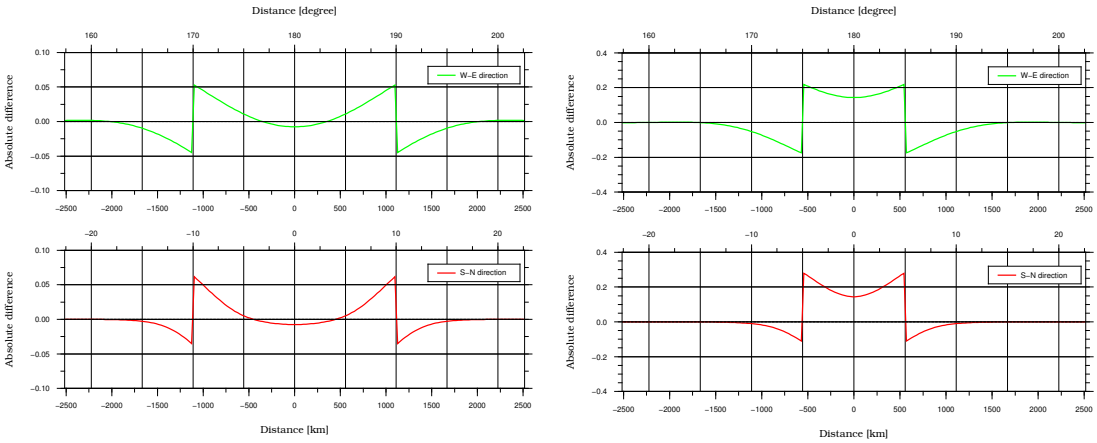

(e) r_0=500 km, r_1=1000 km, m_1=15 **(f)** r_0=500 km, r_1=1000 km, m_1=15

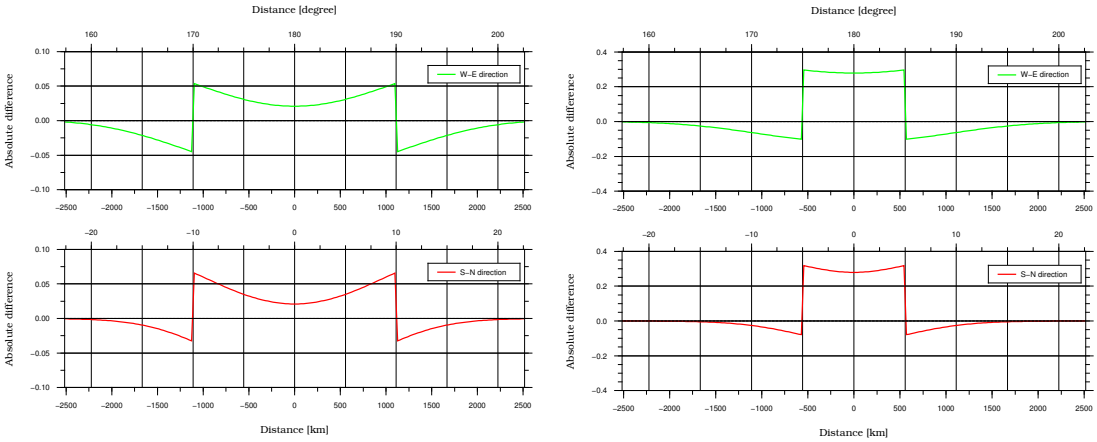

Figure A.6: West-east (green line) and south-north (red line) cross-sections of the difference between input and recovered masses when applying Han's anisotropic smoothing.

(a) Han's anisotropic filter for r_0=125 km, r_1=250 km and 10° disc

Validation results illustrated in Figure A.5a and Figure A.6a are somewhat similar to that applying the same filter to disc mass Ia (see Section 5.4.3). However, undulating patterns related to the Gibbs phenomenon are mostly visible in south-north direction rather than west-east. Therefore, leakage is more pronounced in west-east than south-north direction as confirmed by the differences illustrated in Figure A.6a. This behaviour can also be seen by the distances at which the differences outside of the disc reach zero, which are 250 km in south-north and about 500 km in west-east (e.g., twice as large). Also total leakage is slightly higher with 85.4% of the mass recovered and 9.0% related to spatial leakage (see Table 5.2 in Section 5.5).

(b) Han's anisotropic filter for r_0 = 125 km, r_1 = 250 km and 5° disc

The spatial distribution of the recovered mass illustrated in Figure A.5b is similar to that of the previous scenario with varying behaviour in west-east and south-north direction. The differences illustrated in Figure A.6b, though, are quite different when compared to the results obtained by applying the same filter to disc mass Ia (see Section 5.4.3). With respect to the latter the differences are higher at the disc's edge showing different magnitudes in west-east and south-north direction, thus the anisotropy is more pronounced. The total mass recovered is 75.9% with spatial leakage accounting for 17.8% (see Table 5.3 in Section 5.5).

(c) Han's anisotropic filter for r_0=250 km, r_1=500 km and 10° disc

Increasing the filter radii leads to a clearer anisotropic behaviour (see Figure A.5c) when compared to both the previous two scenarios and the corresponding scenario when applying the same filter to disc mass Ia (see Section 5.4.3). Leakage in west-east direction is much more pronounced than in south-north direction. This is also documented in the differences illustrated in Figure A.6c. The distances at which the differences outside the disc reach zero are now about 500 km in south-

north and close to 1000 km in west-east direction. In this scenario the total mass recovered is 80.6% of the initial disc mass with 12.9% accounting for spatial leakage (see Table 5.2 in Section 5.5).

(d) Han's anisotropic filter for r_0=250 km, r_1=500 km and 5° disc

With respect to the previous scenario the anisotropic behaviour is even more dominant when applying the same filter to the spatially more concentrated disc mass IIb as illustrated in Figure A.5d. This behaviour can clearly be seen in the differences illustrated in Figure A.6d with considerable different behaviour in west-east and south-north direction. The differences in west-east direction show an even larger distance at which the differences outside the disc reach zero (larger than 1000 km). Again this is different to the behaviour shown in Section 5.4.3 for the disc mass Ia. Total leakage has increased again with only 69.7% of the initial disc mass recovered and spatial leakage accounting now to 17.8% (see Table 5.3 in Section 5.5).

(e) Han's anisotropic filter for r_0=500 km, r_1=1000 km and 10° disc

The anisotropic behaviour is again visible when applying strong anisotropic smoothing to the disc mass IIa as illustrated in Figure A.5e. Leakage is more pronounced in west-east than south-north direction as also visible in the differences illustrated in Figure A.6e, which shows a similar behaviour as the last scenarios considered, though the distance at which the differences outside the disc reach zero has further increased. These distances are now close to 1000 km in south-north and about 1500 km in west-east direction. Now only 57.9% of the original mass is recovered with spatial leakage accounting for 35.9% (see Table 5.2 in Section 5.5).

(f) Han's anisotropic filter for r_0=500 km, r_1=1000 km and 5° disc

Both the most pronounced anisotropic behaviour as well as the largest leakage effect is obtained when applying strong anisotropic smoothing to the spatially more

concentrated disc mass IIb. Figure A.5f shows a highly elliptical nature of the recovered mass distribution with respect to a circular input mass. Furthermore, Figure A.5f shows massive leakage with highly increased leakage in west-east direction. The massive leakage is documented by a recovery of only 26.4% of the original disc mass (see Table 5.3 in Section 5.5). In this case spatial leakage with 61.1% is the dominating contribution. This extreme case is also documented by the differences illustrated in Figure A.6f. Differences outside the original disc now extend to more than 1000 km in south-north and almost 2000 km in west-east direction before reaching values close to zero.

A.1.4 Kusche's de-correlated anisotropic filter

Also for disc masses IIa and IIb the third validation is based on Kusche's de-correlated anisotropic smoothing using the three filters DDK3, DDK2 and DDK1, representing "weak", "medium" and "strong" smoothing. Applied to the recovery of the disc masses IIa and IIb the following six validation scenarios are considered:

(a) DDK3: $a = 1 \times 10^{12}$ and $p = 4$, disc radius is 10°
(b) DDK3: $a = 1 \times 10^{12}$ and $p = 4$, disc radius is 5°
(c) DDK2: $a = 1 \times 10^{13}$ and $p = 4$, disc radius is 10°
(d) DDK2: $a = 1 \times 10^{13}$ and $p = 4$, disc radius is 5°
(e) DDK1: $a = 1 \times 10^{14}$ and $p = 4$, disc radius is 10°
(f) DDK1: $a = 1 \times 10^{14}$ and $p = 4$, disc radius is 5°

Also here the filter has been selected to have stronger smoothing in west-east than in south-north direction. Examples for the input and recovered mass distributions given as west-east and south-north cross-sections are provided by Figure 5.13 in Section 5.4.4.

The validation results for all scenarios are shown in Figure A.7 for the recovered mass distributions and in Figure A.8 for west-east and south-north cross-sections of the differences between the input and recovered masses. Statistical values for the recovered masses and the differences to the input masses are listed in

Table 5.2 and Table 5.3 in Section 5.5. Results are generally similar to the case of applying Kusche's de-correlated anisotropic smoothing to disc masses Ia and Ib (see Section 5.4.4). Therefore, here only the main features are briefly presented and differences highlighted.

(a) Kusche's de-correlated anisotropic filter DDK3 and 10° disc

Applying the DDK3 filter to the disc mass IIa results in quite different spatial patterns for the recovered mass distribution when compared to Gaussian isotropic smoothing and somewhat different when compared to Han's anisotropic smoothing (see Section A.1.2 and Section A.1.3). The recovered mass distribution illustrated in Figure A.7a shows a clear anisotropic pattern with increased leakage in west-east direction. This is not as clearly visible when applying the DDK3 filter to the disc mass Ia (see Section 5.4.4). The anisotropic behaviour is also visible in the differences illustrated in Figure A.8a that shows a quite different behaviour for the west-east and south-north profiles with the latter exhibiting much less leakage. The distances at which the differences outside the disc reach zero are different in south-north (250 km) and west-east direction (500 km). In this case 86.7% of the total mass is recovered with 7.1% of the mass loss due to spatial leakage (see Table 5.2 in Section 5.5). These levels are similar to other filters applied to the same disc mass.

(b) Kusche's de-correlated anisotropic filter DDK3 and 5° disc

The anisotropic nature of the DDK3 filter is even more clearly visible when applying DDK3 to the spatially more concentrated disc mass IIb as illustrated in Figure A.7b. Leakage in west-east direction is much more pronounced than in south-north direction. This behaviour is also clearly visible in the differences illustrated in Figure A.8b where the west-east cross-section has much increased differences at the disc's edge when compared to the west-east cross-section. Also the distances at which the differences outside the disc reach zero are different in south-north (250 km) and west-east direction (500 km). The total mass recov-

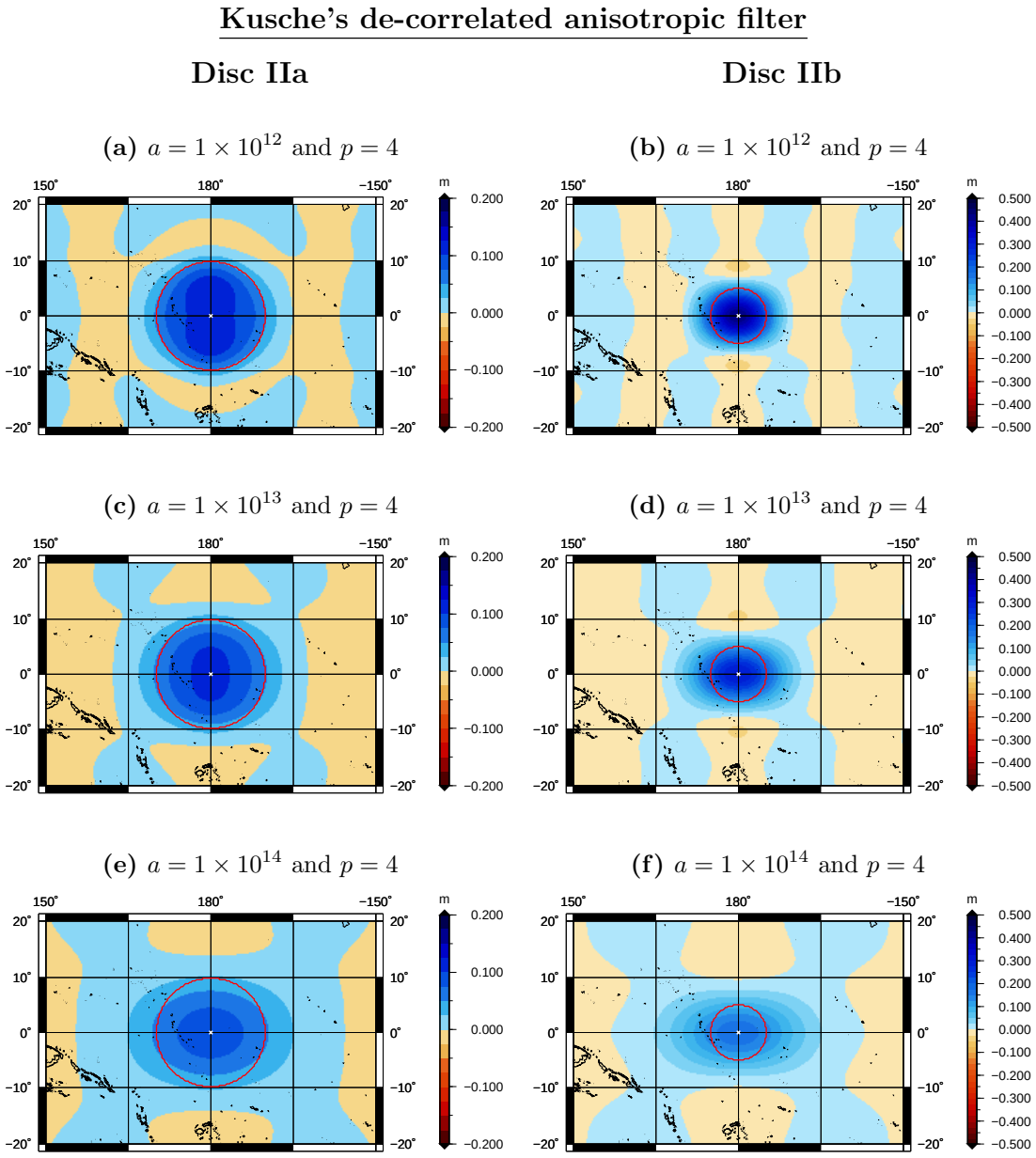

Figure A.7: Recovered masses for discs IIa and IIb with radii 10° and 5°, respectively, after applying de-correlation anisotropic smoothing. The discs are centred at $\phi = 0°, \lambda = 180°$. The red circle indicates the spatial extension of the input disc mass.

Kusche's de-correlated anisotropic filter

Disc Ia

(a) $a = 1 \times 10^{12}$ and $p = 4$

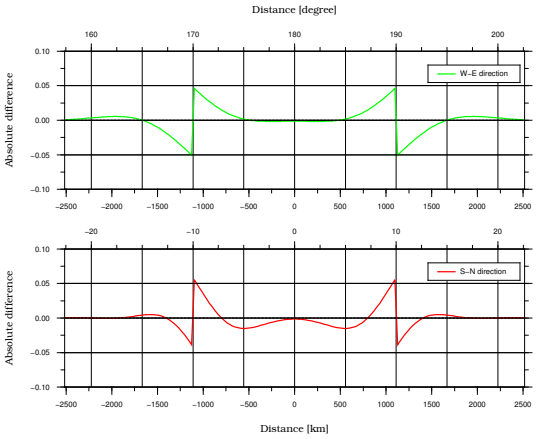

(c) $a = 1 \times 10^{13}$ and $p = 4$

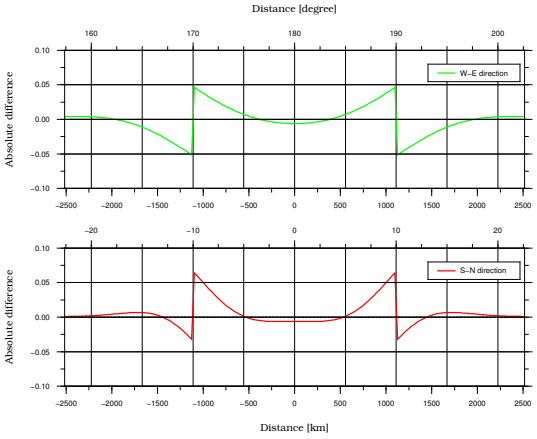

(e) $a = 1 \times 10^{14}$ and $p = 4$

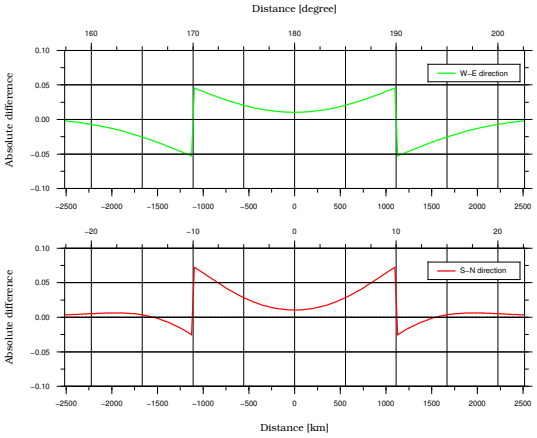

Disc Ib

(b) $a = 1 \times 10^{12}$ and $p = 4$

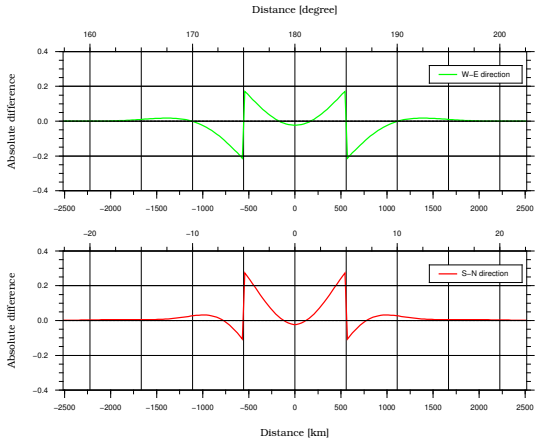

(d) $a = 1 \times 10^{13}$ and $p = 4$

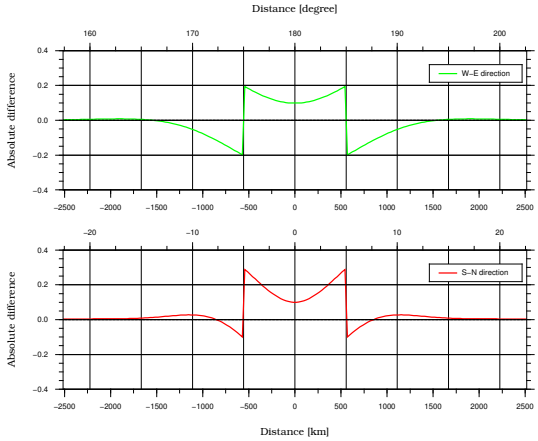

(f) $a = 1 \times 10^{14}$ and $p = 4$

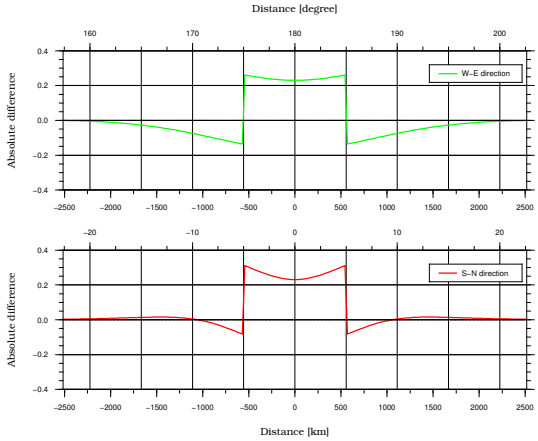

Figure A.8: West-east (green line) and south-north (red line) cross-sections of the difference between input and recovered masses when applying de-correlated anisotropic smoothing.

ered is 71.5% with 16.0% of the mass loss due to spatial leakage (see Table 5.3 in Section 5.5).

(c) Kusche's de-correlated anisotropic filter DDK2 and 10° disc

A similar behaviour as for scenario (a) for the recovered mass distribution is obtained when applying the DDK2 filter to the disc mass IIa. The anisotropic behaviour is clearly visible in Figure A.7c and Figure A.8c. In the latter again the differences at the disc's edge in west-east direction are considerably larger than in south-north direction. The distances at which the differences outside the disc reach zero are different in south-north (250 km) and west-east direction (800 km). Again this behaviour is quite different to that of applying DDK3 to the disc mass Ia. In the examined validation scenario spatial leakage has increased to 14.9% with 78.9% of the total mass recovered (see Table 5.2 in Section 5.5).

(d) Kusche's de-correlated anisotropic filter DDK2 and 5° disc

Again the anisotropic nature has been amplified when applying the same DDK2 filter to the spatially more concentrated disc mass IIb. In Figure A.7d considerable leakage is visible in west-east direction but not in south-north direction. This behaviour is also visible in the differences illustrated in Figure A.8d with higher differences at the disc's edge in west-east than south-north direction. The distances at which the differences outside the disc reach zero are now about 250 km in south-north and almost 1000 km in west-east direction. The total mass recovered is 55.6% with 32.0% of the mass loss due to spatial leakage (see Table 5.3 in Section 5.5).

(e) Kusche's de-correlated anisotropic filter DDK1 and 10° disc

The anisotropic behaviour increases further when applying the DDK1 filter on disc mass IIa as illustrated in Figure A.7e. Like for the application of strong anisotropic smoothing on disc mass IIa (see Section A.1.3) leakage is much more

pronounced in west-east than south-north direction. This is also clearly visible in Figure A.8e showing the corresponding differences in west-east and south-north direction. The distances at which the differences outside the disc reach zero are now about 400 km in south-north and about 1500 km in west-east direction. For this case only 63.9% of the total mass has been recovered while 29.9% of the mass loss is due to spatial leakage (see Table 5.2 in Section 5.5).

(f) Kusche's de-correlated anisotropic filter DDK1 and 5° disc

Finally, the most pronounced anisotropic behaviour in the recovered mass distribution is obtained when applying the DDK1 filter to the disc mass IIb. Leakage in west-east direction is much larger in both magnitude and spatial extension as compared to the south-north direction. The distances at which the differences outside the disc reach zero are now about 500 km in south-north and close to 2000 km in west-east direction. Also in this case with a level of 52.8% spatial leakage is massive and only 34.7% of the original mass has been recovered (see Table 5.3 in Section 5.5).

A.2 Validation Results for Disc Masses IIIa and IIIb

The third validation presented here provides results obtained for the disc masses IIIa and IIIb (see Section 5.3) that simulate ice mass changes over Antarctica at the location ϕ = -75°, λ = 250° (see Figure A.9). Again both disc masses have the same total mass but differ by their spatial extent with a spherical radius of 10° for disc mass IIIa and 5° for disc mass IIIb. This simulates spatially more wide spread or more concentrated mass changes.

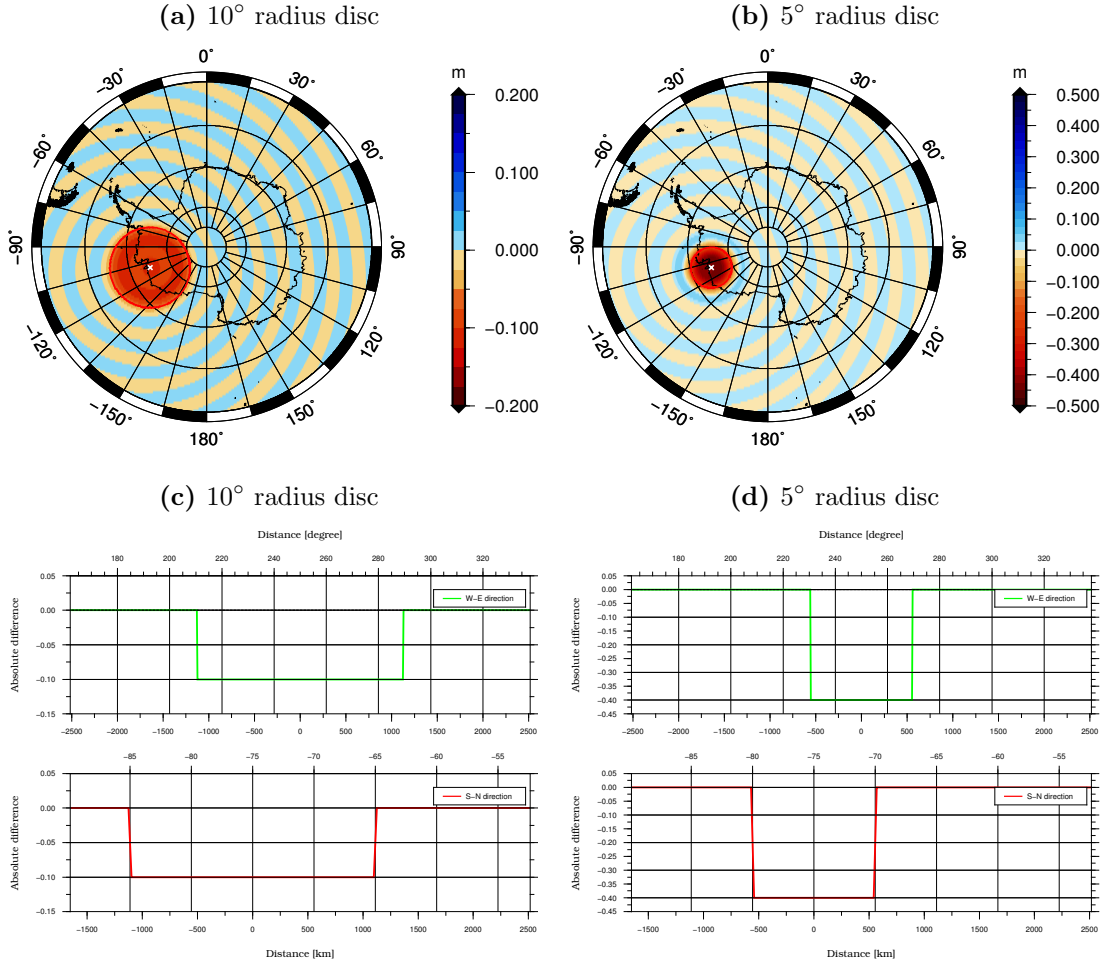

Figure A.9: Simulated disc masses IIIa and IIIb with radii 10° and 5°, respectively, centred at $\phi = -75°, \lambda = 250°$ (panels a and b) and west-east and south-north cross sections (panels c and d).

Also this validation considers four cases with respect to the smoothing of the Stokes coefficients within the validation procedure (see Section 5.1). These are:

(1) No filter
(2) Gaussian isotropic filter
(3) Han's anisotropic filter
(4) Kusche's de-correlated, anisotropic filter

Again, the description of the validation results concentrates mostly on differences to the results obtained from previous validations as the general results are very similar.

A.2.1 Results for no filter

The first validation does not employ any type of smoothing. Like for the previous validation scenarios it examines the ability to recover the input masses by the use of a band-limited representation of the input mass using spherical harmonic expansions up to the maximum degree of $l_{max} = 60$. The difference to the previous validations is that this case uses the highest geographic latitude, thus may be affected most by effects related to meridian convergence when using geographic coordinates. The recovered mass distribution illustrated in Figure A.10 is dominated by the Gibbs phenomenon manifesting as undulating patterns over the discs but mostly radiating away from the discs. Cross-sections in west-east and south-north directions illustrated in Figure A.10 reveal again that the largest differences occur at the disc's edge while the undulations outside the disc quickly taper down to values of effectively zero.

As documented in Table 5.2 and Table 5.3 in Section 5.5, in this case spectral leakage is 5.7% and 11.7%, respectively for disc mass IIIa and IIIb, thus 94.3% and 88.3% of the initial masses have been recovered. While this is the highest recovery rate (or smallest spectral leakage) when compared to the previous two geographic locations all three cases examined provide a very similar level of recovery between 93.8% and 94.3% for disc masses with a spherical radius of 10° and between 87.5% and 88.3% for disc masses with a spherical radius of 5°.

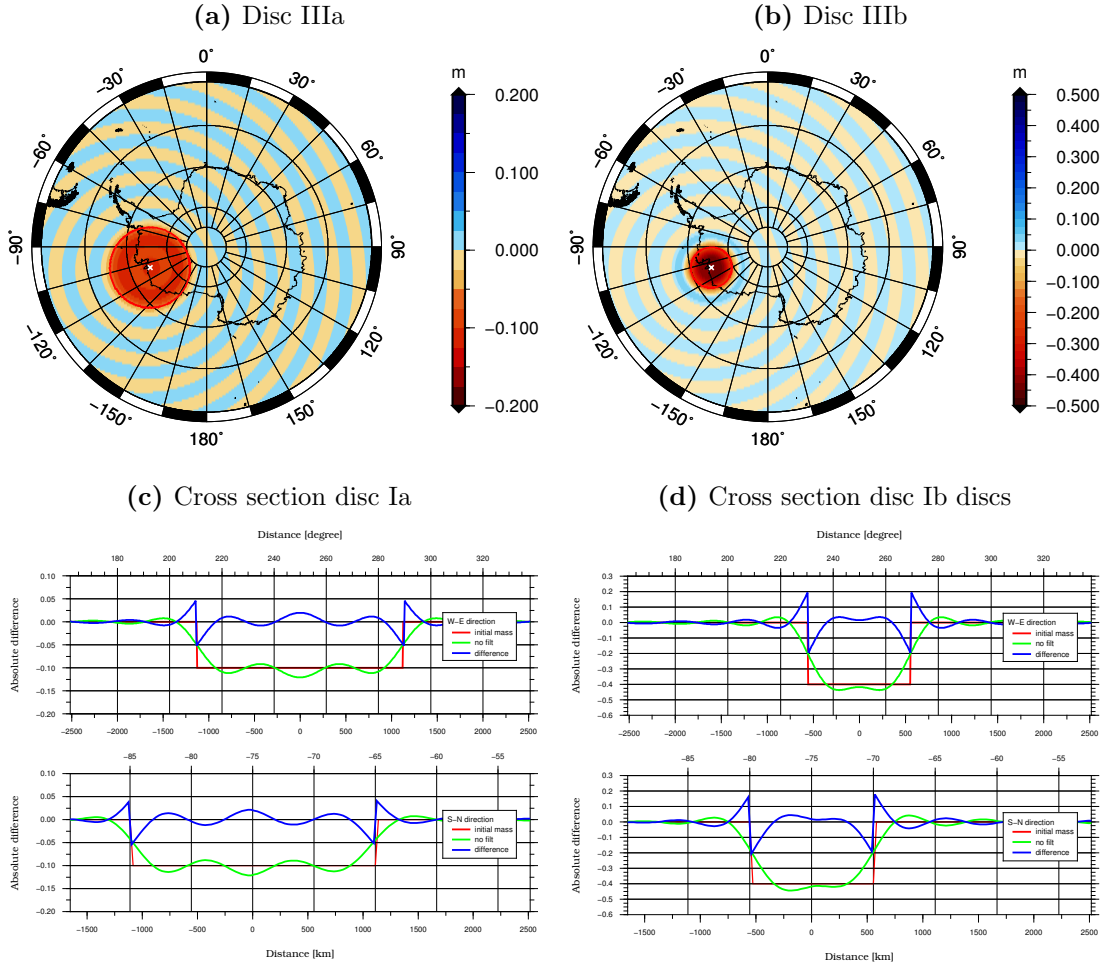

Figure A.10: Recovered disc masses IIIa and IIIb with radii 10° and 5° centred, respectively, at $\phi = -75°, \lambda = 250°$ (panels a and b) and west-east and south-north cross sections (panels c and d). No smoothing filter has been applied.

A.2.2 Gaussian isotropic filter

Gaussian isotropic smoothing to smooth the Stokes coefficients within the validation procedure (see Section 5.1) is applied to the disc masses IIIa and IIIb. With the same three smoothing radii as in the previous validations six combinations are considered referring again to "weak" smoothing using $r_g = 125$ km, "medium" smoothing using $r_g = 250$ km and "strong" smoothing using $r_g = 500$ km:

(a) $r_g = 125$ km / disc radius is 10°

(b) $r_g = 125$ km / disc radius is 5°

(c) $r_g = 250$ km / disc radius is 10°

(d) r_g = 250 km / disc radius is 5°

(e) r_g = 500 km / disc radius is 10°

(f) r_g = 500 km / disc radius is 5°

Examples for the input and recovered mass distributions given in west-east and south-north cross-sections are provided by Figure 5.7 in Section 5.4.2.

All validation results are shown in Figure A.11 for the recovered mass distribution and in Figure A.12 for west-east and south-north cross-sections of the differences between the input and recovered masses. Statistical values for the recovered masses and the differences with respect to the input masses are listed in Table 5.2 and Table 5.3 in Section 5.5.

(a) Gaussian isotropic filter for r_g = 125 km and 10° disc

Figure A.11a presents the recovered mass distribution when applying weak Gaussian isotropic smoothing to disc mass IIIa. The result is almost identical with that when no smoothing has been applied (see Figure A.10 in Section 5.5). The total mass recovered is 91.5% of the input mass, thus only 2.8% less than without applying any smoothing (see Table 5.2), which is attributed to spatial leakage. Neglecting the sign change, the differences illustrated in Figure A.12a are almost identical to the result of "weak" Gaussian isotropic smoothing applied to disc mass Ia (see Section 5.4.2).

(b) Gaussian isotropic filter for r_g = 125 km and 5° disc

Also the application of "weak" Gaussian isotropic smoothing to the spatially more concentrated disc mass IIIb leads to almost identical results when no smoothing has been applied (see Figure A.10), though leakage is slightly higher. In this case 82.7% of the input mass has been recovered while 5.6% of the mass loss is attributed to spatial leakage (see Table 5.3 in Section 5.5). Neglecting the sign change, the differences illustrated in Figure A.12b again are almost identical to

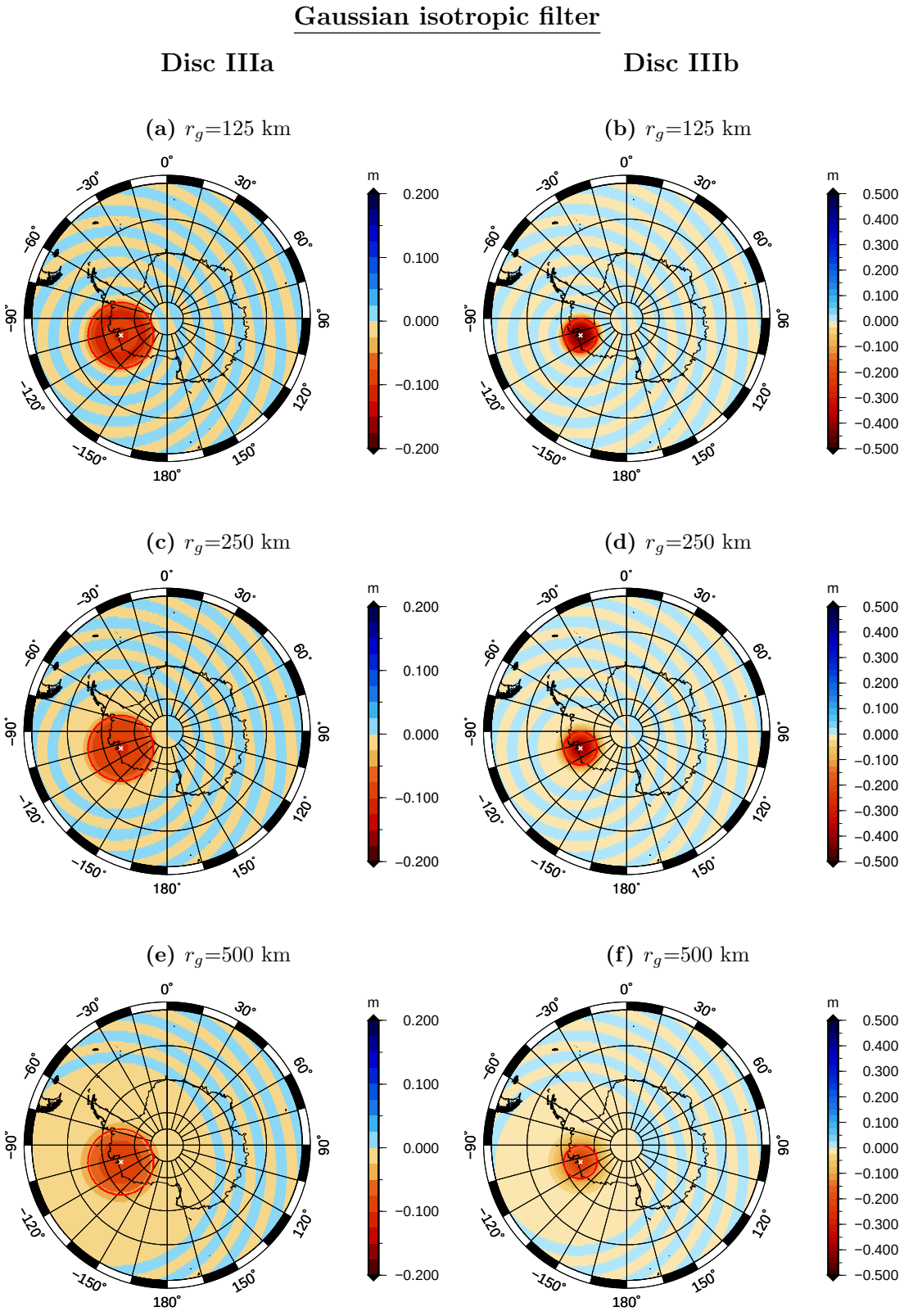

Figure A.11: Recovered masses for discs IIIa and IIIb with radii 10° and 5°, respectively, after applying Gaussian isotropic smoothing. The discs are centred at $\phi = -75°, \lambda = 250°$. The red circle indicates the spatial extension of the input disc mass.

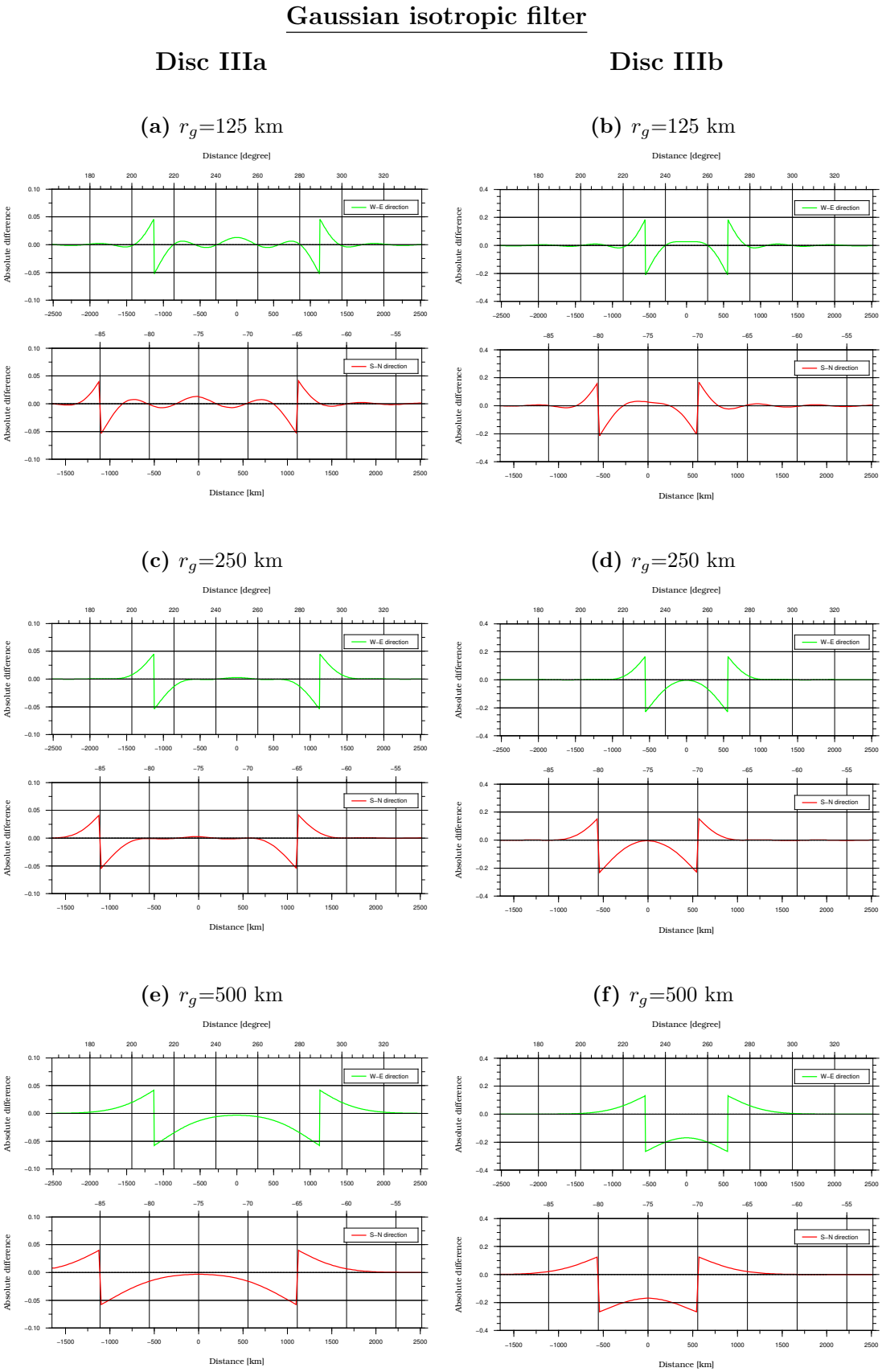

Figure A.12: West-east (green line) and south-north (red line) cross-sections of the difference between input and recovered masses when applying Gaussian isotropic smoothing.

the result of "weak" Gaussian isotropic smoothing applied to disc mass Ib (see Section 5.4.2).

(c) Gaussian isotropic filter for r_g = 250 km and 10° disc

Figure A.11c illustrates the recovered mass distribution when applying medium Gaussian isotropic smoothing to the disc mass IIIa. While the Gibbs phenomenon is still clearly visible there is also an increased zone around the disc that indicates increased leakage. The total mass recovered is 85.1% where 9.1% of the mass loss is due to spatial leakage (see Table 5.2 in Section 5.5). Again the differences illustrated in Figure A.12c are practically identical to the result of medium Gaussian isotropic smoothing applied to disc mass Ia (see Section 5.4.2), albeit neglecting the sign change.

(d) Gaussian isotropic filter for r_g = 250 km and 5° disc

With respect to the previous validation leakage has increased when applying medium Gaussian isotropic smoothing to the spatially more concentrated disc mass IIIb. The total mass recovered is now 70.2% with 18.1% of the mass loss attributed to spatial leakage (see Table 5.3 in Section 5.5). Also in this case, when neglecting the sign change, the differences illustrated in Figure A.12d are almost identical to the result of medium Gaussian isotropic smoothing applied to disc mass Ib (see Section 5.4.2).

(e) Gaussian isotropic filter for r_g = 500 km and 10° disc

Applying strong Gaussian isotropic smoothing to the disc mass IIIa now results in a spatial pattern of the recovered mass distribution that is dominated by leakage, which affects a large area around the input disc mass (see Figure A.11e). The differences in Figure A.12e indicate that mass from large parts of the disc are leaked outside the original disc. This can also be seen by the large distance of about 1000 km at which the differences reach the level of zero. With 70.6%

considerably less mass is recovered when compared to the application of medium Gaussian isotropic smoothing to the disc mass IIIa (see scenario (c) above). Spatial leakage accounts for 23.7% of the total mass loss (see Table 5.2 in Section 5.5). Again the differences illustrated in Figure A.12e are almost identical to the result of strong Gaussian isotropic smoothing applied to disc mass Ia (see Section 5.4.2).

(f) Gaussian isotropic filter for r_g = 500 km and 5° disc

Finally, the most dominant leakage signal is obtained when applying strong Gaussian isotropic smoothing to the spatially more concentrated disc mass IIIb. Figure A.11f illustrates the mass distribution of the recovered mass where considerable leakage is visible around the original input mass. In this scenario spatial leakage accounts for 43.7% of the mass loss whereas the total mass recovered is only 44.6% of the original input mass. As for all previous scenarios the differences illustrated in Figure A.12f are almost identical to the result of strong Gaussian isotropic smoothing applied to disc mass Ib (see Section 5.4.2).

A.2.3 Han's anisotropic filter

Also here Han's anisotropic smoothing filter is applied to disc masses IIIa and IIIb with the same parameters as in the validations based on disc masses Ia and Ib (see Section 5.4.3) and disc masses IIa and IIb (see Section A.1.3). As before, the selection of three smoothing radii combinations results in the following six scenarios (all using the parameter m_1= 15) for the validation:

(a) r_0=125 km, r_1=250 km, disc radius is 10°
(b) r_0=125 km, r_1=250 km, disc radius is 5°
(c) r_0=250 km, r_1=500 km, disc radius is 10°
(d) r_0=250 km, r_1=500 km, disc radius is 5°
(e) r_0=500 km, r_1=1000 km, disc radius is 10°
(f) r_0=500 km, r_1=1000 km, disc radius is 5°

The particular selection of the smoothing radii is again referred to "weak", "medium" and "strong" anisotropic smoothing. Examples for the input and recovered mass distributions given as west-east and south-north cross-sections are provided by Figure 5.10 in Section 5.4.3. The validation results for the six scenarios are shown in Figure A.13 for the recovered mass distributions and in Figure A.14 for west-east and south-north cross-sections of the difference between the input and recovered masses. Statistical values for all validation scenarios are listed in Table 5.2 and Table 5.3 in Section 5.5.

(a) Han's anisotropic filter for r_0=125 km, r_1=250 km and 10° disc

The spatial pattern of the recovered mass distribution illustrated in Figure A.13a is very similar to the application of "weak" Gaussian smoothing to the disc mass IIIa. It shows the typical Gibbs phenomenon with little difference in west-east and south-north direction. The total mass recovered is 89.8% of the input mass with 4.4% of the mass loss due to spatial leakage (see Table 5.2 in Section 5.5). The differences illustrated in Figure A.14a are very similar to the results of "weak" anisotropic smoothing applied to disc mass Ia (see Section 5.4.3).

(b) Han's anisotropic filter for r_0 = 125 km, r_1 = 250 km and 5° disc

Also the application of "weak" anisotropic smoothing to the spatially more concentrated disc mass IIIb leads to almost identical results when compared to "weak" Gaussian smoothing applied to the disc mass IIIb (see Section A.2.2). Also in this scenario the spatial pattern of the recovered mass distribution illustrated in Figure A.13b shows the typical Gibbs phenomenon with little difference in west-east and south-north direction. In this scenario 79.0% of the input mass has been recovered while 9.3% of the mass loss is attributed to spatial leakage (see Table 5.3 in Section 5.5). Like for the previous scenario the differences illustrated in Figure A.14b are very similar to the results of "weak" anisotropic smoothing applied to disc mass Ib (see Section 5.4.3).

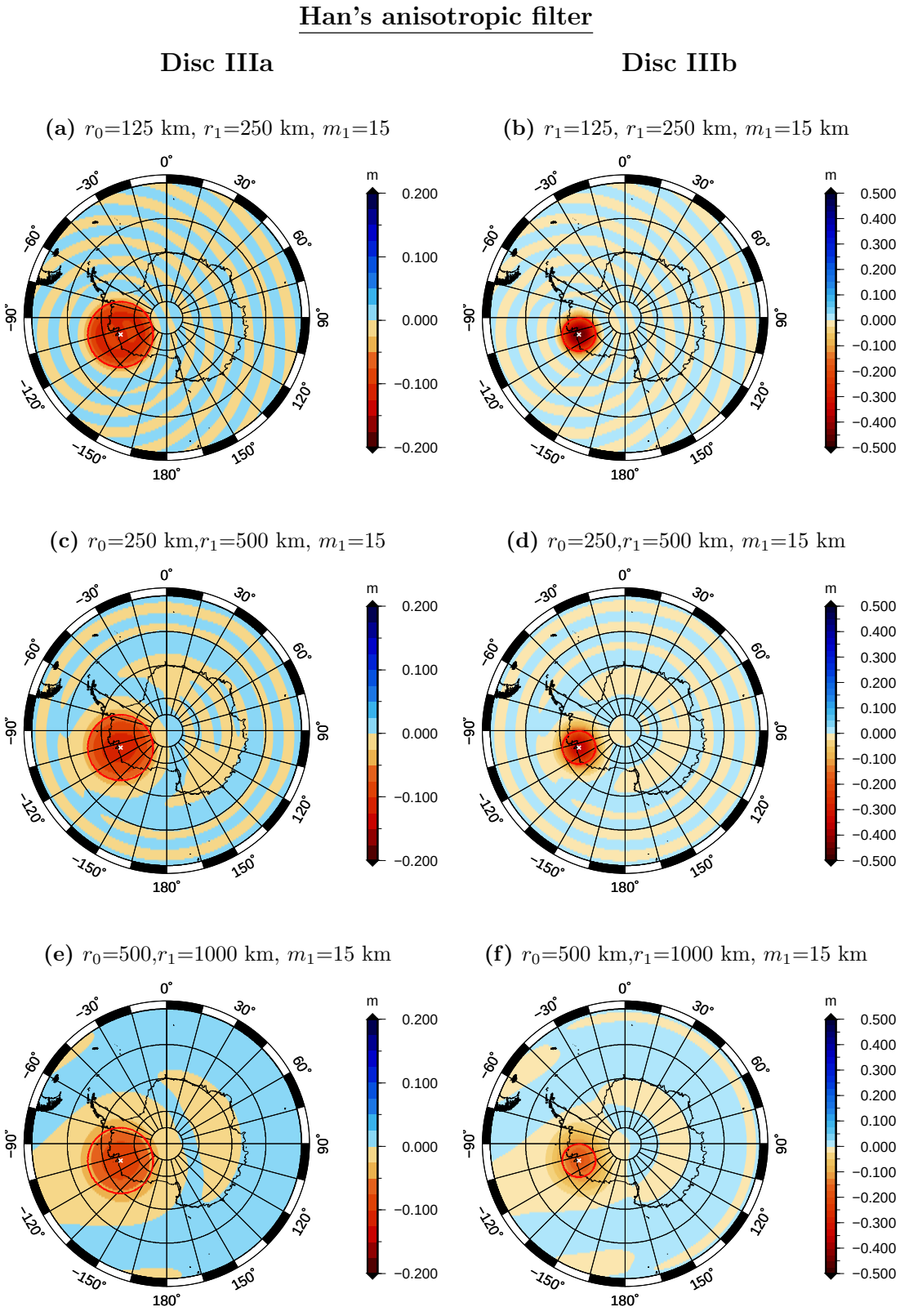

Figure A.13: Recovered masses for discs IIIa and IIIb with radii 10° and 5°, respectively, after applying Han's anisotropic smoothing. The discs are centred at $\phi = -75°, \lambda = 250°$. The red circle indicates the spatial extension of the input disc mass.

Han's anisotropic filter

Disc IIIa **Disc IIIb**

(a) r_0=125 km, r_1=250 km, m_1=15 **(b)** r_0=125 km, r_1=250 km, m_1=15

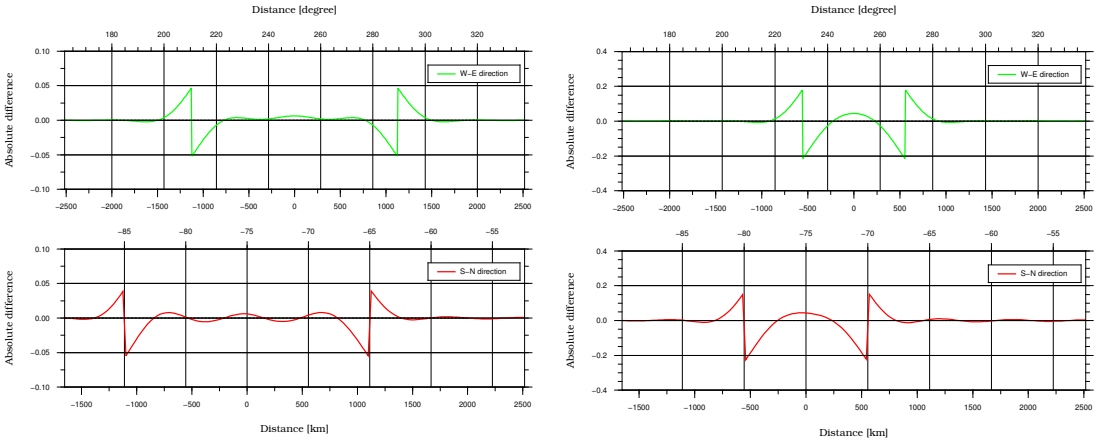

(c) r_0=250 km, r_1=500 km, m_1=15 **(d)** r_0=250 km, r_1=500 km, m_1=15

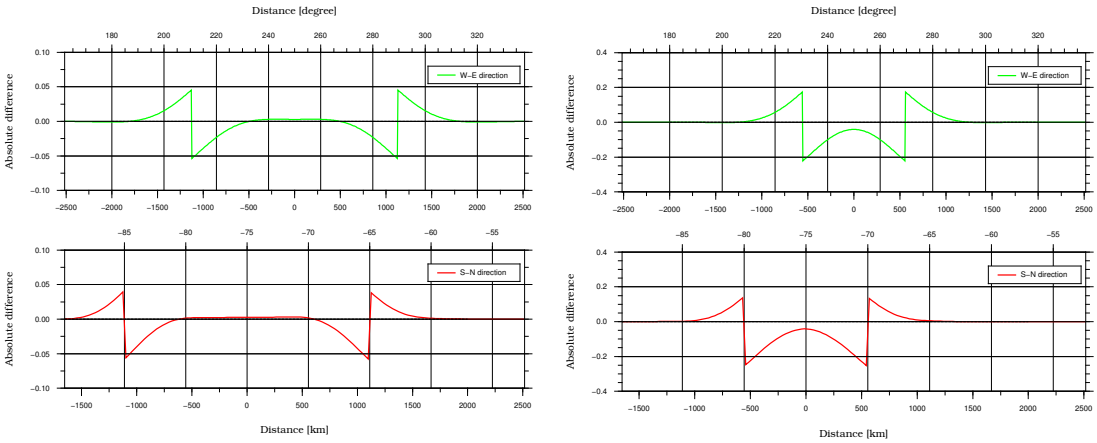

(e) r_0=500 km, r_1=1000 km, m_1=15 **(f)** r_0=500 km, r_1=1000 km, m_1=15

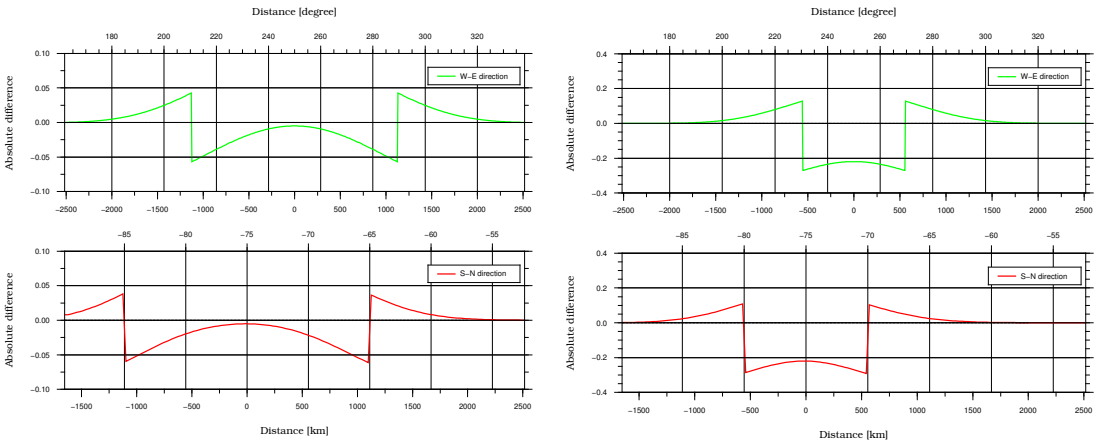

Figure A.14: West-east (green line) and south-north (red line) cross-sections of the difference between input and recovered mass when applying Han's anisotropic smoothing.

(c) Han's anisotropic filter for r_0=250 km, r_1=500 km to 10° radius disc

The typical Gibbs phenomenon is now considerably disturbed when applying medium anisotropic smoothing to disc mass IIIa as illustrated in Figure A.13c. With 82.1% of the total mass recovered leakage is considerably larger than in the corresponding scenario for "weak" anisotropic smoothing. Of the total mass loss 12.1% can be attributed to spatial leakage (see Table 5.2 in Section 5.5). The anisotropic character starts to become also visible in the differences illustrated in Figure A.14c. Again the differences are very similar to the results of medium anisotropic smoothing applied to disc mass Ia (see Section 5.4.3).

(d) Han's anisotropic filter for r_0=250 km, r_1=500 km and 5° disc

Again application of the same filter to the spatially more concentrated disc mass IIIb leads to increased leakage. The contribution of spatial leakage to the total mass loss is now 24.8% whereas the total mass recovered is 63.4% (see Table 5.3 in Section 5.5). Also here the anisotropic character considerably disturbs the typical Gibbs phenomenon and introduces slight differences into the relative differences for the west-east and north south cross-sections illustrated in Figure A.14d. However, the differences are still very similar to the results of medium anisotropic smoothing applied to disc mass Ib (see Section 5.4.3).

(e) Han's anisotropic filter for r_0 = 500 km, r_1 = 1000 km and 10° disc

The typical Gibbs phenomenon has now been completely disturbed through the application of strong anisotropic smoothing to the disc mass IIIa as illustrated in Figure A.13e. Leakage has considerably increased and now shows an anisotropic behaviour. The total mass recovered is 66.8% with 27.5% of the mass loss due to spatial leakage (see Table 5.2 in Section 5.5). The differences illustrated in Figure A.14e show the anisotropic behaviour through slightly different cross-sections in west-east and south-north direction. Again the differences are very similar

to the results of strong anisotropic smoothing applied to disc mass Ia (see Section 5.4.3).

(f) Han's anisotropic filter for $r_0 = 500$ km, $r_1 = 1000$ km and 5° disc

A similar anisotropic behaviour as in the previous scenario is visible when applying strong anisotropic smoothing to the disc mass IIIb as can be seen in Figure A.13f. This case leads to the highest leakage with only 37.2% of the total mass recovered and 51.1% of the mass loss attributed to spatial leakage (see Table 5.3 in Section 5.5). This extreme case is also documented in the differences illustrated in Figure A.14f, which are very similar to the differences that result from strong anisotropic smoothing applied to disc mass Ib (see Section 5.4.3).

A.2.4 Kusche's de-correlated anisotropic filter

Lastly, disc masses IIIa and IIIb are subjected to Kusche's de-correlated anisotropic smoothing using the same filters DDK3, DDK2 and DDK1, representing "weak", "medium" and "strong" smoothing. Applied to the recovery of the disc masses IIIa and IIIb the following six validation scenarios are considered:

(a) DDK3: $a = 1 \times 10^{12}$ and $p = 4$, disc radius is 10°
(b) DDK3: $a = 1 \times 10^{12}$ and $p = 4$, disc radius is 5°
(c) DDK2: $a = 1 \times 10^{13}$ and $p = 4$, disc radius is 10°
(d) DDK2: $a = 1 \times 10^{13}$ and $p = 4$, disc radius is 5°
(e) DDK1: $a = 1 \times 10^{14}$ and $p = 4$, disc radius is 10°
(f) DDK1: $a = 1 \times 10^{14}$ and $p = 4$, disc radius is 5°

Examples for the input and recovered mass distributions given as west-east and south-north cross-sections are provided by Figure 5.13 in Section 5.4.4.

The validation results for all combinations are shown in Figure A.15 for the recovered mass distributions and in Figure A.16 for west-east and south-north

cross-sections of the differences between the input and recovered masses. Statistical values for the recovered masses and the differences to the input masses are listed in Table 5.2 and Table 5.3 in Section 5.5.

(a) Kusche's de-correlated anisotropic filter DDK3 and 10° disc

Application of the DDK3 filter to the disc mass IIIa results in a spatial pattern of the recovered mass that is similar to all previous scenarios applying either no or "weak" smoothing. The recovered mass distribution illustrated in Figure A.15a clearly shows the typical Gibbs phenomenon and practically no anisotropy. The total mass recovered is 91.2% with 3.1% of the mass loss attributed to spatial leakage (see Table 5.2 in Section 5.5). Like for Gaussian isotropic and Han's anisotropic smoothing the differences presented in Figure A.16b are almost identical to the scenario when applying the DDK3 filter to disc mass Ia (see Section 5.4.4).

(b) Kusche's de-correlated anisotropic filter DDK3 and 5° disc

Still no anisotropic behaviour is visible in the recovered mass when applying the DDK3 filter to the spatially more concentrated disc mass IIIb as illustrated in Figure A.15b. Leakage is small as documented by a level of 82.3% of total mass recovered while 5.9% of the mass loss is attributed to spatial leakage (see Table 5.3 in Section 5.5). Again the differences presented in Figure A.16a are almost identical to the scenario when applying the DDK3 filter to disc mass Ib (see Section 5.4.4).

(c) Kusche's de-correlated anisotropic filter DDK2 and 10°disc

A similar behaviour as for the first two validation scenarios is obtained when applying the DDK2 filter to the disc mass IIIa, though the typical undulations related to the Gibbs effect have widened. Figure A.15c shows only minimal anisotropic character, which is also confirmed by the differences illustrated in

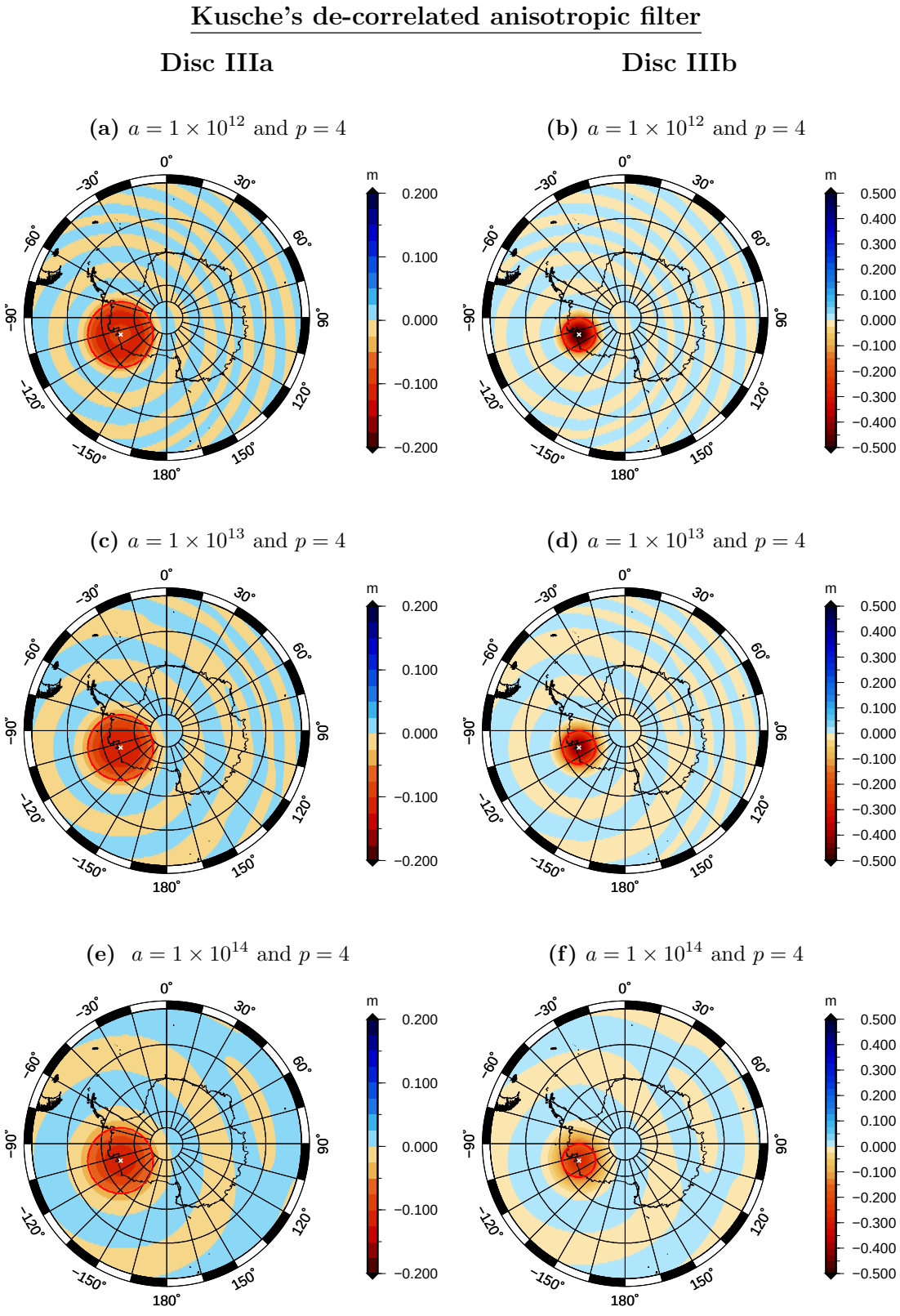

Figure A.15: Recovered masses for discs IIIa and IIIb with radii 10° and 5°, respectively, after applying Kusche's de-correlated anisotropic smoothing. The discs are centred at $\phi = -75°, \lambda = 250°$. The red circle indicates the spatial extension of the input disc mass.

Kusche's de-correlated anisotropic filter

Disc IIIa

(a) $a = 1 \times 10^{12}$ and $p = 4$

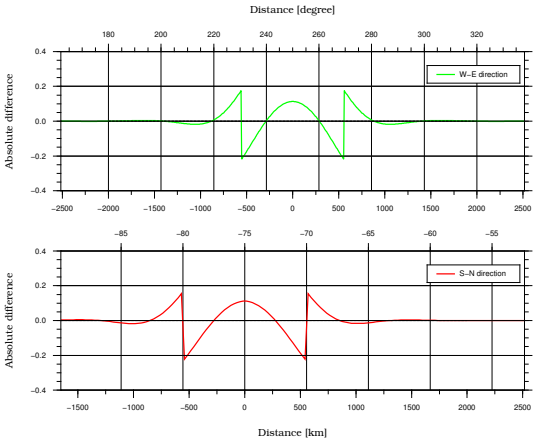

(c) $a = 1 \times 10^{13}$ and $p = 4$

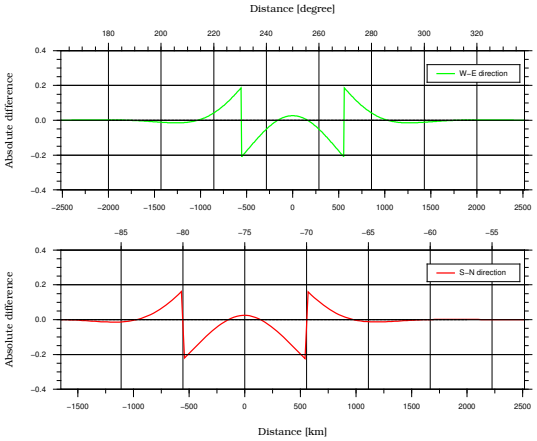

(e) $a = 1 \times 10^{14}$ and $p = 4$

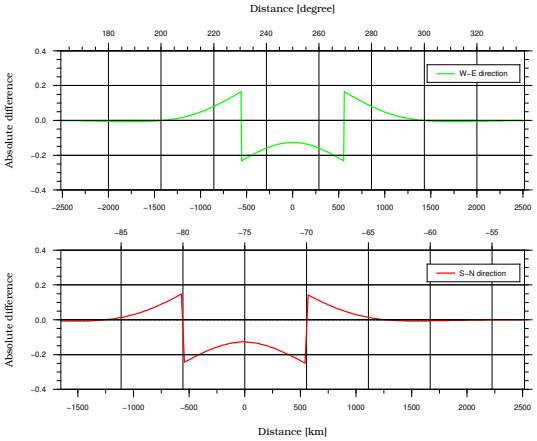

Disc IIIb

(b) $a = 1 \times 10^{12}$ and $p = 4$

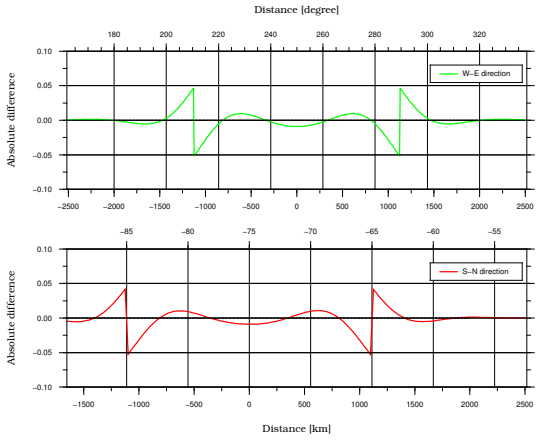

(d) $a = 1 \times 10^{13}$ and $p = 4$

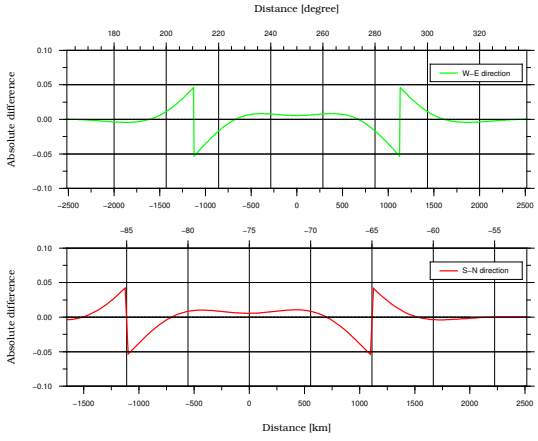

(f) $a = 1 \times 10^{14}$ and $p = 4$

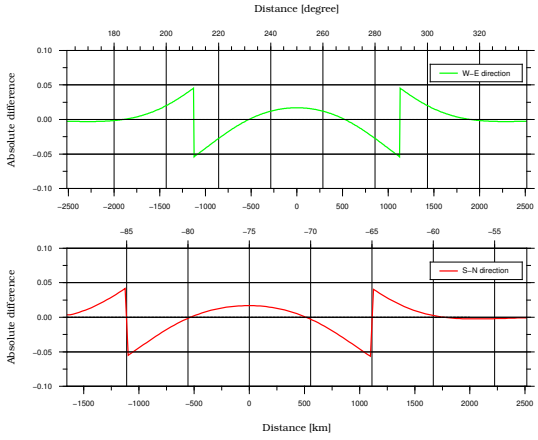

Figure A.16: West-east (green line) and south-north (red line) cross-sections of the difference between input and recovered masses when applying Kusche's de-correlated anisotropic smoothing.

Figure A.16d. The total mass recovered is 87.3% where 6.9% of the mass loss is attributed to spatial leakage (see Table 5.2 in Section 5.5). As before, the differences presented in Figure Figure A.16d are almost identical to the scenario when applying the DDK2 filter to disc mass Ib (see Section 5.4.4).

(d) Kusche's de-correlated anisotropic filter DDK2 and 5° disc

A result similar to that of the previous scenario is obtained when applying the DDK2 filter to the spatially more concentrated disc mass IIIb. Again almost no anisotropic character is visible in the recovered mass distribution as illustrated in Figure A.15d and confirmed by the differences illustrated in Figure A.16c. In this scenario the total mass recovered is 73.4% while 14.9% of the mass loss is attributed to spatial leakage (see Table 5.3 in Section 5.5). Again the differences presented in Figure A.16c are almost identical to the scenario when applying the DDK2 filter to disc mass Ia (see Section 5.4.4).

(e) Kusche's de-correlated anisotropic filter DDK1 and 10° disc

In contrast to the application of strong anisotropic smoothing the application of the DDK1 filter to the disc mass IIIa does not result in a pronounced anisotropic pattern in the recovered mass distribution as illustrated in Figure A.15e. This is also confirmed by the differences illustrated in Figure A.16f that does not show significant differences between the west-east and south-north cross-sections. Also leakage is not as large as for strong Gaussian isotropic or Han's anisotropic smoothing. The total mass recovered is 80.3% with a spatial leakage component of only 14.0% (see Table 5.2 in Section 5.5). As before, the differences presented in Figure A.16f are almost identical to the scenario when applying the DDK1 filter to disc mass Ia (see Section 5.4.4).

(f) Kusche's de-correlated anisotropic filter DDK1 and 5° radius disc

Finally, also the application of the DDK1 filter to the disc mass IIIb does not introduce a strong anisotropic behaviour in the recovered mass distribution as illustrated in Figure A.15f. Some leakage is visible but not as strong as for Gaussian isotropic or Han's anisotropic smoothing. The total mass recovered is 53.4% while 34.9% of the mass loss is due to spatial leakage (see Table 5.3 in Section 5.5). As for all previous validations, the differences presented in Figure A.16e are almost identical to the scenarios when applying the DDK1 filter to disc mass Ib (see Section 5.4.4).

Appendix B

Results from more realistic masses

While the validation results for some selected scenarios are provided in Chapter 6 the complete overview of all validation results based on the more realistic mass distributions (see Section 6.2) are provided in this appendix. The following six regional mass distributions have been considered:

(1) Alaska - ice mass change
(2) Greenland - ice mass change
(3) Amazon - land hydrology
(4) West Antarctica - ice mass change
(5) Sumatra-Andaman - earthquake
(6) Lake Victoria - land hydrology

For each mass distribution the following smoothing scenarios have been applied:

(1) No smoothing
(2) Gaussian isotropic smoothing
(3) Han's anisotropic smoothing
(4) Kusche's's de-correlated anisotropic smoothing

B.1 Validation Results for Alaska

B.1.1 Initial mass

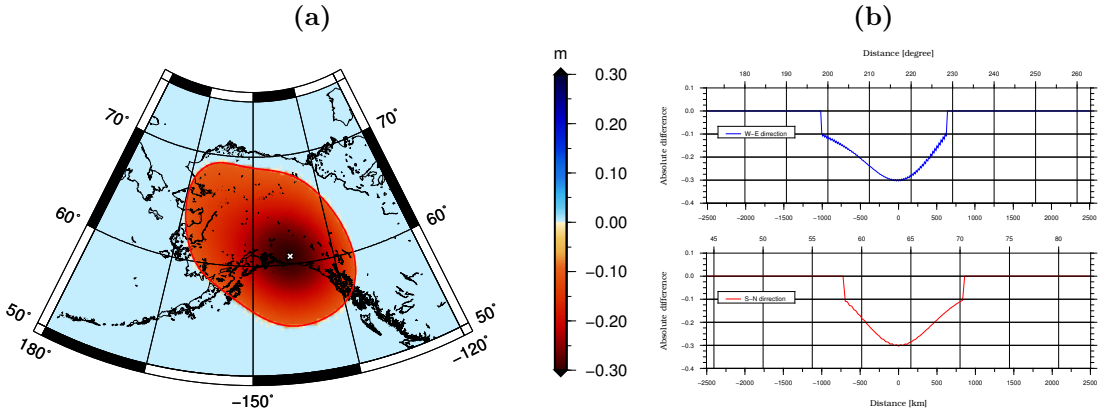

Figure B.1: (a) Initial mass distribution over Alaska, (b) Cross-sections in west-east (blue line) and south-north (red line) directions.

B.1.2 Recovered mass with no filter applied

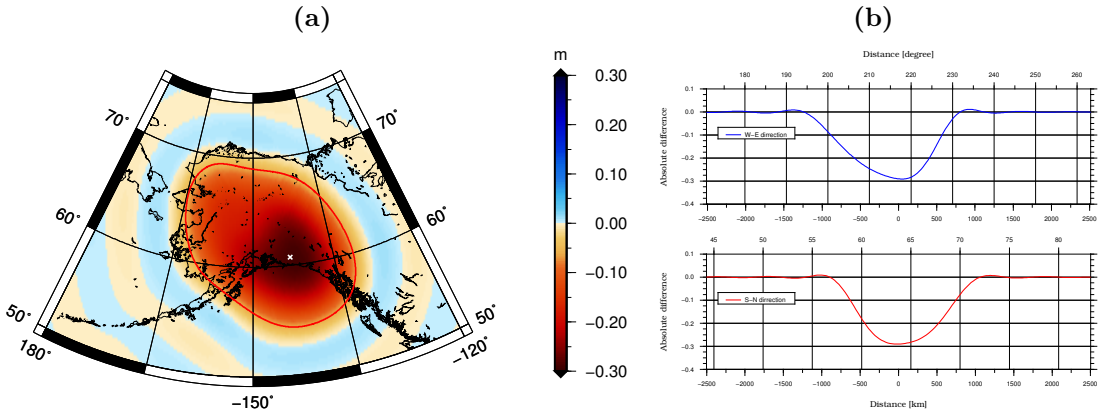

Figure B.2: (a) Recovered mass over Alaska, (b) Cross-sections in west-east (blue line) and south-north (red line) directions.

B.1.3 Results from different smoothing techniques

Gaussian isotropic smoothing

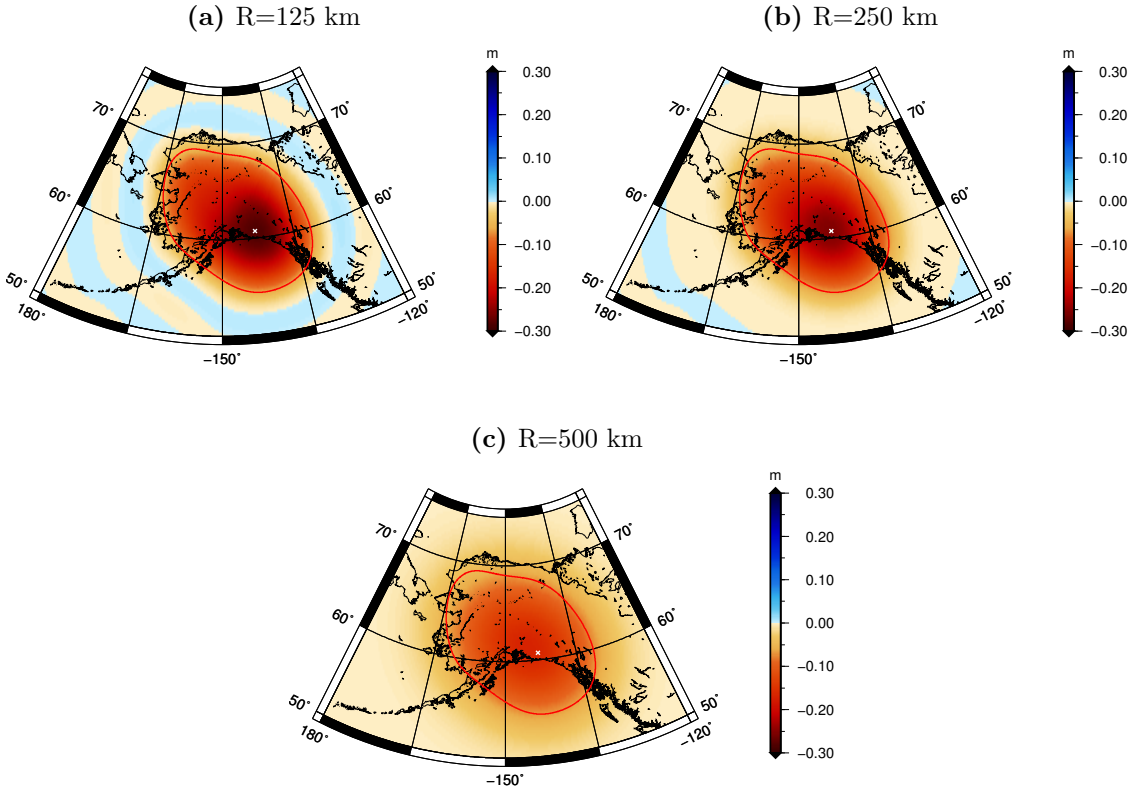

Figure B.3: Recovered masses over Alaska after applying Gaussian isotropic smoothing.

(a) R= 125 km

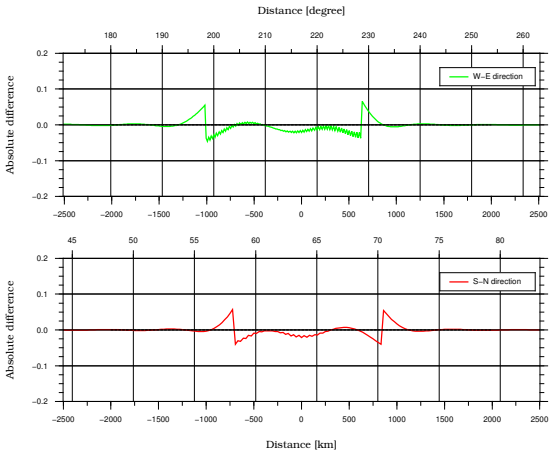

(b) R= 250 km

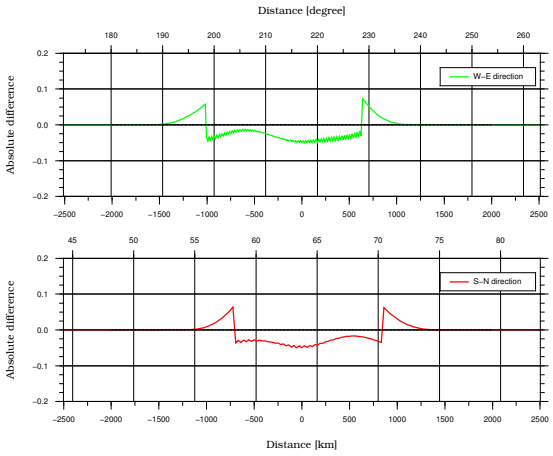

(c) R= 500 km

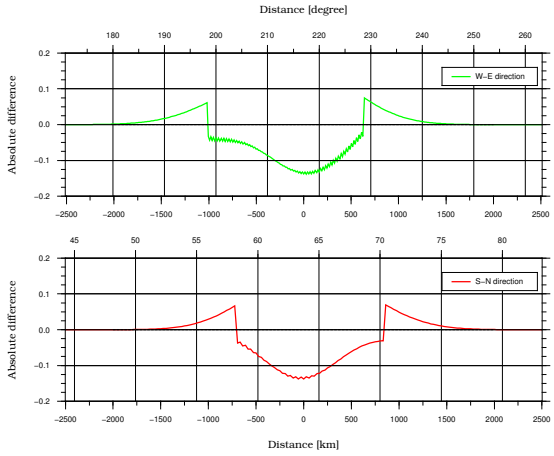

Figure B.4: Difference between the initial and recovered mass for Alaska with Gaussian isotropic smoothing applied. West-east (green line) and south-north (red line) cross sections are displayed.

Han's anisotropic smoothing

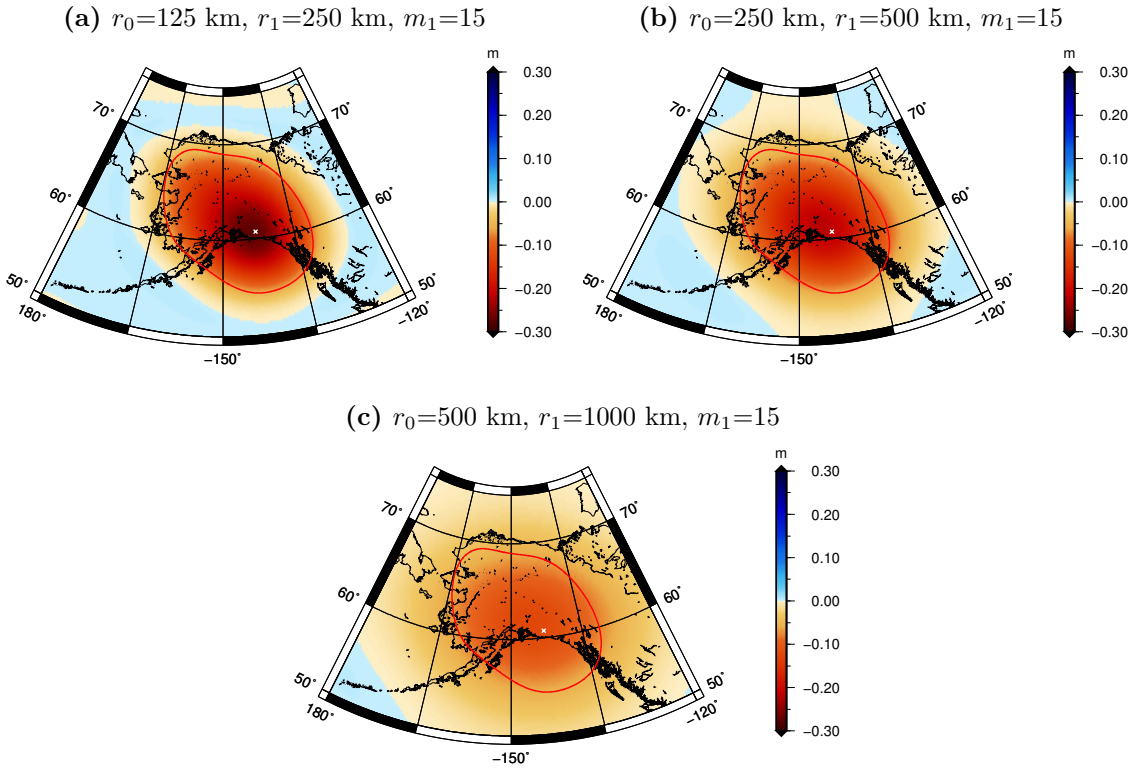

Figure B.5: Recovered masses over Alaska after applying Han's anisotropic smoothing.

(a) r_0=125 km, r_1=250 km, m_1=15

(b) r_0=250 km, r_1=500 km, m_1=15

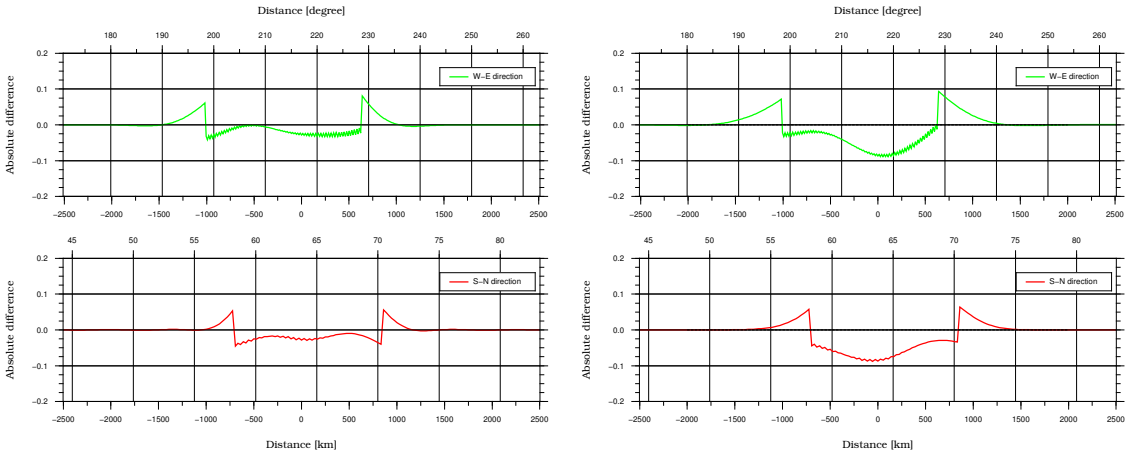

(c) r_0=500 km, r_1=1000 km, m_1=15

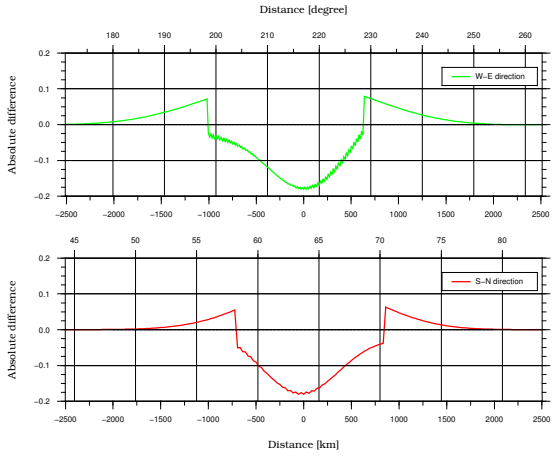

Figure B.6: Difference between the initial and recovered mass for Alaska with Han's anisotropic smoothing applied. West-east (green line) and south-north (red line) cross sections are displayed.

Kusche's de-correlated anisotropic smoothing

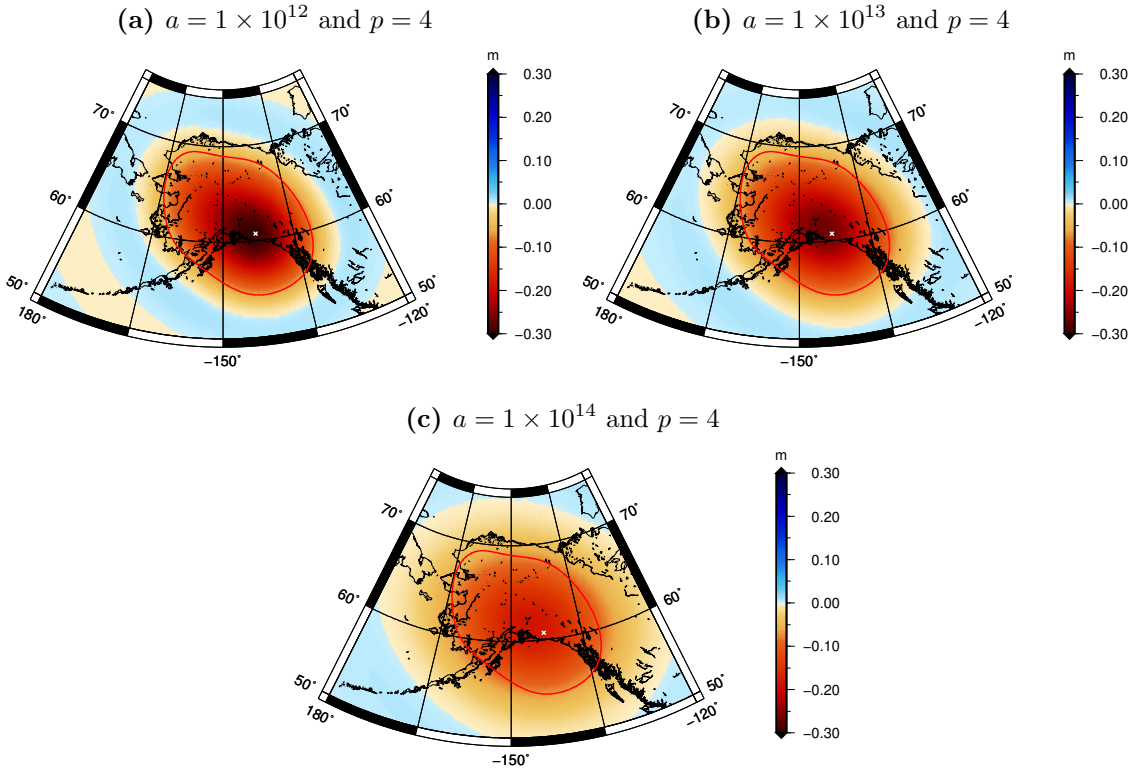

Figure B.7: Recovered masses over Alaska after applying Kusche's de-correlated anisotropic smoothing.

(a) $a = 1 \times 10^{12}$ and $p = 4$

(b) $a = 1 \times 10^{13}$ and $p = 4$

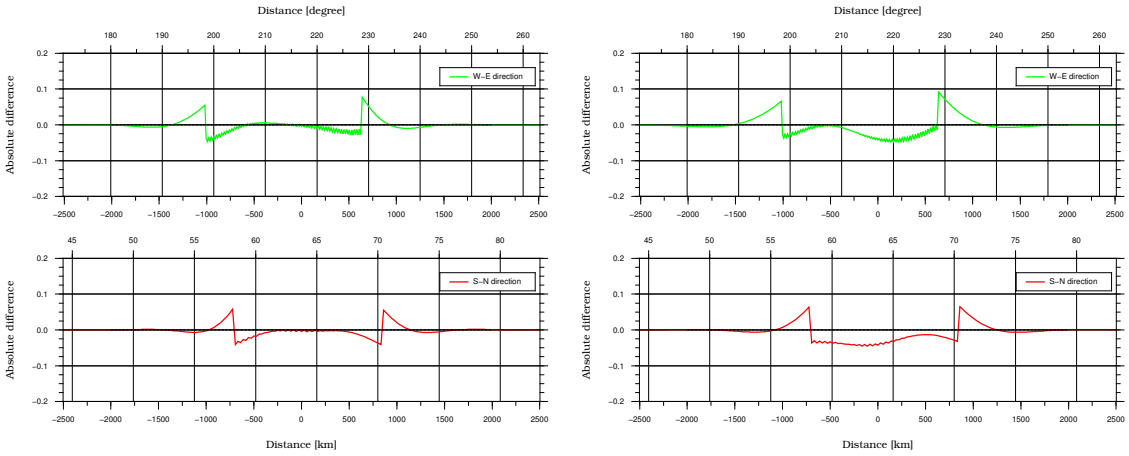

(c) $a = 1 \times 10^{14}$ and $p = 4$

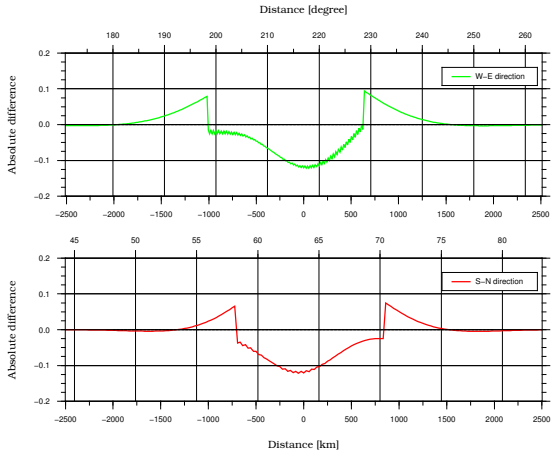

Figure B.8: Difference between the initial and recovered mass for Alaska with Kusche's de-correlated anisotropic smoothing applied. West-east (green line) and south-north (red line) cross sections are displayed.

B.2 Validation Results for Greenland

B.2.1 Initial mass

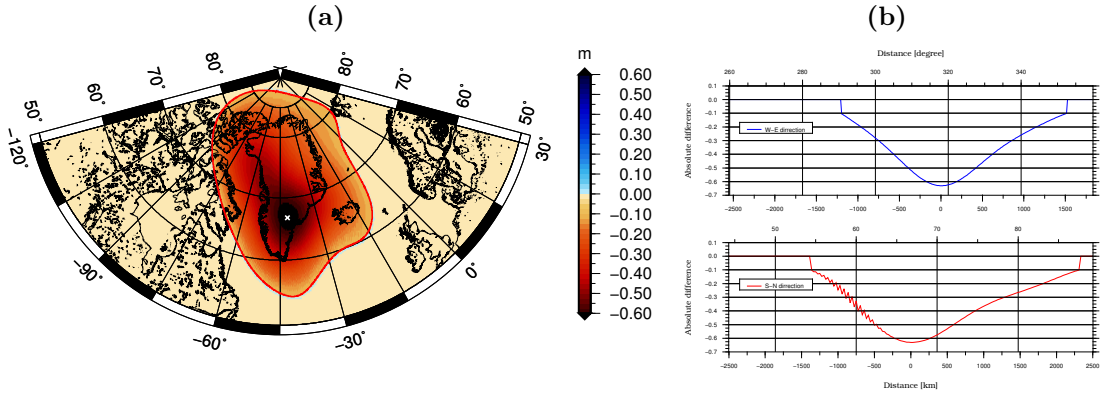

Figure B.9: (a) Initial mass distribution over Greenland, (b) Cross-sections in west-east (blue line) and south-north (red line) directions.

B.2.2 Recovered mass with no filter applied

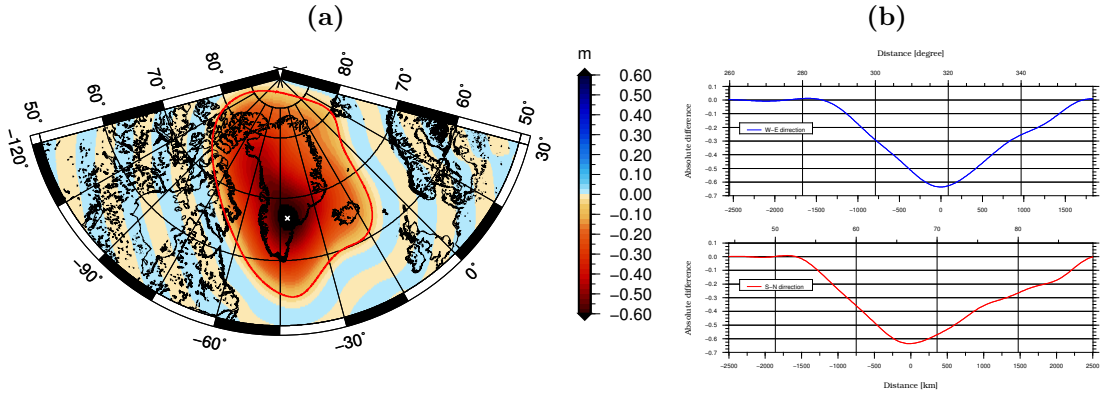

Figure B.10: (a) Recovered mass over Greenland, (b) Cross-sections in west-east (blue line) and south-north (red line) directions.

B.2.3 Results from different smoothing techniques

Gaussian isotropic smoothing

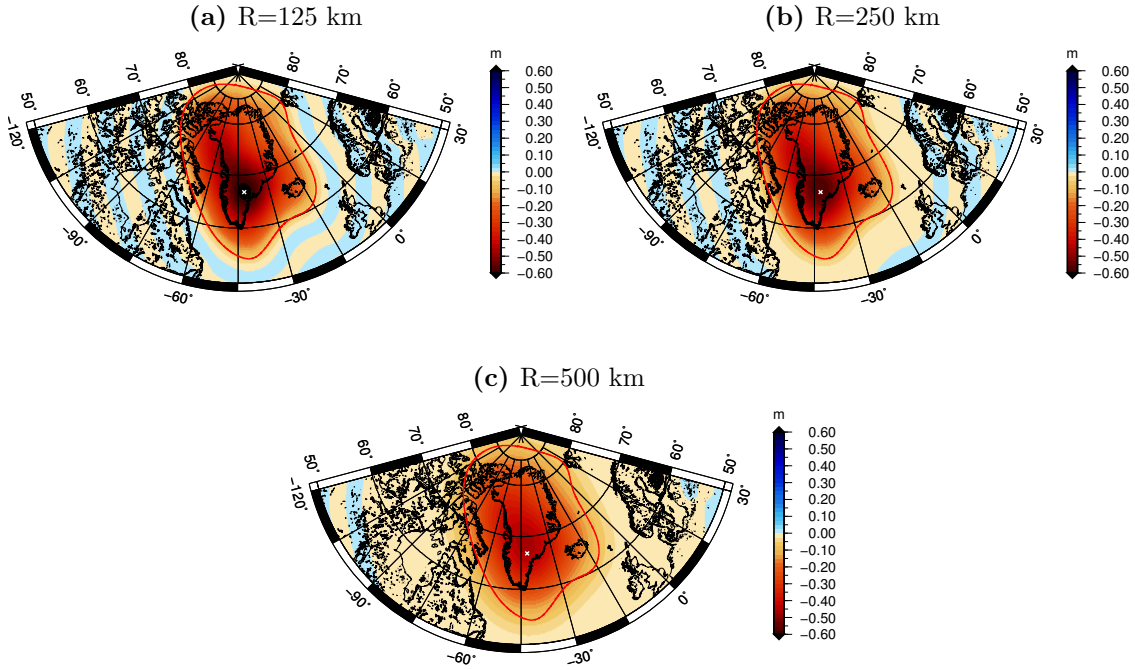

Figure B.11: Recovered masses over Greenland after applying Gaussian isotropic smoothing.

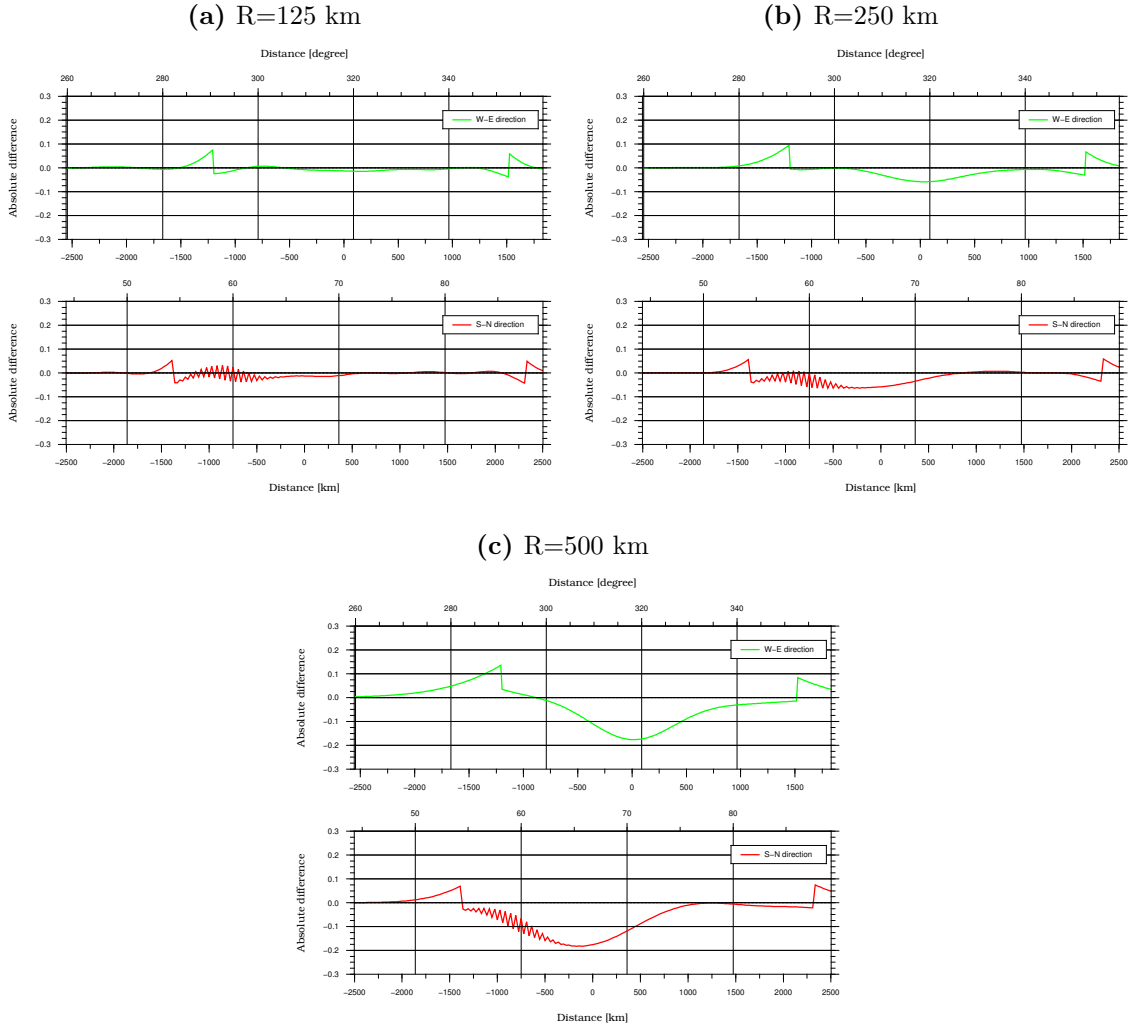

Figure B.12: Difference between the initial and recovered mass for Greenland with Gaussian isotropic smoothing applied. West-east (green line) and south-north (red line) cross sections are displayed.

d

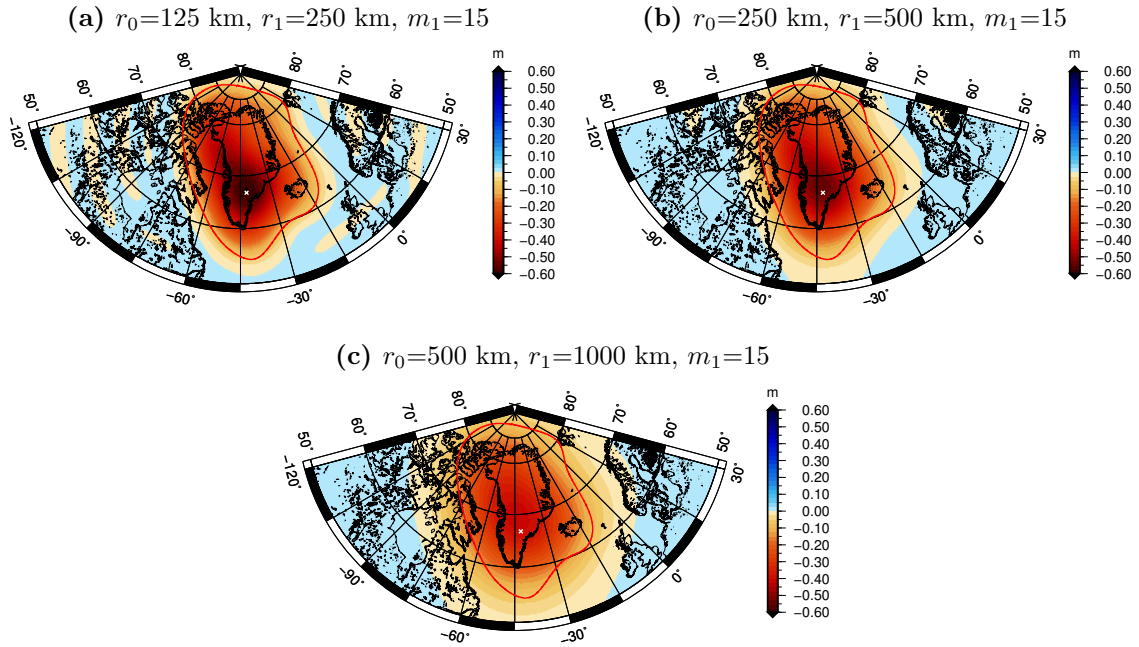

Figure B.13: Recovered masses over Greenland after applying Han's anisotropic smoothing.

(a) r_0=125 km, r_1=250 km, m_1=15

(b) r_0=250 km, r_1=500 km, m_1=15

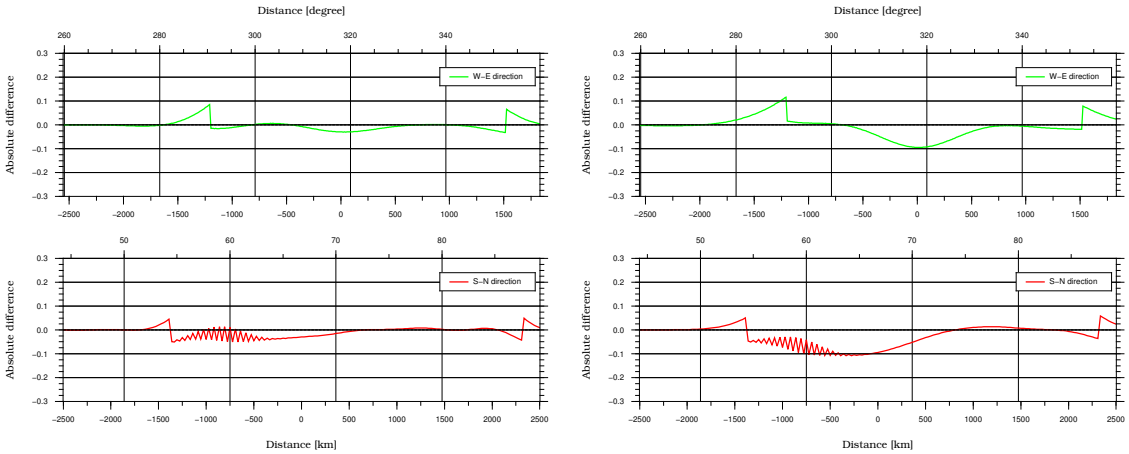

(c) r_0=500 km, r_1=1000 km, m_1=15

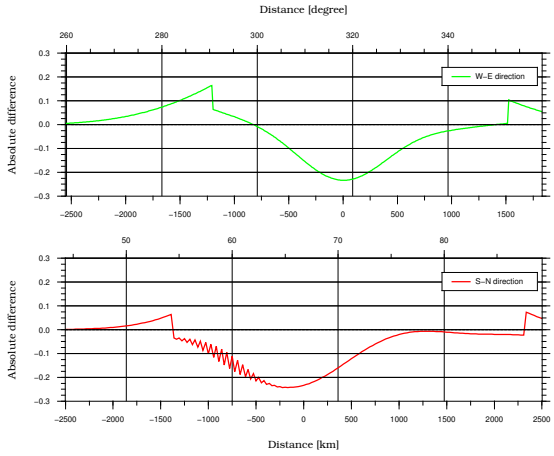

Figure B.14: Difference between the initial and recovered mass for Greenland with Han's anisotropic smoothing applied. West-east (green line) and south-north (red line) cross sections are displayed.

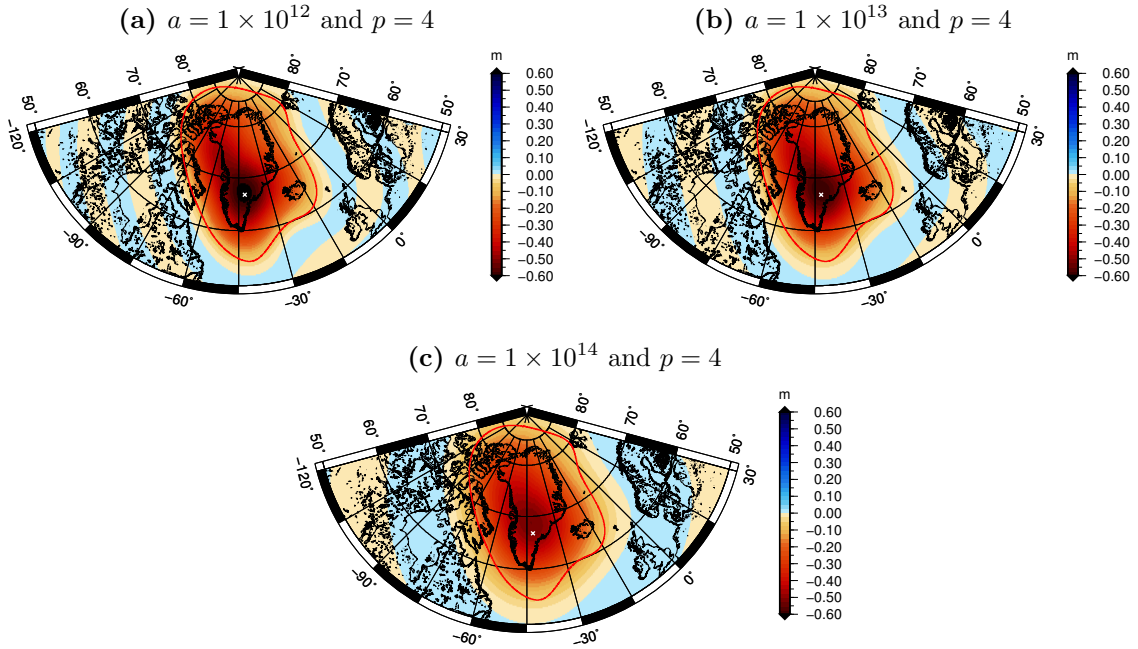

Figure B.15: Recovered masses over Greenland after applying Kusche's de-correlated anisotropic smoothing.

(a) $a = 1 \times 10^{12}$ and $p = 4$

(b) $a = 1 \times 10^{13}$ and $p = 4$

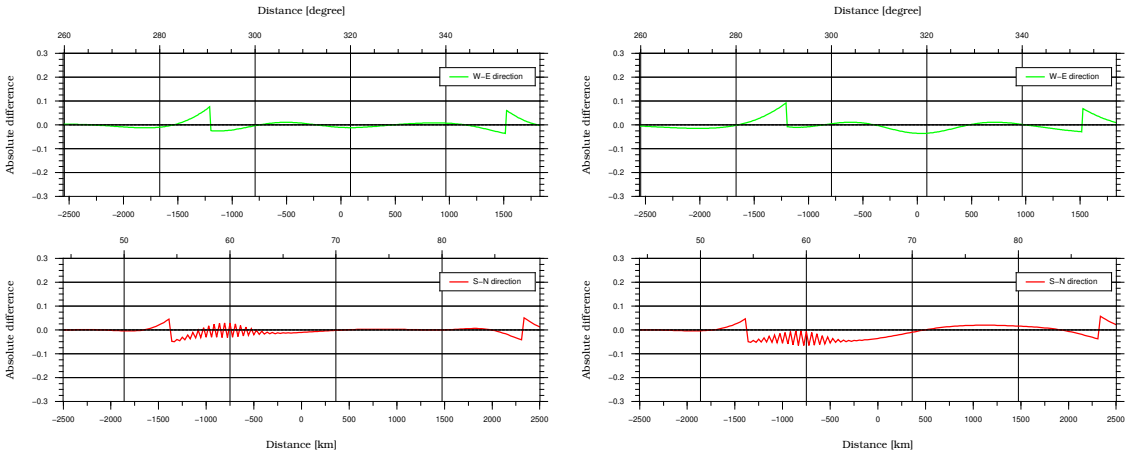

(c) $a = 1 \times 10^{14}$ and $p = 4$

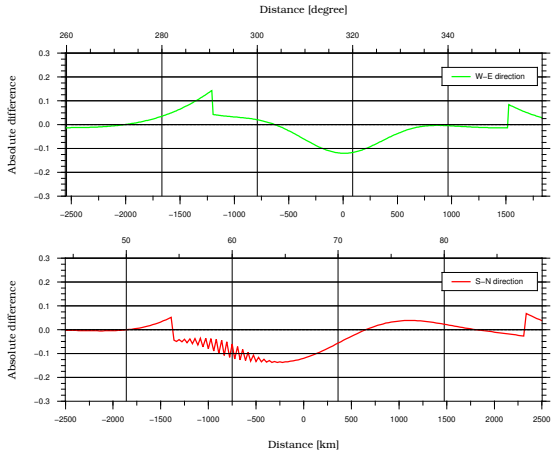

Figure B.16: Difference between the initial and recovered mass for Greenland with Kusche's de-correlated anisotropic smoothing applied. West-east (green line) and south-north (red line) cross sections are displayed.

B.3 Validation Results for Amazon Basin

B.3.1 Initial mass

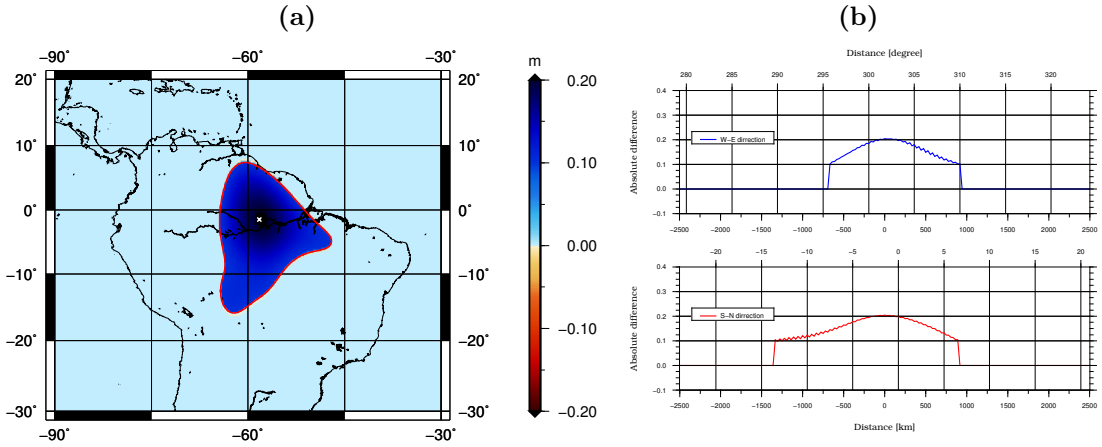

Figure B.17: (a) Initial mass distribution over Amazon Basin, (b) Cross-sections in west-east (blue line) and south-north (red line) directions.

B.3.2 Recovered mass with no filter applied

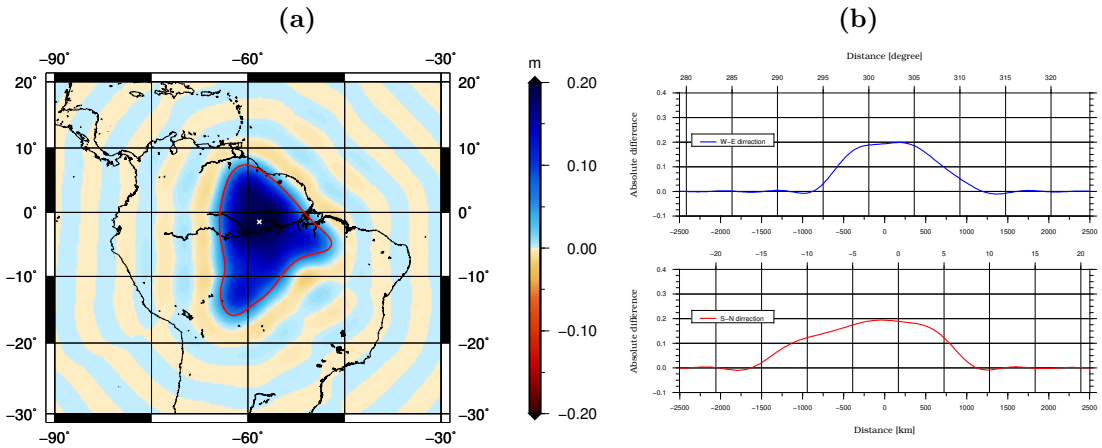

Figure B.18: (a) Recovered mass over Amazon Basin, (b) Cross-sections in west-east (blue line) and south-north (red line) directions.

B.3.3 Results from different smoothing techniques

Gaussian isotropic smoothing

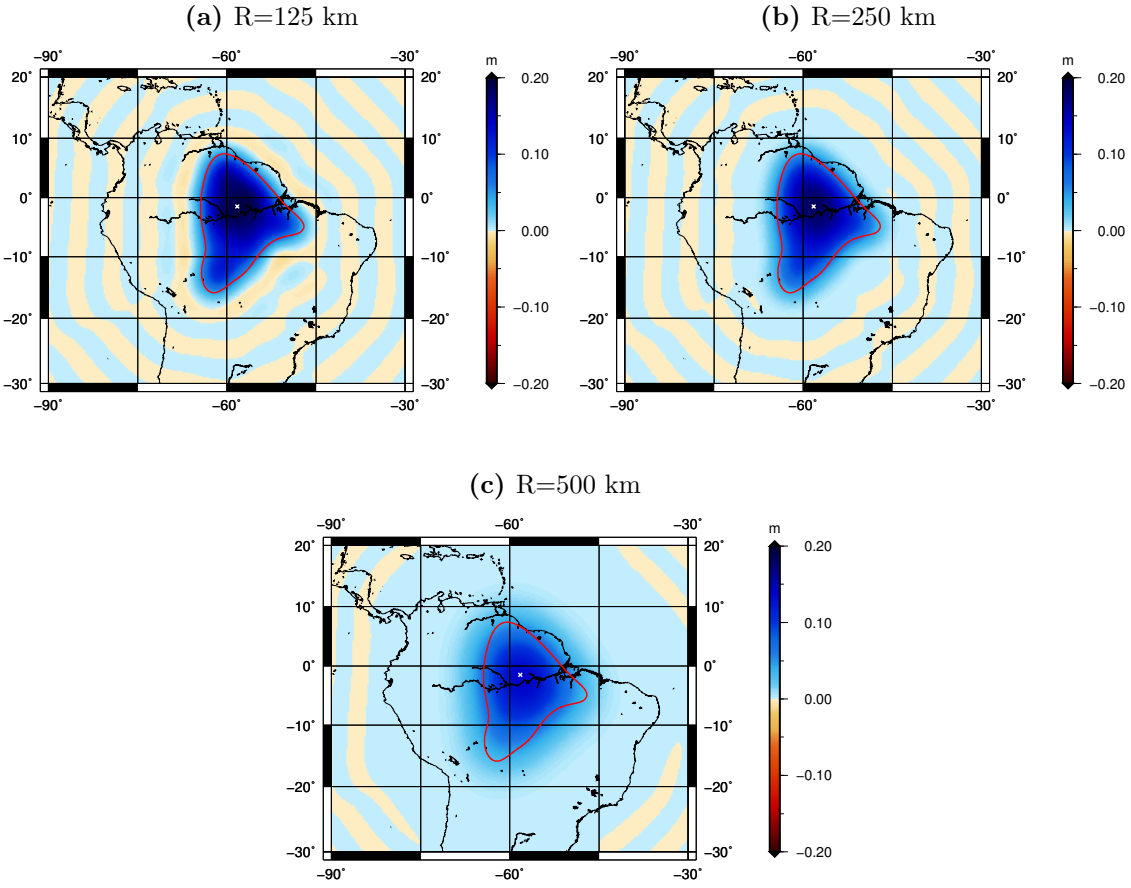

Figure B.19: Recovered masses over Amazon Basin after applying Gaussian isotropic smoothing.

(a) R=125 km

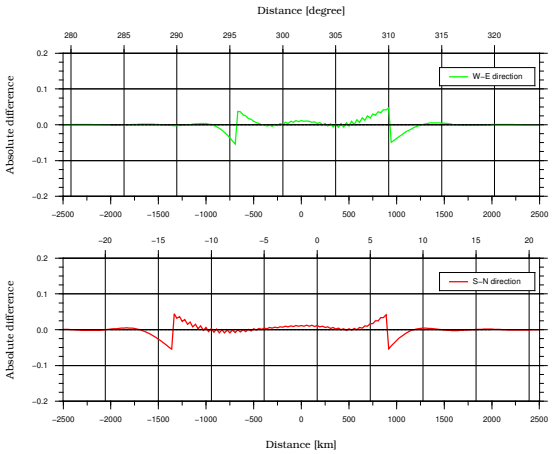

(b) R=250 km

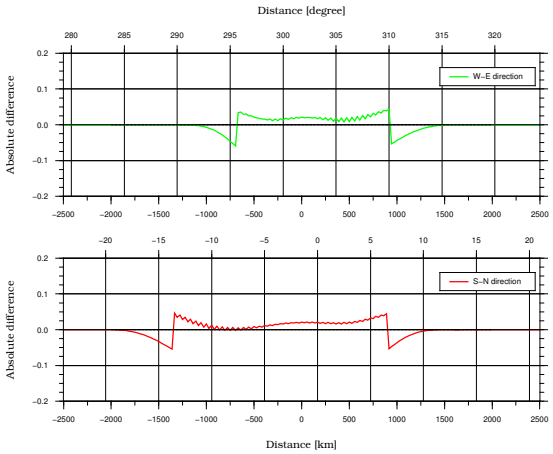

(c) R=500 km

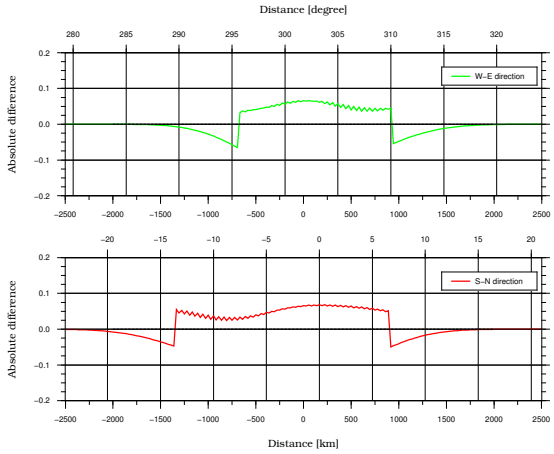

Figure B.20: Difference between the initial and recovered mass for Amazon Basin with Gaussian isotropic smoothing applied. West-east (green line) and south-north (red line) cross sections are displayed.

Han's anisotropic smoothing

d

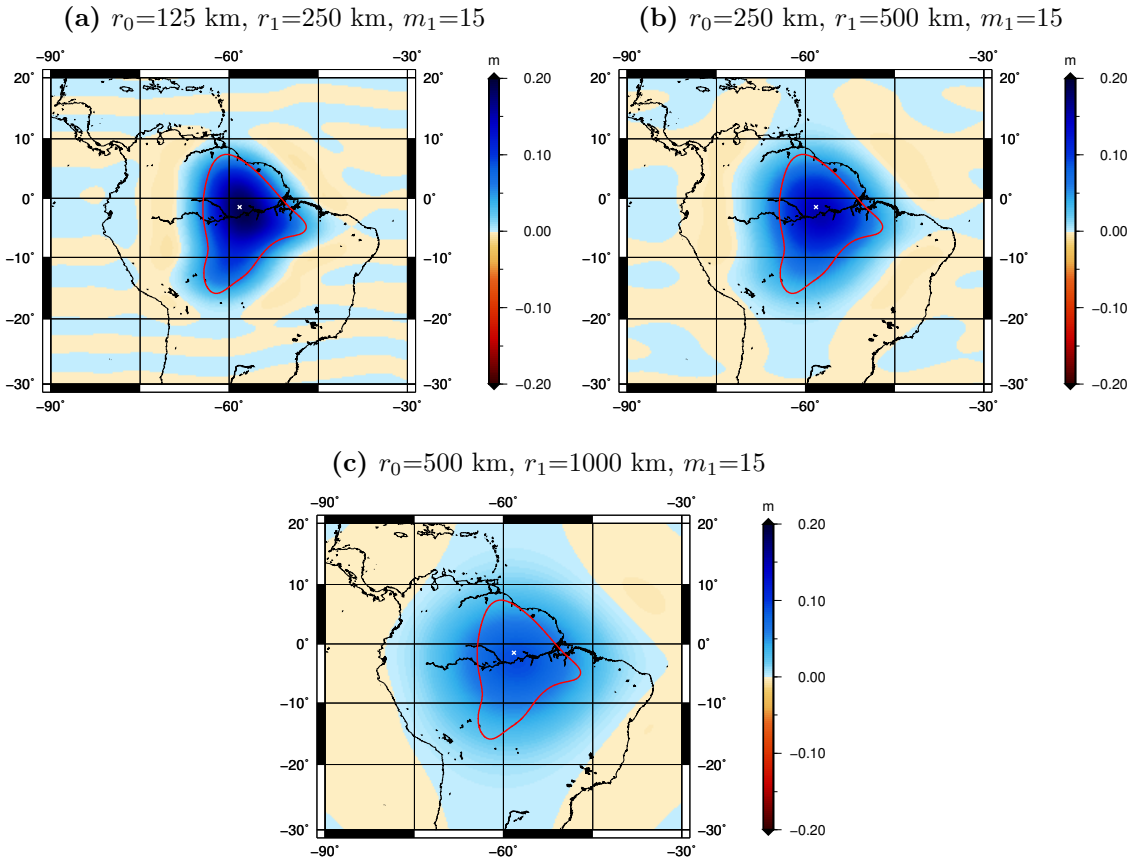

Figure B.21: Recovered masses over Amazon Basin after applying Han's anisotropic smoothing.

(a) r_0=125 km, r_1=250 km, m_1=15

(b) r_0=250 km, r_1=500 km, m_1=15

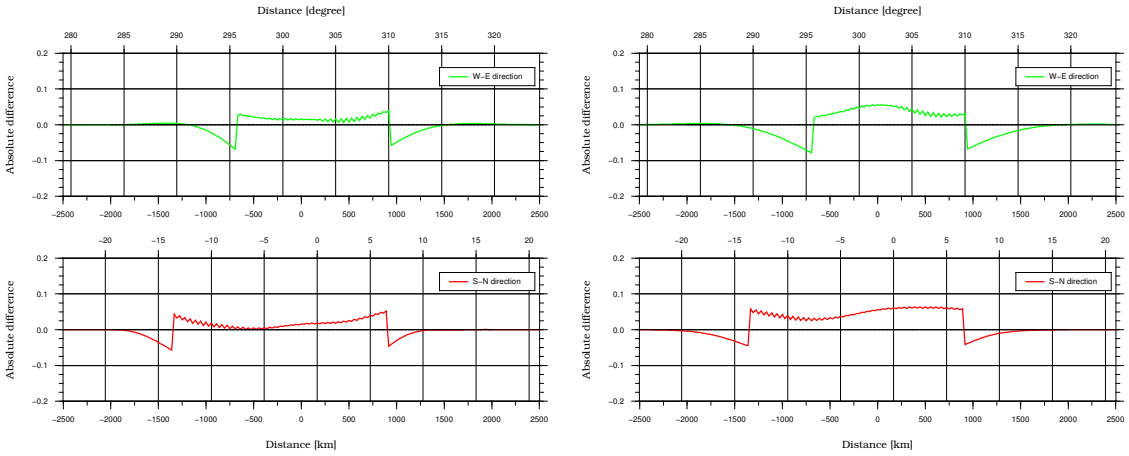

(c) r_0=500 km, r_1=1000 km, m_1=15

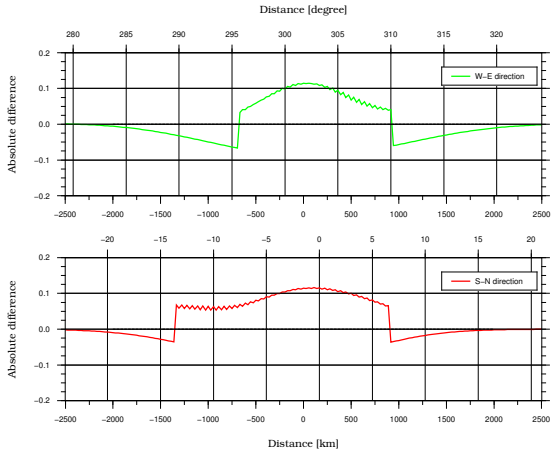

Figure B.22: Difference between the initial and recovered mass for Amazon Basin with Han's anisotropic smoothing applied. West-east (green line) and south-north (red line) cross sections are displayed.

Kusche's de-correlated anisotropic smoothing

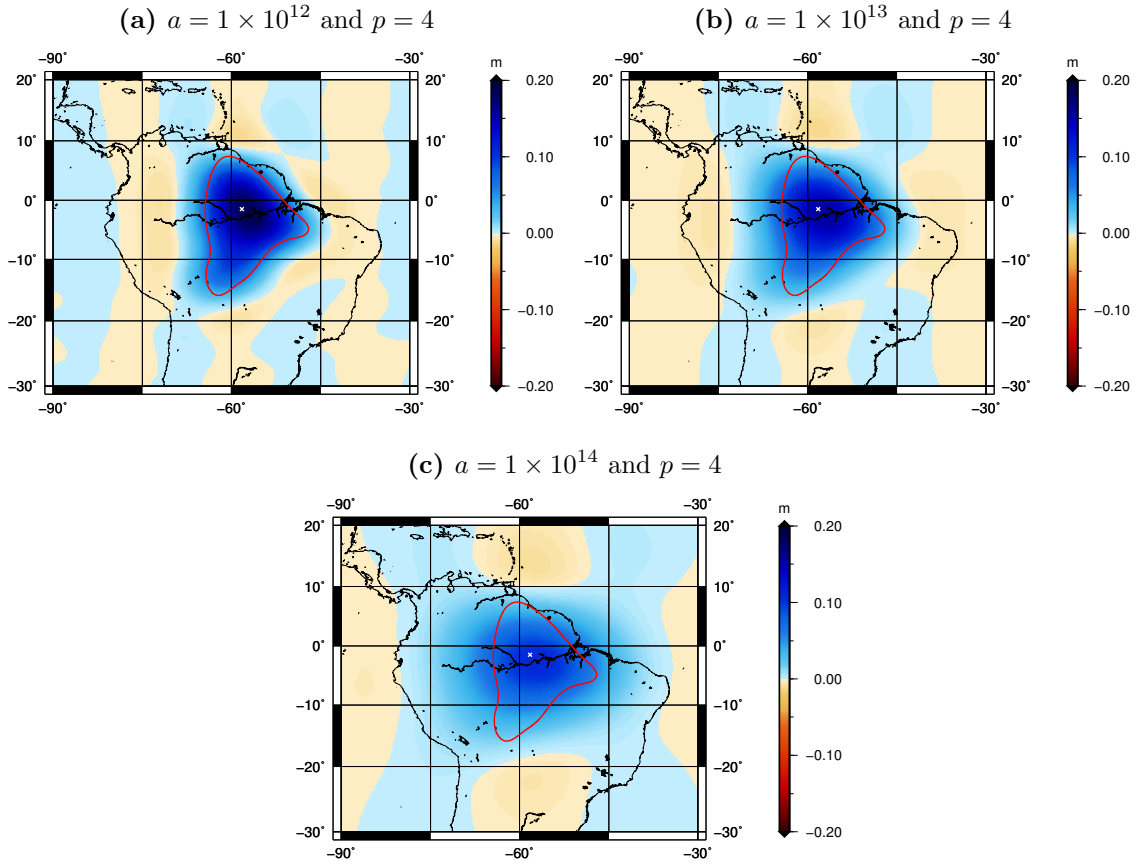

Figure B.23: Recovered masses over Amazon Basin after applying Kusche's de-correlated anisotropic smoothing.

(a) $a = 1 \times 10^{12}$ and $p = 4$

(b) $a = 1 \times 10^{13}$ and $p = 4$

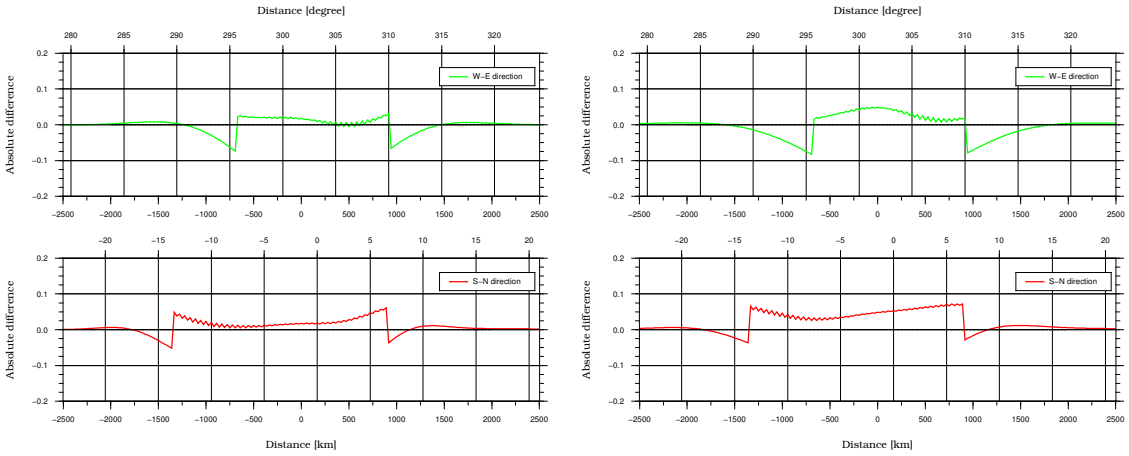

(c) $a = 1 \times 10^{14}$ and $p = 4$

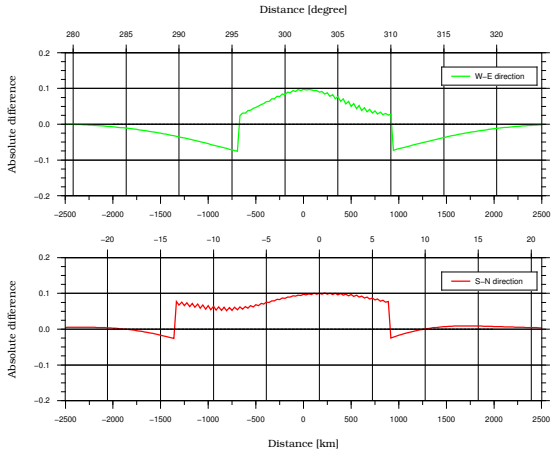

Figure B.24: Difference between the initial and recovered mass for Amazon Basin with Kusche's de-correlated anisotropic smoothing applied. West-east (green line) and south-north (red line) cross sections are displayed.

B.4 Validation Results for West Antarctica

B.4.1 Initial mass

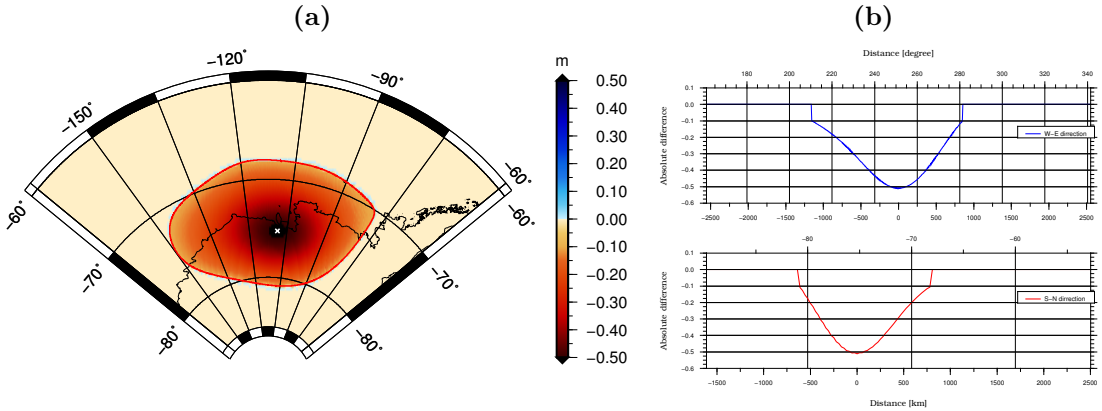

Figure B.25: (a) Initial mass distribution over West Antarctica, (b) Cross-sections in west-east (blue line) and south-north (red line) directions.

B.4.2 Recovered mass with no filter applied

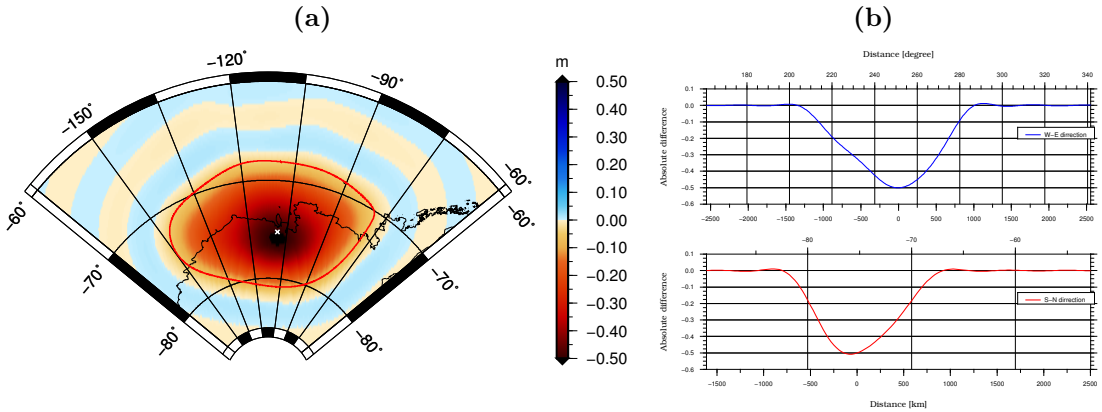

Figure B.26: (a) Recovered mass over West Antarctica, (b) Cross-sections in west-east (blue line) and south-north (red line) directions.

B.4.3 Results from different smoothing techniques

Gaussian isotropic smoothing

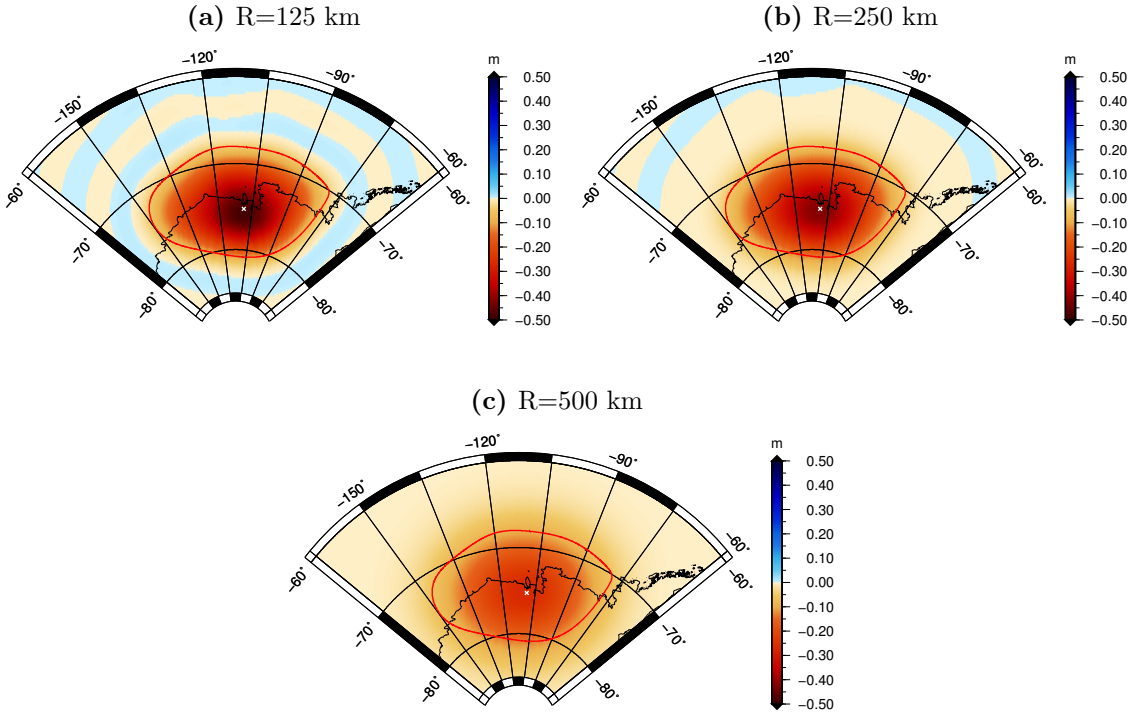

Figure B.27: Recovered masses over West Antarctica after applying Gaussian isotropic smoothing.

(a) R=125 km

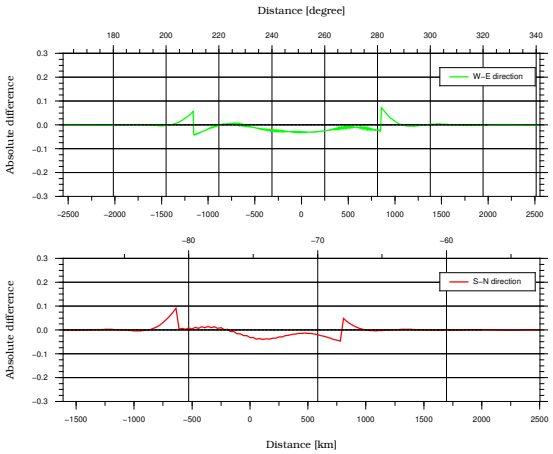

(b) R=250 km

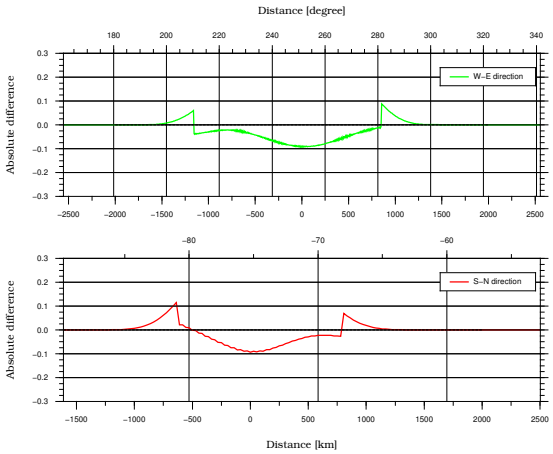

(c) R=500 km

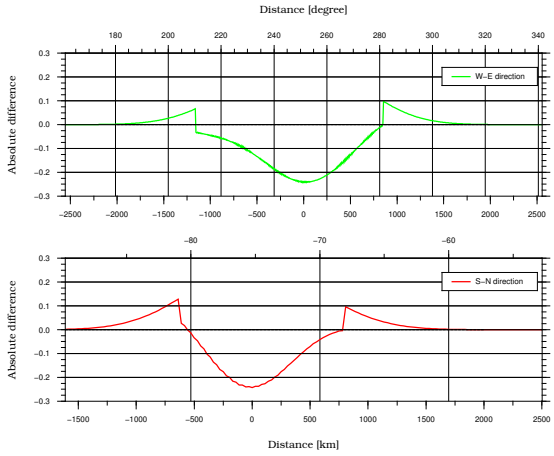

Figure B.28: Difference between the initial and recovered mass for West Antarctica with Gaussian isotropic smoothing applied. West-east (green line) and south-north (red line) cross sections are displayed.

d

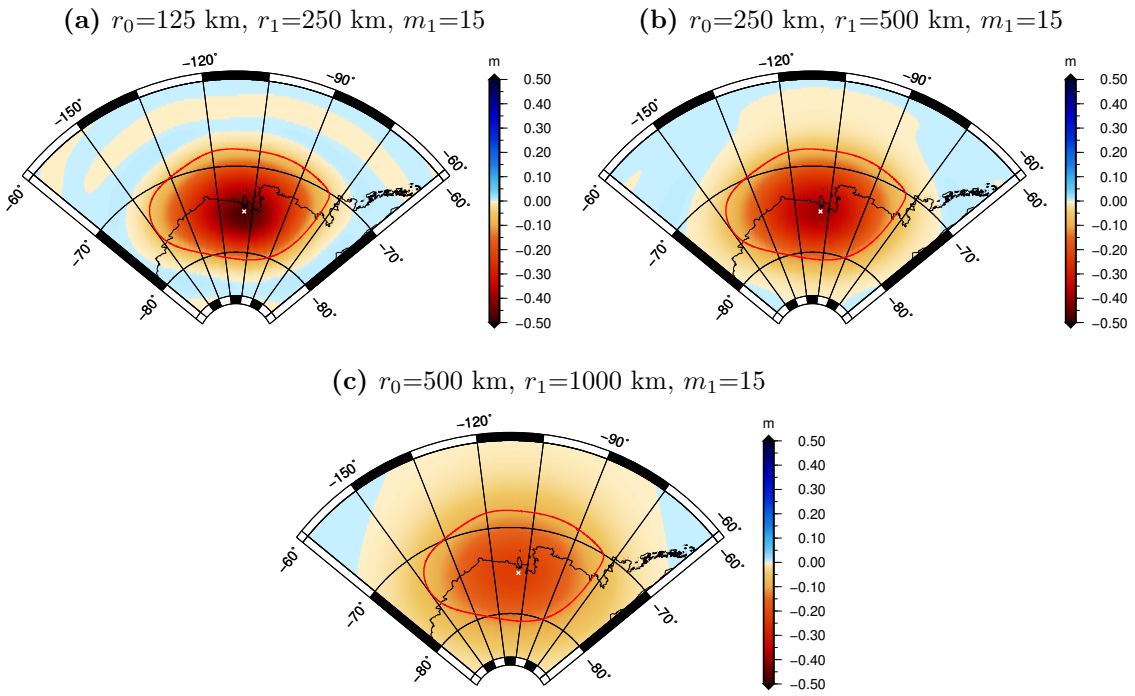

Figure B.29: Recovered masses over West Antarctica after applying Han's anisotropic smoothing.

(a) r_0=125 km, r_1=250 km, m_1=15

(b) r_0=250 km, r_1=500 km, m_1=15

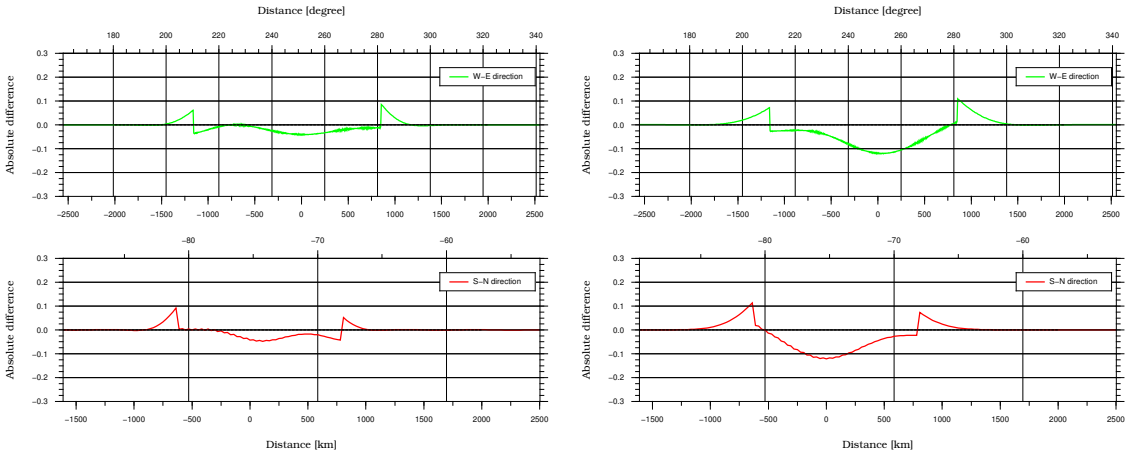

(c) r_0=500 km, r_1=1000 km, m_1=15

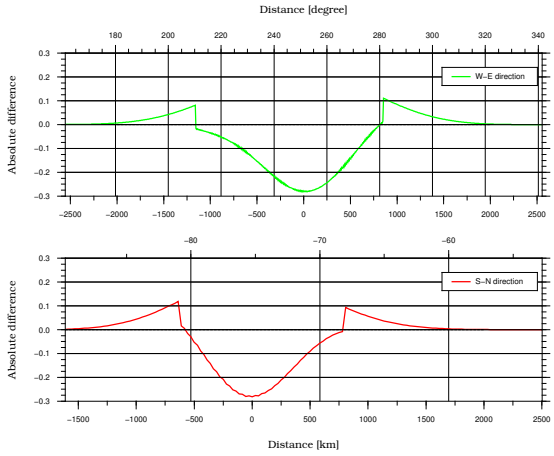

Figure B.30: Difference between the initial and recovered mass for West Antarctica with Han's anisotropic smoothing applied. West-east (green line) and south-north (red line) cross sections are displayed.

Kusche's de-correlated anisotropic smoothing

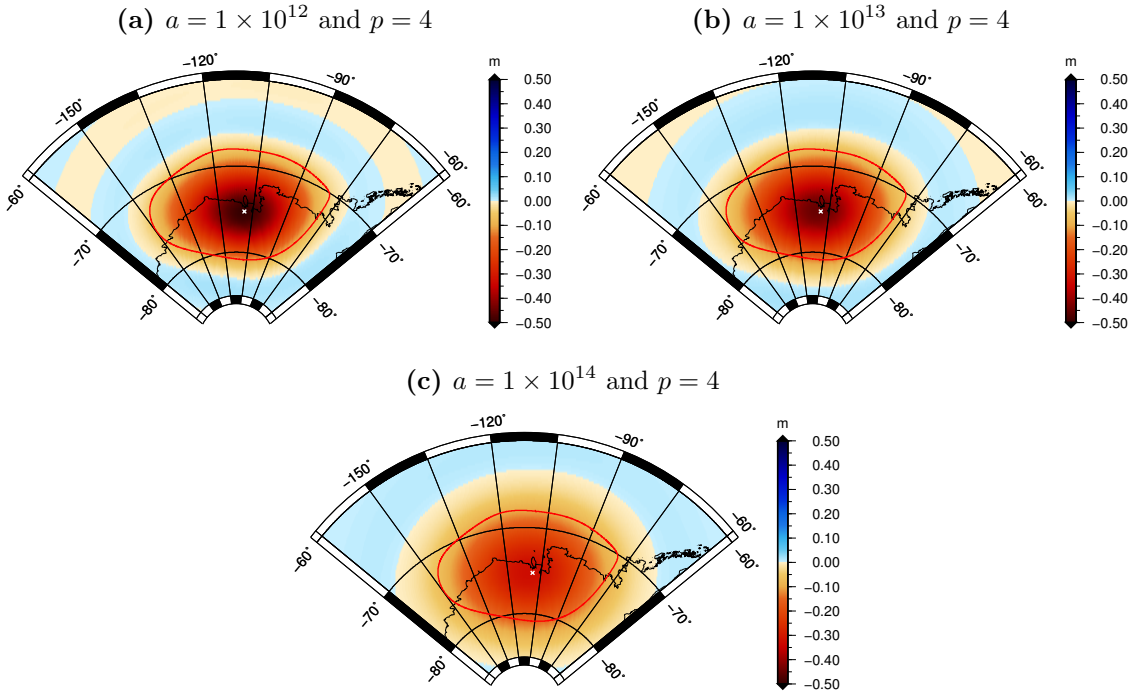

Figure B.31: Recovered masses over West Antarctica after applying Kusche's de-correlated anisotropic smoothing.

(a) $a = 1 \times 10^{12}$ and $p = 4$

(b) $a = 1 \times 10^{13}$ and $p = 4$

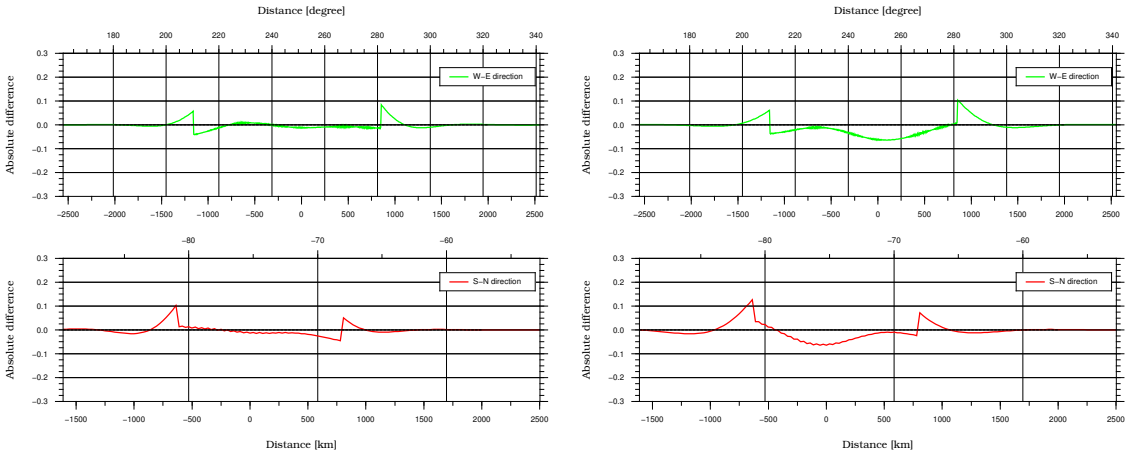

(c) $a = 1 \times 10^{14}$ and $p = 4$

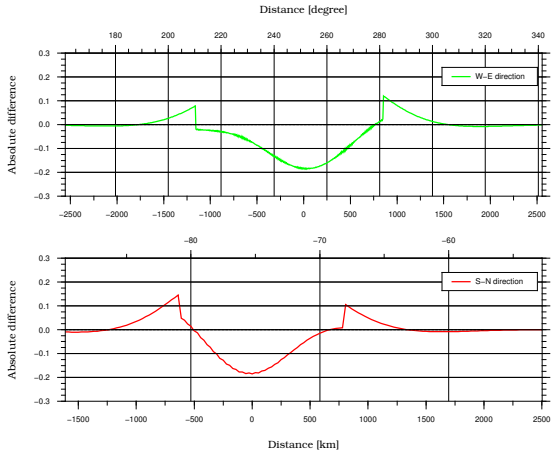

Figure B.32: Difference between the initial and recovered mass for West Antarctica with Kusche's de-correlated anisotropic smoothing applied. West-east (green line) and south-north (red line) cross sections are displayed.

B.5 Validation Results for Sumatra-Andaman

B.5.1 Initial mass

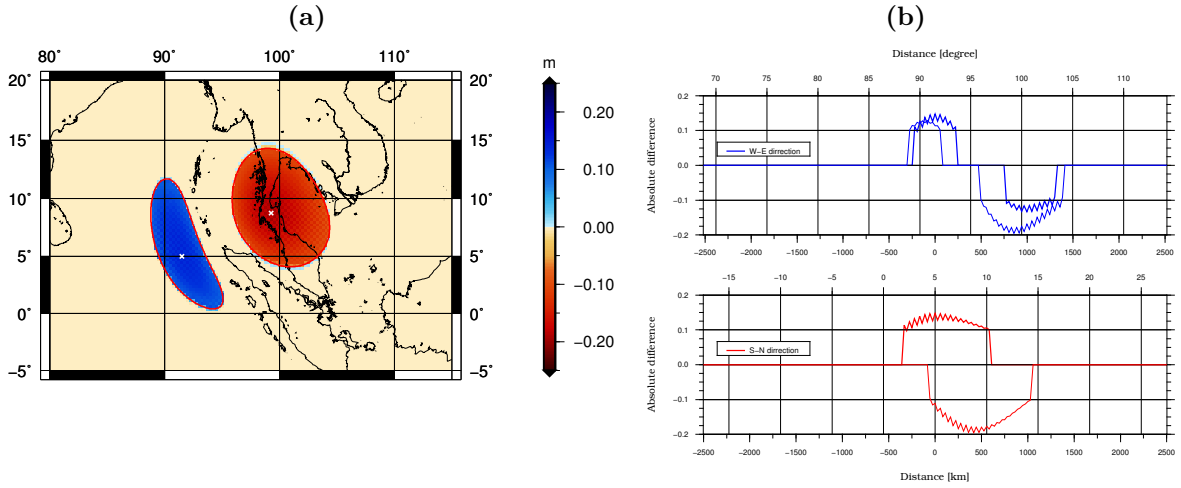

Figure B.33: (a) Initial mass distribution over Sumatra-Andaman, (b) Cross-sections in west-east (blue line) and south-north (red line) directions.

B.5.2 Recovered mass with no filter applied

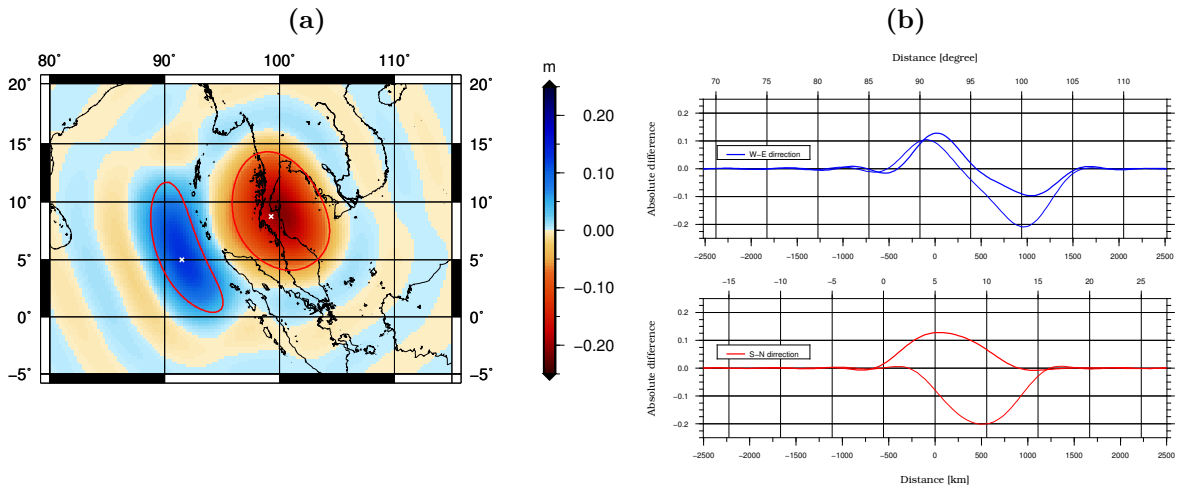

Figure B.34: (a) Recovered mass over Sumatra-Andaman, (b) and (c) Cross-sections in west-east (blue line) and south-north (red line) directions.

B.5.3 Results from different smoothing techniques

Gaussian isotropic smoothing

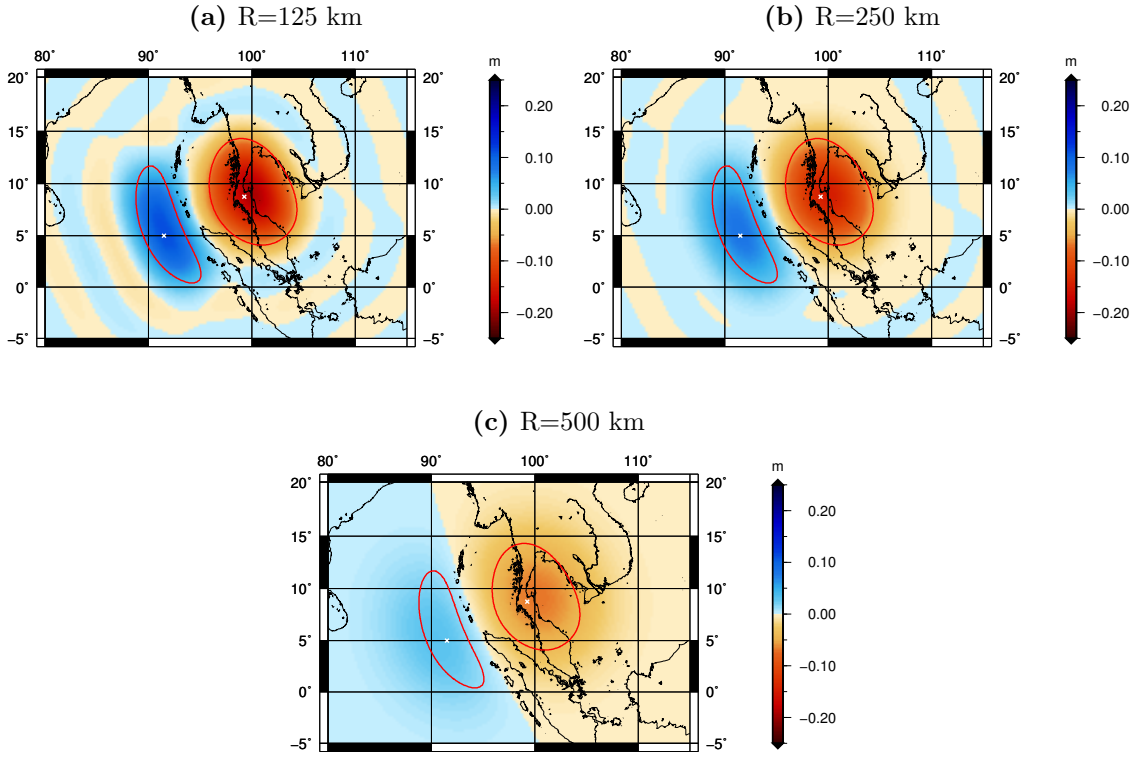

Figure B.35: Recovered masses over Sumatra-Andaman after applying Gaussian isotropic smoothing.

(a) R=125 km

(b) R=250 km

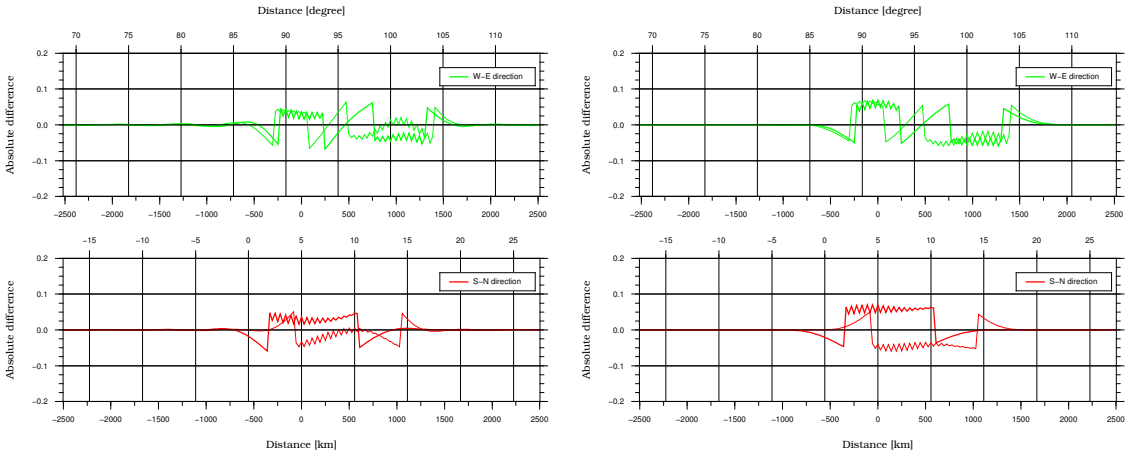

(c) R=500 km

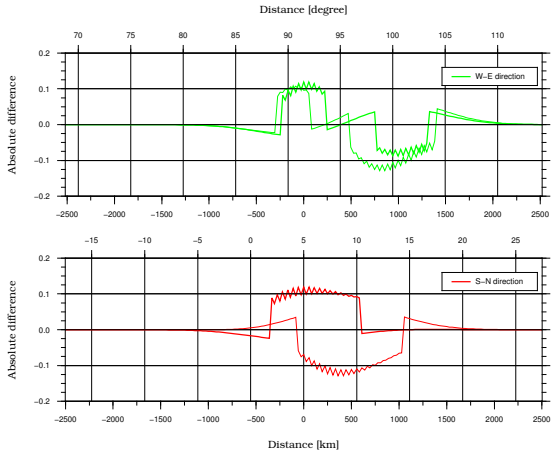

Figure B.36: Difference between the initial and recovered mass for Sumatra-Andaman with Gaussian isotropic smoothing applied. West-east (green line) and south-north (red line) cross sections are displayed.

Han's anisotropic smoothing

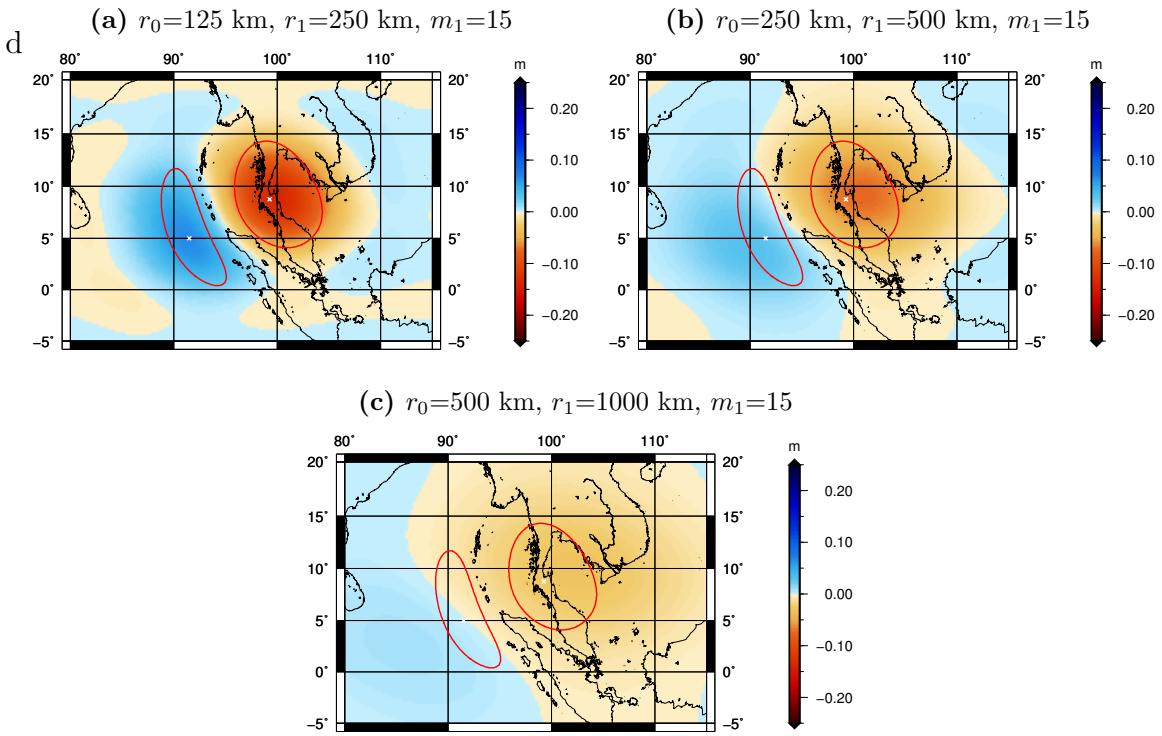

Figure B.37: Recovered masses over Sumatra-Andaman after applying Han's anisotropic smoothing.

(a) r_0=125 km, r_1=250 km, m_1=15

(b) r_0=250 km, r_1=500 km, m_1=15

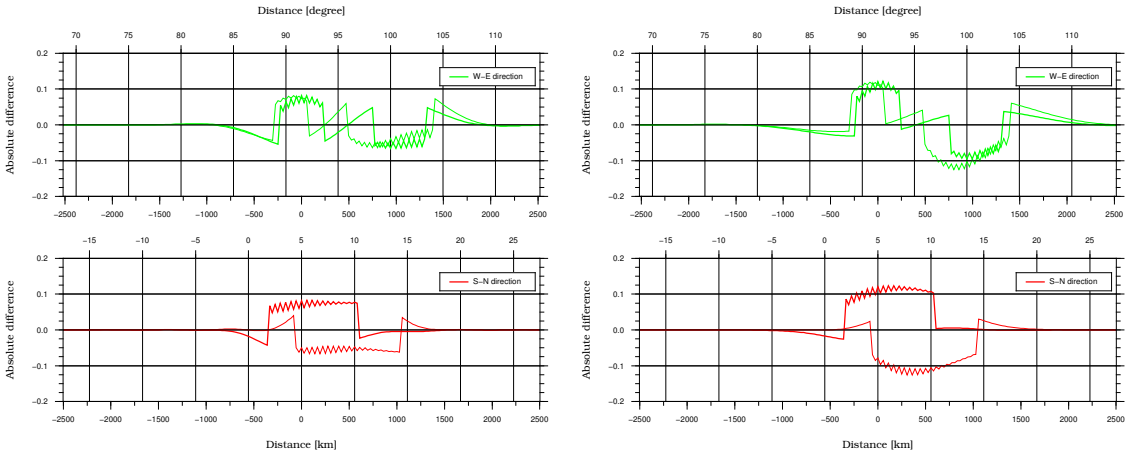

(c) r_0=500 km, r_1=1000 km, m_1=15

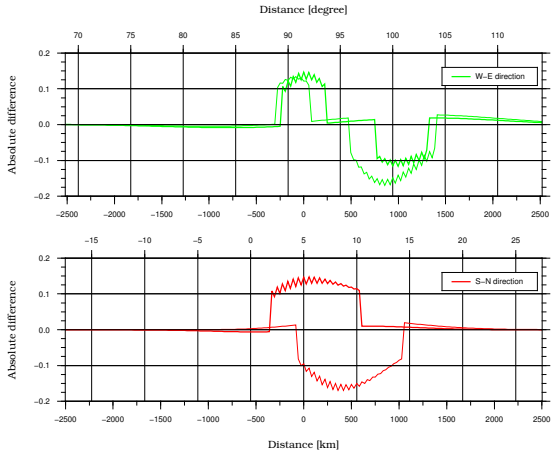

Figure B.38: Difference between the initial and recovered mass for Sumatra Andaman with Han's anisotropic smoothing applied. West-east (green line) and south-north (red line) cross sections are displayed.

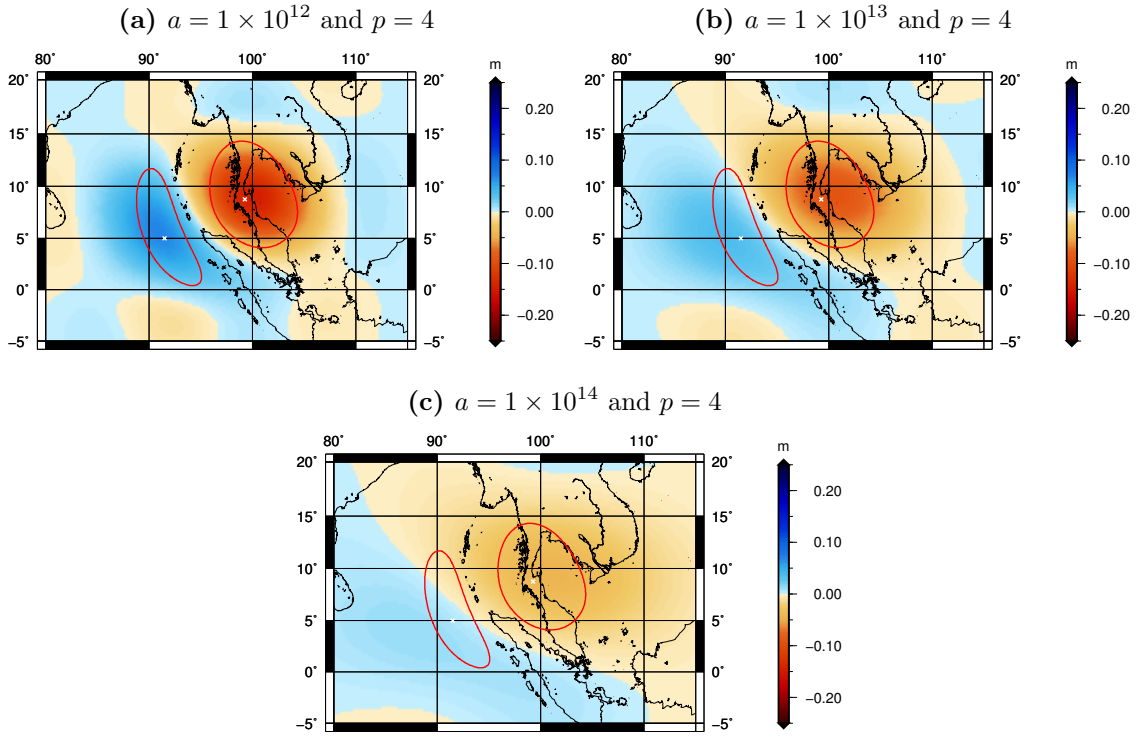

Figure B.39: Recovered masses over Sumatra-Andaman after applying Kusche's de-correlated anisotropic smoothing.

(a) $a = 1 \times 10^{12}$ and $p = 4$

(b) $a = 1 \times 10^{13}$ and $p = 4$

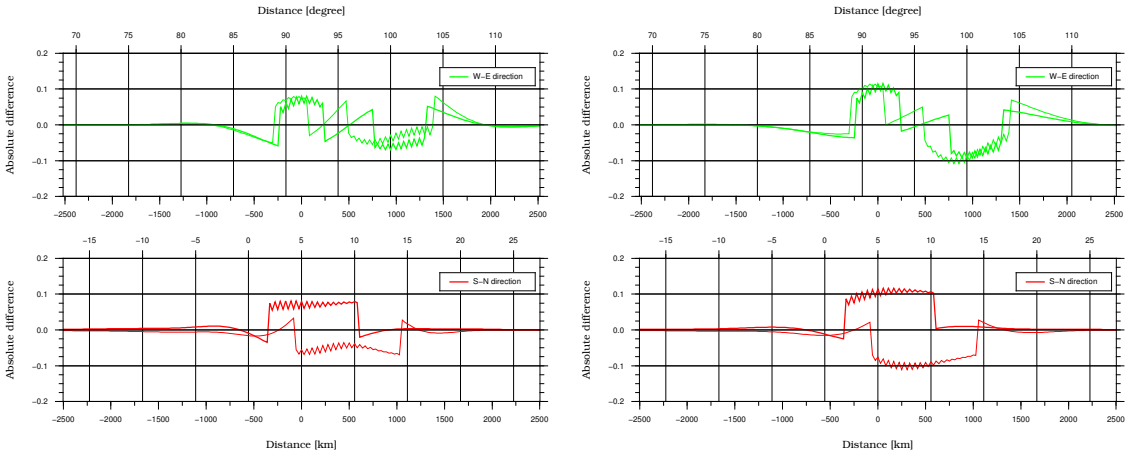

(c) $a = 1 \times 10^{14}$ and $p = 4$

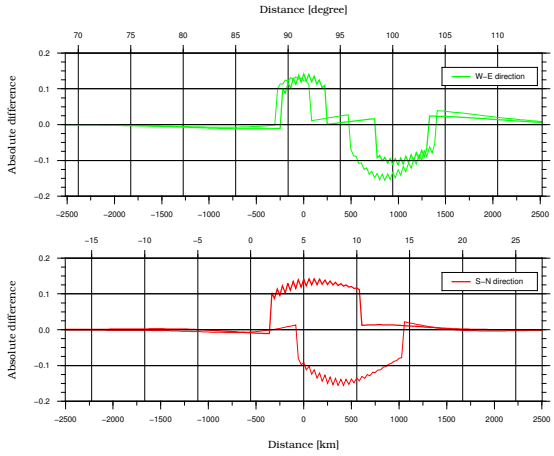

Figure B.40: Difference between the initial and recovered mass for Sumatra-Andaman with Kusche's de-correlated anisotropic smoothing applied.

B.6 Validation Results for Lake Victoria

B.6.1 Initial mass

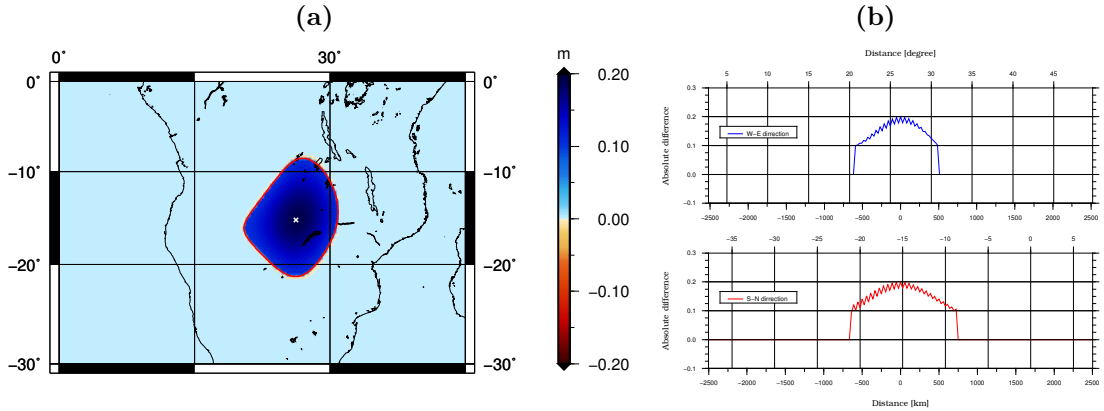

Figure B.41: (a) Initial mass distribution over Lake Victoria, (b) Cross-sections in west-east (blue line) and south-north (red line) directions.

B.6.2 Recovered mass with no filter applied

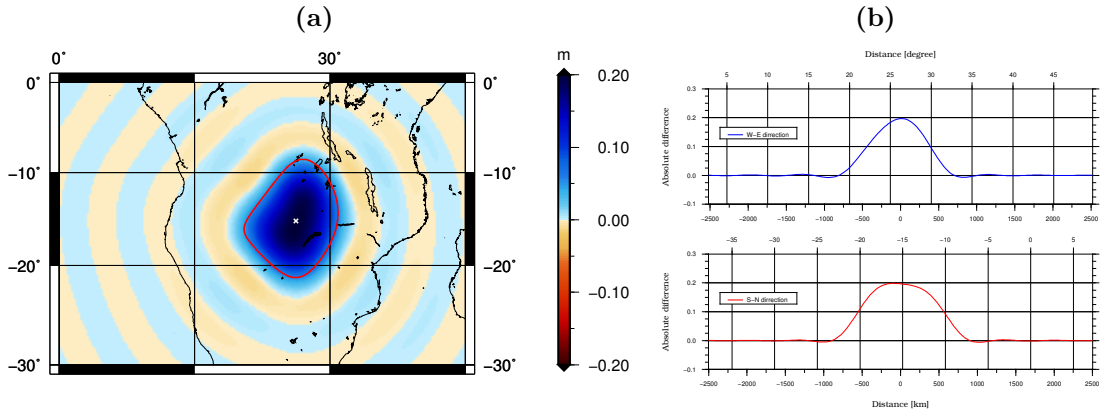

Figure B.42: (a) Recovered mass over Lake Victoria, (b) Cross-sections in west-east (blue line) and south-north (red line) directions.

B.6.3 Results from different smoothing techniques

Gaussian isotropic smoothing

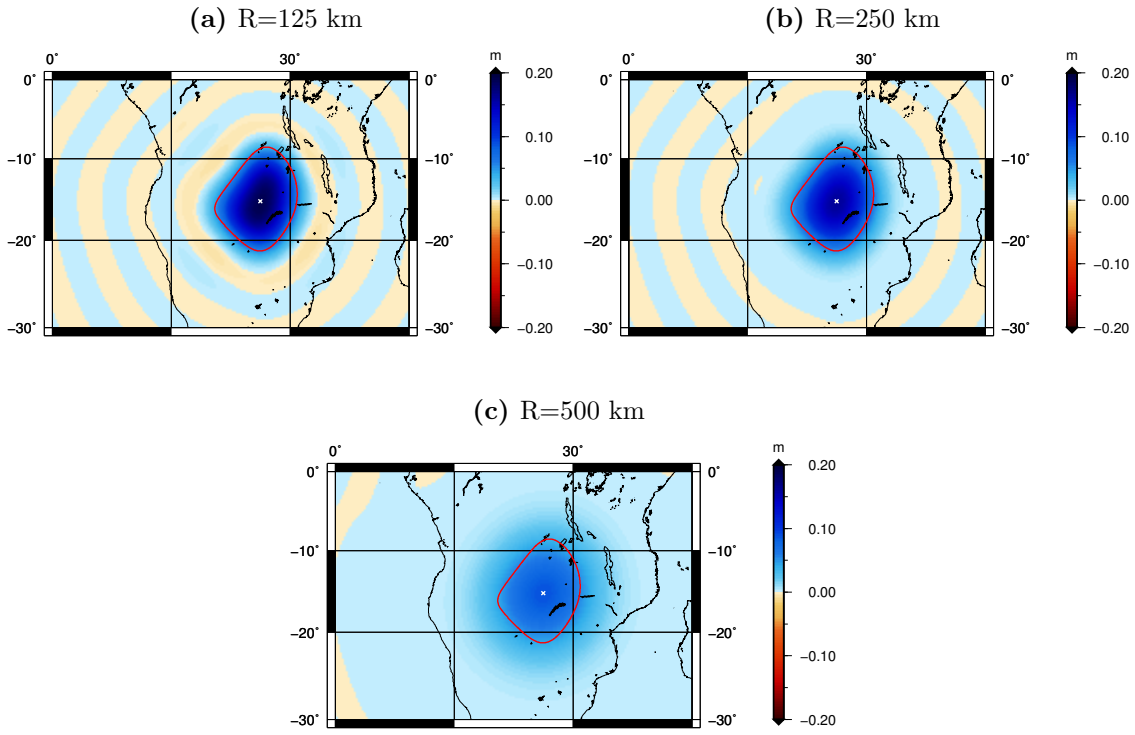

Figure B.43: Recovered masses over Lake Victoria after applying Gaussian isotropic smoothing.

(a) R=125 km

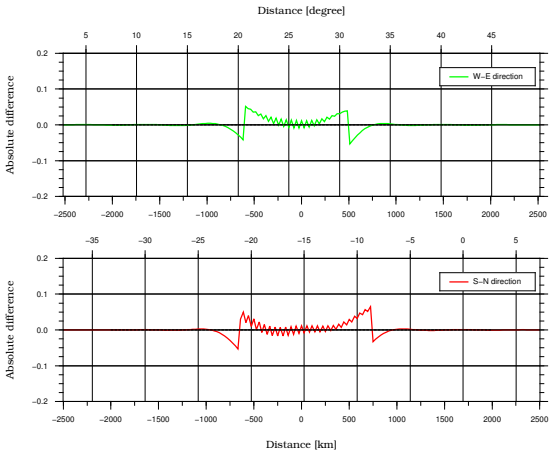

(b) R=250 km

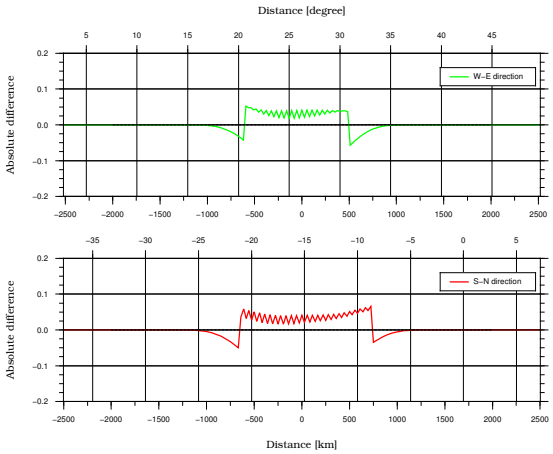

(c) R=500 km

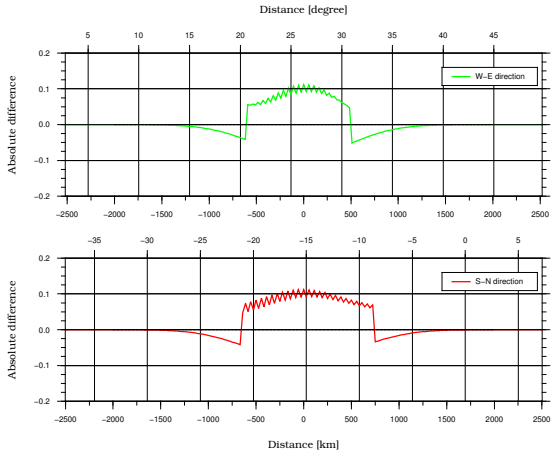

Figure B.44: Difference between the initial and recovered mass for Lake Victoria with Gaussian isotropic smoothing applied. West-east (green line) and south-north (red line) cross sections are displayed.

Han's anisotropic smoothing

d

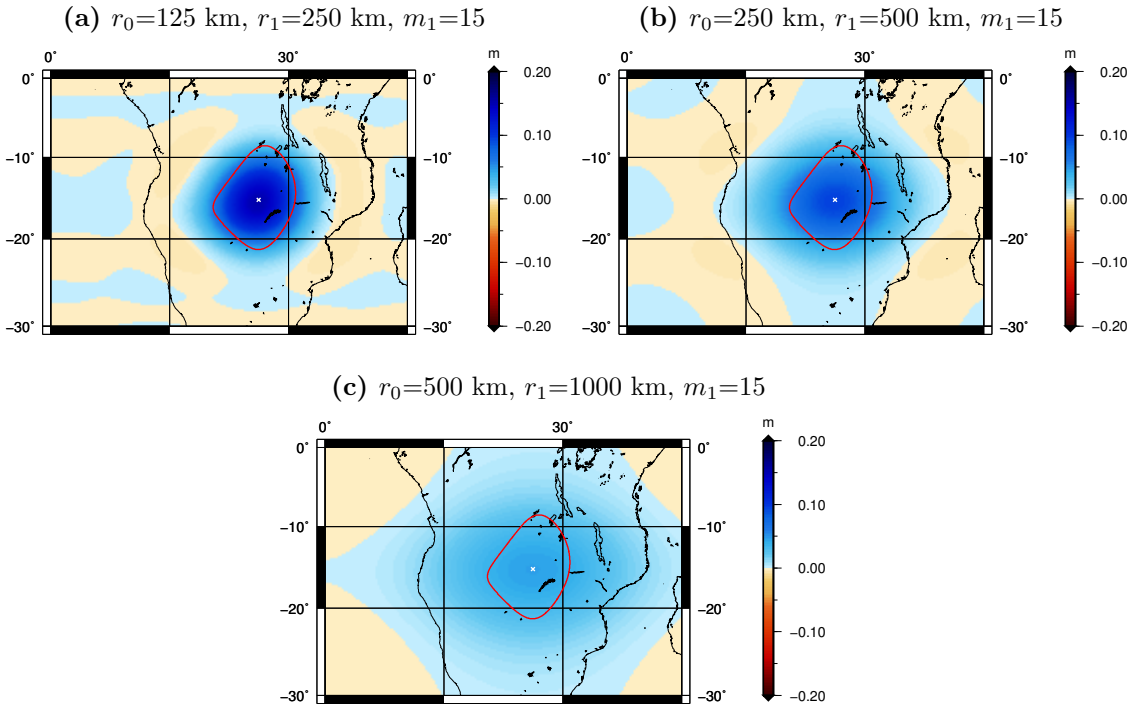

Figure B.45: Recovered masses over Lake Victoria after applying Han's anisotropic smoothing.

(a) r_0=125 km, r_1=250 km, m_1=15

(b) r_0=250 km, r_1=500 km, m_1=15

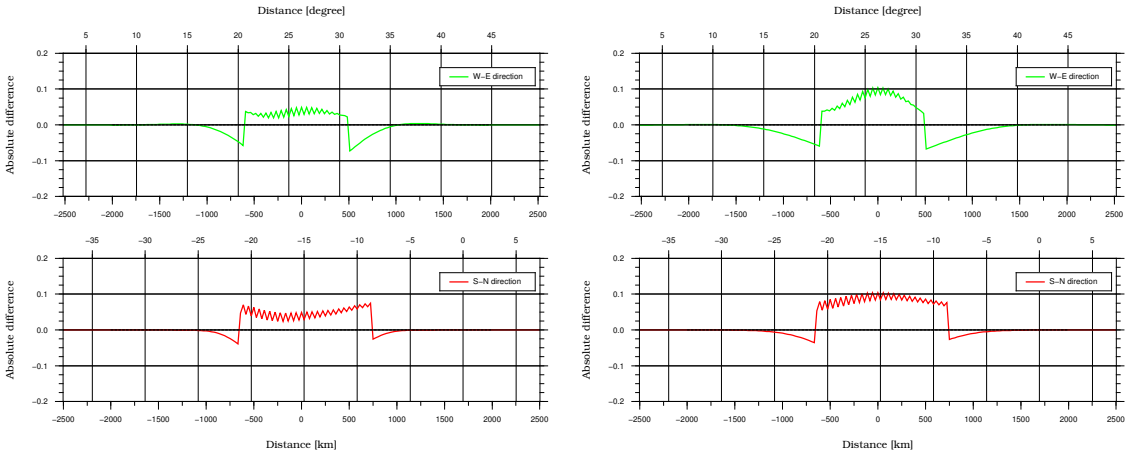

(c) r_0=500 km, r_1=1000 km, m_1=15

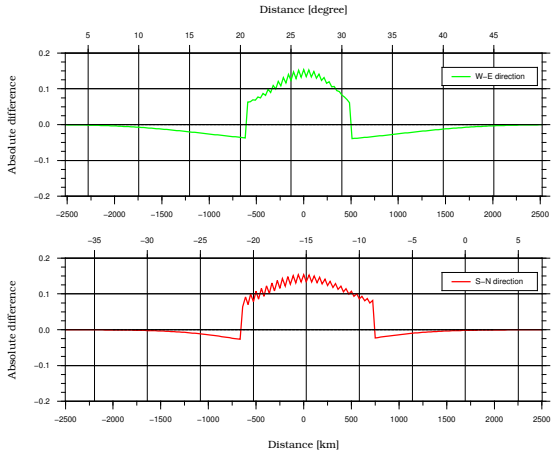

Figure B.46: Difference between the initial and recovered mass for Lake Victoria with Han's anisotropic smoothing applied. West-east (green line) and south-north (red line) cross sections are displayed.

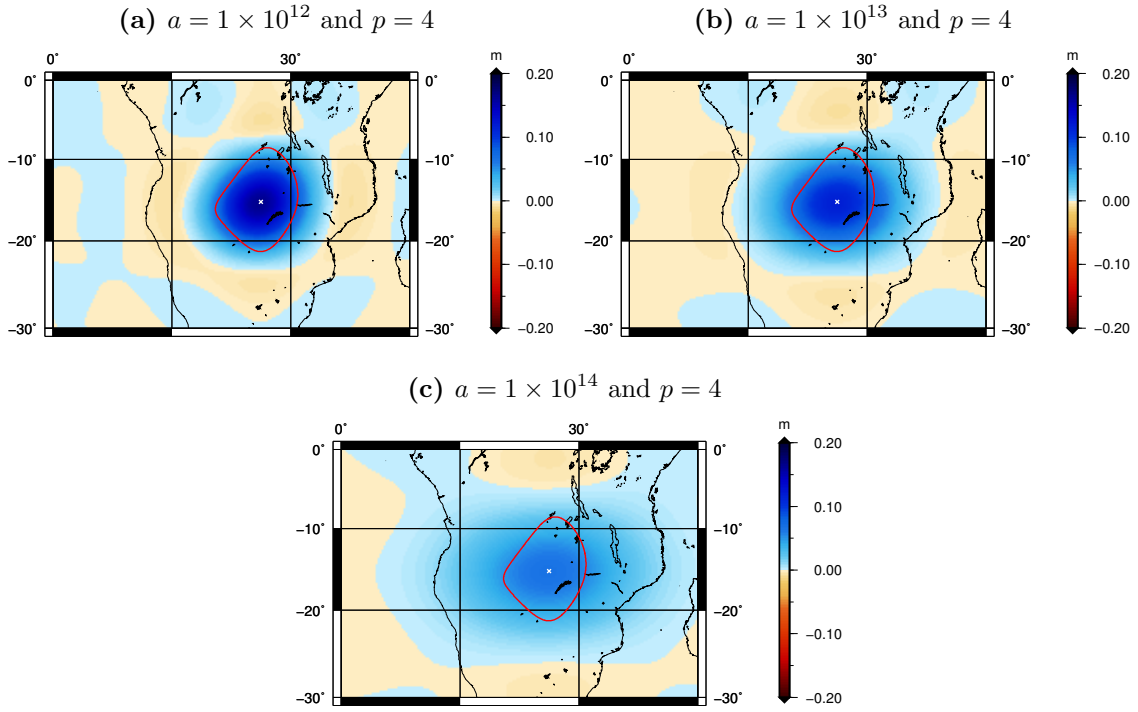

Figure B.47: Recovered masses over Lake Victoria after applying Kusche's de-correlated anisotropic smoothing.

(a) $a = 1 \times 10^{12}$ and $p = 4$

(b) $a = 1 \times 10^{13}$ and $p = 4$

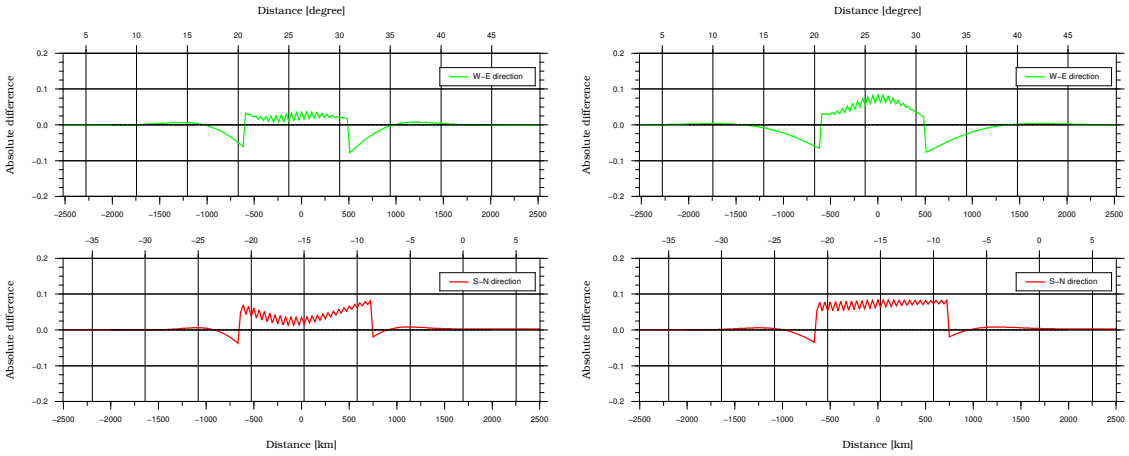

(c) $a = 1 \times 10^{14}$ and $p = 4$

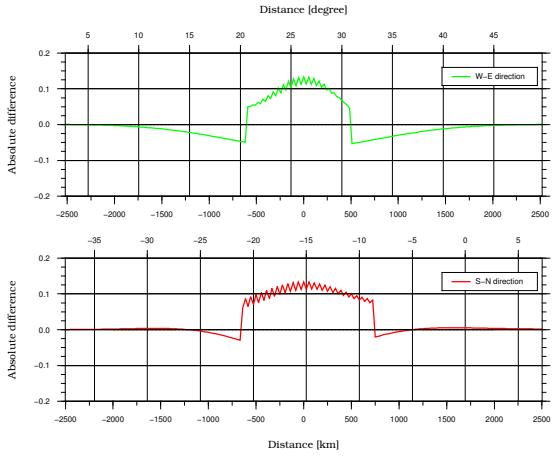

Figure B.48: Difference between the initial and recovered mass for Lake Victoria with Kusche's de-correlated anisotropic smoothing applied. West-east (green line) and south-north (red line) cross sections are displayed.